Freie Universität Berlin

Silicon isotope fractionation at low temperatures in the presence of Aluminum:

An experimental approach and application to different weathering regimes

Dissertation

zur Erlangung des Grades eines

Doktors der Naturwissenschaften (doctor rerum naturalium)

am Fachbereich Geowissenschaften

der Freien Universität Berlin

vorgelegt von:

Marcus Oelze

Berlin 2015

(I was not able to decide which citation describes me and my work best, therefore I decided to give two citations here!)

Our whole universe was in a hot dense state,
Then nearly fourteen billion years ago expansion started. Wait...
The Earth began to cool,
The autotrophs began to drool,
Neanderthals developed tools,
We built a wall (we built the pyramids),
Math, science, history, unraveling the mysteries,
That all started with the big bang!

"Since the dawn of man" is really not that long,
As every galaxy was formed in less time than it takes to sing this song.
A fraction of a second and the elements were made.
The bipeds stood up straight,
The dinosaurs all met their fate,
They tried to leap but they were late
And they all died (they froze their asses off)
The oceans and pangea
See ya, wouldn't wanna be ya
Set in motion by the same big bang!

It all started with the big BANG!

It's expanding ever outward but one day
It will cause the stars to go the other way,
Collapsing ever inward, we won't be here, it wont be hurt
Our best and brightest figure that it'll make an even bigger bang!

Australopithecus would really have been sick of us
Debating out while here they're catching deer (we're catching viruses)
Religion or astronomy, Encarta, Deuteronomy
It all started with the big bang!

Music and mythology, Einstein and astrology
It all started with the big bang!
It all started with the big BANG!

(This nerdy song describes my nerdy universe!)
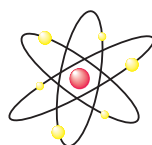
It's been a long road
Getting from there to here
It's been a long time
But my time is finally near
And I can feel the change in the wind right now
Nothing's in my way
And they're not gonna hold me down no more
No they're not gonna hold me down

'Cause I've got faith of the heart
I'm going where my heart will take me
I've got faith to believe, I can do anything
I've got strength of the soul
And no one's gonna bend or break me
I can reach any star, I've got faith
I've got faith, faith of the heart

It's been a long night
Trying to find my way
Been through the darkness
Now I finally have my day
And I will see my dream come alive at last
I will touch the sky
And they're not gonna hold me down no more
No they're not gonna change my mind

'Cause I've got faith of the heart
I'm going where my heart will take me
I've got faith to believe, I can do anything
I've got strength of the soul
And no one's gonna bend or break me
I can reach any star, I've got faith
Faith of the heart

I've known a wind so cold and seen the darkest days
But now the winds I feel are only winds of change
I've been through the fire and I've been through the rain but I'll be fine

'Cause I've got faith of the heart
I'm going where my heart will take me
I've got faith to believe, I can do anything
I've got strength of the soul
And no one's gonna bend or break me
I can reach any star, I've got faith
Faith of the

Faith of the heart
I'm going where my heart will take me
I've got faith to believe
That no one's gonna bend or break me

I can reach any star
'Cause I've got faith
'Cause I've got faith
Faith of the heart

It's been a long road

(and this one my long road!)

Eidesstattliche Erklärung

Ich versichere hiermit an Eides Statt, dass diese Arbeit von niemand anderem als meiner Person verfasst worden ist. Alle verwendeten Hilfsmittel wie Berichte, Bücher, Internetseiten oder ähnliches sind im Literaturverzeichnis angegeben, Zitate aus fremden Arbeiten sind als solche kenntlich gemacht. Die Arbeit wurde bisher in gleicher oder ähnlicher Form keiner anderen Prüfungskommission vorgelegt. Die Teile der Arbeit die schon veröffentlicht oder eingereicht wurden, sind im Vorwort ("Preface") kenntlich gemacht. Weiterhin ist im Vorwort ("Preface") dargelegt, zu welchem Teil der Arbeit andere Wissenschaftler beigetragen haben.

March 25, 2015

Marcus Oelze

Danksagung

bis hin zu präkambrischen Ablagerungen beleuchtet haben. Für seine nicht abnehmende Bereitschaft, meinen kritischen Fragen zu trotzen und für seine Freundschaft danke ich ihm.

Ich danke auch unseren technischen Mitarbeiterinnen Jutta Bartel, Josefine Buhk sowie Cathrin Schulz für die Unterstützung im Labor, denn ohne sie würden die Arbeiten im Labor sehr viel langsamer von der Hand gehen.

Last but not least möchte ich meiner Familie danken, die mir durch finanzielle Unterstützung mein Studium erst ermöglicht und mir immer mit Rat und Tat zu Seite gestanden hat. Meiner "Exfreundin" (und jetzigen Frau) Hella Wittmann-Oelze und unserem Sohn Marten danke ich, weil sie mir Kraft gegeben haben, mich immer geduldig (zumindest meistens) unterstützt haben, und Hella für die vielen, vielen Stunden des Korrekturlesens, der vielen kritischen Fragen und Anmerkungen und der ständigen Bereitschaft zur Diskussion.

Abschließen möchte ich meine Danksagung mit einem Zitat aus Friedrich Schiller's "Die Glocke", welches ich immer vor Augen und im Kopf habe, da es an meinem Elternhaus verewigt ist.

Arbeit ist des Bürgers Zierde,
Segen ist der Mühe Preis,
Ehrt den König seine Würde,
Ehret uns der Hände Fleiß.

"Das Lied von der Glocke"
von Friedrich Schiller

(hier in etwas abgewandelter Form:
Publizieren ist des Wissenschaftlers Zierde,
Zitate sind der Mühe Preis,
Ehrt den Professor seine Würde,
Ehret uns des Geistes Fleiss.)

Summary

During the weathering of minerals and rocks elements are released into the ambient solution. In the last 10 years stable Si isotope ratios have emerged as a powerful proxy for the quantification of this release, and to disclose the associated low-temperature water-mineral and water-rock interactions. The isotope ratios potentially trace the way Si is released from Si-bearing solids into soil and (diagenetic) interstitial solutions. They also trace how silica is precipitated into secondary solids from these solutions. Given the useful information Si stable isotopes provide along this pathway, the resulting isotope ratios have been increasingly explored as a tool to trace silicate weathering, sediment diagenesis and the associated silicification, precipitation of siliceous sediments from hydrothermal vents, and the genesis of Precambrian cherts and banded iron formation. In general, dissolved silica in soil and in river waters is enriched in the heavy isotopes as compared to the primary silicate minerals where Si is sourced from. In siliceous precipitates from hydrothermal solutions, the common picture emerging is one of preferential incorporation of light isotopes in the precipitates. To date, only a few notable studies have explored Si isotope fractionation during fixation of Si from solution under controlled experimental conditions.

In particular, the partitioning of Si isotopes in the presence of Al has not been explored in detail under controlled laboratory conditions and the related Si isotope fractionation factors need to be determined. The determination of these fractionation factors is so important as in virtually all Earth surface reactions, Si being released from primary silicates is accompanied by variable amounts of Al. Crucial in the understanding of Si isotope fractionation in the presence of Al are two processes: 1.) Si isotope fractionation during adsorption onto Al precipitates and 2.) Si isotope fractionation during Si precipitation from solutions in the presence of variable Al concentrations.

To better understand Si isotope fractionation during secondary precipitate formation processes (adsorption and precipitation), I conducted Si isotope fractionation experiments during the adsorption of Si onto gibbsite at three different initial Si concentrations. To explore Si isotope fractionation during precipitation of Si from the solution, a new experimental approach was used. In this approach alternating dissolution-precipitation, implying depolymerization-polymerization of silica, is induced by freezing and thawing for predefined cycle length over a long run duration. This experimental setup allowed me to analyze the temporal change in the Si isotope fractionation factor as the system evolves from a state that is characterized by high net Si removal rates (dominated by unidirectional kinetic isotope fractionation), to a state where the net change for precipitation and dissolution is close to zero (Si isotope fractionation closer to equilibrium). Si precipitation experiments reveal that during cyclic freeze-thaw of dissolved Si-containing solutions, Si is removed from the solution. In the absence of appreciable amounts of Al this removal is not accompanied by a fractionation of Si isotopes. In contrast if Al is present in these solutions at high concentrations (here 1 mmol/l), Si removal is faster and accompanied by strong Si isotope fractionation favoring the light isotopes in the solids. For these high-Al experiments I calculate a fractionation factor of up to $\alpha^{30/28}Si_{solid/solution}$ =0.9950 ($10^3ln\alpha_{solid/solution}$ = -5‰) for the first 20 days of the experiment. With ongoing runtime the early formed precipitates are reorganized wholesale, and $\alpha^{30/28}Si_{solid/solution}$ approaches 1 ($10^3ln\alpha_{solid/solution}$ = 0‰). The presence of Al increases the precipitation rate and therefore Si isotopes will fractionate according to the Al/Si ratio. The difference between the rapidly precipitating Al-containing phase compared to the slowly precipitating

Al-free phase can then be predicted to be mirrored in the Si isotope composition of these two phases, with the higher enrichment of ^{28}Si in the Al-containing phase.

The conducted adsorption experiments presented in Chapter 3 reveal that adsorption of monomeric silicic acid onto gibbsite is accompanied by a significant kinetic Si isotope fractionation and that light Si isotopes are preferentially adsorbed. The calculated Si isotope fractionation factors are dependent on the initial Si concentration. High initial Si concentrations result in a strong kinetic Si isotope fractionation during adsorption. This initial kinetic signature begins to re-equilibrate only after ca. two months. This behavior is compatible with a change from high net adsorption rates to low net adsorption rates (almost constant Si concentration at the end of experiments).

Having established the principle fractionation factors in these experiments I explored the Si isotopic composition of natural samples to investigate the dependence of Si isotope fractionation related to soil processes under different kinetic regimes. To be able to precisely and accurately analyze the natural samples I also extended the established digestion method for natural samples by a removal step of organic carbon from solid and water samples (Chapter 2). I show further how external Mg addition improves the accuracy and stability of Si isotope measurements under dry plasma conditions in comparison to wet plasma measurements without Mg addition.

After extending the digestion method, the goal here was to study the influence of parameters like soil residence time, denudation rate (erosion and weathering rate) and elemental chemical depletion on Si isotope fractionation in settings that are steadily eroding. These relations can only be studied when comparing different weathering regimes. Here I explore Si isotopes in different weathering regimes that range from highly weathered thick tropical soils in the tectonically inactive mountain range of the Highlands of Sri Lanka representing supply limited conditions where the weathering erosion relationship is mainly dominated by chemical dissolution, to the rapidly uplifting Swiss Alps. There the sampling site is located in the upper Rhone valley, representing the kinetically limited counterpart where physical erosion dominates. The intermediate weathering regime is located in the southern Sierra Nevada mountain range, California, where chemical weathering and physical erosion are balanced. The Si isotope measurements of the amorphous and clay fraction extracted from soils and saprolites reveal that a strong relationship between the Si isotopic composition of these pools and the regolith residence time of the three different weathering regimes exists. An increase in regolith residence time leads to lower $^{30}Si/^{28}Si$ ratios for secondary silicates formed in different weathering regimes. In Sri Lanka, the setting with the longest regolith residence time, the lowest $^{30}Si/^{28}Si$ ratios for the amorphous and clay phase are measured. Extracted phases of the Sierra Nevada sampling site, where regolith residence time are shorter than in Sri Lanka, show relative higher $^{30}Si/^{28}Si$ ratios for the amorphous and clay phase. Amorphous and clay fractions of the Swiss Alps sampling site (lowest regolith residence time of all settings) show the highest $^{30}Si/^{28}Si$ ratios of three sampled weathering regimes. An isotope mass balance model reveal that the proportion of particulate export flux increases over the dissolved import Si flux according to the decrease in regolith residence time. This change is mirrored in the $^{30}Si/^{28}Si$ ratios of secondary precipitates.

Zusammenfassung

Während der chemischen Verwitterung von gesteinsbildenden Mineralen und anstehendem Festgestein werden Elemente in die umgebene Bodenlösung abgegeben. In den letzten 10 Jahren wurden Si Isotope benutzt, um solche Reaktionen zwischen primären Mineralen bzw. dem anstehenden Festgestein und den sie umgebenen Fluiden zu untersuchen. Verhältnisse der stabilen Si Isotope zeigen dabei den möglichen Pfad von Si von der Freisetzung bei der Verwitterung von primären Mineralen und anstehenden Festgestein bis zum anschließenden Einbau in sekundäre Minerale auf. Weiterhin wurden stabile Si Isotope eingesetzt, um die Ausfällung von hydrothermalem Si, die Genese von prä-Kambrischem Cherts und von gebänderten Eisenerz–Formationen besser zu verstehen. Die generelle Beobachtung ist, dass das gelöste Si im Boden oder Flusswasser isotopisch schwerer ist im Vergleich zu dem in gesteinsbildenden Mineralen gebundenem Si. Das dazugehörige Reservoir von leichten Si Isotopen findet sich in den sekundären Si Phasen. Auch Neubildungen aus hydrothermalen Lösungen zeigen einen bevorzugten Einbau von leichten Si Isotopen.

Trotz der konsistenten Beobachtung, dass leichte Si Isotope bevorzugt in sekundäre Minerale eingebaut werden, wurde die Isotopenfraktionierung von Si im System Si-Al noch nicht im Detail unter kontrollierten Laborbedingungen untersucht. Dabei ist die Bestimmung von Si Isotopenfraktionierungsfaktoren von Reaktionen zwischen Al und Si von grundlegender Bedeutung, da es sich mit hoher Wahrscheinlichkeit um die ersten Reaktionen nach der Freisetzung der beiden Elemente handelt. Bei Reaktionen von Al und Si nehmen zwei wesentliche Prozesse eine führende Rolle ein: 1.) Si Isotopenfraktionierung bei der Adsorption von Si an Al Ausfällungen und 2.) Si Isotopenfraktionierung bei der Ausfällung von Si aus wässrigen Lösungen in An- und Abwesenheit von Aluminium.

Um die Si Isotopenmuster während der Verwitterung von Gestein und der einhergehenden Neubildung von sekundären Silikaten erklären zu können, ist die Kenntnis der Si Isotopenfraktionierung bei der Bildung von sekundären Silikaten durch Adsorption und Ausfällung von Si notwendig. Aus diesem Grund wurden in einem ersten experimentellen Ansatz die Si Isotopenfraktionierungsfaktoren bei der Adsorption von Si an Gibbsit bei unterschiedlichen Si Konzentrationen untersucht. Um die Isotopenfraktionierung bei der Ausfällung von Si aus wässrigen Lösungen zu untersuchen, wurde ein neuartiger experimenteller Ansatz gewählt, bei dem die Ausfällung von Si durch ein alternierendes Auflösen und Ausfällen von Si erzwungen wird. Dieses alternierende Auflösen und Ausfällen wurde induziert durch einen kontinuierlichen Wechsel von Gefrier- und Tauzyklen über einen langen Zeitraum hinweg, was zu einer Polymerisierung und Depolymerisierung von Si führt. Dieser neuartige experimentelle Ansatz erlaubt die Umsetzung des zeitlichen Verlaufs von Wechsel zwischen hohen Si Ausfällungsraten (und damit einhergehender ausgeprägter kinetischer Si Isotopenfraktionierung) hin zu einem Systemzustand von annährend ausgeglichen Ausfällungs- und Auflösungsraten (und damit möglicher Si Gleichgewichts–Isotopenfraktionierung). Die durchgeführten Si Ausfällungsexperimete zeigen, dass es beim zyklischen Gefrieren und Auftauen von Si enthaltenen Lösungen zur Ausfällung von Si kommt (Kapitel 4). Wenn es sich dabei um reine Si Lösungen (ohne Zugabe von Al) handelt, dann findet bei der Ausfällung keine Si Isotopenfraktionierung statt. Im Gegensatz zu den Al freien Si Ausfällungsexperimenten ist die Si Ausfällung bei der Zugabe von Al (hier 1 mmol/l) schneller und geht mit einer Si Isotopenfraktionierung einher, bei der bevorzugt leichtes Si in die Ausfällungen eingebaut wird. Für die Si Ausfällungsexperimente mit hohen Al Konzentrationen wurden Si Isotopenfraktionierungsfaktoren

von bis zu $10^3 ln\alpha_{solid/solution}$ = -5‰ für die ersten 20 Tage des Experimentes ermittelt. Mit zunehmender Laufzeit der Experimente findet eine Reorganisation der anfänglich gebildeten Si Ausfällungen statt, wobei sich ein Si Isotopenfraktionierungsfaktor von $10^3 ln\alpha_{solid/solution}$ = 0‰ einstellt. Nach Erreichen eines gleichgewichtsähnlichen Zustandes (Si Konzentration annähernd konstant) findet bei der Reorganisation der Si Ausfällungen keine Isotopenfraktionierung mehr statt. Demzufolge wird durch die Anwesenheit von Al die Si Ausfällungsraten erhöht und daraus resultiert eine Beziehung zwischen der Si Isotopenfraktionierung und dem Al/Si Verhältnis. Der Unterschied zwischen den sich schnell bildenden Al enthaltenen Si Phasen und den sich langsam bildenden Al freien Phasen wird daher in den resultierenden Si Isotopenverhältnissen abgebildet.

Die in Kapitel 3 gezeigten Si Adsorptionsexperimente zeigen, dass es bei der Adsorption von Monokieselsäure an Gibbsit zu einer signifikanten Si Isotopenfraktionierung kommt, wobei die leichten Si Isotope bevorzugt adsorbiert werden. Die von mir bestimmten Si Isotopenfraktionierungsfaktoren sind stark abhängig von der initialen Si Konzentration. Hohe initiale Si Konzentrationen resultieren in einer stärkeren kinetischen Si Isotopenfraktionierung während der Adsorption. Die initiale kinetische Si Isotopensignatur zeigt Anzeichen einer Reequilibrierung erst nach ca. zwei Monaten Versuchsdauer. Dieses Verhalten geht einher mit einem Wechsel von hoher netto–Adsorptionsrate hin zu langsamen netto–Adsorptionsraten (d.h. die Si Konzentration am Ende der Experimente ist annähernd konstant).

Weiterhin habe ich die Isotopenzusammensetzung von natürlichen Proben und den Zusammenhang zwischen Si Isotopensignatur und Bodenbildungsprozessen in unterschiedlichen Verwitterungsregimen untersucht.

Um die Si Isotopie an natürlichen Proben richtig und präzise zu bestimmen, habe ich zunächst die Methodik des Probenaufschlusses und der Messung der Si Isotope an natürlichen Proben um einen weiteren Arbeitsschritt erweitert, in dem in den Proben enthaltener organischer Kohlenstoff entfernt wird. Weiterhin zeige ich, wie der Zusatz von Mg die Richtigkeit und Präzision der Si Isotopenmessungen erheblich verbessert (Kapitel 2). Meine Arbeit an natürlichen Proben hatte das Ziel den Einfluss von Bodenbildungsparametern wie Bodenverweilzeit, Denudationsrate (Erosions- und Verwitterungsrate), sowie die Abreicherung von Elementen auf die Si Isotopenfraktionierung in verschieden Verwitterungsregimen zu untersuchen. Diese Zusammenhänge können nur untersucht werden wenn verschiedene Verwitterungsregime miteinander verglichen werden. Ein untersuchtes Verwitterungsregime ist das von mächtigen, stark verwitterten Böden gezeichnete, tektonisch inaktive Hochland von Sri Lanka, welches das Nachlieferungs–limitierte Verwitterungsregime ("supply-limited") repräsentiert. In Sri Lanka ist der Zusammenhang zwischen Verwitterung und Erosion dominiert von der chemischer Auflösung der Gesteine. Das kinetisch limitierte Verwitterungsregime liegt im oberen Rhone Tal in den tektonisch aktiven Schweizer Alpen. Im Gegensatz zu dem in Sri Lanka beprobten Verwitterungsregime dominiert hier physikalische Erosion den Denudationsprozess. Der Gebirgszug der südlichen Sierra Nevada, USA, repräsentiert das Verwitterungsregime in dem chemische Verwitterung und physikalische Erosion ausgeglichen sind.

Resultate der Si Isotopenmessungen der amorphen Si Fraktion und der Tonfraktion von Böden und Saprolit zeigen, dass es einen starken Zusammenhang zwischen der Si Isotopenzusammensetzung dieser Phasen und der Verweilzeit im Regolith in den unterschiedlichen Verwitterungsregimen gibt (Kapitel 5). Längere Regolith–Verweilzeiten führen zu niedrigeren ^{30}Si/^{28}Si Verhältnissen in den sekundär gebildeten Si Ausfällungen. Die niedrigsten ^{30}Si/^{28}Si Verhältnisse wurden in Sri Lanka gemessen, dem Verwitterungsregime mit der

längsten Regolith Verweilzeit. Die extrahierten Fraktionen aus den Proben der Sierra Nevada, wo die Regolith Verweilzeit kürzer als in Sri Lanka ist, zeigen relativ höhere $^{30}Si/^{28}Si$ Verhältnisse für die amorphe Si Fraktion und die Tonfraktion. Die amorphe Si Fraktion sowie die Tonfraktion der Schweizer Alpen, dem Beprobungsstandort mit der kürzesten Regolith Verweilzeit, zeigt die höchsten $^{30}Si/^{28}Si$ Verhältnisse der drei beprobten Verwitterungsregime. Ein Isotopen–Massenbilanzmodel zeigt, dass das Verhältnis von partikulären Export von Si enthalten in sekundären Phasen zu dem Import von gelösten Si in die Verwitterungszone ansteigt, wenn die Regolith–Verweilzeit abnimmt. Dieser Wechsel wird in den $^{30}Si/^{28}Si$ Verhältnissen der sekundär gebildeten Si Ausfällungen abgebildet.

Preface

This thesis is composed of several Chapters. Here I will declare which parts of the individual chapters are my work and which parts of the chapter is work from colleagues that I collaborated with on these projects. Further will I provide a short summary of the content of the individual chapters. All Chapters are prepared in a way that they can be read individually. Therefore some introductory material is repeated in the individual Chapters.

Chapter 1 summarizes the chemical characteristics of Si and its isotopes and further provides a short summary of isotope fractionation processes.

In Chapter 2 an extension of the established digestion method for natural samples is described. Further it is shown how external Mg doping improves the accuracy and stability of Si isotope measurements by multi-collector inductively coupled plasma mass spectrometers (MC-ICP-MS). All performed experiments, measurements, data evaluation and data interpretation were conducted by me and I also wrote the manuscript. The idea to remove organic carbon from natural solid and water samples was developed jointly by me and Grit Steinhoefel. Most of the tests to establish this "carbon burning" technique were conducted by Grit Steinhoefel.

Chapter 3 has been published in *Chemical Geology* (Marcus Oelze, Friedhelm von Blanckenburg, Daniel Hoellen, Martin Dietzel, Julien Bouchez 2014; DOI: 10.1016/ j.chemgeo. 2014.04.027). Adsorption experiments were carried out at pH 7 with different initial Si concentrations of 0.36, 0.71 and 1.42 mmol/l Si starting concentrations. As Al-hydroxide adsorbent, 30 g/l crystalline gibbsite were used to provide equal surface area in all experiments. Adsorption rates are higher with higher initial Si concentration. At the same time, calculated apparent isotope fractionation factors $10^3\ln\alpha_{\mathrm{adsorbed/solution}}$ decrease from -1.8 to -3 ‰ with increasing initial Si concentration. These observations may provide an explanation for the light Si isotope signature that clay minerals formed during weathering carry: the light Si isotope composition is being inherited early on during Si adsorption onto amorphous Al-hydroxides and is potentially carried over during all further stages of transformation.
Martin Dietzel and Daniel Hoellen conducted the adsorption experiments. I conducted all isotope measurements, performed data evaluation and data interpretation and wrote the manuscript. Julien Bouchez, Friedhelm von Blanckenburg, Martin Dietzel and Daniel Hoellen contributed to data interpretation, writing and discussion.

Chapter 4 is submitted to *Chemical Geology* and is accepted pending minor revisions. A series of precipitation experiments in which continuous precipitation and dissolution of Si solids is forced by daily cyclic freezing (solid formation) and thawing (solid re-dissolution) was conducted. Six Si precipitation experiments, lasting for about 120 days were conducted, with constant initial Si concentrations and varying amounts of Al . No Si isotope fractionation occurs during formation of almost pure Si solids, which is interpreted to show the absence of Si isotope fractionation during polymerization of silicic acid. Si isotope fractionation occurs only in the high-Al concentration experiments, characterized by an enrichment of the light Si isotopes in the solids forming early. With ongoing runtime re-dissolution of these solids is indicated by the Si isotope value of the complementary solution that shifts to lighter values and eventually reaches near-starting compositions.

The results of the experiments suggest that the enrichment of light Si isotopes found in natural environments is caused exclusively by an unidirectional kinetic isotope effect during fast precipitation of solids, aided by co-precipitation of Al phases or other carrier phases. In contrast, during slow precipitation, or in the absence of a carrier phase like Al, no Si isotope fractionation is expected and solids obtain the composition of the ambient fluid.

Martin Dietzel and Daniel Hoellen conducted the freeze-thaw experiments. I conducted all isotope measurements, performed data evaluation and data interpretation and wrote the manuscript. Julien Bouchez, Friedhelm von Blanckenburg, Martin Dietzel and Daniel Hoellen contributed to data interpretation, writing and discussion.

In Chapter 5 it is tested whether the kinetic isotope effect explored in controlled laboratory experiments in Chapter 3 and Chapter 4 is also expressed during natural weathering reactions. Three different study sites were chosen, representing different weathering and erosional regimes. Si isotopes are used to trace differences in these different weathering regimes, ranging from highly weathered thick tropical soil-mantled hillslopes, present in the tectonically inactive mountain range of the Highlands of Sri Lanka. This setting represents supply limited conditions, where primary mineral dissolution is almost complete. The rapidly uplifting Swiss Alps sampling site located in the upper Rhone valley represents the kinetically limited counterpart where physical erosion dominates. An intermediate weathering regime is located in the southern Sierra Nevada mountain range, California, where chemical weathering and physical erosion are balanced. The goal is to study the influence of parameters like soil residence time, denudation rate (erosion and weathering rate), elemental chemical depletion, and their influence on Si isotope fractionation.

The sampling and further the generation of background data (XRF bulk soil data, major element concentration in river water) of the described samples were conducted during an ongoing project of the Earth Surface Geochemistry Group at GFZ Potsdam. Some results of these measurements are shown in the Appendix of this Chapter (XRF bulk soil data, major element concentration in river water) to provide a complete picture of the sampled sites and are taken from the GFZ-ESG-DR (GFZ-Earth Surface Geochemistry-Data Repository) or from already published literature. I conducted the sample processing for Si isotope measurements, Si isotope measurements, data evaluation and data interpretation.

Contents

---

[1]This Chapter is published in *Chemical Geology*: Oelze et al. (2014); http://dx.doi.org/10.1016/j.chemgeo.2014.04.027

Chapter 1

Introduction

1.1 Background on Si and on stable Si isotopes

Silicon has been under geological investigation since its discovery in the 18th century as it is the second most abundant element in the earth crust. Being a constituent of almost all geological processes from mountain building to core formation, its chemical behavior has been thoroughly investigated. With the developing ability to measure the abundance of the stable isotopes of the elements and to explore the processes leading to their fractionation in the mid 20th century, also the stable isotopes of Si became a field of interest in geochemistry research. Silicon has three stable isotopes with the relative abundances ^{28}Si = 92.23 %, ^{29}Si = 4.67 % and ^{30}Si = 3.10 %. Si isotope data is reported relative to the standard reference material NBS28 (quartz sand) in the delta notation according to Coplen (2011) as $\delta(^{29/28}$Si$)_{\text{NBS28}}$ and $\delta(^{30/28}$Si$)_{\text{NBS28}}$ expressed in per mill (‰) by multiplication of Equation 1.1 and Equation 1.2 with a factor of 10^3:

$$\delta(^{29/28}\text{Si})_{\text{NBS28}} = \left(\frac{\left(\frac{^{29}\text{Si}}{^{28}\text{Si}} \right)_{\text{sample}}}{\left(\frac{^{29}\text{Si}}{^{28}\text{Si}} \right)_{\text{NBS28}}} - 1 \right) \tag{1.1}$$

$$\delta(^{30/28}\text{Si})_{\text{NBS28}} = \left(\frac{\left(\frac{^{30}\text{Si}}{^{28}\text{Si}} \right)_{\text{sample}}}{\left(\frac{^{30}\text{Si}}{^{28}\text{Si}} \right)_{\text{NBS28}}} - 1 \right) \tag{1.2}$$

To complete the isotopic terminology further used in this thesis definitions for isotope fractionation factors and isotopic differences are also given here:

$$\alpha_{A-B} = \frac{R_A}{R_B} = \frac{1000 + \delta_A}{1000 + \delta_B} \tag{1.3}$$

Where α_{A-B} denotes the isotopic fractionation factor between substance A and B. R_A and R_B denote the isotope ratios of substance A and B, respectively. The isotopic fractionation factor can also be expressed in permil (‰) by:

$$\Delta_{A-B} \simeq 1000 * ln(\alpha_{A-B}) \tag{1.4}$$

The isotopic difference between two substances A and B is defined as:

$$\Delta_{A-B} = \delta_A - \delta_B \tag{1.5}$$

The isotopic composition of Si-containing materials has been measured first by Reynolds and Verhoogen (1953) by converting Si into SiF_4 and measuring gaseous SiF_4 by gas mass spectrometry. Before the development of multi-collector inductively coupled plasma mass spectrometers (MC-ICP-MS) in the early 2000's, Si has been measured as SiF_4 by gas mass spectrometry. The ability to measure Si isotopes on a MC-ICP-MS resulted in the opportunity to distinguish between reservoirs with only small isotopic variation, due to the much higher precision of the isotope ratios determined by MC-ICP-MS compared to conventional gas mass spectrometers. Cardinal et al. (2003) carried out the first precise measurements of stable Si isotopes. Since then many studies have been published that report Si stable isotope compositions of a whole variety of compartments of the Earth, from mantle rocks and minerals to the foliage of trees.

According to Iler (1979) is the term "silicon" used for the element Silicon (Si) and the term "silica" is used as a short form of "silicon dioxide". Si can be found in a variety of bonding environments (silicate minerals) but only rarely in elemental form at the Earth's surface due to the high affinity to binding with oxygen. In bonding environments, Si usually has the oxidation state 4^+. Si and also the oxide SiO_2 are almost insoluble in all acids, except for HF-HNO_4 mixtures. Si has a high solubility in hot bases but SiO_2 reacts slowly in aqueous bases. To digest Si oxides, the most common way is to use alkaline fusion techniques, where an alkaline flux (e.g. NaOH) is added to the sample. During the melting process at temperatures between 600 and 800℃, easily soluble alkaline silicates are formed.

Caused by the low solubility of Si and SiO_2, only small amounts of Si can be found as monosilicic acid (H_4SiO_4) in natural waters (<100 mg/l). In dilute solutions monosilicic acid is only a weak acid and and does not dissociate below neutral pH. This causes the constant solubility of Si below pH 7. At low pH the dissociation can be described by the following reaction:

$$SiO_{2(solid)} + H_2O \rightleftharpoons H_4SiO_4$$
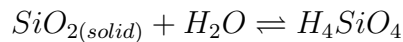
With increasing pH the weak diprotonic monosilicic acid starts to dissociate, which causes the increase in solubility (see Figure 1.1) according to the following reactions:

$$H_4SiO_4 \rightleftharpoons H_3SiO_4^- + H^+$$

$$H_3SiO_4^- \rightleftharpoons H_2SiO_4^{2-} + H^+$$
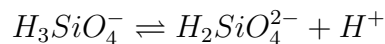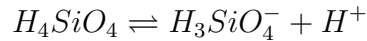
At concentrations of monosilicic acid that are above the solubilty of amorphous Si (see Figure 1.2) and also at high pH values silicic acid has the affinity to polymerize and form compounds of higher order (Figure 1.3).

According to Railsback (2003) the unique nature of Si can be summarized as follows: Si^{4+} has an ionic potential at the boundary between the relatively insoluble cations of intermediate ionic potential and cations of high ionic potential that form soluble radicals.

Silicon is distributed in roughly equal proportions between residuals from weathering (e.g., in sands and sandy or kaolinitic soils) and in natural waters, such as river water (where dissolved silica is the second most abundant dissolved species) and seawater (where it is the 11th most abundant dissolved species).

The high abundance of Si as 2nd most abundant element in the Earth's crust and the ionic potential at the boundary between insoluble and soluble cations also leads to an interesting feature in plant physiology. Plant essential nutrients are in general taken up as solutes (like NO_3^-). Si^{4+} with its unique ionic potential can also be taken up as a solute (as $Si(OH)_4^0$). However, Si^{4+} is sufficiently insoluble that some plants build masses of opaline silica in their tissue. This amorphous silica within plant tissues, exists because Si^{4+} is sufficiently abundant and soluble to be taken up through roots in solution but sufficiently insoluble to be maintained as a solid within wet plant tissue.
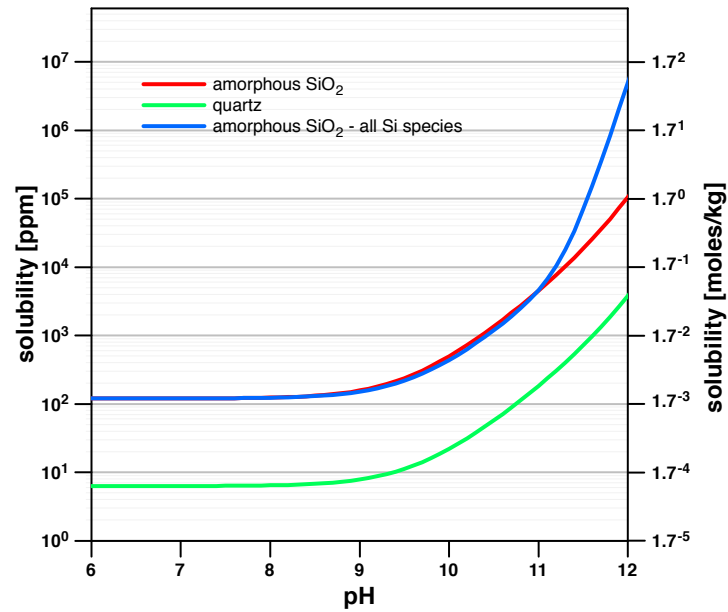
Figure 1.1: Calculated pH dependence of silica (SiO_2) solubility at 25℃ derived from the stability constants of silicic acid (see Dietzel and Böhme (1997)); the red and green curves are calculated according to the equilibrium constants for amorphous silica and quartz, respectively, assuming that monosilicic acid is the only present dissolved Si species. The blue curve is calculated assuming that all dissolved Si species listed in Table 1.1 contribute to the solubility of Si.
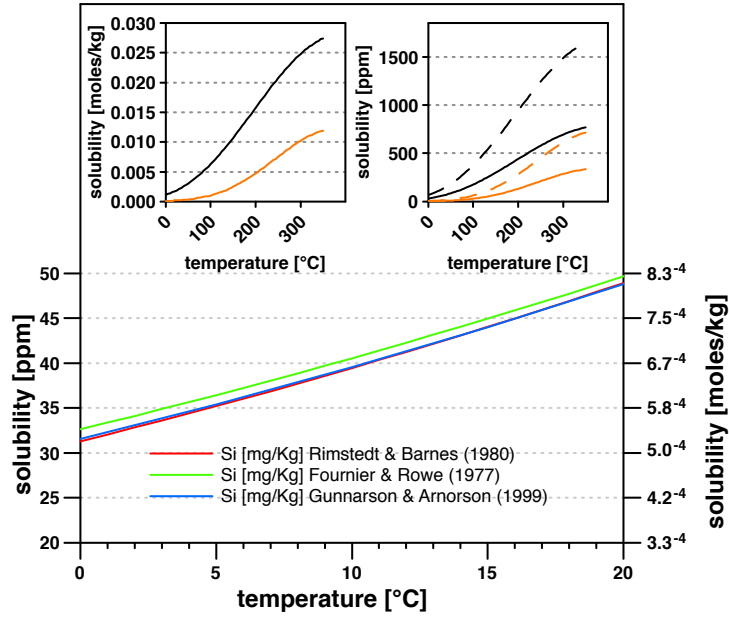
Figure 1.2: Solubility curves for amorphous Si in the temperature range from 0 to 20℃ using the empirical relationships of Fournier and Rowe (1977), Rimstidt and Barnes (1980) and Gunnarsson and Arnorsson (2000). The upper left panel shows the solubilities in [moles/kg] of amorphous silica (black) and quartz (orange) in the temperature range from 0 to 350℃, calculated using the empirical relationship of Gunnarsson and Arnorsson (2000). The upper right panel shows the solubilities in [ppm] of amorphous Si (solid black) and quartz as Si (solid orange) and of amorphous SiO_2 (stippled black) and quartz as SiO_2 (stippled orange)
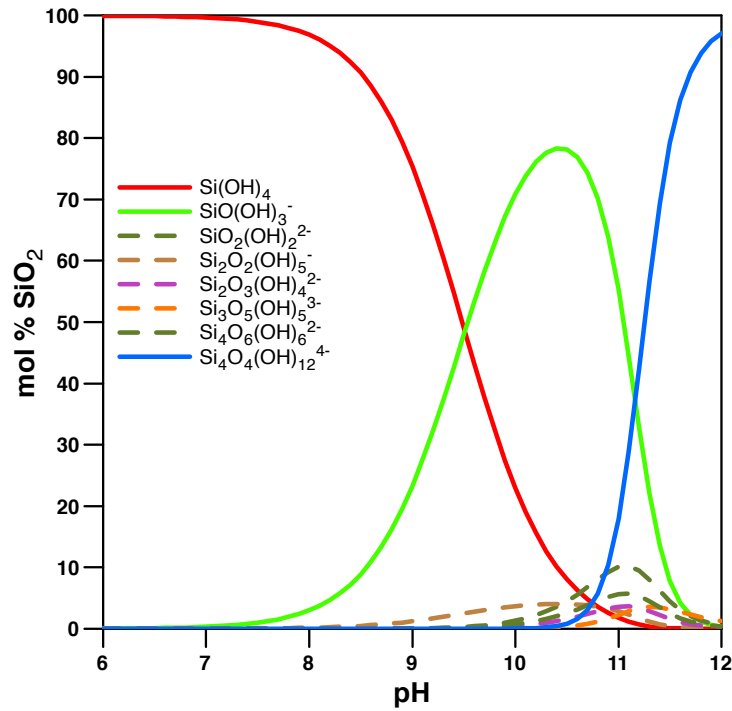
Figure 1.3: Calculated mol% SiO_2 concentration of silica contained in monomeric or polymeric form at 25℃ as a function of pH, derived from stability constants of silicic acid (see Dietzel and Böhme (1997)) using all Si species shown in Table 1.

1.2   Isotope fractionation processes

Fractionation, the process that changes the relative abundance of stable isotopes, can be separated into non-equilibrium (kinetic) and equilibrium effects (Criss, 1999).

Equilibrium isotope fractionation is caused during the substitution of bonded light isotopes by heavy isotopes, which leads to a decrease in vibrational frequencies that is directly proportional to the vibrational energy of the bond. With lowering the vibrational energy, the bond becomes more stable and has a lower "zero point energy" (ZPE). A prerequisite to reach isotopic equilibrium is that chemical equilibrium must be attained (Mills and Urey, 1940; Schauble, 2004; Criss, 1999).

Kinetic isotope fractionation is caused by incomplete exchange, unidirectional or fast reactions (Schauble, 2004; Criss, 1999). There are several processes where kinetic isotope fractionation might occur, for example diffusion, evaporation or differences in energy barriers. For some of these processes simple mathematical relationships have been formulated where the relation between isotopic mass and kinetic isotope fractionation becomes clear. We will distinguish between those occurring during transport of isotopes ("transport-limited") and into processes where isotope fractionation occurs due to energetic barrier differences ("reaction-limited").

In an ideal gas isotope fractionation processes that are transport-limited can be approximately described by Equation 1.6.

$$\frac{v_1}{v_2} = \sqrt{\frac{m_2}{m_1}} \tag{1.6}$$

Where v_1 is the velocity of the light isotopic (or molecular) mass m_1 and v_2 is the velocity of the heavy isotopic (or molecular) mass m_2. The higher velocity of m_1 causes the kinetic isotope effect, favoring light isotopes, which is observed during diffusion or evaporation (Richter et al., 2006; Young et al., 2002). This relationship arises from the assumption that all isotopes (or molecules) have the same kinetic energy at the same temperature. The equation in this form is only applicable for an ideal gas.

Another relationship helps to understand the kinetic effect occurring when energy barriers are overcome as it is the case for the reaction-limited regime defined here. This relationship follows from the well-known Arrhenius equation (Equation 1.7) which is commonly used to describe the dependency of the reaction rate constant on temperature. This equation can also be used to explain why light isotopes are favored during attachment or detachment to a solid such as adsorption or desorption:

$$k = A \times e^{-\frac{E_a}{RT}} \tag{1.7}$$

Where k is the reaction rate, A is the pre-exponential factor, E_a is the activation energy, R is the universal gas constant and T is temperature. A reaction occurs when the activation energy E_a is reached and bonds are formed. As it is known from thermodynamics, bonds with heavier isotopes have lower ZPE as light isotopes (Urey, 1947), implying that (see also Figure 1.4):

$$E_{a-light} < E_{a-heavy} \tag{1.8}$$

From Equation 1.7 and Equation 1.8, it follows that the reaction rate constant k of light isotopes is larger. The larger reaction rate constant leads to a higher reaction rate of light isotopes compared to heavy isotopes. The effect of slight differences in the energy at the transition state occurs during all chemical reactions when evolving from educt to product ("forward reaction") as well as when evolving from product to educt ("backward reaction").
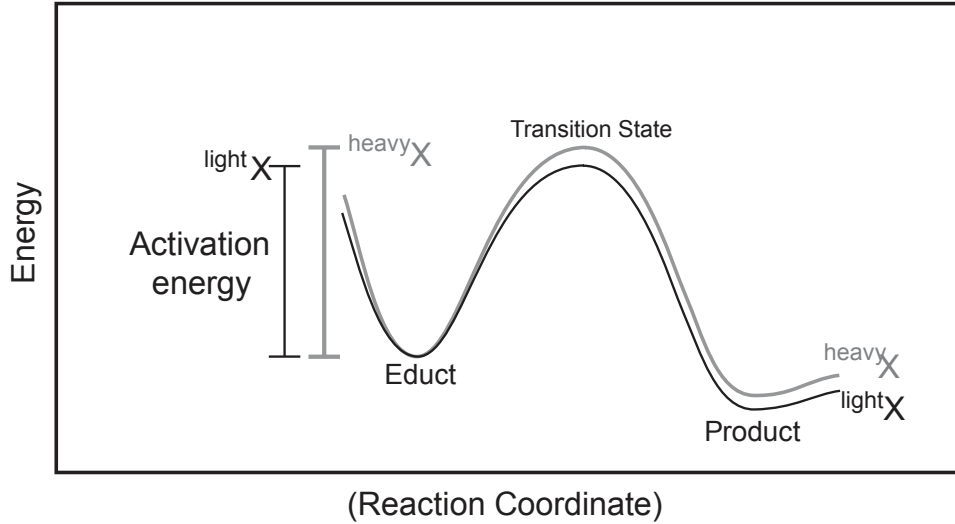
Figure 1.4: Energy diagram showing different activation energies for heavy and light isotopes for a dissociation reaction, adapted from Schauble (2004)

During formation of solids from aqueous solutions both processes, equilibrium and kinetic non-equilibrium isotope fractionation, can control the observed isotopic fractionation. DePaolo (2011) developed a framework where the competition of equilibrium and non-equilibrium isotope fractionation is described. The presented framework, from here on called "DePaolo-Model", potentially explains fractionation trends observed in our data. The developed approach models the observed isotopic fractionation during inorganic calcite precipitation. The model is based on simple definitions of a forward reaction rate R_f (forming of new phases), a backward reaction rate R_b (dissolution of newly formed phases) and the net precipitation rate R_p ($R_p = R_f - R_b$). The forward and backward rates are associated with isotope fractionation factors (α_f and α_b, respectively). An apparent fractionation factor α_p arises from the relationship R_p/R_b.

The main finding of this framework is that if the net precipitation rate R_p is much larger than the backward rate R_b, the apparent isotope fractionation during calcite precipitation will be kinetically dominated (favoring light isotopes). Whereas if R_p is much smaller than R_b, the precipitation system will reach isotopic equilibrium during precipitation (see Figure 1.5). The occurrence of competing isotope fractionation mechanisms will be explored in the following sections.
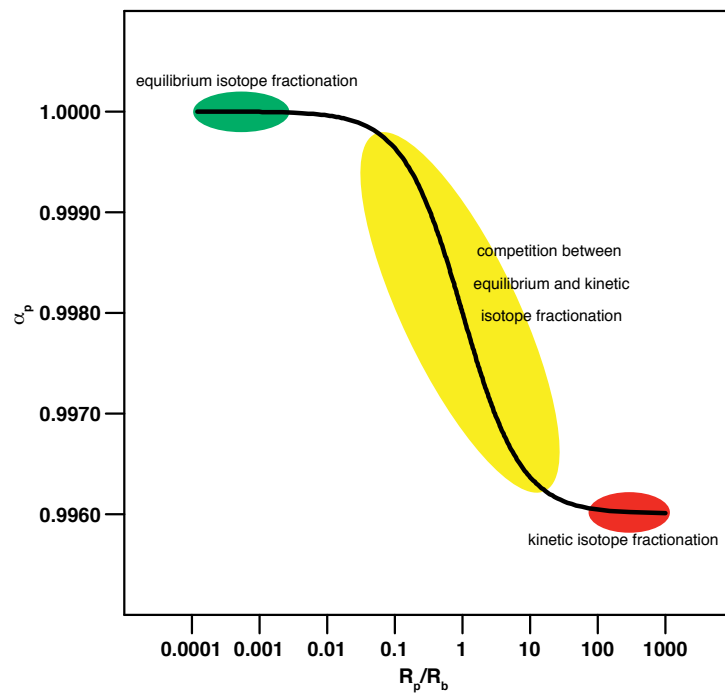
Figure 1.5: Calculated model curve for an apparent fractionation factor α_p by using Equation 11 of DePaolo (2011) for arbitrary values for R_p and R_b and using $10^3 ln\alpha_f = -4$ and $10^3 ln\alpha_{eq} = 0$.

1.3 Appendix Chapter 1

1.3.1 Tables

Table 1.1: Possible species of Si present as dissolved form and corresponding pK and K values used for Figure 1.3

species	pK	K	source
Quartz	3.98	$1.05*10^{-04}$	Fournier and Potter II (1982)
$Si(OH)_4$	2.70	$2.00*10^{-03}$	Rimstidt and Barnes (1980)
$SiO(OH)_3^-$	9.51	$3.09*10^{-10}$	Holleman and Wiberg (1995)
$SiO_2(OH)_2^{2-}$	11.74	$1.82*10^{-12}$	Holleman and Wiberg (1995)
$Si_2O_2(OH)_5^-$	8.10	$7.94*10^{-09}$	Guillaumont et al. (2003)
$Si_2O_3(OH)_4^{2-}$	19.00	$1.00*10^{-19}$	Guillaumont et al. (2003)
$Si_3O_6(OH)_3^{3-}$	28.60	$2.51*10^{-29}$	Guillaumont et al. (2003)
$Si_3O_5(OH)_5^{3-}$	27.50	$3.16*10^{-28}$	Guillaumont et al. (2003)
$Si_4O_8(OH)_2^{2-}$	92.96	$1.10*10^{-93}$	Volosov et al. (1972)
$Si_4O_6(OH)_6^{2-}$	13.40	$3.98*10^{-14}$	Baes and Mesmer (1976)
$Si_4O_7(OH)_5^{3-}$	25.50	$3.16*10^{-26}$	Guillaumont et al. (2003)
$Si_4O_4(OH)_{12}^{4-}$	34.90	$1.26*10^{-35}$	Guillaumont et al. (2003)

Chapter 2

Si stable isotope ratio determination of natural samples by MC-ICP-MS

2.1 Abstract

It is shown how Mg addition improves the measurement repeatability of Si isotope determination under dry plasma conditions. Several tests were conducted to show how Mg addition helps to circumvent non-spectral matrix effects when measuring Si stable isotopes using a desolvation unit. These tests show that the use of Mg as "matrix modifier" has several benefits when measuring Si stable isotopes under dry plasma conditions. In general, the addition of Mg reduces variations in the instrumental mass bias between sample and standards. Conducted tests reveal that: 1) Mg addition increases the sensitivity by up to a factor of 3 compared to Mg free solutions. 2) Given a mismatch of Si and Mg concentration between samples and bracketing standards, this mismatch may vary of up to $\pm 50\%$ with no visible effect observed on instrumental mass bias. 3) Given a molarity mismatch between samples and standard in the range of 0.05 to 0.2 mol/l measured against a 0.1 mol/l bracketing standard solution does not result in observable changes in the instrumental mass bias. 4) Also, remaining anionic impurities (SO_4, PO_4, NO_3) show no effect on mass bias if the ratio of [anion] to Si is lower than 1. Therefore, the addition of Mg is highly recommended when measuring Si isotopes under dry plasma conditions.

2.2 Introduction

In this Chapter a description is provided of the analytical procedures and digestion steps conducted to measure Si isotopes on natural samples using multi-collector inductively coupled plasma mass spectrometers (MC-ICP-MS). Results of conducted tests (concentration matching, molarity matching, anion contamination with SO_4, PO_4 and NO_3) show the influence of different sample matrices on the mass bias (instrumental mass fractionation) when measuring Si stable isotopes. When measuring Si stable isotopes in wet plasma mode which is liquid sample nebulization into a glass spray chamber before introduction into the plasma, both accuracy and precision are limited by the resulting low intensity for the individual isotopes (highly likely that counting statistics of ^{30}Si is the limiting factor). Therefore often a desolvation unit (here: ESI Apex Sample Inlet System) is used to introduce the samples dissolved in acids into the plasma (dry plasma mode) as this usually increases sensitivity. This increase in sensitivity is caused by the reduction of wa-

ter matrix load delivered to the plasma (Gray, 1986). The reduction of water load further decreases the amount of oxides and hydroxides formed within the plasma (Tsukahara and Kubota, 1990; Lam and McLaren, 1990).

One disadvantage of the overall reduced matrix load is the increased sensitivity to remaining impurities in samples that have previously been chemically purified. Such impurities induce a different matrix load between samples and standards. These differences in matrix load cause different mass bias effects for samples and standards, respectively. This effect is often called non-spectral matrix effect. Therefore the use of a standard - sample - bracketing (SSB) method to correct for mass bias is questionable. This effect has been observed for measurements of Si stable isotopes where the change in instrumental mass bias is induced by sulfur remaining after column purification (van den Boorn et al., 2009). Hughes et al. (2011) suggested to maintain the mass-bias constant during SSB by means of excessive addition of sulfuric and/or nitric acid, i.e. matrix matching between samples and standards used for calibration.

The need to control mass bias during Si measurements under dry plasma conditions seems necessary as test measurements of Si reference materials (BHVO–2G, Diatomite, BigBatch, IRMM-17) measured without matrix matching between samples and standard used for calibration during SSB resulted in an offset from the reference values (Figure 2.1). These test measurements of Si stable isotopes using a desolvation unit without sample matrix modification results in good measurement repeatability of isotope ratios but bad accuracy. Systematic errors probably by non-identical matrices during SSB, differ in the direction and magnitude of the bias (Figure 2.1). It is most likely that space charge effects within the plasma or different fluid properties during nebulization are generating these bias which are probably caused by anionic remaining's in the purified sample solutions. However, also other factors like concentration or molarity mismatch between samples and standards as well as high DOC contents in the sample might be responsible for the observed bias. As all measured isotope ratios plot on the terrestrial fractionation line (Figure 2.1), isobaric interferences on Si during measurements can be excluded.
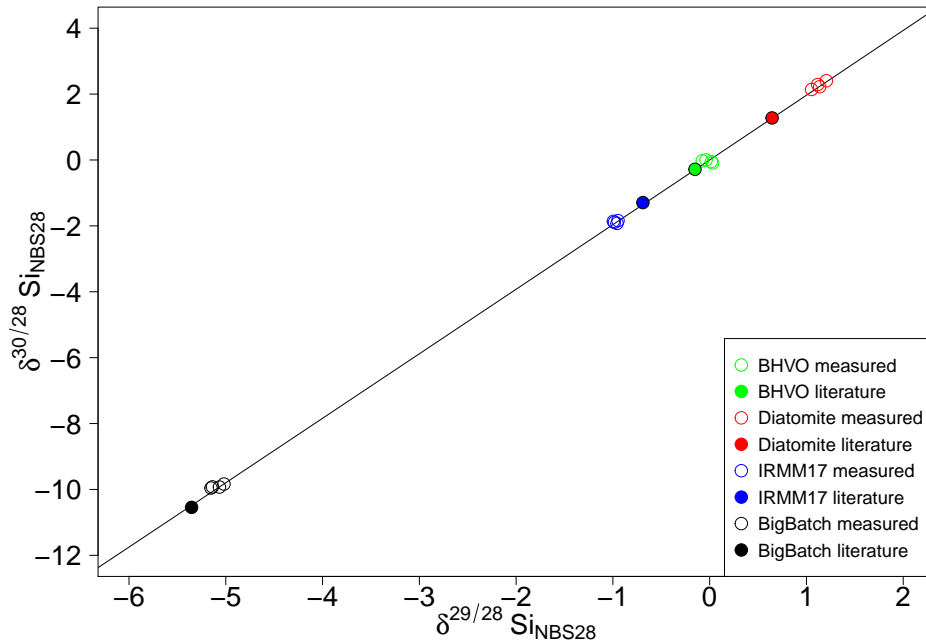
Figure 2.1: Bias due to systematic errors during measurements of Si isotope reference material without Mg addition to the sample and standard solutions using dry plasma conditions.

To circumvent the excessive use of sulfuric and/or nitric acid to stabilize the instrumental mass bias as suggested by Hughes et al. (2011), I show here that Mg addition during Si stable isotope measurements under dry plasma conditions improves accuracy and improves precision during Si stable isotope measurements in comparison to wet plasma or dry plasma conditions without Mg addition. Further a comparison between wet plasma measurement without Mg addition and dry plasma measurements with Mg addition is shown to highlight the advantages of Si stable isotope measurements with Mg addition consistent with findings of previously published studies using Mg addition (Cardinal et al., 2003; Engström et al., 2006; Zambardi and Poitrasson, 2011). The goal here is to reach a target measurement uncertainty for Si isotope measurement similar to published values which are in the range of 0.1 ‰ (2SD) on the $\delta(^{30/28}Si)_{NBS28}$ value (e.g. **?**). Furthermore, some tests were conducted (concentration matching, molarity matching, anion impurities) that show the stabilizing effect of Mg addition on the instrumental mass bias.

In the following a digestion procedure for natural samples is presented and furthermore directions for accurate and precise MC-ICP-MS analyses of stable Si isotopes are given.

2.3 Sample digestion

2.3.1 Solid samples

Solid samples were ground in a planetary mill, weighed and digested by alkaline fusion using NaOH after a method adapted from Georg et al. (2006b) and Zambardi and Poitrasson (2011). Depending on Si concentration, different sample amounts (5-20 mg) were weighed in into silver crucibles (SilverSurfer AG, M.Arvel) and NaOH pellets (100-200 mg) were added. The capped crucibles were placed in a muffle furnace for 15 min at 750 ℃. After fusion, crucibles were removed from the furnace and cooled-down on air, wiped from the

outside and placed into PTFE beakers. Depending on beaker size different amounts of Milli-Q water were added and beakers were stored in darkness for 24 hours. Afterwards the sample solution was transferred into pre-cleaned PE bottles. More Milli-Q water was added while the crucibles were remaining in PTFE beakers. Milli-Q water was then acidified with a calculated amount of HCl to reach a pH of 1.5. The beakers were then stored for additional 6 hours, sonicated and slightly shaken in between. This second solution was then added to the first solution into the PE bottle. The total solution was then acidified with a calculated amount of HCl to a final pH of 1.5. Due to the low solubility of Si in acidic solutions (Gunnarsson and Arnorsson, 2000), the concentration of Si should be below $\sim$50 ppm to avoid silica precipitation during sample storage. Si blanks of the fusion procedure are in general below 1 μg.

2.3.2   Water samples

The extraction of silicon from natural water samples is complicated by occasional high concentration of dissolved organic carbon (DOC). To ensure absence of the organic compounds in solution, water samples were treated before column purification. To digest DOC in water samples a fusion method was developed. Water samples were pre–concentrated (if necessary) by evaporation in PTFE beakers to a final amount of Si processed of $\sim$100 μg. After pre–concentration the remaining samples were transferred into silver crucibles and finally evaporated to dryness. The silver crucibles were then placed in a muffle furnace and heated to 750 ℃ to incinerate the organic carbon. Depending on the initial DOC content, the carbon incineration time had to be adjusted (depending on visual inspection after carbon incineration). To redissolve samples, 5 ml 1M NaOH were added to silver crucibles and evaporated to dryness. The crucibles were then placed a second time into a muffle furnace, using the alkaline fusion method described above for solid samples to redissolve the "carbon free" water samples. The re-dissolution of the fusion cake is then handled in the same way as for solid samples.

If high amounts of anions were present in the sample solutions a co–precipitation step is conducted prior to DOC decomposition. Iron as $Fe(NO_3)_3$ in 0.3 M HNO_3 is added to the sample solution to reach a final Fe:Si ratio by mass of 100:1. This solution is then well-mixed and precipitation of $Fe(III)OOH$ is forced by addition of $NH_4(OH)$ to attain a pH of $\approx$10. During Fe precipitation Si will be scavenged by the Fe precipitates and separated from the anions. The samples were then centrifuged and the supernatant was decanted. The precipitate was redissolved in 0.1 M HCl and transferred into silver crucibles and treated in the same way as common water samples. Several tests were conducted, where BHVO - 2G solution (digested using the above outlined method) was treated as water solution. No Si isotope fractionation was observed when using this method. Si blanks of the fusion and column separation procedure are in general below 1 μg which is less than 1 % of the total amount Si processed.

2.4   Column chemistry and preparation of Mg addition solution

Digested solid samples and pre - treated water samples are further purified using a cation exchange resin (Method adapted from Georg et al. (2006b)). This method uses 1.8 ml resin of Dowex 50 WX8 (200-400 mesh) filled into polypropylen columns (resin bed area

8 x 10 x 16 mm (IDxODxlength)). The resin was cleaned and conditioned with 3M and 6M HCl and 7M HNO_3 before samples were loaded. Depending on Si concentrations up to 20 ml of samples were loaded. The eluate was collected in pre-cleaned PE tubes and fully removed from resin with 5 ml Milli-Q water. Si concentration and purity of samples after column chemistry was checked on an ICP-OES.

The Mg solution was prepared from a 10000 ppm Mg standard solution in 0.5 M HNO3 acquired from Merck. This solution (0.3 ml) was evaporated to dryness, re-dissolved in Milli-Q water, evaporated again to dryness and again re-dissolved in Milli-Q water. The final solution was then transferred into a pre-cleaned PE bottle and diluted to a Mg concentration of $\sim$50 ppm Mg in H_2O.

2.5 MC-ICP-MS analysis

Determination of the Si isotope composition was performed in medium or high mass resolution on a Thermo Neptune MC-ICP-MS equipped with an H-skimmer cone and the Thermo® Jet-interface using a normal sample cone (wet plasma) or a Jet cone (dry plasma). Si stable isotopes have been measured under wet plasma conditions without Mg addition and under dry plasma conditions with Mg addition. Here the instrumental settings for both measuring conditions are summarized.

2.5.1 Wet plasma conditions without Mg addition

The purified sample solutions were introduced into the plasma using the Thermo stable introduction system (SIS) glass spray chamber (wet-plasma) equipped with a self–aspirating 120 μl/min nebulizer. Samples measured in wet plasma conditions were diluted to 2.5 ppm in 0.1 M HCl which typically resulted in an intensity of 2 V/ppm on ^{28}Si (10^{11} Ω resistor). Si stable isotope measurements were conducted in static mode on the interference-free low-mass side of the three Si isotopes. Si isotopes were collected in L4 (^{28}Si), L1 (^{29}Si) and C (^{30}Si) cups, respectively. To correct for instrumental mass bias, we used a standard-sample-bracketing procedure. Samples and Si isotope reference material were measured at least 4 times during a sequence; each sample or standard was measured for 30 cycles with an integration time for each cycle of 4 s. Pure 0.1 M HCl solutions were measured before and after each standard-sample-standard block and were used for on-peak zero correction. Typical intensities of ^{28}Si in blank solutions were below 5 mV.

2.5.2 Dry plasma conditions with Mg addition

The sample solutions were introduced into the plasma via a desolvation unit for dry plasma conditions (Apex, ESI®) equipped with a 100 μl/ min nebulizer. Measurements were conducted on the interference-free low-mass side of the three Si isotopes. Si stable isotope measurements were conducted in dynamic magnet switching mode and the Si isotopes were collected in L4 (^{28}Si), L1 (^{29}Si) and C (^{30}Si) cups, respectively. After magnet switching (idle time 3 s), Mg isotopes are collected in L2 (^{24}Mg), center cup (^{25}Mg) and H3 (^{26}Mg). Samples and Si isotope reference material were measured at least 4 times during a sequence; each sample or standard was measured for 30 cycles with an integration time for each cycle of 4 s for Si as well as for Mg in dynamic mode. Pure HCl solutions (0.1 M) were repeatedly measured during a sequence and typical intensities of ^{28}Si in blank solutions were below 15 mV. To correct for instrumental mass bias an

external normalization scheme using Mg - addition is applied. Here we combine standard - sample - bracketing with an exponential mass bias law (Cardinal et al., 2003) and correct the measured Si isotope ratios using:

$$\left(\frac{^{30}Si}{^{28}Si}\right)_{corrected} = \left(\frac{^{30}Si}{^{28}Si}\right)_{measured} \times \left(\frac{Mass^{30}Si}{Mass^{28}Si}\right)^{f} \tag{2.1}$$

The Si isotope ratios are corrected for instrumental mass bias using an instrumental fractionation factor f determined from simultaneous measurements of Mg isotope ratios:

$$f = ln\frac{\left(\frac{^{26}Mg}{^{24}Mg}\right)_{corrected}}{\left(\frac{^{26}Mg}{^{24}Mg}\right)_{measured}}/ln\frac{Mass^{26}Mg}{Mass^{24}Mg} \tag{2.2}$$

A positive side effect of the matrix modification by Mg addition is that the Si sensitivity is enhanced when measuring under dry plasma conditions, as it boosts signal intensity. We observed an increase in intensity by up to a factor of 3 between solutions without Mg addition and solutions with Mg addition, respectively. Sample solutions measured without Mg addition resulted in intensities of $\sim$6 V/ ppm on ^{28}Si (using a 10^{11} Ω resistor) in 0.1 M HCl. Solutions with Mg added ([Si]/[Mg] = 1) typically result in an intensity of $\sim$15 V/ ppm on ^{28}Si (using a 10^{11} Ω resistor) in 0.1 M HCl. Typical Si concentrations in measurement ready solutions are in the range of 0.8 to 1 ppm, which results in typical Si intensities on ^{28}Si of 12 to 15 V (using a 10^{11} Ω resistor).

2.5.3 Reporting Si isotope ratios

We report Si isotope values in the delta notation (δ) according to Coplen (2011) as $\delta(^{29/28}Si)_{NBS28}$ and $\delta(^{30/28}Si)_{NBS28}$ relative to the international isotope measurement standard NBS28 (quartz sand) in per mill (‰) by multiplying Equation 2.3 and Equation 2.4 with a factor of 10^3:

$$\delta(^{29/28}Si)_{NBS28} = \left(\frac{(^{29}Si/^{28}Si)_{sample}}{(^{29}Si/^{28}Si)_{NBS28}} - 1\right) \tag{2.3}$$

$$\delta(^{30/28}Si)_{NBS28} = \left(\frac{(^{30}Si/^{28}Si)_{sample}}{(^{30}Si/^{28}Si)_{NBS28}} - 1\right) \tag{2.4}$$

Reported uncertainties on delta values are the 95% confidence interval (CI) calculated according to Equation 2.5 where $\overline{\delta(^{30/28}Si)}$ is the mean of the measured delta values for samples or standards (at least n= 4 mass spectrometric repeats), t_{n-1} is a critical value from tables of the Student-t distribution and SE is the standard error of the mean:

$$CI = \overline{\delta(^{30/28}Si)_{NBS28}} \pm t_{n-1} * SE \tag{2.5}$$

2.5.4 Results of measured Si isotope reference materials

Literature values of Si isotope reference materials

The well defined Si isotope reference material BHVO–2G, a basalt standard, was usually measured as control standard during measured sequences for wet plasma and dry plasma measurements. Further the pure Si metal standard IRMM-17, the Diatomite (natural

opal sample) and the Big Batch (an artificial SiO_2 material) Si reference materials were used to verify the measured isotope values. Table 2.1 provides mean values of the reported values in the literature of the measured Si isotope reference materials.

Table 2.1: Literature values of the measured Si isotope reference materials. Reported here are mean values of the different literature sources of the different Si reference materials and their corresponding confidence interval and standard deviation. Note: BHVO is the mean value for literature values of BHVO–1, BHVO–2 and BHVO–2G

name	$\delta(^{29/28}Si)_{NBS28}$ [‰]	CI [‰]	SD [‰]	$\delta(^{30/28}Si)_{NBS28}$ [‰]	CI [‰]	SD [‰]	# of mean values
BHVO[1]	-0.154	0.012	0.049	-0.292	0.010	0.041	18
IRMM-17[2]	-0.690	0.090	0.036	-1.293	0.100	0.040	3
Diatomite[3]	0.645	0.023	0.030	1.276	0.44	0.062	10
Big Batch[4]	-5.353	0.043	0.041	-10.544	0.062	0.050	5

[1] Abraham et al. (2008); Fitoussi et al. (2009); Georg et al. (2009); Savage et al. (2010); Zambardi and Poitrasson (2011),
Armytage et al. (2011b); Hughes et al. (2011); Armytage et al. (2011a); Savage et al. (2011),
Steinhoefel et al. (2011); Pringle et al. (2013)

[2] Ding et al. (1996); Coplen et al. (2002b); Chmeleff et al. (2008)

[3] Abraham et al. (2008); Reynolds et al. (2007); Armytage et al. (2011a),
van den Boorn et al. (2010, 2006); Brzezinski et al. (2006),
Chakrabarti and Jacobsen (2010); Fitoussi et al. (2009); Georg et al. (2009),
Savage et al. (2011)

[4] Abraham et al. (2008); Reynolds et al. (2007); Chmeleff et al. (2008),
van den Boorn et al. (2006); Cardinal et al. (2003); Chakrabarti and Jacobsen (2010)

Results of measured Si isotope reference materials under wet plasma conditions without Mg addition

Several digestion procedures and chemical separations of Si were performed. Measurements of Si isotope reference material under wet plasma conditions without addition of Mg result in $\delta(^{30/28}Si)_{NBS28}$ values of: $\delta(^{30/28}Si)_{NBS28}$ = -0.269±0.032; n = 57 for the BHVO - 2G Si isotope reference material (Figure 2.2 and Table 2.2), $\delta(^{30/28}Si)_{NBS28}$ = -1.388±0.039; n = 55 for the IRMM-17 Si isotope reference material (Figure 2.3 and Table 2.2) and $\delta(^{30/28}Si)_{NBS28}$ = 1.0 ± 0.13; n = 11 for the Diatomite Si isotope reference material (Figure 2.4 and Table 2.2).

The measured values of the BHVO - 2G and IRMM-17 Si isotope reference materials under wet plasma conditions without Mg addition are the same, within uncertainty, as those reported in the literature (see Table 2.1). The determined value for the Diatomite Si isotope reference material measured under wet plasma conditions without additions of Mg results in a lower $\delta(^{30/28}Si)_{NBS28}$ value compared to the reported mean literature value.

Table 2.2: Mean values of the Si isotope reference materials measured under wet plasma conditions. Reported are mean values of all measured Si isotope reference materials and their corresponding confidence interval (CI) and their standard deviation (SD) to show the spread within the data.

name	$\delta(^{29/28}Si)_{NBS28}$ [‰]	CI [‰]	SD [‰]	$\delta(^{30/28}Si)_{NBS28}$ [‰]	CI [‰]	SD [‰]	n
BHVO - 2G	-0.136	0.027	0.101	-0.269	0.032	0.120	57
IRMM-17	-0.708	0.023	0.087	-1.388	0.039	0.145	55
Diatomite	0.516	0.110	0.164	0.998	0.130	0.191	11
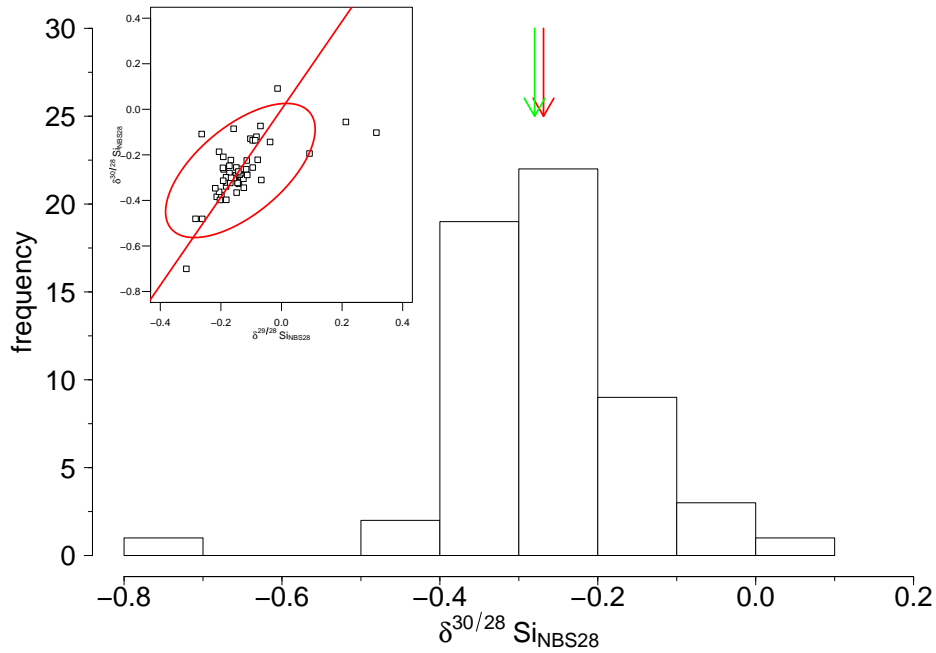
Figure 2.2: Frequency distribution of $\delta(^{30/28}Si)_{NBS28}$ values for BHVO - 2G measured in the absence of Mg under wet plasma conditions (average = -0.269 ± 0.032; n=57). The red arrow depicts the measured mean value (Table 2.2) and the green arrow depicts the literature mean value (Table 2.1). The inset shows all measured data points in a $\delta(^{30/28}Si)_{NBS28}$ vs. $\delta(^{29/28}Si)_{NBS28}$ diagram. The drawn ellipse denotes the 95% confidence region.
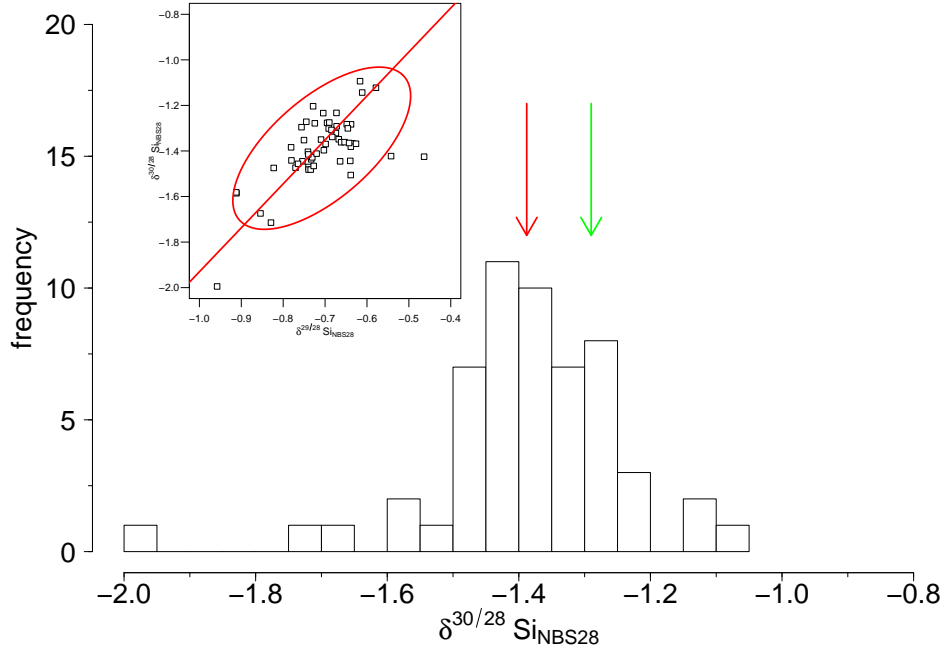
Figure 2.3: Frequency distribution of $\delta(^{30/28}Si)_{NBS28}$ values for IRMM - 17 measured in the absence of Mg under wet plasma conditions (average = -1.388 ± 0.039; n=55). The red arrow depicts the measured mean value (Table 2.2) and the green arrow depicts the literature mean value (Table 2.1). The inset shows all measured data points in a $\delta(^{30/28}Si)_{NBS28}$ vs. $\delta(^{29/28}Si)_{NBS28}$ diagram. The drawn ellipse denotes the 95% confidence region.
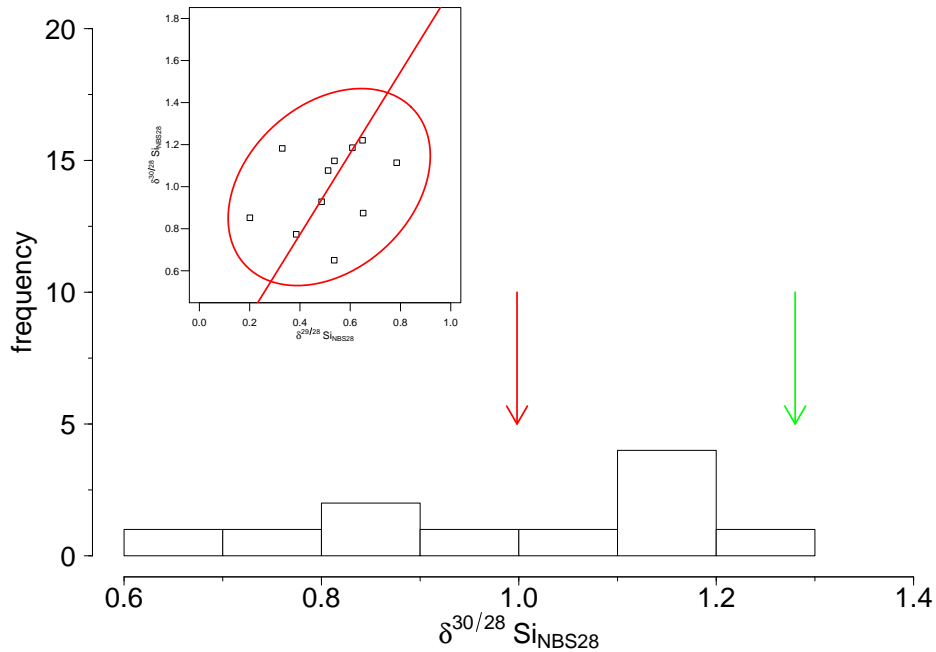
Figure 2.4: Frequency distribution of $\delta(^{30/28}Si)_{NBS28}$ values for Diatomite measured in the absence of Mg under wet plasma conditions (average = 0.998 ± 0.130; n = 11). The red arrow depicts the measured mean value (Table 2.2) and the green arrow depicts the literature mean value (Table 2.1). The inset shows all measured data points in a $\delta(^{30/28}Si)_{NBS28}$ vs. $\delta(^{29/28}Si)_{NBS28}$ diagram. The drawn ellipse denotes the 95% confidence region.
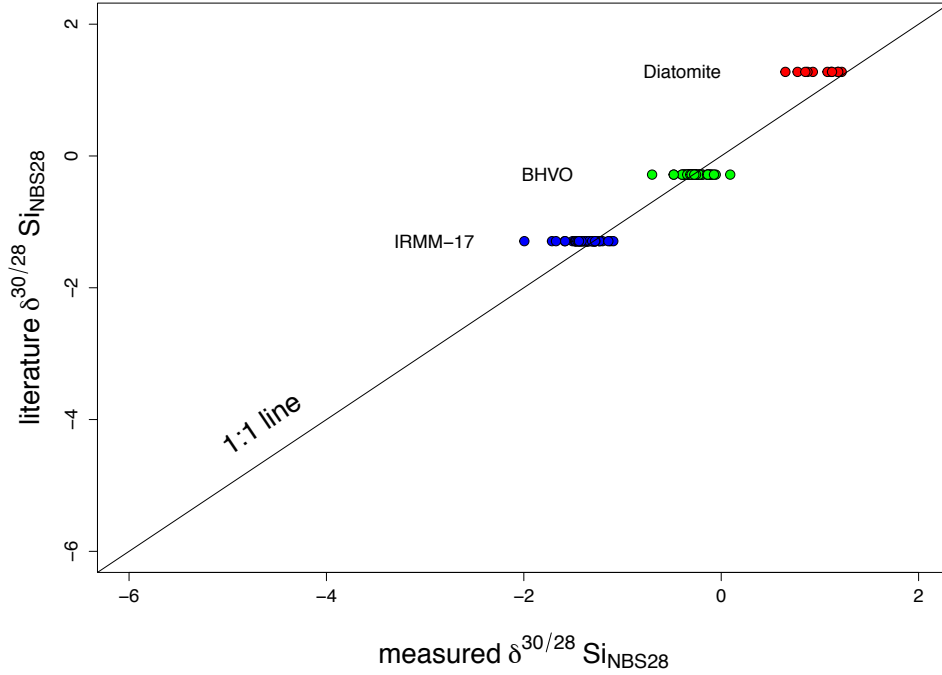
Figure 2.5: Comparison of Si isotope reference materials between measured $\delta(^{30/28}Si)_{NBS28}$ values and literature $\delta(^{30/28}Si)_{NBS28}$ values for measurements under wet plasma conditions in the absence of Mg.

Results of measured Si isotope reference materials under dry plasma conditions with Mg addition

Several digestions procedures and chemical separations of Si were performed. Measurements under dry plasma conditions with Mg addition result in $\delta(^{30/28}Si)_{NBS28}$ values of: $\delta(^{30/28}Si)_{NBS28}$ = -0.302±0.012; n = 133 for the BHVO - 2G Si isotope reference material (Figure 2.6 and Table 2.3), $\delta(^{30/28}Si)_{NBS28}$ = -1.373±0.016; n = 106 for the IRMM-17 Si isotope reference material (Figure 2.7 and Table 2.3), $\delta(^{30/28}Si)_{NBS28}$ = 1.217 ± 0.035; n = 24 for the Diatomite Si isotope reference material(Figure 2.8 and Table 2.3) and $\delta(^{30/28}Si)_{NBS28}$ = -10.682 ± 0.033; n = 26 for the Big Batch Si isotope reference material (Figure 2.9 and Table 2.3).

The measured values of the Si isotope reference materials BHVO-2G, IRMM-17 and Diatomite are the same, within uncertainty, as those reported in the literature (see Table 2.1). The determined value for the Big Batch Si isotope reference material measured under dry plasma conditions with Mg addition results in a lower $\delta(^{30/28}Si)_{NBS28}$ value compared to the reported mean literature value, but falls in the range of the reported values for this reference material (see Reynolds et al. (2007)).

Table 2.3: Mean values of the Si isotope reference material measured under dry plasma conditions. Reported here are mean values of all measured Si isotope reference material and their corresponding confidence interval (CI) and their standard deviation (SD) to show the spread within the data.

name	$\delta(^{29/28}Si)_{NBS28}$ [‰]	CI [‰]	SD [‰]	$\delta(^{30/28}Si)_{NBS28}$ [‰]	CI [‰]	SD [‰]	n
BHVO - 2G	-0.155	0.008	0.045	-0.302	0.012	0.069	133
IRMM-17	-0.710	0.009	0.044	-1.373	0.016	0.084	106
Diatomite	0.623	0.022	0.053	1.217	0.035	0.083	24
Big Batch	-5.456	0.018	0.046	-10.682	0.033	0.083	26
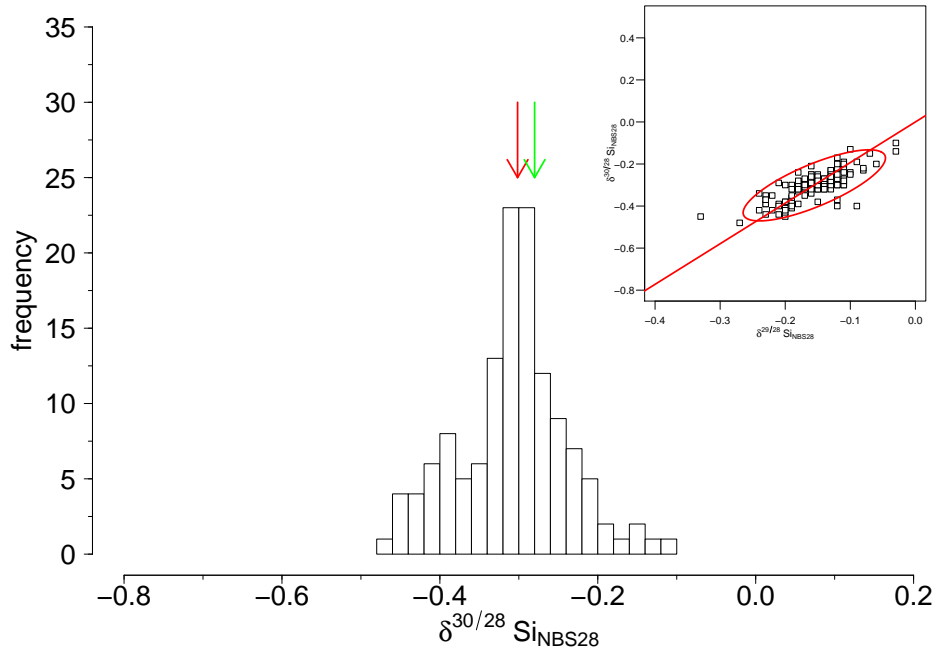
Figure 2.6: Frequency distribution histogram of $\delta(^{30/28}Si)_{NBS28}$ values for BHVO - 2G measured in the presence of Mg under dry plasma conditions (average = -0.302 ± 0.012; n = 133). The red arrow depicts the measured mean values (Table 2.2) and the green arrow depicts the literature mean value (Table 2.1). The inset shows all measured data points in a $\delta(^{30/28}Si)_{NBS28}$ vs. $\delta(^{29/28}Si)_{NBS28}$ diagram. The drawn ellipse denotes the 95% confidence region.
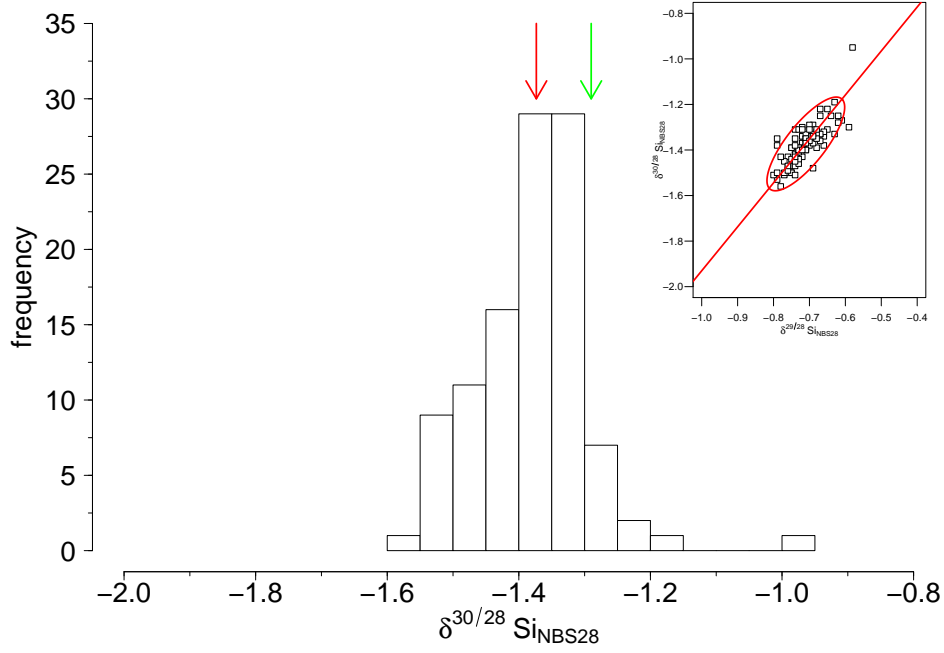
Figure 2.7: Frequency distribution histogram of $\delta(^{30/28}Si)_{NBS28}$ values for IRMM - 17 measured in the presence of Mg under dry plasma conditions (average = -1.373 ± 0.016; n = 106). The red arrow depicts the measured mean values (Table 2.2) and the green arrow depicts the literature mean value (Table 2.1). The inset shows all measured data points in a $\delta(^{30/28}Si)_{NBS28}$ vs. $\delta(^{29/28}Si)_{NBS28}$ diagram. The drawn ellipse denotes the 95% confidence region.
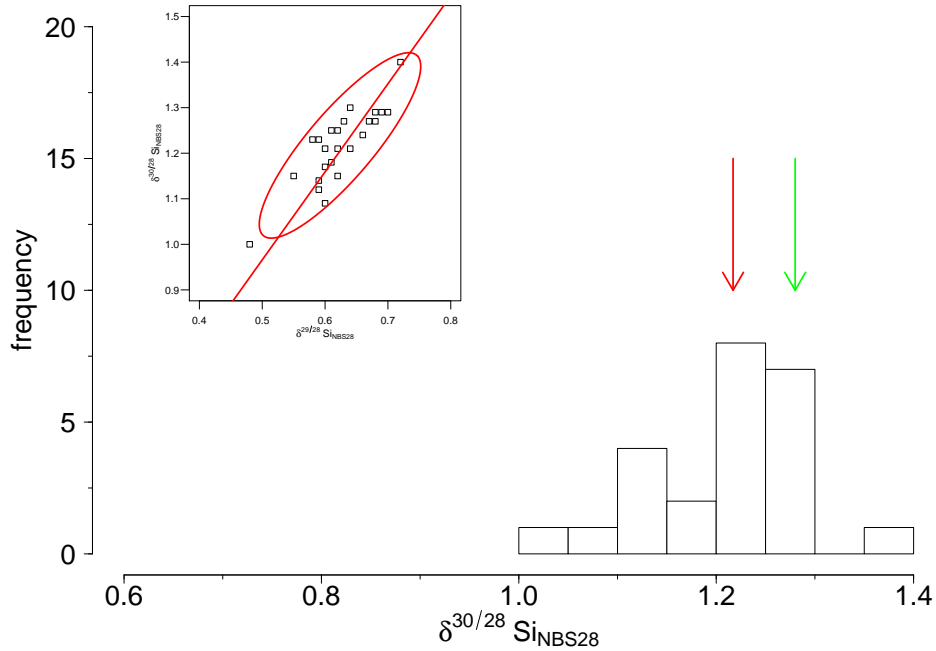
Figure 2.8: Frequency distribution histogram of $\delta(^{30/28}Si)_{NBS28}$ values for Diatomite measured in the presence of Mg under dry plasma conditions (average = 1.217 ± 0.035; n = 24). The red arrow depicts the measured mean values (Table 2.2) and the green arrow depicts the literature mean value (Table 2.1). The inset shows all measured data points in a $\delta(^{30/28}Si)_{NBS28}$ vs. $\delta(^{29/28}Si)_{NBS28}$ diagram. The drawn ellipse denotes the 95% confidence region.
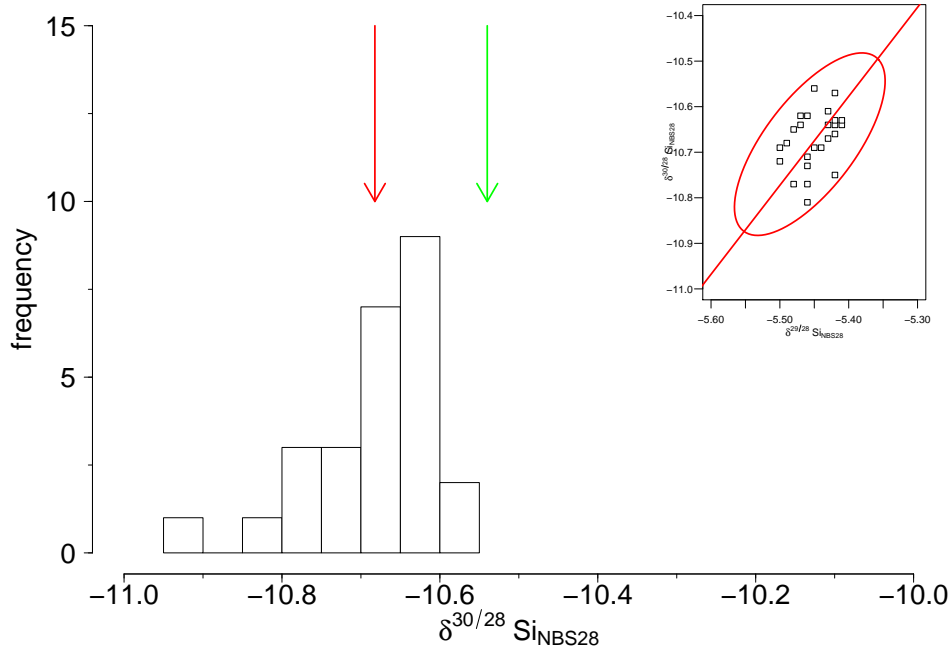
Figure 2.9: Frequency distribution histogram of $\delta(^{30/28}Si)_{NBS28}$ values for BigBatch measured in the presence of Mg under dry plasma conditions (average = -10.682 $\pm$ 0.033; n = 26). The red arrow depicts the measured mean values (Table 2.2) and the green arrow depicts the literature mean value (Table 2.1). The inset shows all measured data points in a $\delta(^{30/28}Si)_{NBS28}$ vs. $\delta(^{29/28}Si)_{NBS28}$ diagram. The drawn ellipse denotes the 95% confidence region.
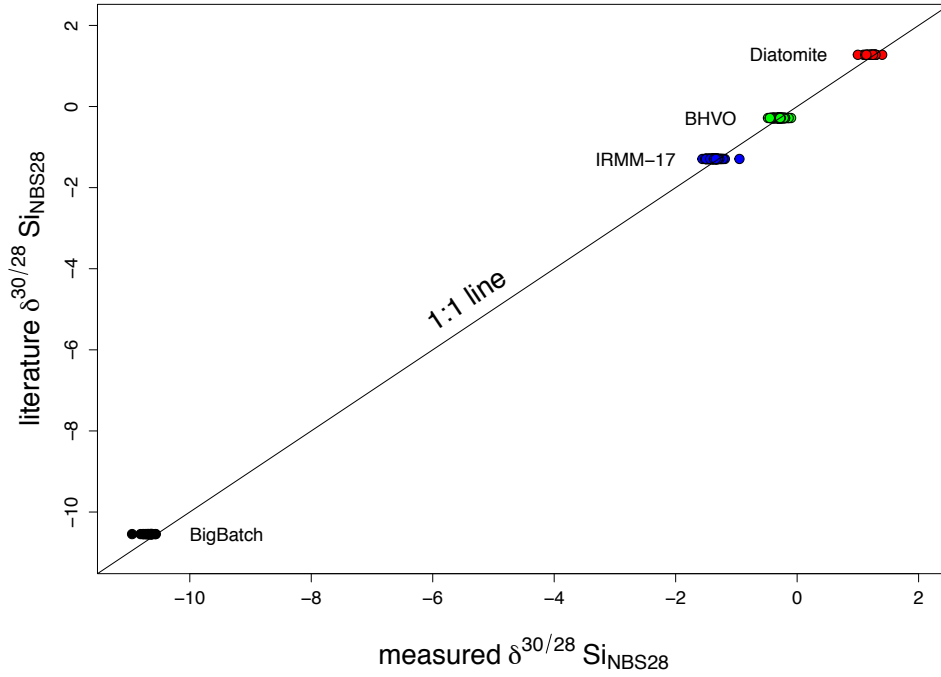
Figure 2.10: Comparison of Si isotope reference material between measured $\delta(^{30/28}Si)_{NBS28}$ values and literature $\delta(^{30/28}Si)_{NBS28}$ values for measurements under dry plasma conditions in the presence of Mg.

2.6 Tests conducted under wet and dry plasma conditions

Despite these very encouraging results for wet plasma as well as for dry plasma conditions, several tests for wet and dry plasma conditions were performed to infer the influence of matrix matching between samples and standards during stable Si isotope measurements. Based on the standard deviation of the measured BHVO–2G Si isotope reference material a target measurement uncertainty of 0.14 ‰ is defined. This is the measurement uncertainty which can be reached during repeated measurements of natural samples. Therefore, the results of the performed tests are evaluated based on this defined target measurement uncertainty.

For all performed tests a purified NBS28 solution was used which then was artificially "contaminated". Anion standards (Merck) were processed as samples on a Si column to remove cations. An "artificial" contaminated NBS28 solution was measured against the bracketing pure NBS28 solution. For simplicity, the artificially contaminated NBS28 solutions are called "samples". During the conducted tests always only one parameter was changed and all other parameters were held constant. It can not be excluded that during sample preparation also other parameters, that were assumed to be constant, change due to uncertainty of the sample preparation procedure. It is assumed here that the uncertainty induced during sample preparation on constant parameters result in a minor contribution to the overall uncertainty. The following tests were performed:

1. Si concentration matching (dry plasma): The Si concentration was varied $\pm 50\%$ relative to the bracketing standard, while the Mg concentration remained constant between bracketing standard and sample.

2. Mg concentration matching (dry plasma): The Si concentration was held constant while the Mg concentration was changed relative to the bracketing standard by –80% to +25%.

3. Molarity matching (wet and dry plasma): Usually, standard and samples were measured using 0.1 M HCl. To test the sensitivity to molarity, the molarity of the samples was changed relative to the bracketing standard to 0 M HCl (Milli-Q water), 0.04 M, 0.08 M, 0.12 M, 0.16 M, 0.2 M, 0.3 M, 0.4 M and 0.5 M HCl for dry plasma conditions. For wet plasma conditions the molarity was changed relative to the bracketing standard from 0.05 to 0.15 mol/l HCl.

4. Column fractionation : 10 ml of NBS28 solution were loaded onto a column and the eluate was collected in 1 ml steps to check whether Si fractionates during this purification step if recovery is incomplete.

5. Anion contamination (wet and dry plasma): Solutions containing different [anion]/ [Si] ratios ($[\mu g]/ [\mu g]$) were prepared 0.01, 0.05, 0.1, 0.2, 0.4, 0.8, 1.6, 3.4 and 6.4 and measured against an anion free bracketing standard.

2.6.1 Si concentration matching for dry plasma conditions

The Si concentration matching experiments show, in the tested range of $\pm 50\%$ of the bracketing Si concentration, no influence in the resulting $\delta(^{30/28}Si)_{NBS28}$ values of the samples. The measured values for uncorrected or corrected data are identical within

uncertainty. The absolute values did not change regardless of whether the external normalization correction scheme, using Mg isotope ratios to determine the instrumental fractionation factor f, was applied or not applied.
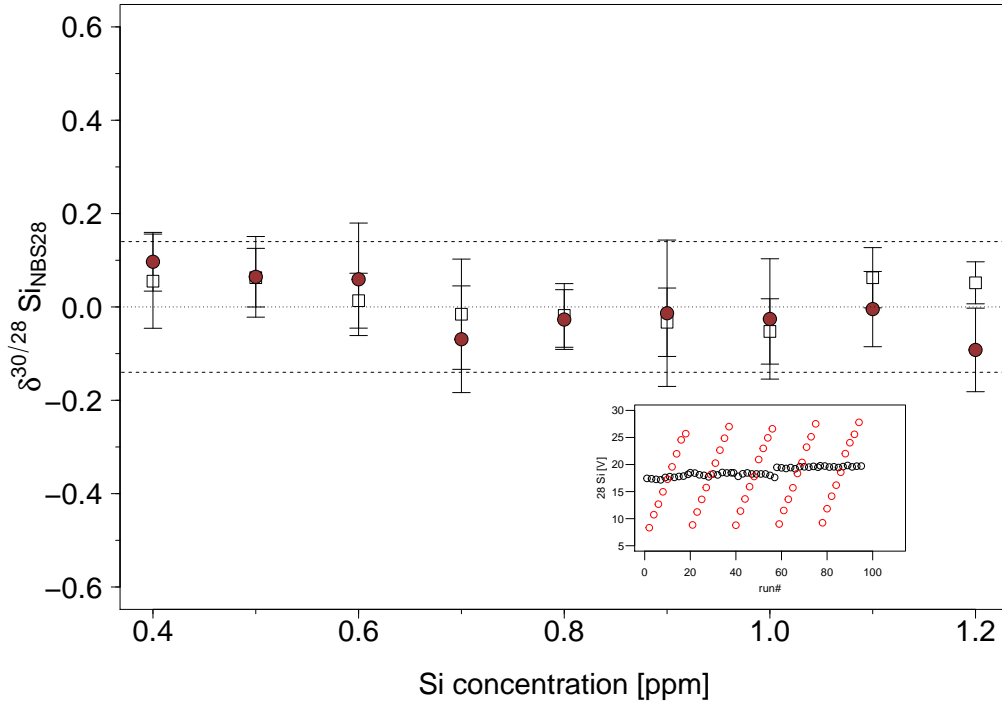
Figure 2.11: $\delta(^{30/28}Si)_{NBS28}$ values of measured samples under dry plasma conditions plotted against their Si concentration in the presence of Mg. Samples were measured against a 0.8 ppm Si NBS28 bracketing standard solution, doped with 0.8 ppm Mg. Red circles depict uncorrected values and open squares depict data where Mg correction scheme was applied; error bars are the 95 % confidence interval of the test measurements. The stippled line denotes the expected value. The dotted line denote the target measurement uncertainty of 0.14 ‰. The inset shows the ^{28}Si intensity against run number (time) during the Si concentration test run. Open circles show the ^{28}Si intensity of the NBS28 bracketing standard and red circles the intensity of the different Si concentrations measured (5 replicates) against the bracketing standard, respectively.

2.6.2 Mg concentration matching for dry plasma conditions

The second test in which the Mg concentration was changed according to the bracketing standard shows a similar result as the Si concentration test. Samples within a range $\pm 25\%$ of the bracketing standard show no deviation from the expected value. The samples which deviate more than 50% from the Mg concentration of the bracketing standard show a slight deviation from the expected value. The measured values for uncorrected or corrected data are identical within uncertainty. The absolute values did not change whether the external normalization correction scheme, using Mg isotope ratios to determine the instrumental fractionation factor f, was applied or not applied.
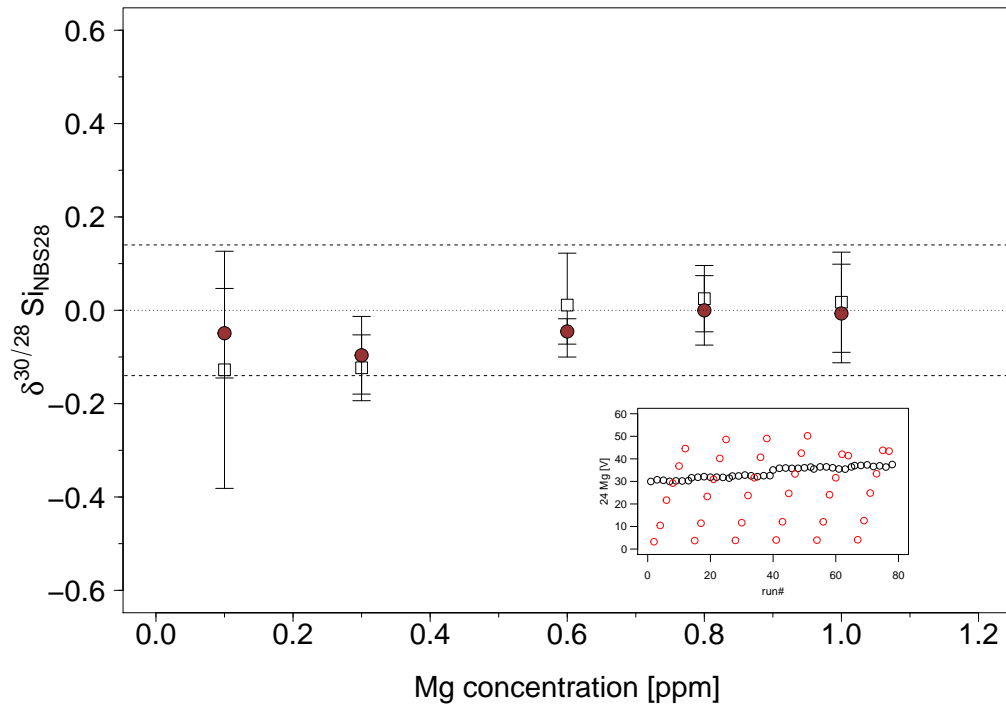
Figure 2.12: $\delta(^{30/28}Si)_{NBS28}$ values of measured samples under dry plasma conditions plotted against the Mg concentration of the Mg solution added. Samples were measured against a 0.8 ppm Si NBS28 bracketing standard solution, doped with 0.8 ppm Mg. Red circles depict uncorrected values and open squares depict data where Mg correction scheme was applied; error bars are the 95 % confidence interval of the test measurements. The stippled line denotes the expected value. The dotted line denote the target measurement uncertainty of 0.14 ‰. Inset shows the ^{24}Mg intensity against run number (time) during the Mg concentration test run. Open circles show the ^{24}Mg intensity of the NBS28 bracketing standard and red circles the intensity of the different Mg concentrations measured (6 replicates) against the bracketing standard, respectively.

2.6.3   Molarity matching for wet and dry plasma conditions

The third test evaluated the influence of molarity matching of the acidic HCl matrix between samples and bracketing standards. This test was conducted also under wet - plasma conditions to show how Mg addition helps to stabilize mass bias effects. The bracketing standard molarity was set to 0.1 mol/l HCl and the sample molarity was varied between 0 to 0.5 mol/l for samples with Mg addition (Figure 2.13) and from 0.05 to 0.15 mol/l HCl for tests without Mg addition (Figure 2.14) under wet plasma conditions. A strong influence of matrix molarity is observed when measuring without Mg addition. In contrast to measurements without Mg addition, no influence in the measured $\delta(^{30/28}Si)_{NBS28}$ values was observed, in the tested range of 0.04 to 0.2 mol/l HCl. Further no effect when applying the external Mg addition correction scheme was observed in the range between 0.04 to 0.2 mol/l HCl. In the molarity range between 0.3 and 0.5 mol/l, a significant deviation for the uncorrected samples from the expected $\delta(^{30/28}Si)_{NBS28}$ value is observed. If the external normalization correction scheme using Mg was applied to the data, the expected value was achieved.
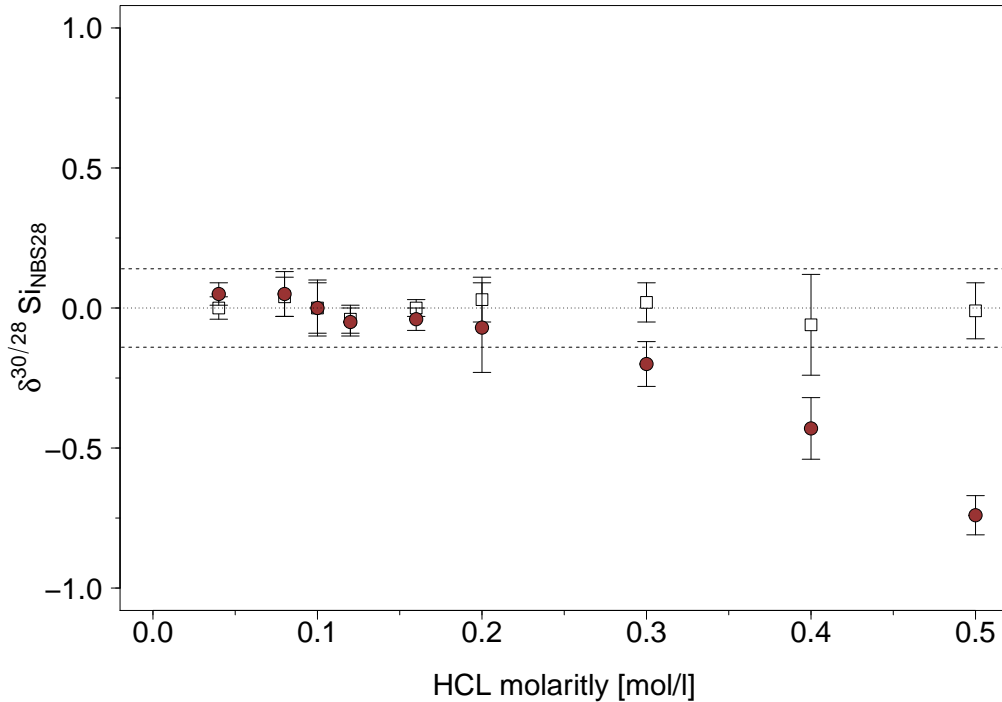
Figure 2.13: $\delta(^{30/28}Si)_{NBS28}$ values of measured samples under dry plasma conditions plotted against their molarity of the HCl matrix in the presence of Mg. Red circles depict the uncorrected values and open squares depict the data where Mg correction scheme was applied; error bars are the 95 % confidence interval of the test measurements. The stippled line denotes the expected value.The dotted line denote the target measurement uncertainty of 0.14 ‰.
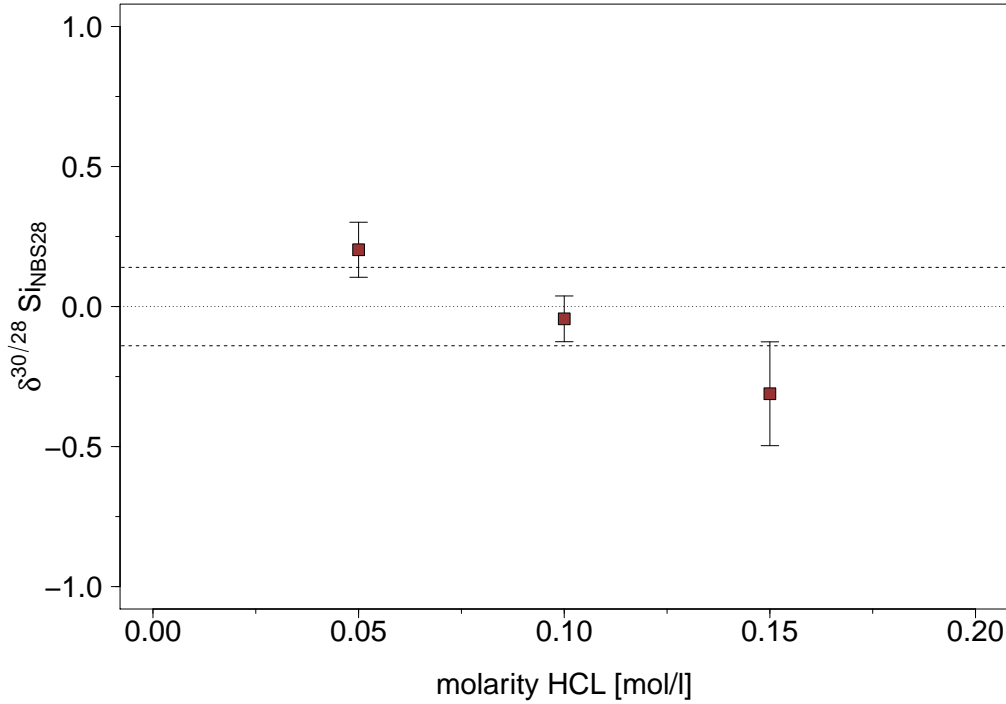
Figure 2.14: $\delta(^{30/28}Si)_{NBS28}$ values of measured test samples in the absence of Mg and measured under wet plasma conditions plotted against their molarity of the HCl matrix. The stippled line denotes the expected value.The dotted line denote the target measurement uncertainty of 0.14 ‰.

2.6.4   Column fractionation

According to Fitoussi et al. (2009) Si isotope fractionation during column chemistry is expected if the pH of the sample solution is not adjusted within the pH range of 2.1 - 2.4. Fitoussi et al. (2009) found Si isotope fractionation of up to $\delta(^{30/28}Si)_{NBS28} = 0.4$‰ during column chemistry if the pH was lower than 2.1. Furthermore they observed a reduction of the Si column yield. Therefore a test was performed to infer whether this type of Si isotope fractionation was present in the above described column procedure. Different standard solutions (NBS28 or BHVO-2G) were loaded on a column and the column yield was artificially reduced by collecting the eluted sample in several different fractions. Some of the collected splits where then measured for their Si isotope composition. As it can be seen in Figure 2.15 no isotope fractionation is observed even at low Si yields when compared to measurement uncertainty.
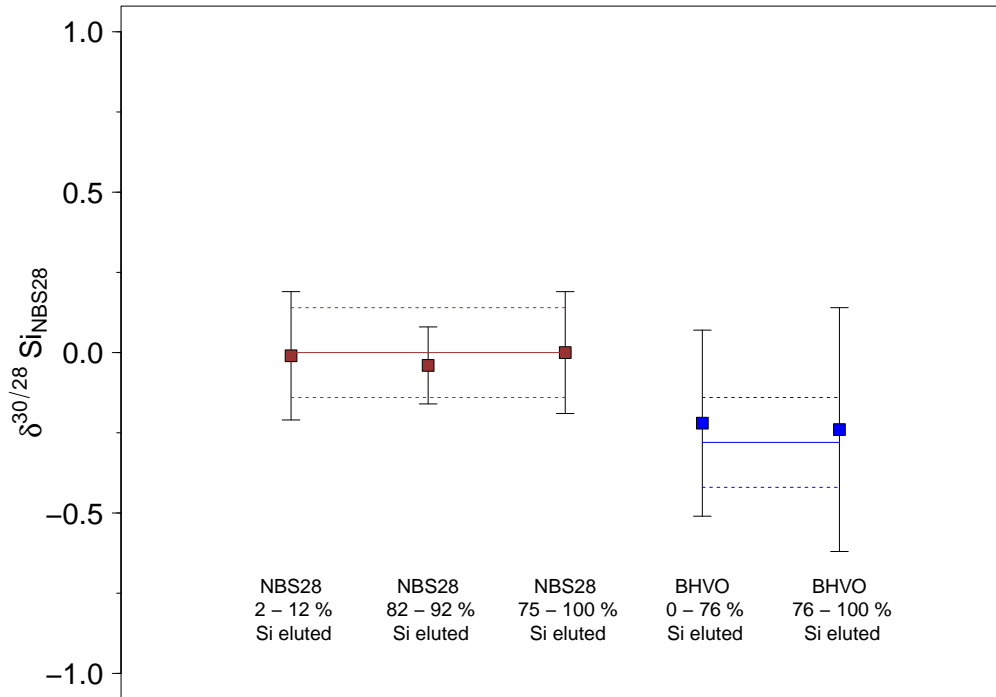
Figure 2.15: $\delta(^{30/28}Si)_{NBS28}$ values of measured test solutions plotted against the column yield [%] of the particular measured NBS28 (red) and BHVO-2G (blue) standard solutions; error bars represent the 95 % confidence interval of the test measurements. The solid line denotes the expected value. The dotted line denote the target measurement uncertainty of 0.14 ‰.

2.6.5 Anion contamination

In this test series measurements of artificially contaminated samples against a pure NBS28 bracketing standard were conducted, using anion standard solutions. Si and Mg concentrations were kept constant in all samples. If anion contamination has no effect on the mass bias of Si and Mg, no deviation of the measured value from zero ($\delta(^{30/28}Si)_{NBS28}=$ 0 ‰) should be observed. Further a test under wet-plasma conditions was conducted to show how remaining SO_4 anions change the mass bias when measuring without Mg addition.

Anion contamination with SO_4 for wet and dry plasma conditions

Samples contaminated with sulfate and measured under wet-plasma conditions without Mg addition show a deviation from the expected $\delta(^{30/28}Si)_{NBS28}$ value at SO_4/Si ratios above 0.05 (Figure 2.16). In contrast to these findings show sulfate contaminated samples, measured with Mg addition, below a SO_4/Si ratio of 1.6 no significant deviation from the expected value ($\delta(^{30/28}Si)_{NBS28}=$ 0 ‰; see Figure 2.17). Further no deviation between the uncorrected and corrected value was observed below a SO_4/Si ratio of 1.6. For samples with an SO_4/Si ratio >1.6 differences between the corrected and uncorrected measured values were observed. Applying the exponential external correction scheme to samples with a SO_4/Si ratios of >1.6, results in an "overcorrection" of the measured data. One reason for this "overcorrection" might be that contamination with SO_4 affects Si and Mg in different proportions and therefore the external correction scheme cannot be applied. The finding that SO_4 contamination of up to a SO_4/Si ratio of 1.6 does not effect Si

isotope measurements is in contrast to the study of van den Boorn et al. (2009). These authors found deviations from the expected value of up to 1.4‰ for SO_4/Si ratios above 0.02. It has to be noted that van den Boorn et al. (2009) used a different desolvation unit (Cetac Aridus membrane desolvation device) and further measured without external Mg addition but also on a Thermo Neptune MC-ICP-MS.
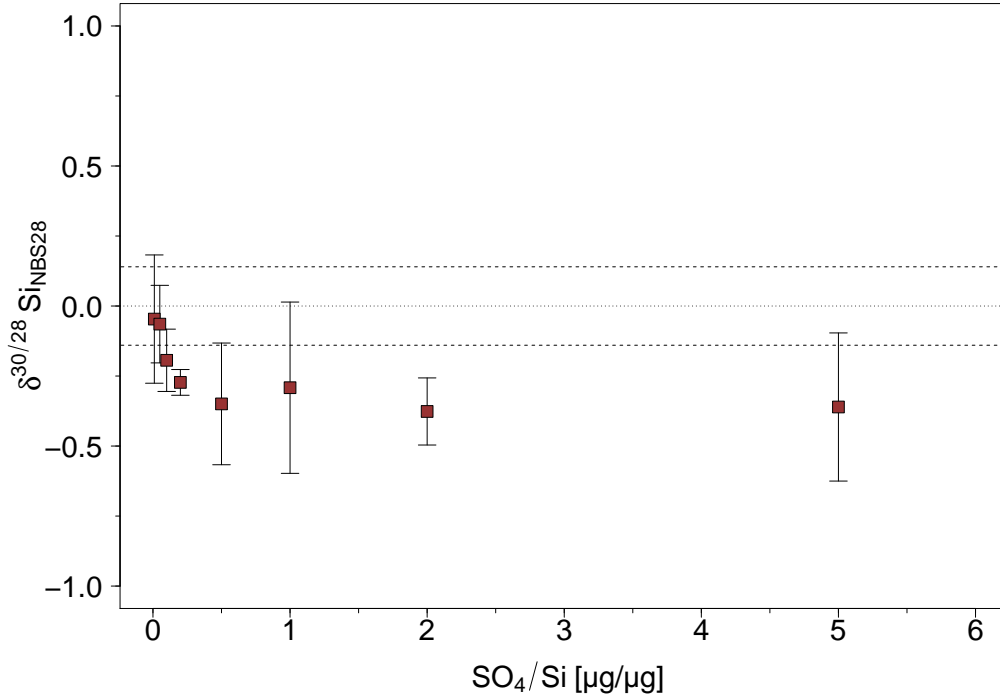
Figure 2.16: $\delta(^{30/28}Si)_{NBS28}$ values of samples contaminated with SO_4 measured against an anion free NBS28 bracketing standard in the absence of Mg under wet plasma conditions. The stippled line denotes the expected value. The dotted line denote the target measurement uncertainty of 0.14 ‰.
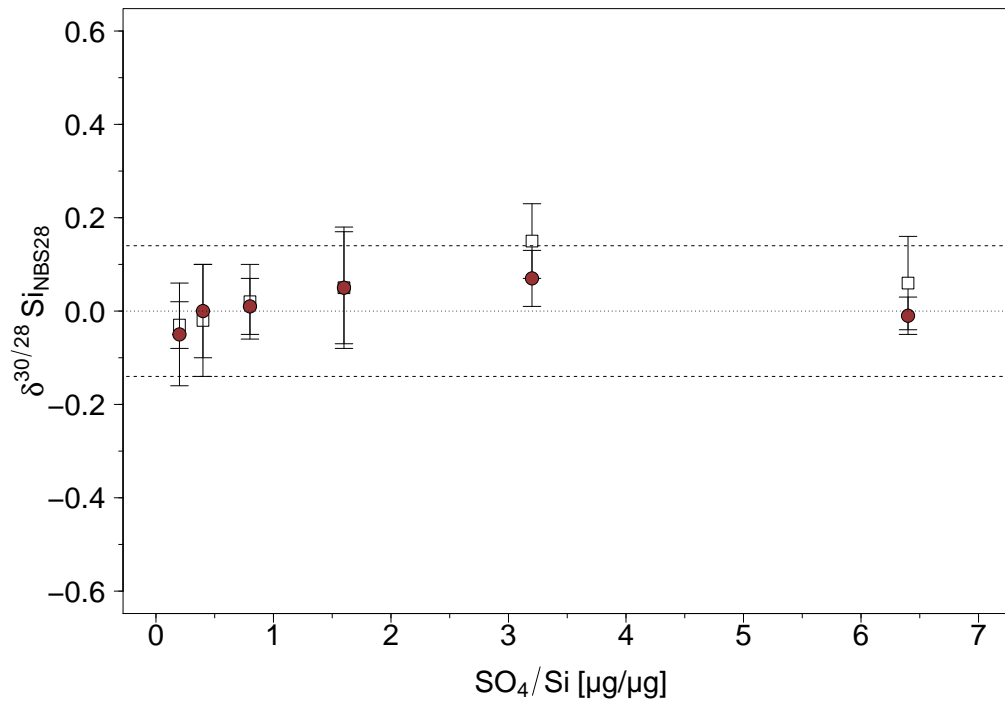
Figure 2.17: $\delta(^{30/28}Si)_{NBS28}$ values of samples contaminated with SO_4 measured under dry plasma condition against an anion free NBS28 bracketing standard in the presence of Mg. Red circles depict the uncorrected values and open squares depict the data where Mg correction scheme was applied; error bars represent the 95 % confidence interval of the test measurements. The stippled line denotes the expected value. The dotted line denote the target measurement uncertainty of 0.14 ‰.

Anion contamination with PO$_4$ under dry plasma conditions

For PO$_4$ anion contamination tests, almost the same results as for SO$_4$ test are obtained. For a PO$_4$ anion contamination below a PO$_4$/Si ratio of 1 no deviation from the expected value is observed. Above a PO$_4$/Si ratio of 1 a divergent behavior of the corrected and uncorrected values is observed. It seems that the Mg corrected values are systematically higher than the uncorrected Si isotope ratios which might be an indication that Mg and Si interact/react differently with PO$_4$ contaminating anions. However, both values, the uncorrected and Mg corrected Si isotope ratio, fall within the range of the defined target measurement uncertainty.
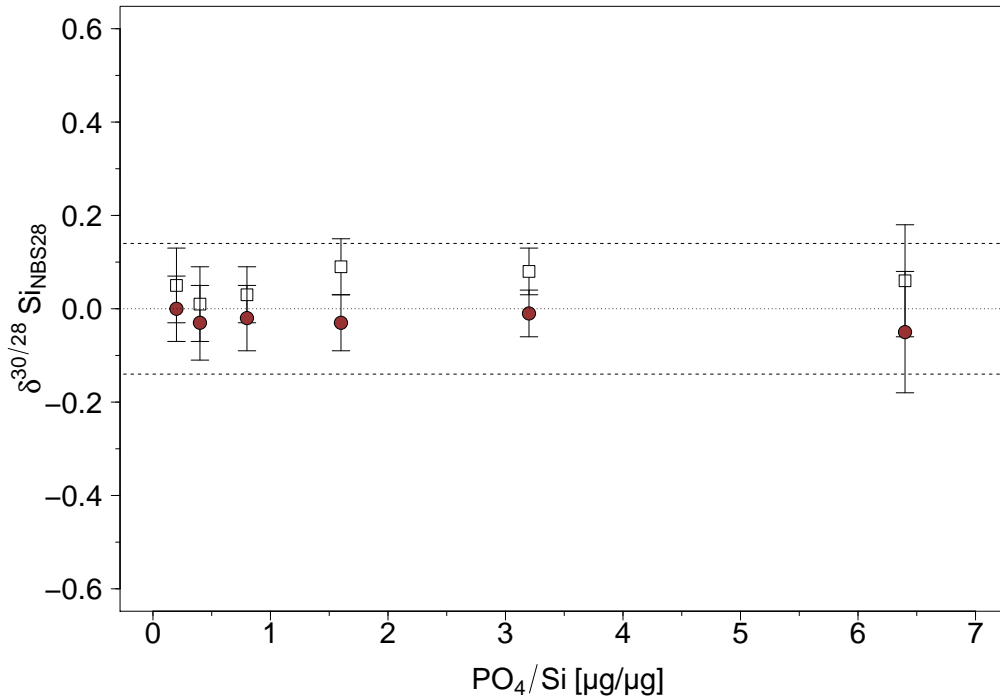
Figure 2.18: $\delta(^{30/28}Si)_{NBS28}$ values of samples contaminated with PO$_4$ measured under dry plasma conditions against an anion free NBS28 bracketing standard in the presence of Mg. Red circles depict the uncorrected values and open squares depict the data where Mg correction scheme was applied; error bars represent the 95 % confidence interval of the test measurements. The stippled line denotes the expected value. The dotted line denote the target measurement uncertainty of 0.14 ‰.

Anion contamination with NO$_3$ under dry plasma conditions

The results of the artificial contamination experiment using NO$_3$ anions show no deviation for the entire tested range from the unbiased value ($\delta(^{30/28}Si)_{NBS28}$= 0 ‰) up to a NO$_3$/Si ratio of 6.4. Furthermore no deviation between the corrected and uncorrected Si isotope ratios is observed as it is recognized for the SO$_4$ and PO$_4$ anion contamination experiments.
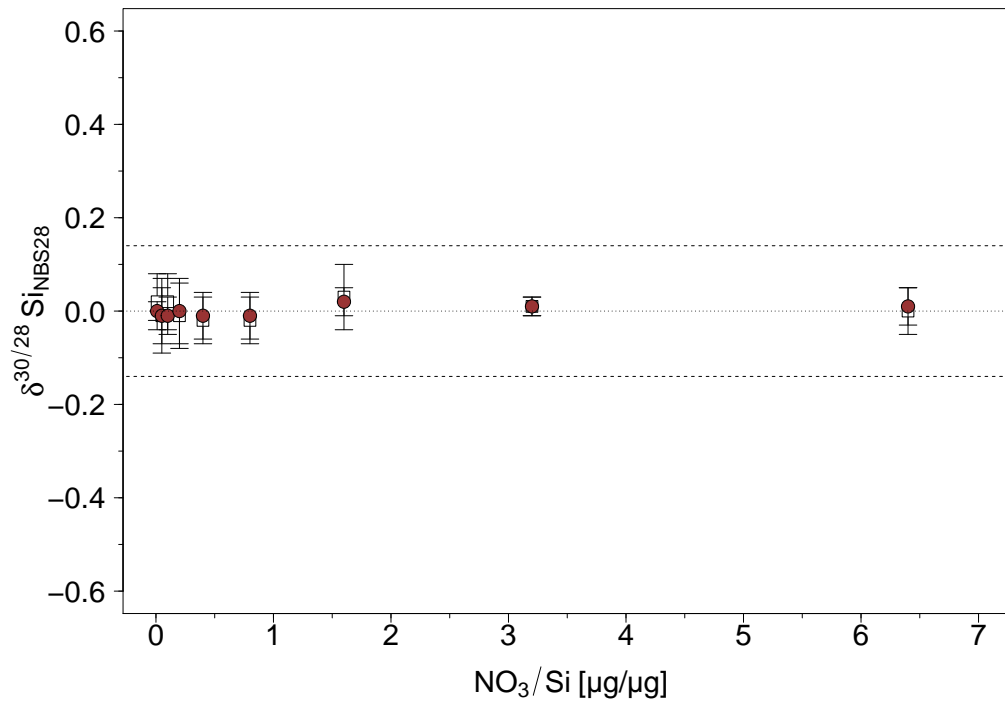
Figure 2.19: $\delta(^{30/28}Si)_{NBS28}$ values of samples contaminated with NO_3 measured under dry plasma conditions against an anion free NBS28 bracketing standard in the presence of Mg. Red circles depict the uncorrected values and open squares depict the data where Mg correction scheme was applied; error bars represent the 95 % confidence interval of the test measurements. The stippled line denotes the expected value. The dotted line denote the target measurement uncertainty of 0.14 ‰.

2.7   Summary

An extension of the established digestion method for natural samples by an organic removal step for solid and water samples is described in detail. Further it is shown how external Mg additions improves the accuracy and stability of Si isotope measurements under dry plasma conditions in comparison to wet plasma measurements without Mg addition (see Table 2.2 and Table 2.3 and Figures 2.2 to 2.9). Measurements of Si reference material under dry plasma conditions with Mg addition compared to wet plasma conditions without Mg addition show lower SD values, respectively (Table 2.2 and Table 2.3). The use of Mg as "matrix modifier" to improve the measurement repeatability of isotope measurements has been also shown for measurements of Pb by Barling and Weis (2008) and is also effective for Si. The use of external Mg addition further helps to circumvent several known issues when measuring stable isotopes using a desolvation unit. The use of Mg as "matrix modifier" has several benefits when measuring Si stable isotope under dry plasma conditions:

1. The addition of Mg increases the sensitivity by up to a factor of 3 when measuring under dry plasma conditions.

2. The addition of Mg reduces variations in mass bias between sample and standards induced by different sample standards matrices:

   (a) Concentration matching: Si and Mg concentration can vary between samples and bracketing standards of up to $\pm50\%$ with no visible effect observed on instrumental mass bias.

   (b) Molarity matching: A molarity mismatch between samples and standard in the range of 0.05 to 0.2 mol/l measured against a 0.1 mol/l bracketing standards does not result in observable changes. For a sample-standard molarity mismatch above 0.2 mol/l to 0.5 mol/l Si isotope fractionation of up to $\delta(^{30/28}Si)_{NBS28}$= -0.7 ‰ occurs for the uncorrected values. When applying the external Mg correction scheme, no deviation from the expected value is observed.

   (c) Anion contamination: No effect on mass bias is observed for anion contaminations with SO_4 and PO_4 below an [anion]/Si ratio of 1. For an anion contamination with NO_3 no change in mass bias is observable below an [anion]/Si ratio of 6.4.

When using Mg as matrix modifier, the solution matrix is dominated by the high amount of Mg added and not by remaining impurities or sample standard mismatch (e.g. anions, discrepancies in Si concentration or molarity mismatching between sample and bracketing standard). One possible reason for this increased performance when using Mg addition is the low ionization potential of Mg (Mg = 7.65 eV). Therefore when Mg is introduced into the ICP, Mg will ionize more efficiently and therefore dominate the plasma environment. Small changes in the ionization environment due to anion contamination or concentration/molarity mismatching will be retained by the dominating Mg ions and will not affect the Si ionization efficiency. Several tests reveal that Si isotope measurements conducted with external Mg addition are less sensitive to sample and standard matrix mismatch as expected from measurements under wet plasma conditions without Mg addition. A further test of potential Si isotope fractionation during Si column separation procedure reveal that no Si isotope fractionation occurs.

2.8 Appendix Chapter 2

2.8.1 Tables

Table 2.4: Mg corrected and uncorrected $\delta(^{29/28}Si)_{NBS28}$ and $\delta(^{30/28}Si)_{NBS28}$ values for measured test samples of the Si concentration matching test under dry plasma conditions.

[Si]	not Mg corrected				Mg corrected			
	$\delta(^{29/28}Si)$	CI	$\delta(^{30/28}Si)$	CI	$\delta(^{29/28}Si)$	CI	$\delta(^{30/28}Si)$	CI
[ppm]	[‰]	[‰]	[‰]	[‰]	[‰]	[‰]	[‰]	[‰]
0.4	0.032	0.060	0.097	0.063	0.011	0.067	0.055	0.101
0.5	0.038	0.042	0.064	0.086	0.037	0.046	0.063	0.063
0.6	0.032	0.098	0.059	0.121	0.009	0.059	0.013	0.059
0.7	-0.057	0.061	-0.069	0.114	-0.029	0.072	-0.016	0.118
0.8	-0.011	0.042	-0.027	0.064	-0.010	0.039	-0.018	0.068
0.9	0.005	0.084	-0.014	0.157	-0.004	0.043	-0.033	0.073
1	-0.015	0.058	-0.026	0.129	-0.025	0.026	-0.053	0.070
1.1	-0.004	0.033	-0.005	0.081	0.030	0.029	0.063	0.065
1.2	-0.053	0.040	-0.092	0.090	0.020	0.009	0.052	0.045

Table 2.5: Mg corrected and uncorrected $\delta(^{29/28}Si)_{NBS28}$ and $\delta(^{30/28}Si)_{NBS28}$ values for measured test samples of the Mg concentration matching test under dry plasma conditions.

[Mg]	not Mg corrected				Mg corrected			
	$\delta(^{29/28}Si)$	CI	$\delta(^{30/28}Si)$	CI	$\delta(^{29/28}Si)$	CI	$\delta(^{30/28}Si)$	CI
[ppm]	[‰]	[‰]	[‰]	[‰]	[‰]	[‰]	[‰]	[‰]
0.1	-0.065	0.027	-0.049	0.096	-0.104	0.126	-0.128	0.254
0.3	-0.050	0.050	-0.096	0.083	-0.063	0.067	-0.123	0.071
0.6	-0.036	0.034	-0.045	0.027	-0.007	0.061	0.011	0.111
0.8	0.001	0.095	0.000	0.074	0.014	0.066	0.025	0.071
1	0.005	0.052	-0.007	0.106	0.017	0.064	0.017	0.107

Table 2.6: Mg corrected and uncorrected $\delta(^{29/28}Si)_{NBS28}$ and $\delta(^{30/28}Si)_{NBS28}$ values for measured test samples of the HCl molarity matching experiments under dry plasma conditions.

	not Mg corrected				**Mg corrected**			
[molarity]	$\delta(^{29/28}Si)$	CI	$\delta(^{30/28}Si)$	CI	$\delta(^{29/28}Si)$	CI	$\delta(^{30/28}Si)$	CI
[mol/l]	[‰]	[‰]	[‰]	[‰]	[‰]	[‰]	[‰]	[‰]
0	1.358	2.700	1.377	2.721	0.628	1.809	-0.056	1.273
0.04	0.023	0.021	0.052	0.045	-0.001	0.041	0.003	0.037
0.08	0.022	0.035	0.046	0.081	0.019	0.039	0.039	0.069
0.1	0.004	0.056	-0.002	0.097	0.005	0.053	0.001	0.091
0.12	-0.038	0.057	-0.049	0.049	-0.033	0.032	-0.040	0.045
0.16	-0.013	0.046	-0.044	0.040	0.008	0.044	-0.003	0.034
0.2	-0.012	0.144	-0.069	0.161	0.039	0.097	0.032	0.077
0.3	-0.081	0.045	-0.203	0.084	0.033	0.037	0.021	0.066
0.4	-0.202	0.059	-0.427	0.108	-0.013	0.126	-0.056	0.177
0.5	-0.354	0.049	-0.738	0.073	0.017	0.084	-0.010	0.100

Table 2.7: $\delta(^{29/28}Si)_{NBS28}$ and $\delta(^{30/28}Si)_{NBS28}$ values for measured test samples of the HCl molarity matching experiments under wet plasma conditions without Mg addition.

molarity	$\delta(^{29/28}Si)$	CI	$\delta(^{30/28}Si)$	CI
[mol/l]	[‰]	[‰]	[‰]	[‰]
0.05	0.060	0.133	0.203	0.098
0.1	0.029	0.060	-0.044	0.082
0.15	-0.131	0.068	-0.311	0.185

Table 2.8: Mg corrected and uncorrected $\delta(^{29/28}Si)_{NBS28}$ and $\delta(^{30/28}Si)_{NBS28}$ values for measured test samples of the anion matching experiments under dry plasma conditions.

		not Mg corrected				Mg corrected			
anion	anion/Si	$\delta(^{29/28}Si)$	CI	$\delta(^{30/28}Si)$	CI	$\delta(^{29/28}Si)$	CI	$\delta(^{30/28}Si)$	CI
		[‰]	[‰]	[‰]	[‰]	[‰]	[‰]	[‰]	[‰]
SO_4	0.2	-0.024	0.065	-0.054	0.108	-0.006	0.035	-0.028	0.048
SO_4	0.4	-0.016	0.073	-0.003	0.098	-0.018	0.091	-0.018	0.122
SO_4	0.8	-0.002	0.047	0.013	0.060	0.005	0.055	0.015	0.080
SO_4	1.6	0.013	0.070	0.046	0.126	0.025	0.050	0.054	0.116
SO_4	3.2	0.028	0.033	0.072	0.061	0.075	0.044	0.154	0.075
SO_4	6.4	-0.014	0.036	-0.015	0.036	0.026	0.068	0.060	0.097
PO_4	0.2	-0.004	0.020	0.000	0.071	0.026	0.014	0.054	0.079
PO_4	0.4	-0.018	0.037	-0.031	0.080	0.004	0.042	0.008	0.082
PO_4	0.8	-0.003	0.048	-0.024	0.072	0.030	0.046	0.032	0.061
PO_4	1.6	-0.010	0.039	-0.027	0.065	0.052	0.042	0.085	0.056
PO_4	3.2	0.005	0.029	-0.007	0.048	0.055	0.022	0.084	0.048
PO_4	6.4	-0.053	0.065	-0.051	0.133	0.011	0.058	0.065	0.122
NO_3	0.01	-0.011	0.024	0.000	0.018	-0.002	0.021	0.018	0.060
NO_3	0.05	-0.008	0.039	-0.013	0.057	-0.004	0.046	-0.005	0.081
NO_3	0.1	-0.004	0.026	-0.012	0.039	0.011	0.018	0.017	0.060
NO_3	0.2	0.006	0.033	0.004	0.071	0.001	0.044	-0.006	0.074
NO_3	0.4	0.015	0.021	-0.005	0.050	0.007	0.012	-0.022	0.055
NO_3	0.8	-0.004	0.038	-0.009	0.054	-0.010	0.031	-0.019	0.051
NO_3	1.6	0.023	0.026	0.020	0.032	0.019	0.031	0.027	0.065
NO_3	3.2	0.006	0.024	0.014	0.023	0.001	0.029	0.007	0.020
NO_3	6.4	-0.004	0.042	0.012	0.041	-0.014	0.040	0.002	0.052

Table 2.9: $\delta(^{29/28}Si)_{NBS28}$ and $\delta(^{30/28}Si)_{NBS28}$ values for measured test samples of the SO_4 matching experiments under wet plasma conditions without Mg addition.

SO_4/Si	$\delta(^{29/28}Si)$	CI	$\delta(^{30/28}Si)$	CI
	[‰]	[‰]	[‰]	[‰]
0.01	-0.026	0.090	-0.047	0.229
0.05	-0.011	0.046	-0.065	0.138
0.1	-0.108	0.035	-0.194	0.111
0.2	-0.080	0.049	-0.273	0.046
0.5	-0.146	0.062	-0.349	0.217
1	-0.125	0.085	-0.292	0.306
2	-0.123	0.044	-0.377	0.120
5	-0.171	0.066	-0.361	0.265

Chapter 3

Si stable isotope fractionation during adsorption and the competition between kinetic and equilibrium isotope fractionation: implications for weathering systems[1]

3.1 Abstract

The adsorption of Si onto amorphous Al-hydroxides is the cause for the light Si isotope signature that secondary crystalline clay minerals in weathering systems carry. We propose this hypothesis from a series of adsorption experiments in which the light isotopes are being favored during Si adsorption onto crystalline gibbsite and in which the associated fractionation factor depends on the solution's initial Si concentration.

Three adsorption experiments were carried out at pH 7 with different initial Si concentrations of 0.36, 0.71 and 1.42 mmol/l Si start concentrations. As Al-hydroxide adsorbent, 30 g/l crystalline gibbsite were used to provide equal surface area in all experiments. Adsorption rates are higher with higher initial Si concentration. At the same time, calculated apparent isotope fractionation factors $10^3\ln\alpha_{\mathrm{adsorbed/solution}}$ decrease from -1.8 to -3 ‰ with increasing initial Si concentration. As care was taken to avoid isotope fractionation during transport of dissolved Si to the gibbsite surface, the mass dependence of the activation energy barrier at the interface is causing the kinetic isotope fractionation. Within the mass balance framework of DePaolo (2011) the shift in Si isotope fractionation with initial Si concentration is interpreted to be induced by different kinetic isotope fractionation factors associated with the forward reaction. Only after ca. two months do the isotope ratios begin to adjust to an equilibrium isotope fractionation factor that is close to 0 ‰. With such slow re-equilibration Si adsorption differs fundamentally from transition metals that re-equilibrate isotopically within hours after adsorption onto Fe and Mn oxide surfaces.

These observations may provide an explanation for the light Si isotope signature clay minerals formed during weathering carry: the light Si isotope composition is being inherited

---

early on during Si adsorption onto amorphous Al-hydroxides and is potentially carried over during all further stages of transformation.

3.2 Introduction

Weathering of minerals and rocks releases elements into the ambient solution. Si and Al being the second and third most abundant elements in the Earth's crust, respectively, are both key players during weathering of silicates. While Al is almost insoluble under near neutral pH conditions and low dissolved organic carbon contents (Sposito, 1996), Si is partitioned in roughly equal proportions between the dissolved phase and into a solid secondary mineral phase during the dissolution of primary silicate minerals. In the last decade Si stable isotopes have been increasingly used to trace weathering processes.

One major finding of these Si isotopes studies is the relative enrichment of heavy Si isotopes in the ambient soil solution. The isotopically lighter counterpart is found in secondary siliceous solid phases (Ziegler et al., 2005a,b; Georg et al., 2006a, 2007b; Opfergelt et al., 2009; Bern et al., 2010; Opfergelt et al., 2011). Despite this consistent picture, the partitioning of Si isotopes in the presence of Al has not been explored in detail under controlled laboratory conditions. Determining the related isotope fractionation factors is critical as the reaction of Si and Al is likely to be the first crucial reaction occurring in weathering environments after releasing Al and Si from primary silicates.

In the present study, we explore Si isotope fractionation during adsorption of Si onto gibbsite at three different initial Si concentrations. We explain the resulting dependence of the Si isotope fractionation factor on adsorption rate within the conceptual mass balance framework of DePaolo (2011).

3.3 Materials and Methods

3.3.1 Si source for adsorption experiments

Dietzel (1993, 2002) showed that only monomeric silicic acid (H_4SiO_4) is formed when tetraethylorthosilicate (TEOS; $(C_2H_5O)_4Si$) is used as Si source and that its behavior in adsorption experiments is identical to that found in monomeric silicic acid solutions prepared by alternative means. The advantage of using TEOS as Si source is that neither associated cations nor minor elemental amounts (released during the dissolution of silicates (e.g. Na_2SiO_3) or from alkaline standard solutions (SiO_2 in 2% NaOH)) are present in the solution, which then have to be removed to obtain pure silicic acid for experiments. Further monomeric silicic acid can be produced easily by a simple addition of small volumes of TEOS to aqueous solutions where TEOS converts to silicic acid via a hydrolysis reaction. The side product of TEOS hydrolysis is ethanol (a concentration of 296 ppm is calculated). The Si stock solution was prepared by adding 5.9 g (6 ml) TEOS (Merck$^{®}$) to 20 l Milli-Q water (1.42 mmol/l Si).

To avoid formation of polysilicic acid the prepared starting solution was held below the solubility of amorphous silica. In addition, before using the starting solution we first analyzed the solution for the degree of polymerization of dissolved silicic acid and the presence of colloidal silica using the β-silicomolybdate method (for details see subsection 3.7.2 and Iler (1979) and Dietzel (2000)). The amount of colloidal silica is determined by measuring the total Si concentration using ICP-OES minus the concentration of monosilicic acid

determined by the β-silicomolybdate method. For all experiments both Si concentrations show that within the analytical precision of 5% no colloidal Si was present in the experiments. Furthermore, the reaction rate constant for the formation of the β-silicomolybdate complex can be used to evaluate the average polymerization degree of dissolved silicic acid. For the present stock solution a value of 2 min^{-1} was calculated, which clearly indicates the sole presence of monomeric silicic acid.

3.3.2 Adsorption experiments

Adsorption experiments were carried out following a method adapted from Dietzel and Böhme (1997). The experimental solutions were prepared from a TEOS stock solution. Three distinct adsorption experiments were performed with initial Si concentrations of 0.36, 0.71 and 1.42 mmol/l Si corresponding to concentrations of 10, 20 and 40 ppm, respectively. All experimental solutions were adjusted to 0.1 M NaCl by addition of NaCl (p.a. grade Merck®). Si concentrations were below the solubility limit of amorphous silica which is 2.14 mmol/l Si at 25°C and pH <8 (Gunnarsson and Arnorsson, 2000), to prevent polymerization and precipitation of amorphous silica.
In each experimental run 30 g of gibbsite (γ-Al(OH)$_3$; p.a. grade Merck®) with a given specific surface area of 1.18 m^2/g (BET, N$_2$-adsorption) was suspended in 1 l of the experimental solution containing Si in PE bottles. The pH of 7.0 was adjusted and kept constant during the experiment by the addition of diluted HCl or NaOH solution (pH were measured with pH meter WTW 330 and pH electrode WTW SenTix 41, calibrated using pH 4.0 and 7.0 WTW standard buffer solutions). The variability of the pH values throughout the whole experimental runtime were $\pm$ 0.1 pH units. During the first 6 hours of the experiment, the gibbsite suspension was heavily agitated using a IKA RW 20 DZM stirrer at 500 rpm with a Teflon stirring staff. A parafilm cover prevented evaporation of the solution. Subsequently the closed PE bottles were placed in an overhead shaker. Experimental suspensions (15 ml) were sampled with a syringe and filtered (0.45 μm porosity, cellulose acetate) at several intervals; total maximum experimental run time was 1536 hours (64 days). The sampled solutions were split: 10 ml were used for ICP-OES analyses (Varian 720-ES) and Si isotope measurements (Thermo Scientific NEPTUNE). The remaining solutions of 5 ml were immediately analyzed by UV-Vis (UV-VIS 641 Cary 100, Varian).

3.3.3 Chemical separation and purification

Chemical separation of Si was done following the method from Georg et al. (2006b). The filtered solutions were loaded onto pre-cleaned columns (1.5 ml of BioRad DOWEX 50W-X8; 200-400 mesh) and Si was eluted with 5 ml Milli-Q water and stored in pre-cleaned centrifuge tubes. It was assured for all samples that the Si yield was >95%, which was checked by ICP-OES (Varian 720-ES).

3.3.4 Mass spectrometry

Silicon isotope composition was measured on a Thermo Neptune multi-collector inductively coupled mass spectrometer (MC-ICP-MS) equipped with an H-skimmer cone and the newly developed Thermo Scientific® Jet - interface in high-resolution mode (m/Δm > 5000). The purified sample solutions were introduced into the plasma via a desolva-

tion unit for dry plasma conditions (Apex, ESI®, no N_2 addition, no further membrane desolvation) equipped with a 120 μl/min nebulizer.

We used Mg doping combined with standard-sample-bracketing to correct for mass bias during measurements by using an exponential mass bias law (Cardinal et al., 2003). A magnesium solution was added to samples and standards to yield a final concentration of 1 ppm Mg. Sample solutions were diluted to 1 ppm Si concentration in 0.1 M HCl, which typically resulted in an intensity of ~15 V/ppm on ^{28}Si (using a $10^{11}\Omega$ resistor).

Measurements were conducted on the interference-free low-mass side of the three Si isotopes. The most critical interference, caused by ^{14}N^{16}O on the ^{30}Si signal, is usually below 5V which is resolvable from the ^{30}Si signal in the high-resolution mode used. Each sample and standard was measured at least 4 times during a sequence; each sample or standard was measured in dynamic mode for 30 cycles with an integration time for each cycle of 4 s for Si as well as for Mg with an idle time of 3 s after magnet switching. Pure 0.1 M HCl solutions were measured before and after each standard-sample-standard block and were used for on-peak zero correction. Typical intensities of ^{28}Si in blank solutions were below 5 mV. We report Si isotope data relative to the standard reference material NBS28 (quartz sand) in the delta notation according to Coplen (2011) as $\delta(^{29/28}\text{Si})_{\text{NBS28}}$ and $\delta(^{30/28}\text{Si})_{\text{NBS28}}$ expressed in per mill (‰) by multiplication of Equation 3.1 and Equation 3.2 with a factor of 10^3:

$$\delta(^{29/28}\text{Si})_{\text{NBS28}} = \left(\frac{\left(\frac{^{29}\text{Si}}{^{28}\text{Si}}\right)_{\text{sample}}}{\left(\frac{^{29}\text{Si}}{^{28}\text{Si}}\right)_{\text{NBS28}}} - 1 \right) \tag{3.1}$$

$$\delta(^{30/28}\text{Si})_{\text{NBS28}} = \left(\frac{\left(\frac{^{30}\text{Si}}{^{28}\text{Si}}\right)_{\text{sample}}}{\left(\frac{^{30}\text{Si}}{^{28}\text{Si}}\right)_{\text{NBS28}}} - 1 \right) \tag{3.2}$$

All reported errors on delta values are the 95% confidence interval (CI) calculated according to Equation 3.3 where $\overline{\delta(^{30/28}\text{Si})_{\text{NBS28}}}$ is the mean of the measured delta values for the sample or standard (at least n=4), t_{n-1} is a critical value from tables of the *Student's t*-law and SE is the standard error of the mean.

$$\text{CI} = \overline{\delta(^{30/28}\text{Si})_{\text{NBS28}}} \pm t_{n-1} \times \text{SE} \tag{3.3}$$

The well-defined Si isotope reference material BHVO-2g, a basalt standard (measured over a 12 months period of analysis ; including several individual chemical separations as well as several digestions procedures; $\delta(^{30/28}\text{Si})_{\text{NBS28}} = -0.27 \pm 0.02$; n=73), was usually measured as control standard during measured sequences.

3.3.5   Analytical tests

As it is mentioned in subsection 3.3.1 the side product during monomeric silicic acid preparation using TEOS is ethanol. In a separate experiment using similar starting material (Oelze et al., 2015) it has been tested whether the remaining ethanol in the prepared solutions induces analytical artifacts during the preparation and measurement of Si isotopes. Pairs of solutions and the formed solid counterparts were measured. Applying a

mass balance approach showed that all fluid-solid pairs gave the isotopic composition of the starting solution. Hence no mass-spectrometric artifact was induced from the release of ethanol during preparation of Si-containing solutions using TEOS.

A known limitation using the sample purification method of Georg et al. (2006b) is that anions present in the samples remain in the purified Si solutions. As the Si adsorption experiments were conducted in the presence of 0.1 M NaCl and further HCl has been used to adjust the pH, Cl^- anions might have been present after purification and potentially might have caused matrix effects as their amounts are different between sample and bracketing standards. Therefore we tested whether different amounts of Cl^- anions in sample and bracketing standard causes matrix effects by measuring a "Cl^--doped" standard against "pure" bracketing standards. In the estimated range of different Cl^- anion concentrations (difference between "doped" and "pure" of up to 20 %) no bias has been found.

3.4 Results

Si concentrations as well as $\delta(^{29/28}\text{Si})_{\text{solution}}$ and $\delta(^{30/28}\text{Si})_{\text{solution}}$ values are reported in the Appendix Table 3.2.

3.4.1 Evolution of Si concentration

During the adsorption experiments, a continuous decrease in Si concentration with time is observed (Figure 3.1). In all experiments (0.36, 0.71 and 1.42 mmol/l Si starting concentration) the major change of Si concentration occurs during the first 50 hours, and subsequently the changes slow down continuously. Over 60% of the total adsorption takes place during the first 24 hours. Si adsorption rates (Figure 3.2) at the beginning of the experiments differ strongly between the conducted experiments. Adsorption rates for experiments with an initial Si concentration of 1.42 mmol/l are up to four times higher compared to solutions with an initial concentration of 0.36 mmol/l Si; the 0.71 mmol/l Si solution experiment yields intermediate adsorption rates. Using estimates from Karamalidis and Dzombak (2011) of 8 - 8.8 adsorption surface sites/nm^2 on gibbsite and the measured BET surface area of 1.18 m^2/g a maximum possible amount of adsorbed Si of 440 - 484 μg/g (470 - 520 μmol Si total) can be calculated. As the maximum Si amounts adsorbed (definded by the equilibrium constant of the adsorption reaction) were ca. 130, 200, and 250 μmol for the 0.36, 0.71, and 1.42 mmol/l experiment, respectively, in all adsorption experiments an excess of free adsorption surface sites was still available at the end of the experiments.
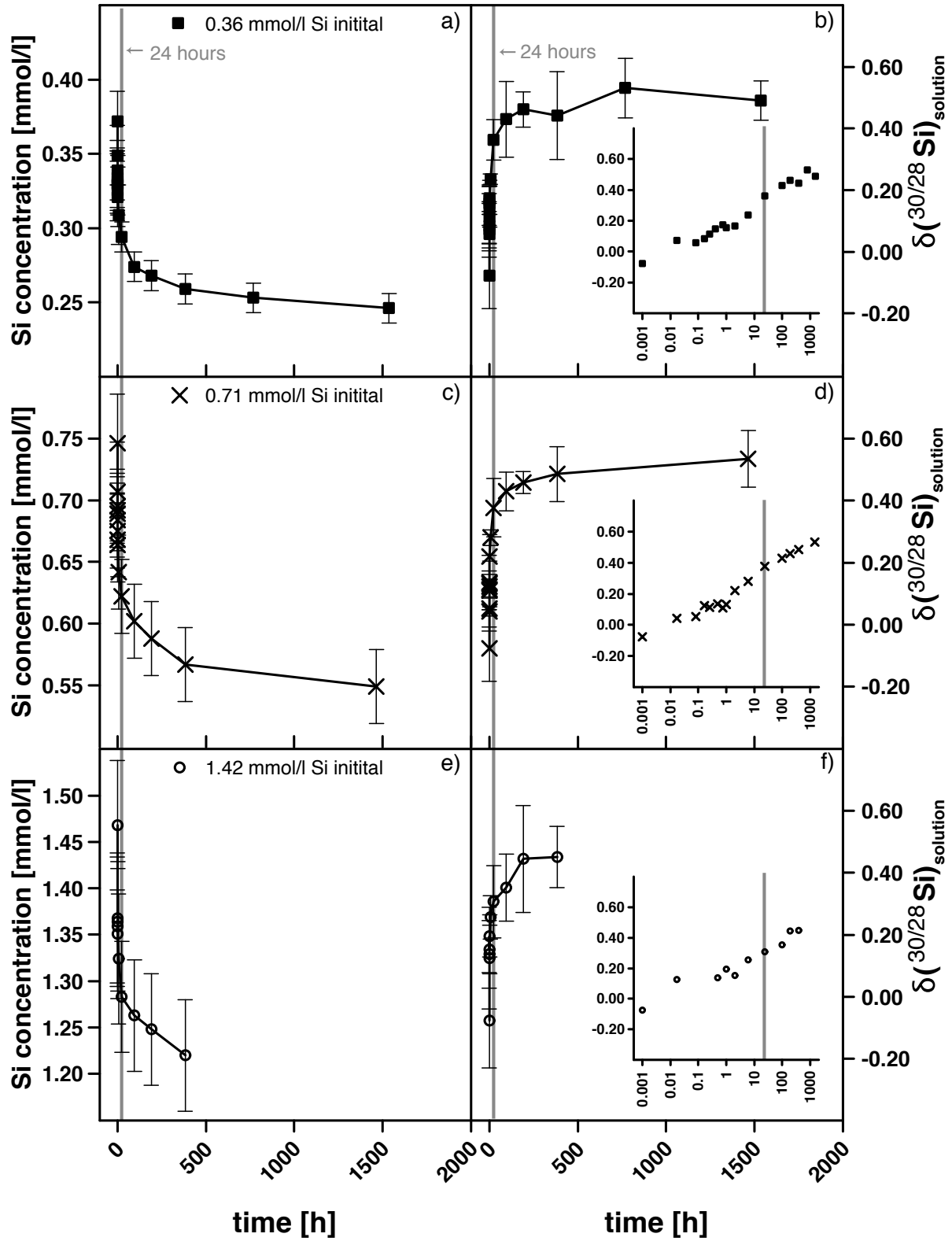
Figure 3.1: Evolution of Si concentration (panels a, c and e) and $\delta(^{30/28}\text{Si})_{solution}$ (panels b, d and f) of the solution with time during adsorption experiments (30 g/l of gibbsite, pH 7.0). Squares, crosses and circles depict experiment with an initial Si concentration of 0.36, 0.71 and 1.42 mmol/l , respectively. Insets in panels b, d and f show the same isotopic datasets plotted vs. log time in hours.
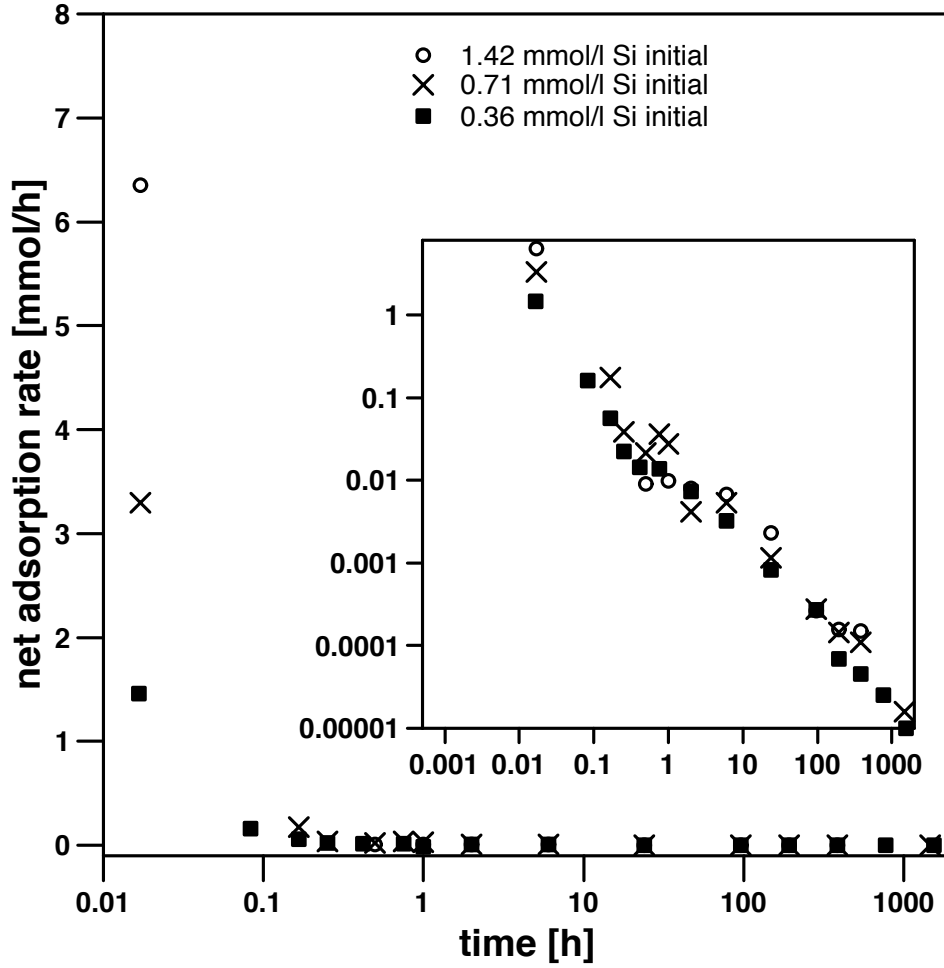
Figure 3.2: The net adsorption rate vs. time in a semi-log diagram (inset log-log scale). Net adsorption rate dq/dt is calculated as the difference between the amount adsorbed in mmol $dq = q_{n+1} - q_n$ divided by the time elapsed in hours $dt = t_{n+1} - t_n$.

3.4.2 Silicon isotopes

We report measured $\delta(^{30/28}\mathrm{Si})_{\mathrm{solution}}$ solution values (measured relative to NBS28) throughout this section. All three adsorption experiments (with initial Si concentrations of 0.36, 0.71 and 1.42 mmol/l) display a similar evolution of their $\delta(^{30/28}\mathrm{Si})_{\mathrm{solution}}$ values. With increasing experimental runtime or decreasing fraction of Si remaining in solution (f_{solution}), the dissolved Si becomes increasingly enriched in $^{30}\mathrm{Si}$, which results in higher $\delta(^{30/28}\mathrm{Si})_{\mathrm{solution}}$ values (Figure 3.3). The largest changes in $\delta(^{30/28}\mathrm{Si})_{\mathrm{solution}}$ are observable during the first 24 hours where also over 60% of the Si adsorption onto gibbsite takes place. After this initial period of rapid change in both Si concentration and $\delta(^{30/28}\mathrm{Si})_{\mathrm{solution}}$, the change in $\delta(^{30/28}\mathrm{Si})_{\mathrm{solution}}$ is much slower. In fact in contrast to the continuously evolving Si concentrations $\delta(^{30/28}Si)_{\mathrm{solution}}$ values are almost constant. Finally a maximum $\delta(^{30/28}\mathrm{Si})_{\mathrm{solution}}$ value is reached where Si concentration and $\delta(^{30/28}\mathrm{Si})_{\mathrm{solution}}$ remain virtually constant (see Appendix Table 3.2). We only used the data of the first 24 hours to determine an apparent isotope fractionation factor $\alpha_{\mathrm{adsorbed/solution}}$ for each of the experiments. We define $\alpha_{\mathrm{adsorbed/solution}}$ ($\alpha_{\mathrm{adsorbed/solution}} = (^{30}\mathrm{Si}/^{28}\mathrm{Si})_{\mathrm{adsorbed}}/(^{30}\mathrm{Si}/^{28}\mathrm{Si})_{\mathrm{solution}}$) as the isotope fractionation factor between adsorbed Si and dissolved Si remaining in solution. However, the composition of Si adsorbed onto gibbsite $\delta(^{30/28}\mathrm{Si})_{\mathrm{adsorbed}}$ was calcu-

lated by mass balance, as the gibbsite remained in the experimental containers throughout the experiment. An "open-system "(Rayleigh mass balance) and a "closed-system" mass balance approach were applied to the data (Johnson et al., 2004). An "open-system" mass balance approach assumes that the product (here adsorbed Si) does not remain in contact with the starting material (here dissolved Si) after formation. In this case the evolution of dissolved Si isotope composition is given by:

$$\frac{(1000 + \delta(^{30/28}\text{Si})_{\text{solution}})}{(1000 + \delta(^{30/28}\text{Si})_{\text{solution-initial}})} = f_{\text{solution}}^{(\alpha_{\text{adsorbed/solution}}-1)} \tag{3.4}$$

In contrast, a "closed-system" approach assumes complete isotope exchange during removal of dissolved Si, leading to:

$$\delta(^{30/28}\text{Si})_{\text{solid}} = \delta(^{30/28}\text{Si})_{\text{solution-initial}} + 1000 * f * (\alpha_{\text{adsorbed/solution}} - 1) \tag{3.5}$$

As f_{solution} did not extend to values of lower than 0.6, our data does not allow to identify whether the experiments follow "open-system" or "closed-system" behavior. We return to this question in subsection 3.5.1. Here we apply both types of mass balance models to our data, and obtain a reasonable fit for each experiment. Three distinct isotope fractionation factors are obtained for both mass balance approaches (see Figure 3.3 and Table 3.1).

Table 3.1: Resulting $\alpha^{30/28}$Si $_{\text{adsorbed/solution}}$ and $10^3 \ln \alpha^{30/28}$Si $_{\text{adsorbed/solution}}$ values using adsorption data of the first 24 hours. To determine isotope fraction factors an open-system and a closed-system mass balance model has been applied to the experimental data. To fit the data we used the nlme-package (Pinheiro et al., 2014) in R (R Core Team, 2014). We report the calculated standard error (SE) of $\alpha^{30/28}$Si and the standard error of the residuals (RMSD) calculated for each experiment.

"open-system" mass balance			
Experiment	$\alpha^{30/28}$Si	$10^3 \ln \alpha^{30/28}$Si	RMSD
0.36 mmol/l Si initial	0.998222± 0.000050	-1.779± -0.050	0.022
0.71 mmol/l Si initial	0.997669± 0.000088	-2.334± -0.088	0.030
1.42 mmol/l Si initial	0.996986± 0.000102	-3.019± -0.102	0.023
"closed-system" mass balance			
Experiment	$\alpha^{30/28}$Si	$10^3 \ln \alpha^{30/28}$Si	RMSD
0.36 mmol/l Si initial	0.998071± 0.000060	-1.931± -0.060	0.025
0.71 mmol/l Si initial	0.997516± 0.000100	-2.487± -0.100	0.033
1.42 mmol/l Si initial	0.996827± 0.000103	-3.178± -0.103	0.022
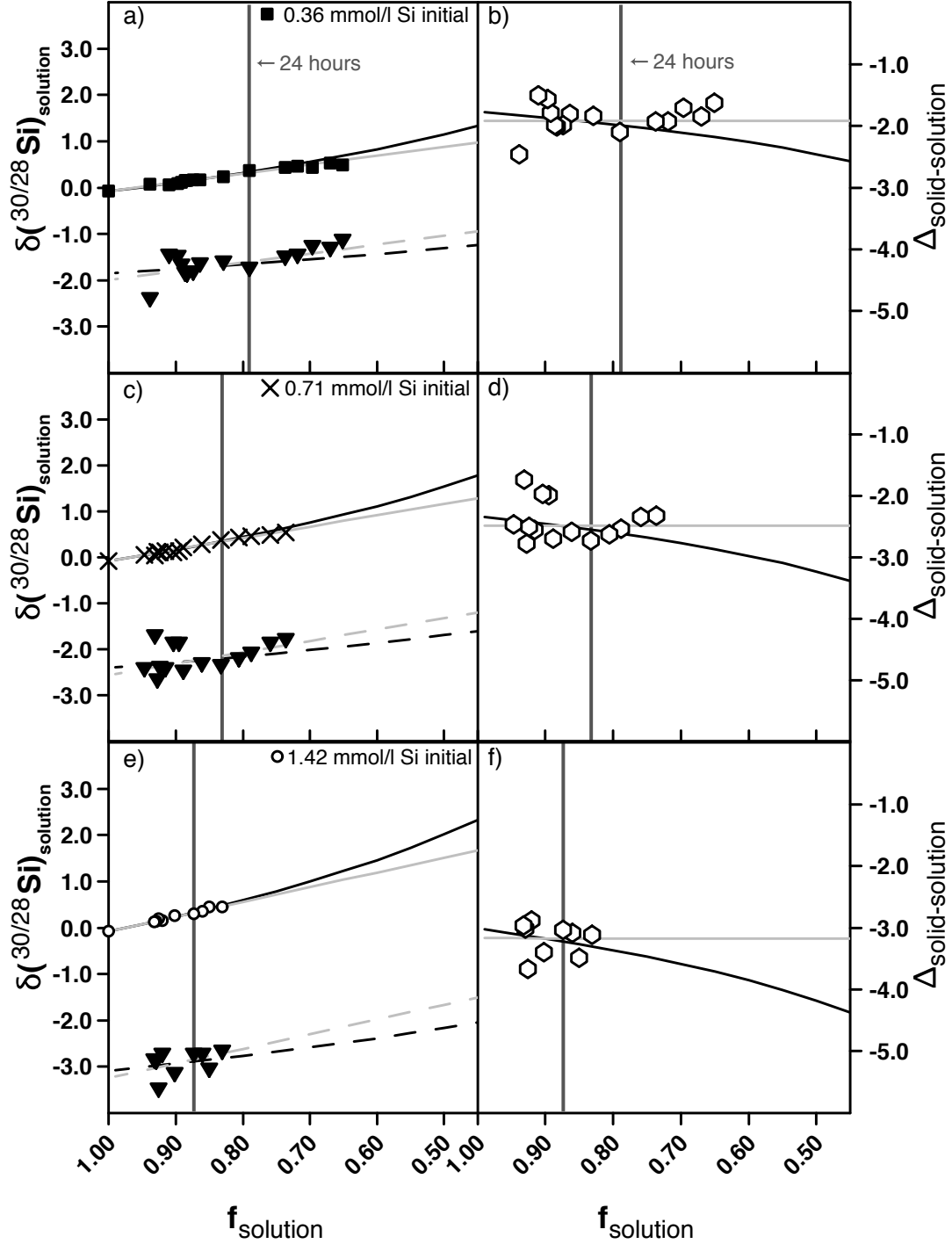
Figure 3.3: The left panels (a, c and e) show the $\delta(^{30/28}\mathrm{Si})_{\mathrm{solution}}$ evolution of the measured solution and the corresponding calculated $\delta(^{30/28}\mathrm{Si})_{\mathrm{adsorbed}}$ of the solid in the adsorption experiments, as a function of the fraction of Si remaining in solution ($\mathrm{f_{solution}}$). The open diamonds in the right panels (b, d and f), show the isotopic difference $\Delta(^{30/28}\mathrm{Si})_{\mathrm{solid\text{-}solution}}$ between solid and solution as a function of the fraction of Si remaining in solution ($\mathrm{f_{solution}}$). In the left panels, squares, crosses and circles depict experiments with initial Si concentrations of 0.36, 0.71 and 1.42 mmol/l, respectively. The triangles depict $\delta(^{30/28}\mathrm{Si})_{\mathrm{adsorbed}}$ calculated for the corresponding Si adsorbed onto solids for each individual experiment. Regression lines for the experimental data (first 24 hours) fitted according to the open-system mass balance approach (black lines; Equation 3.4) and for the closed-system approach (gray lines; Equation 3.5) are also shown (see Table 3.1 for obtained fractionation factors; error bars are smaller than symbol size).

3.5 Discussion

3.5.1 Si isotope fractionation during Si adsorption

During our adsorption experiments significant changes of Si concentration are associated with changes in the $\delta(^{30/28}\text{Si})_{\text{solution}}$ values, where light isotopes are preferentially adsorbed onto the gibbsite surface. We further observe a higher Si isotope fractionation between adsorbed and dissolved Si the higher the initial Si concentration is.

We first explore whether isotope fractionation found between Si adsorbed onto solids and Si remaining in solution follows a "closed-system" behavior (Johnson et al., 2004). In our experiments the range of Si fractions remaining in solution (0.7 to 1.0) experienced does not allow to distinguish the "closed" system behavior from the "open" system case. Therefore, the observed pattern is compatible with a "closed-system" behavior and hence continuous contact and exchange between solids and solution. Such re-equilibration has been shown to be characterized by equilibrium isotope fractionation in previous adsorption experiments (Juillot et al., 2008; Wasylenki et al., 2008, 2011). However, we can rule out equilibrium isotope fractionation as the adsorption rate is high from hours 0 to 400, which argues against attainment of chemical equilibrium - a prerequisite for isotopic equilibrium. Therefore we proceed to discuss our results in terms of the "open-system" behavior.

We next discuss the prevailing mechanism of adsorption of light isotopes onto the gibbsite surfaces. Any transport-induced isotope effect (e.g. isotope fractionation of Si through diffusion) can be ruled out, as the experimental solutions were constantly heavily stirred or shaken. Hence the occurrence of Si isotope fractionation in our experiments can be explained by the adsorption process being "reaction-limited" i.e. the fractionation depends on the kinetics of the adsorption reaction when an activation energy barrier E_a during formation or breaking of bonds has to be overstepped. The Arrhenius equation demands that reactions of light isotopes are preferred over those of heavy isotopes (Bigeleisen, 1965). Yet even this activation energy barrier model does not explain the dependence of $\alpha_{\text{adsorbed/solution}}$ on the initial Si concentration. As also Si adsorption rates differ significantly between our experiments, we next evaluate how reaction kinetics might affect isotope fractionation.

3.5.2 Kinetics of Si adsorption

Adsorption reaction kinetics of Si onto gibbsite were often described as a first-order reaction, at least for some parts of the reaction (Hingston and Raupach, 1967; Adu-Wusu and Wilcox, 1991; Dietzel, 2002). An attempt to explain the overall adsorption reaction with simple kinetic rate laws (first-order, second-order or first-order forward and backward reaction, see subsection 3.7.3) fails. The evolution of Si concentration follows a linear trend in a semi-log diagram (Figure 3.4) and therefore we apply the empirical equation:

$$[Si] = a \times log(time) - b \qquad (3.6)$$

In such a diagram the slope a is a coefficient describing the relative adsorption rate. For each adsorption experiment, the data describe a straight line but different slopes are obtained. This dependence can be interpreted to mean that distinct initial Si concentrations result in different Si adsorption rates. The higher the initial Si concentration, the faster the adsorption (see Figure 3.4).
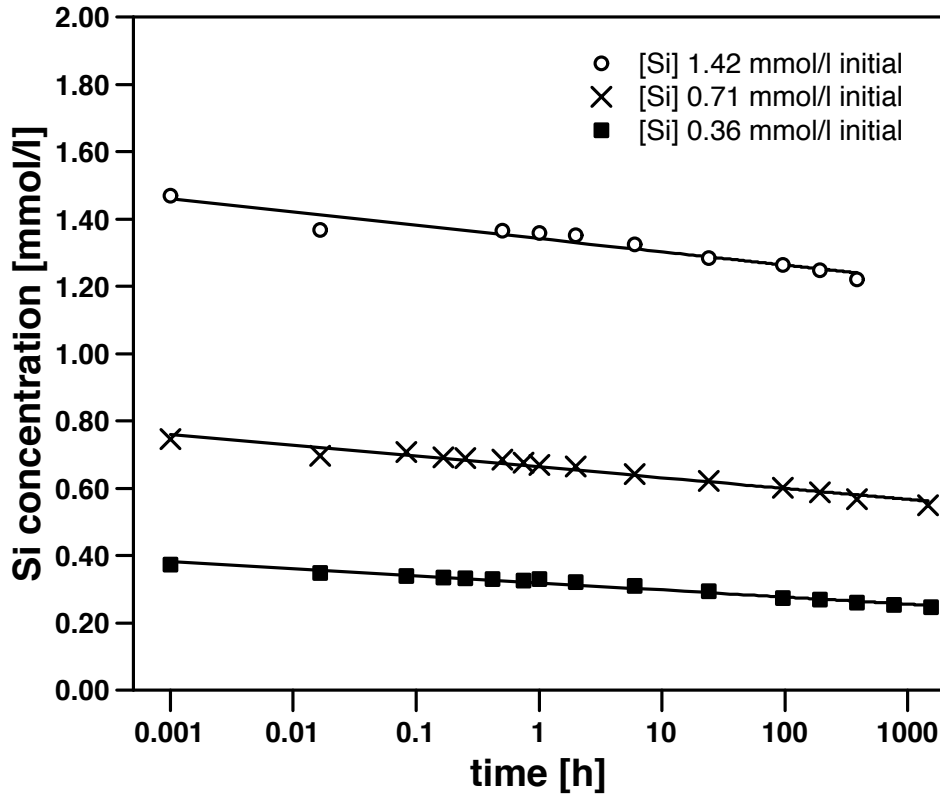
Figure 3.4: Si concentration vs. time (on log scale), where the slopes denotes the overall adsorption rate (Equation 3.6) Squares depict the experiment with an initial Si concentration of 0.36 mmol/l, crosses depict experiment with 0.71 mmol/l and circles the experiment with 1.42 mmol/l initial Si concentration. Adsorption experiments with high initial Si concentration show steeper slopes than lower Si initial concentration experiments, which means the higher the Si initial concentration the higher the adsorption rate.

When for all three adsorption experiments the apparent Si isotope fractionation factor (derived for the first 24 hours from the open-system mass balance model; see Table 3.1) is plotted against the slope obtained from the empirical logarithmic relationship (Equation 3.6) a strong linear relationship is obtained (see Figure 3.5). With increasing adsorption rate the determined fractionation factors decrease. Hence the Si isotope fractionation depends on adsorption rate.
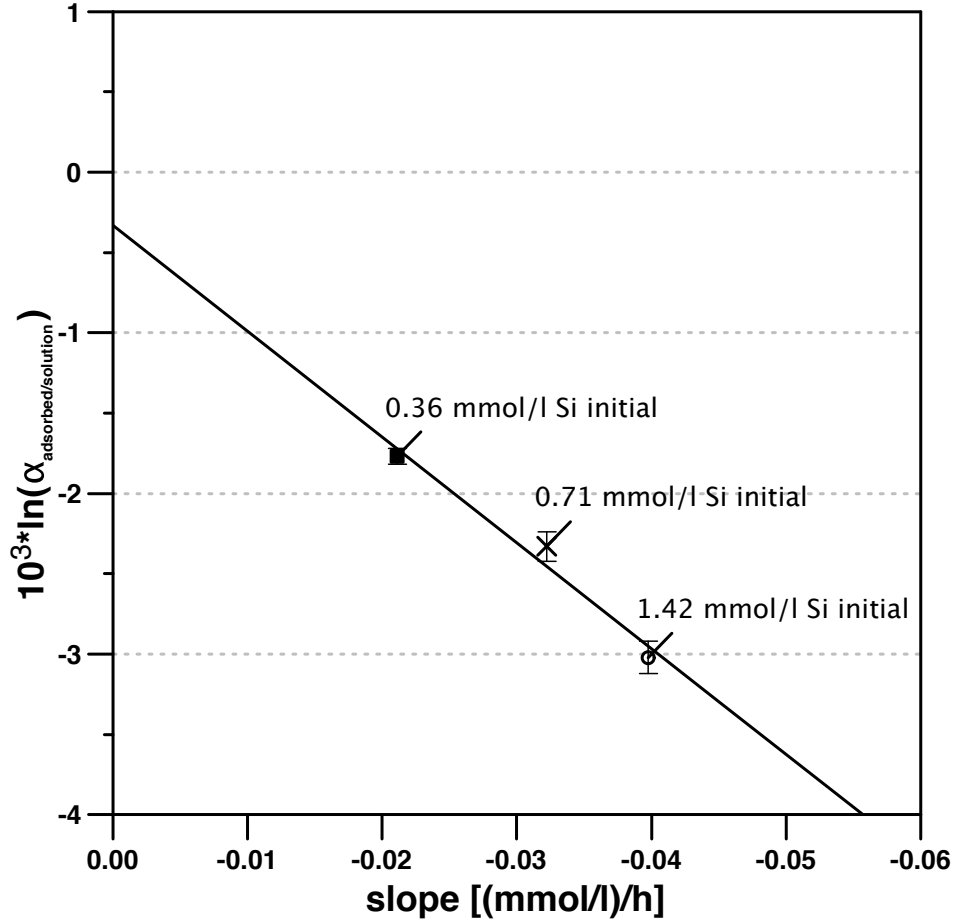
Figure 3.5: Fractionation factors as $10^3\ln(\alpha_{\mathrm{adsorbed/solution}})$ deduced from applying an open-system mass balance to the first 24 hours of the individual adsorption experiments (Table 3.1) vs. the slope derived from applying the empirical logarithmic relationship (Equation 3.6)

3.5.3   The change of the isotope fractionation regime

Two explanations can be invoked to explain the rate dependence of isotope fractionation factors between the three experiments. Given that the isotope-specific energy barrier of a chemical pathway does not depend on adsorption rate, the first explanation is that reactions pathways differ between experiments. The second explanation is that a significant relative rate of a back reaction and the associated isotope fractionation affects the experiments, differs between the experiments. A framework that relates isotope fractionation to the ratio of backward to forward reaction rate has been developed by DePaolo (2011). This conceptual model is based on simple definitions of a forward reaction rate R_f (formation of new phases; here Si adsorption onto gibbsite), a backward reaction rate R_b (dissolution of newly formed phases; here Si desorption from gibbsite) and the net reaction rate R_p ($R_p = R_f - R_b$). The forward and backward rates are associated with distinct kinetic isotope fractionation factors (α_f and α_b, respectively). An apparent fractionation factor α_p arises from the R_p/R_b ratio (see Eq. 11 in (DePaolo, 2011)). The overall prediction is that if the net adsorption rate R_p is much larger than the backward rate R_b, the apparent isotope fractionation will be kinetically dominated (favoring light isotopes). By contrast if R_p is much smaller than R_b, the system reaches isotopic fractionation at equilibrium.

While at intermediate regimes α_p depends on the values of α_f, α_b and R_p/R_b. On the low and on the high end of the R_p/R_b axis (Figure 3.6) plateaus in α_p emerge. We can evaluate whether the dependence of the fractionation factor on adsorption rate can be interpreted within this framework.

First, for a given experiment, net adsorption rates decrease abruptly over the first 24 hours, hence it is most likely that the R_p/R_b ratio changes. However, $\alpha^{30/28}\mathrm{Si_{adsorbed/solution}}$ (α_p in DePaolo (2011)'s terminology) remains constant. This means that the early stage of our experiments cannot be interpreted as being located at intermediate R_p/R_b values where α_p is expected to be strongly dependent on adsorption rate (Figure 3.6). Second, as there is net adsorption during this early stage, the experiments cannot be interpreted as operating near chemical and isotopic equilibrium, hence they are likely not located on the low end of the R_p/R_b axis (Figure 3.6). Therefore, for the first 24 hours in each experiment, the constant α_p value while R_p/R_b ratios change means that the experiments are located, on the "kinetic plateau". There, at the high end of R_p/R_b values, $\alpha_p \sim \alpha_f$. The difference between the apparent isotope fractionation factors then reflects different values of the kinetic isotope fractionation factors associated with the forward reaction.

We therefore conclude that the observed dependence of Si isotope fractionation on the initial Si concentration can only be explained within the DePaolo framework if α_f values differ between the three experiments (Figure 3.6).

After 24 hours $\delta(^{30/28}\mathrm{Si})_{\mathrm{solution}}$ and hence $\alpha^{30/28}\mathrm{Si_{adsorbed/solution}}$ changes. We can interpret this second stage of the experiments within the DePaolo framework as only then R_b increases at the cost of R_f and hence α_p departs from the kinetic plateau and evolves towards equilibrium. We can estimate the equilibrium isotope fractionation factor from the linear correlation of the overall net adsorption rate and the determined closed-system isotope fractionation factors (see Figure 3.5). Extrapolated to a zero net adsorption rate, an equilibrium isotope fractionation factor of $\alpha^{30/28}\mathrm{Si}_{\mathrm{adsorbed/solution}} = 0.9997$ ($10^3\ln\alpha^{30/28}\mathrm{Si}_{\mathrm{adsorbed/solution}} = -0.3$ ‰) results.

That α_f values depend on Si concentrations is an unexpected conclusion that warrants an explanation. At the early stage of this finding we can only speculate on its cause. We can exclude that our high-concentration experiments were limited in adsorption sites, such that the removal mechanism shifted from one of adsorption to one for example of precipitation (see subsection 3.4.1). The most likely process is hence adsorption onto monolayers in all three experiments. It is conceivable that a shift in surface complexation occurs with increasing Si concentration and that different complexes differ by the strength of their adsorption site and are hence associated with different α_f values (Lemarchand et al., 2007). However, this assumption is not supported by surface complexation models which are able to reconcile the evolution of Si adsorption onto gibbsite using only one surface complex (Karamalidis and Dzombak, 2011). We note that the poor fit and the small amount of usable data of that study does not allow to fully rule out this explanation either. A second possible explanation is the polymerization of silicic acid at the gibbsite surface and therefore the formation of Si-O-Si bonds that are probably associated with different isotope fractionation factors. Yokoyama et al. (1982) reported the polymerization of Si at the surface of Al-hydroxides but only for much higher concentrations of dissolved Si. However, in a precipitation experiment Oelze et al. (2015) observed a fractionation factor $\alpha_p = 1$ for polymerization of silicic acid. Therefore further studies on the exact adsorption process of Si onto Al-hydroxides are needed to resolves this issue.
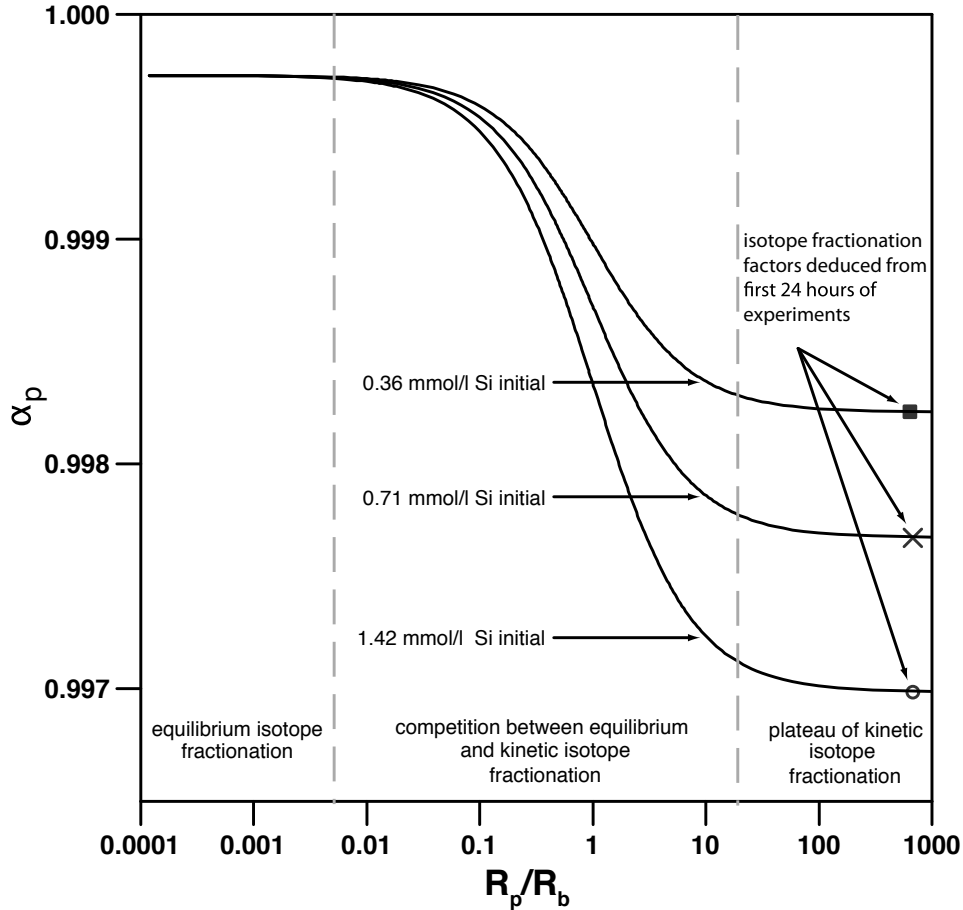
Figure 3.6: Model curve of α_p vs. R_p/R_b using the "DePaolo-Model" (black lines) as a function of R_p/R_b. The α_f values for different initial Si concentrations were deduced from the calculated closed-system isotope fractionation factor for the first 24 hours of the individual experiments (see Figure 3.2 and Table 3.1). The isotope fractionation factor at equilibrium is inferred from the linear correlation of the overall net adsorption rate and the closed-system isotope fractionation factors (see Figure 3.4). For a zero net adsorption rate the equilibrium isotope fractionation factor results to $\alpha_{eq} = -0.9997$

3.5.4   Si adsorption in natural systems

Si adsorption onto gibbsite (this study) and onto Fe-oxides (Delstanche et al., 2009) both favor light Si isotopes while the remaining solution accumulates the heavy Si isotopes. Delstanche et al. (2009) computed fractionation factors for Si adsorption onto Fe-oxides ($10^3 \ln\alpha^{30/28}Si_{ferrihydite/solution}$ = -1.05 ‰ and $10^3 \ln\alpha^{30/28}Si_{goethite/solution}$ = -1.56 ‰). These fractionation factors were shown to be independent of Si concentration (Delstanche et al., 2009). There are two ways to explain the contrasting behavior of Si isotope between these two series of experiments: (i) Delstanche et al. (2009) propose that the Si isotope fractionation during adsorption onto Fe-oxides is caused by the formation of a Fe oxide-monosilicate bi-dendate inner surface complex. The apparent isotope fractionation factor during Si adsorption is expected to depend in particular on the kinetics of the formation of this distinct surface complex. The formation rate of this surface complex might be independent of Si concentration and thus no dependence of Si concentration and isotope fractionation would be observed. (ii) We can also use the "DePaolo-Model" (DePaolo, 2011) to explain this behavior. If we assume that the net adsorption rate is much higher than the backward rate, the resulting α_p is firmly located within the kinetically domi-

nated regime and is thus independent of small changes of R_p/R_b (see Figure 3.6). Both explanations are conceivable.

3.5.5   Comparison to adsorption of transition metals

The isotopic behavior of Si during adsorption differs fundamentally from that observed in studies of transition metals. The adsorption of molybdenum onto Mn-Oxide surfaces was shown to attain equilibrium within <10 hours (Wasylenki et al., 2008). Adsorption of zinc onto ferryhidrite and goethite surfaces attained isotopic equilibrium after <20 hours (Juillot et al., 2008). Adsorption of ferrous iron to surfaces of goethite, quartz, goethite-loaded quartz, and aluminium oxide resulted in attainment of equilibrium within <72 hours (Mikutta et al., 2008). Given such rapid equilibration time scales and the observed "closed-system" behavior, in natural environmental systems such transition metal results can be interpreted in terms of equilibrium isotope fractionation. The opposite is observed for silica. The strong kinetic isotope fractionation accompanying Si adsorption and its sluggish re-equilibration, even after several months of experimental runtime, makes it likely that natural systems are dominated by kinetic isotope effects. This conclusion bears important implications for weathering systems that we explore in the next section.

3.5.6   Implications for silicate weathering environments

Many recent studies attribute the heavy Si isotopic signature of soil and stream water to the formation of secondary minerals containing the complementary reservoir of light Si isotopes (Douthitt, 1982; de La Rocha et al., 2000; Basile-Doelsch et al., 2005; Ziegler et al., 2005a; Basile-Doelsch, 2006; Georg et al., 2006a, 2009; Opfergelt et al., 2011). However, the formation of secondary silicate minerals is sufficiently slow so that equilibrium isotope fractionation can be expected (Iler, 1979; Sposito, 1996). The Si isotope fractionation factors inferred from *ab initio* calculations (Méheut et al., 2009) and experimental studies (Oelze et al., 2015) show that ^{28}Si will not be preferentially incorporated into the clay fraction if dissolved Si and crystalline silicates are in isotopic equilibrium. How then can the enrichment of ^{28}Si in clays found in weathering systems be explained?

With increasing age and/or stage of silicate weathering the composition of secondary solids changes from one dominated by amorphous solids to one dominated by crystalline clay minerals (Ziegler et al., 2003; Joussein et al., 2005). For instance, a known transformation path is the reaction of plagioclase to amorphous alumosilicates such as allophane, subsequently e.g. to halloysite, and finally to clay minerals such as kaolinite. It is indeed more likely that kaolinite is formed via thermodynamically less stable phases which act as precursor such as allophane and halloysite (Steefel and Van Cappellen, 1990).

In any case, the first step is the release of Al and Si from primary minerals such as plagioclase. At pH values between 5 and 7 and at the low dissolved organic carbon concentrations typically prevailing in soils or in interstitial solutions, the solubility of $Al(OH)_3$ is extremely low (Sposito, 1996). Accordingly, Al precipitates as amorphous $Al(OH)_3$ or as crystalline solids such as gibbsite. The affinity of Si to adsorb onto these precipitated Al-hydroxides is high (Hingston and Raupach, 1967; Adu-Wusu and Wilcox, 1991; Dietzel, 2002). As we have shown in this study, Si adsorption onto Al-hydroxides is associated with rather strong Si isotope fractionation, favoring light Si isotopes adsorbed onto the solid surface. In the next step, amorphous alumosilicates like siliceous gels or colloids such as hydroxyaluminosilicate (HAS) are formed. Accordingly, Strekopytov

et al. (2006) suggested that, for HAS formation, the reaction of Si with Al-hydroxides is a prerequisite. Such amorphous Al-Si phases can be re-arranged to structures with higher degrees of order, similar to allophane or imogolite (Sposito, 1996; Doucet et al., 2001). If the transformation from amorphous Al-Si phases without any short range order to phases with distinct short range order like HAS or allophane takes place without substantial exchange of Si, the Si isotope signature of HAS/allophane will be inherited from the initial fast adsorption process of Si. With ongoing weathering, the halloysite content in the soil decreases, whereas the kaolinite content increases (Papoulis et al., 2004). As halloysite has the same structure and chemical compositions as kaolinite except for the higher water content in halloysite (Joussein et al., 2005), we can assume that during the transformation of halloysite to kaolinite no shift in Si isotope composition occurs, as Si will be neither lost nor added. Therefore, we suggest that the Si isotopic signature of crystalline clay minerals, such as kaolinite, is inherited from the kinetically-dominated process occurring during adsorption of Si onto a previously formed amorphous Al-hydroxide.

Our model of inherited isotope signals has important implications for interpreting element cycles in the different weathering regimes observed at the Earth surface. In the kinetically limited weathering regime (where supply into and erosion from the weathering zone is so fast that not all primary minerals are dissolved (West et al., 2005; Ferrier and Kirchner, 2008; Dixon et al., 2012) and solutions are at equilibrium concentrations (Maher, 2011)), the Si isotopic signature of soil or stream water will inevitably show heavy Si isotopic values, as in such regimes only fast processes like adsorption of Si occur and no light Si will be released from secondary minerals due to their short residence time in the weathering zone. In the supply-limited weathering regime (where supply and erosion of primary minerals is so slow that most primary minerals are exhausted (West et al., 2005; Ferrier and Kirchner, 2008; Dixon et al., 2012) and solutions are diluted with respect to equilibrium concentrations (Maher, 2011)), the Si isotopic signature of the soil or stream water will be characterized by the degree of weathering, ranging from heavy Si isotopic signatures, where kinetically dominated Si adsorption is the major process, to light Si isotopic signatures where the system is governed by dissolution of clay minerals. This has been already shown for tropical supply-limited settings in the black-water rivers of the Amazon and Congo basin (Cardinal et al., 2010; Hughes et al., 2013). Where erosion rates of secondary minerals are low, it is also conceivable that adsorption of Si and dissolution of secondary minerals are balanced out which results then in an isotopic signature of soil and stream water indistinguishable from the parent material. The dissolution of previously formed secondary precipitates dominates and these minerals release their inherited light Si (Bouchez et al., 2013). Such temporal evolution has been observed from chronosequences in Hawaii (Ziegler et al., 2005a). These authors measured the isotopic signature of the soil solutions and observed an enrichment of heavy Si in solution with increasing age of the soil. In analogy, Opfergelt et al. (2011) clearly showed from allophane sequences in volcanic soils that the more weathered the soil, the older the allophane and the lighter the Si isotope signature is.

3.6   Summary

The adsorption of monomeric silicic acid onto gibbsite is accompanied by a significant kinetic Si isotope fractionation. In all adsorption experiments, light Si isotopes are preferentially adsorbed. By applying a closed-system mass balance model we calculate Si isotope fractionation factors that are dependent on the initial Si concentration. High ini-

tial Si concentrations result in a strong kinetic Si isotope fractionation during adsorption. This initial kinetic signature does begin to re-equilibrate only after ca. 2 months. With this sluggish behavior Si behaves fundamentally different from transition metals (e.g. Fe, Mo, Zn) that equilibrate isotopically within hours.

Application of the mass balance model of DePaolo (2011) requires the assumption of different isotope fractionation factors (α_f) associated with the forward reaction at different initial Si concentrations, rather than changes in forward to backward reaction rate. A minor shift in isotope ratios after 24 hours of Si adsorption is explained by a change in the isotope fractionation regime from kinetically dominated to dominated by equilibrium isotope fractionation. This behavior is compatible with a change from high net adsorption rates to low net adsorption rates (almost constant Si concentration at the end of experiments).

Our findings have major relevance for explaining Si isotope systematics during silicate weathering. We hypothesize that the light Si isotopes signatures commonly found in secondary siliceous minerals and amorphous solids are obtained from adsorption of Si onto Al-hydroxides during the early stages of weathering. When these amorphous phases slowly age to ordered structures and clay minerals, the low isotope ratio is passed on from the amorphous precursors. The light isotope composition found in clays is therefore inherited from the early stages of primary mineral decomposition.

3.7 Appendix Chapter 3

3.7.1 Tables

Table 3.2: Adsorption experiments; Si concentration ([Si]) (the relative uncertainty ϵ has been estimated by the long term reproducibility to 5%); and $\delta(^{29/28}Si)_{NBS28}$ and $\delta(^{30/28}Si)_{NBS28}$ solution values as well as 95% confidence interval (CI) of the delta values; sample names: (pH)_(sampling time [h])_(Si-start-conc [mmol/l])

name	[Si]	$\delta(^{29/28}Si)_{NBS28}$	CI	$\delta(^{30/28}Si)_{NBS28}$	CI
	[mmol/l]	[‰]	[‰]	[‰]	[‰]
7_start_0.36	0.372± 0.019	-0.038	0.057	-0.078	0.106
7_0.02_0.36	0.349± 0.017	0.031	0.040	0.073	0.048
7_0.08_0.36	0.339± 0.017	0.016	0.034	0.057	0.074
7_0.17_0.36	0.334± 0.017	0.052	0.044	0.083	0.080
7_0.25_0.36	0.332± 0.017	0.058	0.068	0.114	0.102
7_0.42_0.36	0.330± 0.016	0.082	0.049	0.148	0.063
7_0.75_0.36	0.325± 0.016	0.071	0.072	0.173	0.016
7_1_0.36	0.329± 0.016	0.077	0.045	0.156	0.076
7_2_0.36	0.321± 0.016	0.080	0.018	0.168	0.046
7_6_0.36	0.309± 0.015	0.108	0.026	0.236	0.017
7_24_0.36	0.294± 0.015	0.206	0.052	0.363	0.066
7_96_0.36	0.274± 0.014	0.218	0.092	0.430	0.123
7_192_0.36	0.268± 0.013	0.249	0.040	0.462	0.057
7_384_0.36	0.259± 0.013	0.215	0.041	0.442	0.142
7_768_0.36	0.253± 0.013	0.248	0.057	0.531	0.096
7_1536_0.36	0.246± 0.012	0.256	0.032	0.490	0.064
7_start_0.71	0.746± 0.037	-0.038	0.057	-0.078	0.106
7_0.02_0.71	0.695± 0.035	0.023	0.014	0.042	0.063
7_0.08_0.71	0.707± 0.035	0.014	0.024	0.052	0.061
7_0.17_0.71	0.692± 0.035	0.070	0.033	0.123	0.038
7_0.25_0.71	0.689± 0.034	0.048	0.031	0.113	0.025
7_0.5_0.71	0.684± 0.034	0.075	0.007	0.135	0.088
7_0.75_0.71	0.675± 0.034	0.053	0.047	0.110	0.062
7_1_0.71	0.668± 0.033	0.069	0.026	0.131	0.073
7_2_0.71	0.664± 0.033	0.082	0.040	0.219	0.072
7_6_0.71	0.642± 0.032	0.119	0.032	0.281	0.025
7_24_0.71	0.622± 0.031	0.210	0.041	0.377	0.094
7_96_0.71	0.602± 0.030	0.221	0.024	0.430	0.063
7_192_0.71	0.588± 0.029	0.242	0.064	0.459	0.036
7_384_0.71	0.567± 0.028	0.264	0.062	0.486	0.088
7_1464_0.71	0.549± 0.027	0.275	0.037	0.535	0.091
7_start_1.42	1.468± 0.073	-0.054	0.072	-0.077	0.154
7_0.02_1.42	1.368± 0.068	0.049	0.077	0.125	0.165
7_0.5_1.42	1.364± 0.068	0.046	0.057	0.137	0.109
7_1_1.42	1.359± 0.068	0.076	0.024	0.195	0.068
7_2_1.42	1.351± 0.068	0.104	0.071	0.153	0.078
7_6_1.42	1.324± 0.066	0.107	0.103	0.256	0.070
7_24_1.42	1.283± 0.064	0.183	0.062	0.307	0.116
7_96_1.42	1.263± 0.063	0.174	0.121	0.352	0.108
7_192_1.42	1.248± 0.062	0.166	0.065	0.445	0.173

Continued...

name	[Si]	$\delta(^{29/28}Si)_{NBS28}$	CI	$\delta(^{30/28}Si)_{NBS28}$	CI
7_384_1.42	1.220± 0.061	0.247	0.053	0.451	0.099

3.7.2 Determination of monosilicic acid using β-silicomolybdate method

Using the β-silicomolybdate method (described in detail by Iler (1982) and Dietzel (2000)) we verified that the Si stock solution contains only monomeric silicic acid. This method is based on the reaction of molybdate with dissolved monomeric silicic acid to a yellow colored β-silicomolybdate aquocomplex, whose evolution is detected at 390 nm by spectrometry for 20 min (UV-VIS Cary 100, Varian). The reaction rate constant, k, for the unidirectional reaction of molybdate with dissolved monomeric silicic acid obtained by fitting a second-order reaction is 2.1 ±0.2 min^{-1} for the prepared solution. This measured range of k values clearly indicates that only monomeric silicic acid, $Si(OH)_4$, is present in solution as polymeric silicic acid induces k values of 0.03 min^{-1} for dimeric and octameric silicic acid and for silica colloids with about 40 silicon atoms in its structure, respectively (e.g. Iler (1982)).
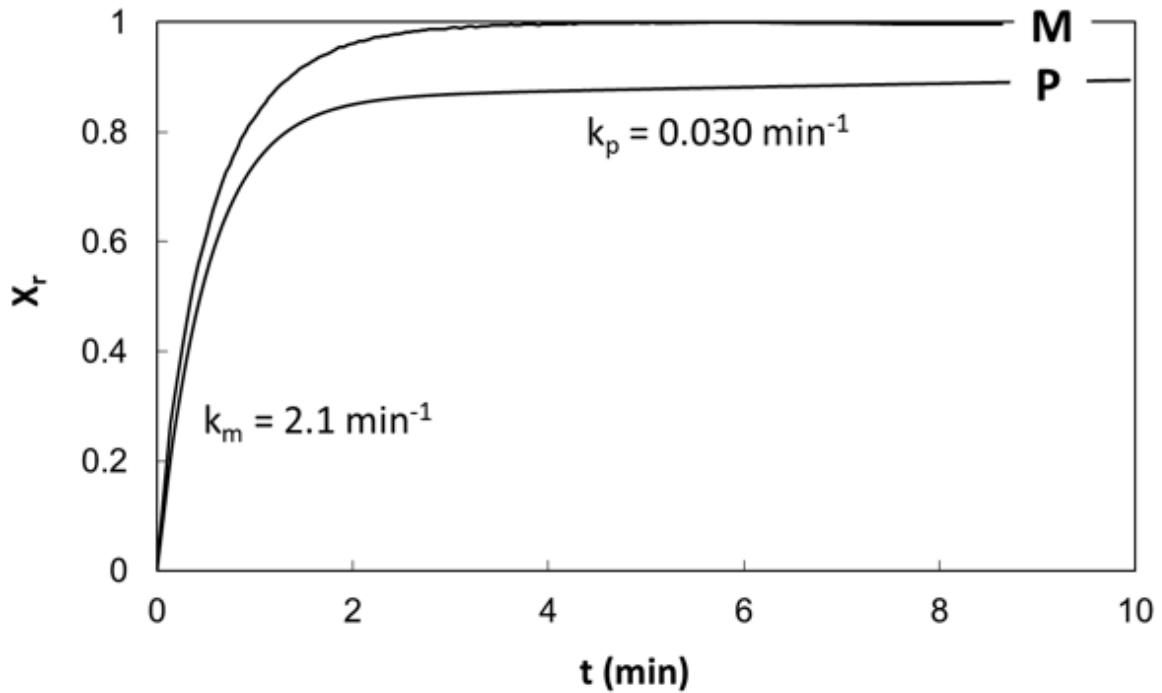
Figure 3.7: Evolution of the β-silicomolybdato complex formation by the reaction of molybdate and dissolved monomeric silicic acid. t: reaction time of the measurement. X_r: molar fraction of total dissolved monomeric silicic acid that has reacted to the silicomolybdato complex (see Dietzel (2000) for details). M: monosilicic acid stock solution. P: solution containing both monosilicic (86%) and polysilicic acid (14%) (soil solution from Wonisch et al. (2008)). Polysilicic acid was not detected in our experimental solutions (evolution according to curve M). k_m and k_p denote the reaction rate constant for the reaction of monosilicic and polysilicic acid to the β-complex, respectively.

3.7.3 Chemical kinetic rate laws applied to Si adsorption on gibbsite

In an attempt to explain the evolution of Si concentration with time we tried to apply well-known chemical rates laws to our data. Here we show that first-order, second-order and first-order forward-backward reaction rate laws are not able to explain the data. Reactions that follow first-order kinetics are only dependent on the concentration change of one reactant (A).

$$R = -\frac{d[A]}{dt} = k[A] \tag{3.7}$$

The integrated form of this equation is:

$$ln[A] = -kt + ln[A]_0 \tag{3.8}$$

If the reaction follows first-order rate kinetics a plot of $ln[A]$ vs. t should result in a straight line with a slope of $-k$. The adsorption of Si onto gibbsite does not follows a first-order rate law (Figure 3.8).
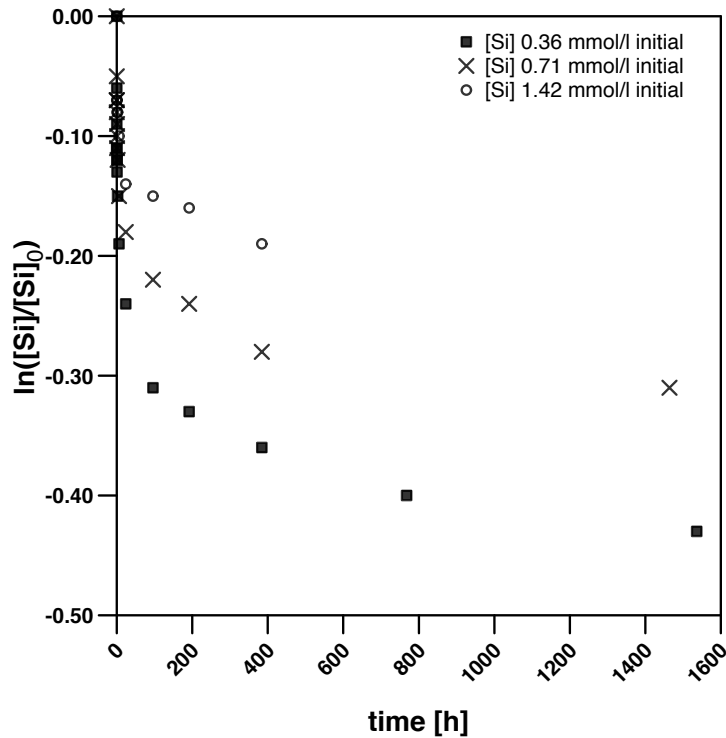
Figure 3.8: $ln\left(\frac{[A]}{[A]_0}\right)$ vs. experimental runtime t. If the adsorption of Si onto gibbsite followed first-order rate kinetics the experimental data should plot on a straight line.

If the adsorption reaction follows a second-order rate law of the form:

$$R = -\frac{d[A]}{dt} = k[A]^2 \tag{3.9}$$

of which the integrated form is:

$$\frac{1}{[A]} = \frac{1}{[A]_0} + kt \tag{3.10}$$

Then the experimental data of the adsorption experiments should fall on a straight line in a plot of $\frac{1}{[A]}$ vs. t, where the slope of this line would be the reaction rate constant k. Figure 3.9 shows obviously that the adsorption of Si onto gibbsite surfaces does not follow a second-order rate law.
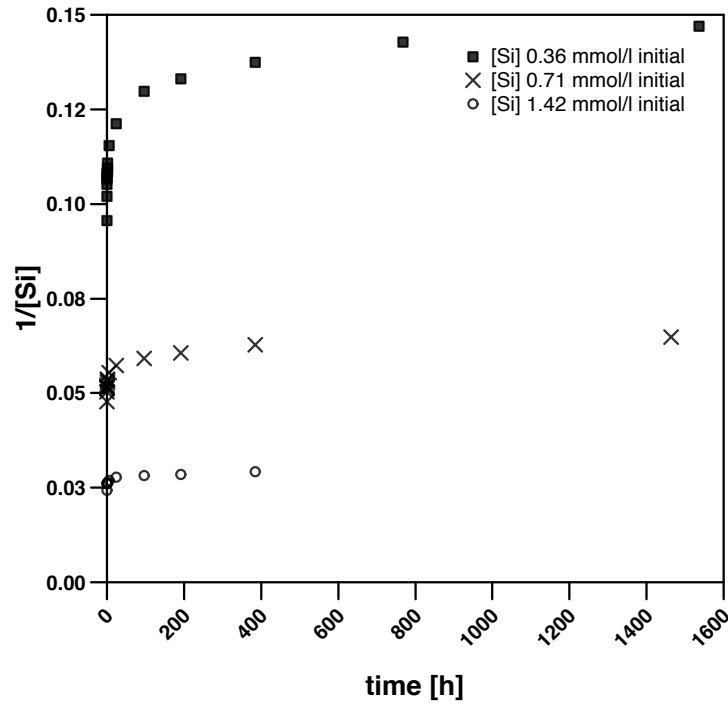
Figure 3.9: $\frac{1}{[A]}$ vs. experimental runtime t. If the adsorption of Si onto gibbsite followed second-order rate kinetics the experimental data should plot on a straight line.

The third attempt was to describe the adsorption kinetics of Si onto gibbsite as a forward-backward reaction (adsorption-desorption reaction). We assume that the individual reactions (forward and backward, respectively) following a first-order rate law. Further we assume that at the beginning of the experiment no Si is adsorbed onto gibbsite. In such case the reaction rate would be:

$$R = -\frac{d[A]}{dt} = k_f[A]_t - k_b[B]_t \tag{3.11}$$

Where k_f and k_b are the reaction rate constants for the forward (adsorption) and backward (desorption) reactions, respectively. The integrated form of this equation is:

$$ln\left(\frac{([A]_0 - [A]_{eq})}{(A]_0 - [A]_{eq})}\right) = (k_f + k_b)t \tag{3.12}$$

If the adsorption of Si onto gibbsite followed Equation 3.12, then all data should fall along a straight line with a slope of $(k_f + k_b)$ in a plot of $ln\left(\frac{[A]_0 - [A]_{eq}}{(A]_0 - [A]_{eq}}\right)$ vs. experimental runtime t. But Figure 3.10 shows that this assumption is not true for the adsorption of Si into gibbsite.
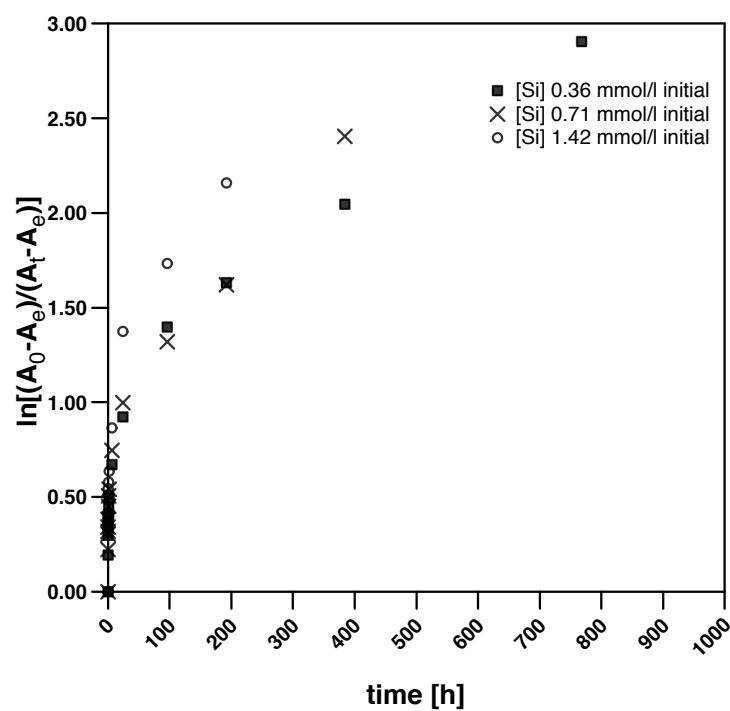
Figure 3.10: $ln\left(\frac{([A]_0-[A]_{eq})}{([A]_0-[A]_{eq})}\right)$ vs. experimental runtime t. If the adsorption of Si onto gibbsite followed the assumption that Si adsorption onto gibbsite occurs via first-order forward and backward reactions the experimental data should plot on a straight line.

Chapter 4

The effect of Al on Si isotope fractionation investigated by silica precipitation experiments[1]

4.1 Abstract

Mass-dependent isotope fractionation occurring during precipitation of solids in low-temperature environments often depends on precipitation rate. Using a series of precipitation experiments in which continuous precipitation and dissolution of Si solids is forced by daily cyclic freezing (solid formation) and thawing (solid re-dissolution), we show this dependence. We conducted six Si precipitation experiments for about 120 days with initial dissolved Si concentration of 1.6 mmol/l Si, at pH values between 4.5 and 7, with additions of 0.1 – 1 mM of dissolved aluminum (Al), and in the absence of Al. During all experiments increasing amounts of an X-ray amorphous silica-containing solid are formed. No Si isotope fractionation occurs during formation of almost pure Si solids, interpreted as an absence of Si isotope fractionation during polymerization of silicic acid. Si isotope fractionation occurs only in the high-Al concentration experiments, characterized by an enrichment of the light Si isotopes in the solids formed early. With ongoing duration of the experiments, a re-dissolution of these solids is indicated as the Si isotope value of the complementary solution shifts to lighter values and eventually reaches near-initial compositions. Hence, our high-Al experiments are characterized by a gradual shift from a regime that is dominated by unidirectional kinetic isotope fractionation with solids formed that are up to $5\text{\textperthousand}$ lighter in their $^{30}Si/^{28}Si$ ratio than the corresponding solution, to one of steady-state between dissolution and precipitation with the $^{30}Si/^{28}Si$ ratio of the solid being almost identical to the solution ($\Delta_{\text{solid-solution}} \approx 0\text{\textperthousand}$). This suggests that the enrichment of light Si isotopes found in natural environments is caused exclusively by a unidirectional kinetic isotope effect during fast precipitation of solids, aided by co-precipitation with Al phases or other carrier phases (e.g. Fe(III)). By contrast, during slow precipitation, or in the absence of a carrier phase like Al, no Si isotope fractionation is expected and solids obtain the composition of the ambient fluid.

4.2 Introduction

Ratios of stable isotopes of Si have emerged as a powerful proxy to distinguish the reactions involved in low-temperature water-mineral and water- rock interaction. The isotope ratios potentially trace the way Si is released from Si-bearing solids into soil and (diagenetic) interstitial solutions. Si isotopes also trace how silica is precipitated into secondary solids from these solutions. Given the useful information Si stable isotopes provide along this pathway, the resulting isotope ratios have been increasingly explored as a tool to trace silicate weathering, sediment diagenesis and the associated silicification, precipitation of siliceous sediments from hydrothermal vents, and the genesis of Precambrian cherts and banded iron formation (e.g. Ziegler et al. (2005a); Robert and Chaussidon (2006); Steinhoefel et al. (2009); van den Boorn et al. (2010); Chakrabarti et al. (2012)). In general, dissolved Si in soil and in river waters is enriched in the heavy isotopes as compared to the primary silicate minerals where Si is sourced from. The corresponding isotopically light reservoir is found in secondary siliceous solid phases (Ziegler et al., 2005a,b; Georg et al., 2007a; Opfergelt et al., 2009; Bern et al., 2010; Steinhoefel et al., 2011). Furthermore, siliceous precipitates from hydrothermal solutions enriched in dissolved Si also show the common picture of preferential incorporation of light isotopes in the precipitates (Douthitt, 1982; Ding et al., 1996; de La Rocha et al., 2000). This pictures is also inferred from the prevalence of low isotope ratios in Precambrian cherts (Andre et al., 2006; Steinhoefel et al., 2009, 2010; van den Boorn et al., 2010). However, for chert formation, the way in which diagenetic silicification modifies the Si isotope composition from that of the original deposits is far from understood. Basile-Doelsch et al. (2005) found some of the lowest Si isotope ratios in Aptian siliceous cements. Chen et al. (2007) also reported low isotope ratios in *Anabarites celoms* (tubular small shelly fossil), and in quartz ocurring in granular phosphates. In contrast, Robert and Chaussidon (2006), Abraham et al. (2011) and Chakrabarti et al. (2012) reported Archean cherts enriched in heavy Si isotopes.

Converting these observations into a quantitative understanding of the movement of silica in low-temperature environments requires knowledge of the isotope fractionation factors associated with precipitation and recrystallization of siliceous solids. However, not only do we lack even first–order experimental estimates of equilibrium isotope fractionation factors, but probably the formation of many siliceous secondary minerals and chemical deposits is affected by non-equilibrium processes, as they are often enriched in light Si isotopes which suggest that the origin of the Si isotope fractionation is mostly kinetic (see e.g. Ziegler et al. (2005a); Georg et al. (2009); DePaolo (2011)). In these conditions, the relative importance of the forward (precipitation) and backward (dissolution) reaction rates determine the net solid formation rate and the associated isotope fractionation factor (DePaolo, 2011). In addition, sedimentary silicates usually do not directly precipitate from aqueous solutions, as documented by the large number of known amorphous silica precursor phases (e.g. Iler (1979)). Therefore the generation of surface area during nucleation, growth and dissolution, and precursor replacement is important as the processes and rates at the mineral-water interface control the isotope composition of the solid material during mineral growth (Cole et al., 1983; Criss et al., 1987; Steefel and Van Cappellen, 1990; Nielsen et al., 2012; Druhan et al., 2013).

To date, only a few notable studies have explored Si isotope fractionation during the fixation of Si from solution under controlled experimental conditions. The Si isotope fractionation during adsorption of Si onto Fe-oxides, the Si isotopic evolution during allophane- and gel-like solid formation and the Si isotope fractionation during abiotic

silica precipitation at low temperatures have been experimentally investigated (Li et al., 1995; Ziegler et al., 2005a; Delstanche et al., 2009; Opfergelt et al., 2009; Geilert et al., 2014). Recently, silicon isotope fractionation during adsorption of Si onto Al-hydroxides has been shown to result in a strong rate dependence of silicon isotope fractionation (Oelze et al., 2014). All these studies demonstrate the preferential incorporation of ^{28}Si into the solid, most likely during Si adsorption onto the solid phase. Isotope fractionation factors $10^3 ln\alpha_{\text{solid/solution}}$ range from -1.0‰ to -1.6‰ for adsorption of Si onto Fe-oxides, -1.8‰ up to -3‰ for adsorption of Si onto Al-hydroxides and up to $\approx$ -3.0‰ for precipitation of allophane- and gel-like solid phases. First-principle calculations predict an enrichment of ^{30}Si in the higher-ordered solid at equilibrium conditions (Ding et al., 1996; Méheut et al., 2007, 2009). However, these predictions suggest that the Si isotope fractionation of the aforementioned experimental studies are dominated by a kinetic isotope effect. Indeed, attaining Si isotopic equilibrium in experimental settings is virtually impossible due to the extremely low exchange rates between solids and fluids in low-temperature processes, especially in the SiO_2-H_2O system. Li et al. (2011) suggested that recrystallization (or re-organization) induced by "Ostwald ripening", the dissolution of small particles and the re-deposition of the dissolved species on the surfaces of larger particles in a saturated solution, is the only way to induce an isotope exchange at low temperature that is not overprinted by kinetic processes. To test whether equilibrium has indeed been attained, experimentalists use the addition of isotopically-enriched species in one of the two compartments (Johnson et al., 2002; Welch et al., 2003; Schuessler et al., 2007). However, this approach is not possible if, as is the case here, Si is precipitated from a homogeneous solution.

A possible experimental approach in which dissolution-precipitation reactions take place is a batch reactor in which solid precipitation is driven by evaporation of the fluid, and solid dissolution driven by dilution of the fluid. However, the slow evaporation rates involved in such an experiment would result in excessively long experimental runtimes. For Si-containing solids, once precipitated, isotopic equilibration times will exceed any feasible experimental runtime due the slow exchange rates. It is most likely that dissolution is the limiting step to reach full exchange between formed solid products and solution. The low dissolution rate for amorphous silica ($\approx 1*10^{-12}$ mol$*$m$^{-2}*$sec^{-1} at 20℃; Icenhower and Dove (2000)) will likely impair attainment of equilibrium as in experiments of $CaCO_3$ precipitation (Tang et al., 2008).

To circumvent these difficulties we designed a novel approach. Alternating dissolution-precipitation, implying depolymerization-polymerization of silica, is induced by freezing and thawing for predefined cycle length over a long run duration (Dietzel, 2005). During freezing, only H_2O molecules are captured in the ice lattice and the remaining solution becomes supersaturated in Si and precipitation of solids from the remaining solution occurs as soon as a critical supersaturation is reached. At the end of the freezing time span, temperatures are increased and the ice previously formed melts. Hence the solution is then undersaturated with respect to the formed solids, leading to their partial dissolution during thawing. By continuing these freeze-thaw cycles steady-state conditions between silica precipitation and dissolution are reached, meaning that the dissolution and precip-itation fluxes compensate each other at the scale of a freeze-thaw cycle. At this stage concentrations of dissolved Si do not change from a freeze-thaw cycle to the next. Our setup allows us to explore the temporal change in the Si isotope fractionation factor as the system evolves from a state that is characterized by high net Si removal rates (domi-nated by unidirectional kinetic isotope fractionation), to a state where the net change for precipitation and dissolution is close to zero.

The rationale for this approach becomes apparent from fundamental experimental studies on dissolution-precipitation kinetics of SiO_2 polymorphs. The process of dissolution and precipitation of SiO_2 polymorphs has been described as fully reversible (Rimstidt and Barnes, 1980; Renders et al., 1995; Carroll et al., 1998). Using the empirical relationships of Rimstidt and Barnes (1980) and Dove et al. (2008) for the dependence of the dissolution rate on temperature and saturation state we can estimate the dissolution rate for an experiment maintained far from equilibrium. The dissolution rate and therefore the time needed to reach full exchange is accelerated by a factor of 60 in comparison to experiments close to equilibrium conditions.

Our experimental approach also provides insight into the numerous geological processes associated with water-solid interaction that involve repeated dissolution-precipitating cycles of silica at the water-solid interface, such as for example during mineral replacement in weathering reactions, diagenesis, silicification, or biogenic ooze maturation. In addition, this experimental approach of repeated freeze-thaw cycles can give insights into the formation process of authigenic silicates in polar regions (Tedrow, 1966; Dickinson and Grapes, 1997).

However, in virtually all Earth surface reactions will Si release from primary silicates be accompanied by variable amounts of Al. Reactions between Si and Al are hence likely the first crucial reactions. Aluminum in the system not only reduces the solubility of Si in aqueous solutions (Dixit et al., 2001; Van Cappellen et al., 2002), it also further provides surface area for fast adsorption of Si (Hingston and Raupach, 1967; Dietzel and Böhme, 1997). In addition, pH will exert a first-order control over the precipitation kinetics of both elements as the solubility of Al and Si are both "pH dependent". Therefore, we performed experiments of Si precipitation from solutions in the presence of variable Al concentrations and different pH.

In the present study, we conducted six Si precipitation experiments for about 120 days with initial dissolved Si concentration of 1.6 mmol/l Si, with additions of different amounts of Al (0, 0.1, 1 mmol/l dissolved Al) and explored the evolution of the dissolved silicon isotope composition. In all experiments increasing amounts of an X-ray amorphous silica-containing solids are formed. The evolution of the dissolved silicon isotope composition can be explained by the presence or absence of dissolved Al.

4.3 Framework for isotope fractionation during precipitation

Because of the diversity of isotope fractionation mechanisms encountered in our experiments, we first review the framework of definitions of these processes. There are several processes during which kinetic isotope fractionation might occur, for example diffusion, evaporation, or due to differences in energy barriers. In the literature, the term "kinetic" actually serves as an umbrella for two fundamentally different processes generating isotope fractionation: (1) differential transport velocity of isotopes over a given distance for example during diffusion ("transport-limited") and (2) differences in the energetic barrier associated with chemical reactions ("reaction-limited").

In "transport-limited" regimes, kinetic isotope fractionation arises from different transport velocities (e.g. different diffusion coefficients) resulting from the mass differences of isotopes (Richter et al., 2006). This regime will not be further discussed in this paper, as under our experimental conditions this effect will be small (see Table 1 in Richter

et al. (2006)). In addition to isotope fractionation due to different diffusion coefficients for isotopes, the influence of a chemical gradient in solution without sufficient stirring must be considered possible (Gislason and Oelkers, 2003). Such an effect is also described as "transport-limited". The observed precipitation and dissolution rates and further the measured isotope fractionation are then influenced by the evolution of a chemical gradient and are no longer dependent on the bulk fluid chemistry but rather on the evolution of the chemical gradient. It is assumed here that mixing of the solution due to ice movement and climate cabinet vibrations will preclude the effects of chemical gradients and can be therefore considered as subordinate.

In the "reaction-limited" case the kinetic effect arises because an activation energy has to be overstepped to form or break bonds. The activation energy is likely to differ between isotopes of an element, as bonds with heavier isotopes have lower zero point energies than light isotopes (Urey, 1947). For example, during ion desolvation kinetic isotope fractionation has been documented to be induced by the difference in activation energy (Hofmann et al., 2012). The Arrhenius equation indicates that at a given temperature, the reaction rate constant of light isotopes is higher than that of heavy isotopes. Importantly, during a reversible reaction the light isotope will be favored in both directions of the reaction. Therefore it follows that the overall isotope fractionation is governed by the relative magnitudes of forward and backward reaction rates, and by the individual isotope fractionation factors for these reactions (DePaolo, 2011).

4.4 Materials and Methods

4.4.1 Description of Experiments

Freeze-thaw experiments were conducted following a method adapted from Dietzel (2005). All experiments were carried out at similar initial Si concentrations and at two pH conditions (near neutral: pH 7 and acidic: pH 4.5 or 5) to mimic typical soil pH values (Schwertmann and Fischer, 1982). Three experimental series were conducted: the first series (a) was carried out without Al addition, the second series (b) with low amounts Al added (low: 0.1 mmol/l Al) and the third series (c) with high Al amounts added (high: 1 mmol/l Al), respectively. All reagent solutions were at least of analytical grade, and Milli-Q water (18.2 $M\Omega$) was used. The pH of the initial solutions was adjusted with diluted HCl and NaOH. Initial solutions of 1.6 mmol/l Si were prepared from a tetraethylorthosilicate (TEOS) solution acquired from Merck. Aluminum was added as $AlNO_3*9H_2O$ and 100 ml of these initial solutions were then evenly distributed into each of several 100 ml polyethylene (PE) bottles. One separate bottle was prepared for each experimental runtime (each data point in Figures 4.1, 4.2, 4.5 and 4.6 is an individual bottle; see also Tables 4.1, 4.2 and 4.3) and was removed for analyses after a given of runtime.

We conducted the cyclic freeze-thaw experiments in a climate cabinet where temperature was changed over 24 hour-cycles from 20℃ to -20℃ (6 h from 20℃ to -20℃, 6 h at -20℃, 6 h from -20℃ to 20℃, 6h at 20℃; heating and cooling rate: 0.11℃ min⁻¹). About 4 h after reaching 0℃ visual inspection showed that the experimental solution was completely frozen or thawed, respectively, but nevertheless small amounts of unfrozen water might still be present even at -20℃ (e.g. Anderson and Tice (1973); Anderson (1981)). During freezing, the formation of ice crystals results in a decrease of the remaining volume of the solution and therefore an elevated concentration of dissolved Si in the solution. Further

the decrease in temperature leads to a decrease in the amorphous Si solubility (Rimstidt and Barnes, 1980). Both effects induce supersaturation with respect to amorphous silica so that precipitation of amorphous silica can occur. During warming of the solution and subsequent thawing of ice crystals, the solution becomes undersaturated with respect to the formed Si-containing solids which are expected to partly redissolve. The amount of silica that is precipitated from solution at a given time interval depends on the rate of ice formation and the kinetics of silica precipitation (see Dietzel (2005) and references therein). Temperature limits, rates of cooling and warming, total solution volume and the initial concentration of dissolved Si are decisive experimental parameters. We performed several pre-experiments to find these parameters. The cooling and thawing rates were set to 0.11℃ min^{-1}, a rate at which we observed that precipitation of Si starts ca. 0.5 hours before the solution is completely frozen.

Freeze-thaw cycles were repeated up to 130 times. Although the solutions were not stirred or shaken, we assume that the solution was sufficiently well mixed through the motions of the ice crystals. During the thawing period, the melt water accumulated at the bottom of the bottles and the residual ice at the top. Additionally, vibration of the climate cabinet due to ventilation enhanced mixing. Therefore isotope fractionation due to diffusion (Richter et al., 2006) can be regarded as negligible. We cannot fully exclude the effect of "transport-limitation" that arises from a chemical gradient (surrounding the particles formed; see Gislason and Oelkers (2003) and Section 4.3). This effect will only affect the reaction rates and therefore the resulting isotope fractionation factors but will not change the reaction mechanism itself. Therefore the derived isotope fractionation mechanisms do not depend on this.

4.4.2 Requirements for Si precipitation experiments

Si initial concentration

The precipitation of amorphous silica requires high concentrations of dissolved Si ($\gg 2$ mmol/l Si at 25℃, the solubility of amorphous silica (Gunnarsson and Arnorsson, 2000)). In addition, as we aimed to analyze both the dissolved Si and the precipitated silica for their Si isotope composition, a significant amount of solid Si has to be formed. Therefore the dissolved Si has to be prepared with even higher Si concentrations than required for the first nucleation. However, it is a requirement that no polymeric Si is present in the experimental initial solution, as its presence would render isotope data interpretation unnecessarily complex. To avoid formation of polysilicic acid, the Si concentration of the initial solution was kept below the solubility of amorphous silica. An initial Si concentration of 1.6 mmol/l was deemed sufficient to meet this requirement. Initial solutions were analyzed for the polymerization degree of dissolved Si (β-silicomolybdate method; see 4.8.2 and for further details Iler (1979) and Dietzel (2000)) by measuring the total Si concentration using ICP-OES and subtracting the concentration of monosilicic acid determined by the β-silicomolybdate method. The results showed that no colloidal Si was present in the initial solution in any of the experiments.

Si source

We used tetraethylorthosilicate (TEOS) as a Si source. Dietzel (1993, 2002) showed that when using TEOS as Si source only monomeric silicic acid is formed below the solubility of amorphous silica and that the behavior of dissolved Si in experiments is

identical to monomeric silicic acid solutions that were prepared by alternative means (e.g. dissolution of silicates). One further advantage of TEOS is that no associated cations of other minor elements (that would be released during the dissolution of other Si sources, such as silicates (e.g. Na_2SiO_3) or alkaline standard solutions (SiO_2 in 2% NaOH)) are present in the solution. These elements would then have to be removed to obtain pure silicic acid for the experiments. Further the solution can be easily produced by adding small volumes of TEOS to water where it converts into silicic acid via a hydrolysis reaction. However, the side product of this reaction is ethanol that we estimate to be present in our experimental solution at a concentration of 6.4 mmol/l. We explored whether the ethanol potentially remaining in the purified mass spectrometric solutions induces analytical artifacts during the preparation and measurement of Si isotopes by measuring the purified solutions and the precipitated solid counterpart of the conducted experiments (see Table 4.3). Mass balance shows that each fluid-solid pair yields a calculated bulk isotopic composition that is identical to that of the initial solution. The fact that the calculated bulk isotope composition of the system at different fluid-solid ratios (mass dissolved Si/mass of precipitated silica) is similar to the composition of the initial solution demonstrates the absence of analytical artifacts induced by the release of ethanol during preparation of Si-containing solutions using TEOS.

4.4.3 Filtration of solutions and chemical separation for Si isotope analyses

The precipitate was separated from the solution by using cellulose acetate filters (0.1 μm). Where sufficient amounts of precipitate were obtained, the precipitate was rinsed off from the filter and dried at 40℃. The filtered precipitates of freeze-thawing experiments were digested ($\approx$ 2 mg sample) using 200 μl 1M NaOH (analytical grade; Si concentration <1 ppb) in Teflon beakers. After digestion, samples were taken up in Milli-Q water for column chemistry. Si was separated from the matrix following the method of Georg et al. (2006b): the filtered solutions and the digested precipitates were loaded onto pre-cleaned columns (1.5 ml of BioRad DOWEX 50W-X8; 200-400 mesh) and Si was eluted with 5 ml Milli-Q water and stored in pre-cleaned centrifuge tubes. It was assured for all samples that the Si yield was >95%, which was checked by ICP-OES (Varian 720-ES).

4.4.4 Mass spectrometry

Determination of Si isotopic composition was usually done in medium resolution mode on a Thermo Neptune multi-collector inductively coupled mass spectrometer (MC-ICP-MS). The purified sample solutions were introduced into the plasma using the Thermo stable introduction system (SIS) glass spray chamber (wet-plasma) equipped with a 120 μl/min nebulizer. Samples measured in wet plasma conditions were diluted to 2.5 ppm in 0.1 M HCl which typically resulted in an intensity of 5 V/ppm on ^{28}Si (10^{11} Ω resistor). To correct for instrumental mass bias, we used a standard-sample-bracketing procedure. Measurements were conducted on the interference-free low-mass side of the three Si isotopes. Samples and secondary standards were measured at least 4 times during a sequence; each sample or standard was measured for 30 cycles with an integration time for each cycle of 4 s. Pure 0.1 M HCl solutions were measured before and after each standard-sample-standard block and were used for on-peak zero correction. Typical intensities of ^{28}Si in blank solutions were below 5 mV. We report Si isotope data relative

to the standard reference material NBS28 (quartz sand) in the delta notation according to Coplen (2011) as $\delta(^{29/28}\text{Si})_{\text{NBS28}}$ and $\delta(^{30/28}\text{Si})_{\text{NBS28}}$ expressed in per mill (‰) by multiplication of Equation 4.1 and 4.2 with a factor of 10^3:

$$\delta(^{29/28}\text{Si})_{\text{NBS28}} = \left(\frac{\left(\frac{^{29}\text{Si}}{^{28}\text{Si}}\right)_{\text{sample}}}{\left(\frac{^{29}\text{Si}}{^{28}\text{Si}}\right)_{\text{NBS28}}} - 1 \right) \tag{4.1}$$

$$\delta(^{30/28}\text{Si})_{\text{NBS28}} = \left(\frac{\left(\frac{^{30}\text{Si}}{^{28}\text{Si}}\right)_{\text{sample}}}{\left(\frac{^{30}\text{Si}}{^{28}\text{Si}}\right)_{\text{NBS28}}} - 1 \right) \tag{4.2}$$

Reported errors on delta values are the 95% confidence interval (CI) were calculated according to Equation 4.3:

$$\text{CI} = \overline{\delta(^{x/28}\text{Si})_{\text{NBS28}}} \pm \text{t}_{\text{n-1}} \times \text{SE} \tag{4.3}$$

where $\overline{\delta(^{x/28}\text{Si})_{\text{NBS28}}}$ is the mean of the measured delta values with $x= {}^{29}\text{Si}$ or ^{30}Si for the sample or standard (at least n=4), $\text{t}_{\text{n-1}}$ is a critical value from tables of the *Student's t*-law and SE is the standard error of the mean. Two reference materials (BHVO-2 and IRMM-017) were used to control accuracy of our measurements. These two standards measured over 12 months and after several individual digestion and chemical separation procedures (digestion and Si separation procedure adapted from Georg et al. (2006b) and Zambardi and Poitrasson (2011)) yielded for BHVO-2g: $\delta(^{30/28}\text{Si})_{\text{NBS28}} = 0.27 \pm 0.02$ ‰ (n=73) and for IRMM-017 $\delta(^{30/28}\text{Si})_{\text{NBS28}} = 1.36 \pm 0.03$ ‰ (n=53). The obtained values of both secondary standards are comparable, within uncertainty, to those reported in the literature for BHVO-2g $\delta(^{30/28}\text{Si})_{\text{NBS28}} = 0.28 \pm 0.02$ ‰ (Reynolds et al., 2007; Fitoussi et al., 2009; Savage et al., 2010; Zambardi and Poitrasson, 2011; Armytage et al., 2011a) and IRMM-017 $\delta(^{30/28}\text{Si})_{\text{NBS28}} = 1.29 \pm 0.10$ ‰ (Ding et al., 1996; Coplen et al., 2002a; Chmeleff et al., 2008).

4.5 Results

Si and Al concentration as well as $\delta(^{29/28}\text{Si})_{\text{NBS28}}$ and $\delta(^{30/28}\text{Si})_{\text{NBS28}}$ values for the freeze-thaw experiments are reported in Tables 4.1, 4.2 and 4.3.

4.5.1 Si and Al concentrations

The evolution of dissolved Si and Al concentrations with time is displayed in Figures 4.1 and 4.2, respectively. X-ray diffraction patterns (XRD, Panalytical X'Pert Pro, Co-Kα) show that the formed precipitates are not crystalline (Figure 4.3). Si concentration decreases with runtime in all experiments. In the zero-Al experimental series (a) a pure Si-containing solid is formed. In the low-Al experimental series (b) (0.1 mmol/l Al) and in the high-Al experimental series (c) (1 mmol/l Al), a Si and Al-containing solid is formed (see Figures 4.1, 4.2 and 4.4).

The zero-Al experimental series (a) shows low Si removal rates and low amounts of solid precipitated. The low-Al experimental series (b) (0.1 mmol/l Al) shows lower removal

rates of dissolved Si than the high-Al experimental series (c) (1 mmol/l Al). At acidic conditions, the zero-Al experimental series (a) shows higher Si removal rates from solution and larger amounts of Si precipitated than at neutral pH conditions. In the low-Al experimental series (b) (0.1 mmol/l Al), the removal of Si is instead more pronounced and rapid at neutral pH conditions. The highest removal rates are observed in the high-Al experimental series (c) (1 mmol/l Al), for the experiments at pH 7, where almost all Si (>95%) is removed during the first 10 days (see Figures 4.1 and 4.2). For comparison, in the low-Al experiment (0.1 mmol/l Al) conducted at pH 4.5 only minor amounts (<5%) of Si were removed from the solution during the first 60 days. The high-Al experiments (1 mmol/l Al) at pH 4.5 and the low-Al experiment (0.1 mmol/l Al) at pH 7 show similar behavior in the evolution of their Si concentrations. After 50 days, more than 50% of the initial amount of dissolved Si was removed from solution. Finally, the low-Al experiment (0.1 mmol/l Al) at pH 7 shows an increase in dissolved Si concentration between day 80 and 100. As each data point corresponds to an individual experiment, irregularities in the preparation of a particular sample might have resulted in such a deviation.

Dissolved Al concentrations decrease with time in most Al-containing experiments, except for the low-Al experiment at pH 4.5. The evolution of Al concentration strongly depends on the pH value and the initial Al concentration (Figure 4.2). In the low-Al experiment (0.1 mmol/l Al; series (b)) at pH 4.5, the Al concentration remains constant during the entire experiment (see Figure 4.2). This contrasts with the low-Al experiment (0.1 mmol/l Al; series (b)) at pH 7, where the Al concentration declines continuously during the first 50 days, until all Al is completely removed from solution. For the high-Al experiment (1 mmol/l Al; series (c)) at pH 4.5, the Al concentration declines during the first 20 days to 0.6 mmol/l and stabilizes around this concentration for the remaining experimental runtime. At pH 7 in the high-Al experiment (1 mmol/l Al; series (c)), all Al was almost quantitatively removed from the solution.

Analysis of dissolved Al concentrations of the respective initial solutions for the high-Al experiment at pH 7 (1 mmol/l Al) at 25℃ indicates substantial precipitation of Al immediately after adding Al even before starting the freeze-thaw cycles. This can be explained by $Al(OH)_3$ formation due to high supersaturation with respect to amorphous $Al(OH)_3$.

To confirm this hypothesis we used the computer code PHREEQC (with database, Parkhurst and Appelo, 1999) to model saturation indices (SI) with respect to amorphous $Al(OH)_3$. The saturation index is calculated by dividing the chemical activities of the dissolved ions of the mineral (ion activity product, IAP) by their solubility product (K_{sp}), such that S.I. = $\log(IAP/K_{sp})$. The calculated saturation indexes (S.I.(amorphous $Al(OH)_3$)) for the low-Al experimental series (b) (0.1 mmol/l Al) are -2.12 and 0.73 (for the reference solutions at 25℃) at a pH of 4.5 and 7, respectively. For the high-Al experimental series (c) (1 mmol/l Al) saturation indexes S.I.(amorphous $Al(OH)_3$) of -1.13 and 1.73 are predicted for the reference solutions at 25℃ at a pH of 4.5 and 7, respectively. Precipitation of Al (and Si) prior to cyclic freezing is only observed for the high-Al experiment (1 mmol/l Al) at pH 7. For the low-Al experiment (0.1 mmol/l Al) at pH 7 the calculation suggests that the solution is also supersaturated with respect to amorphous $Al(OH)_3$, but no precipitation occurs at room temperature.

We calculated the evolution of the Si/Al ratio of the solid (Si/Al_{solid}) with time (Figure 4.2). The Si/Al_{solid} ratio remains constant at ≈1.5 throughout the experimental runtime for the high-Al experiment (1 mmol/l Al; series (c)) conducted at pH 7. For the high-Al experiment (1 mmol/l Al; series (c)) conducted at pH 4.5, Si/Al_{solid} evolves from
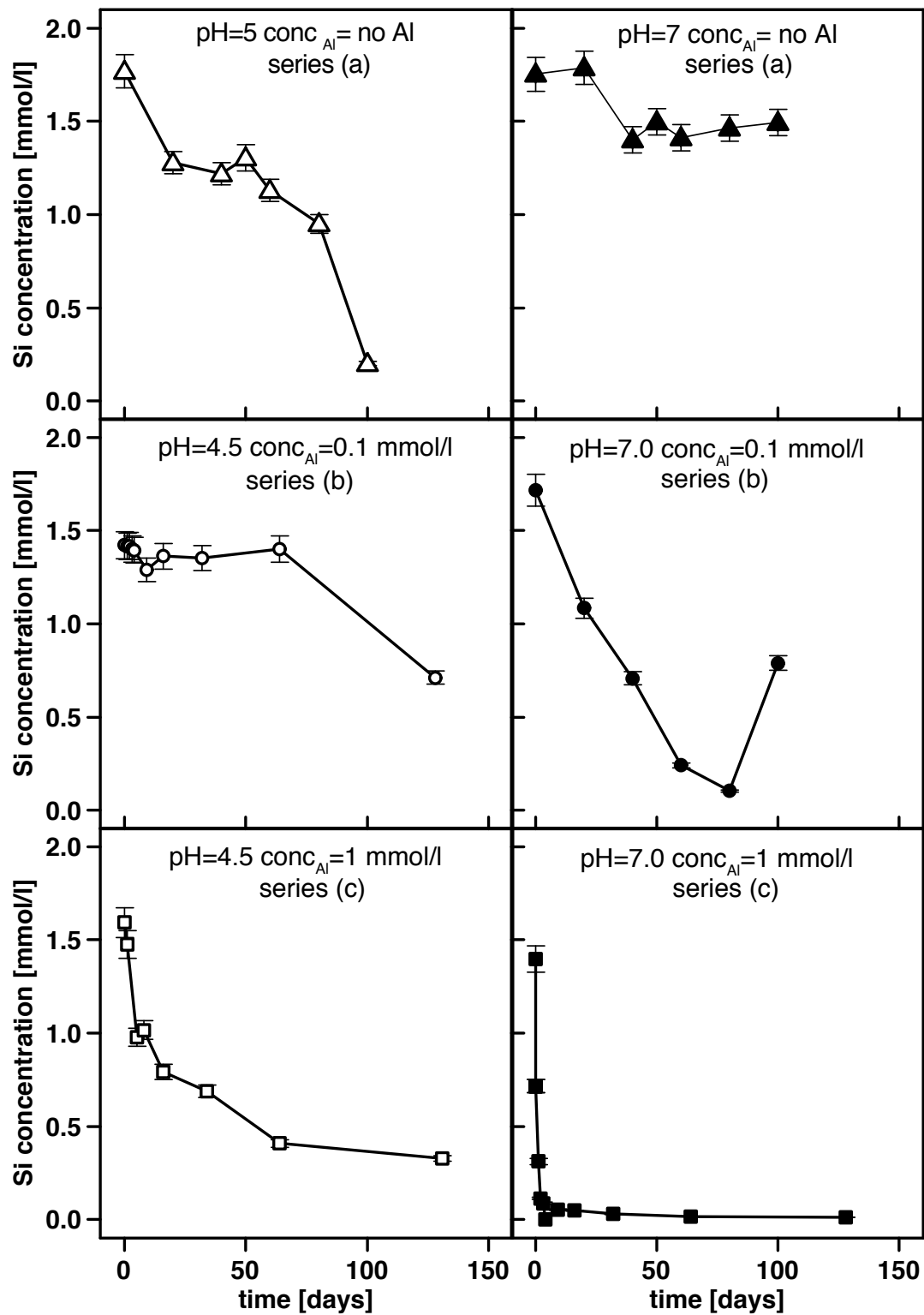
Figure 4.1: Evolution of Si concentration in solutions during freeze-thaw experiments. Open symbols depict experiments at pH 4.5 or pH 5 and solid symbols those at pH 7. Triangles represent zero-Al experiments, circles represent low-Al experiments (0.1 mmol/l Al) and squares high-Al experiments (1 mmol/l Al), respectively (an error of 5% was estimated for concentration measurements)

$\approx$1 to $\approx$2.5. For the low-Al experiments (0.1 mmol/l Al; series (b)), Si/Al$_{solid}$ shows a pronounced increase with time from ratios of $\approx$0.1 to $\approx$15.
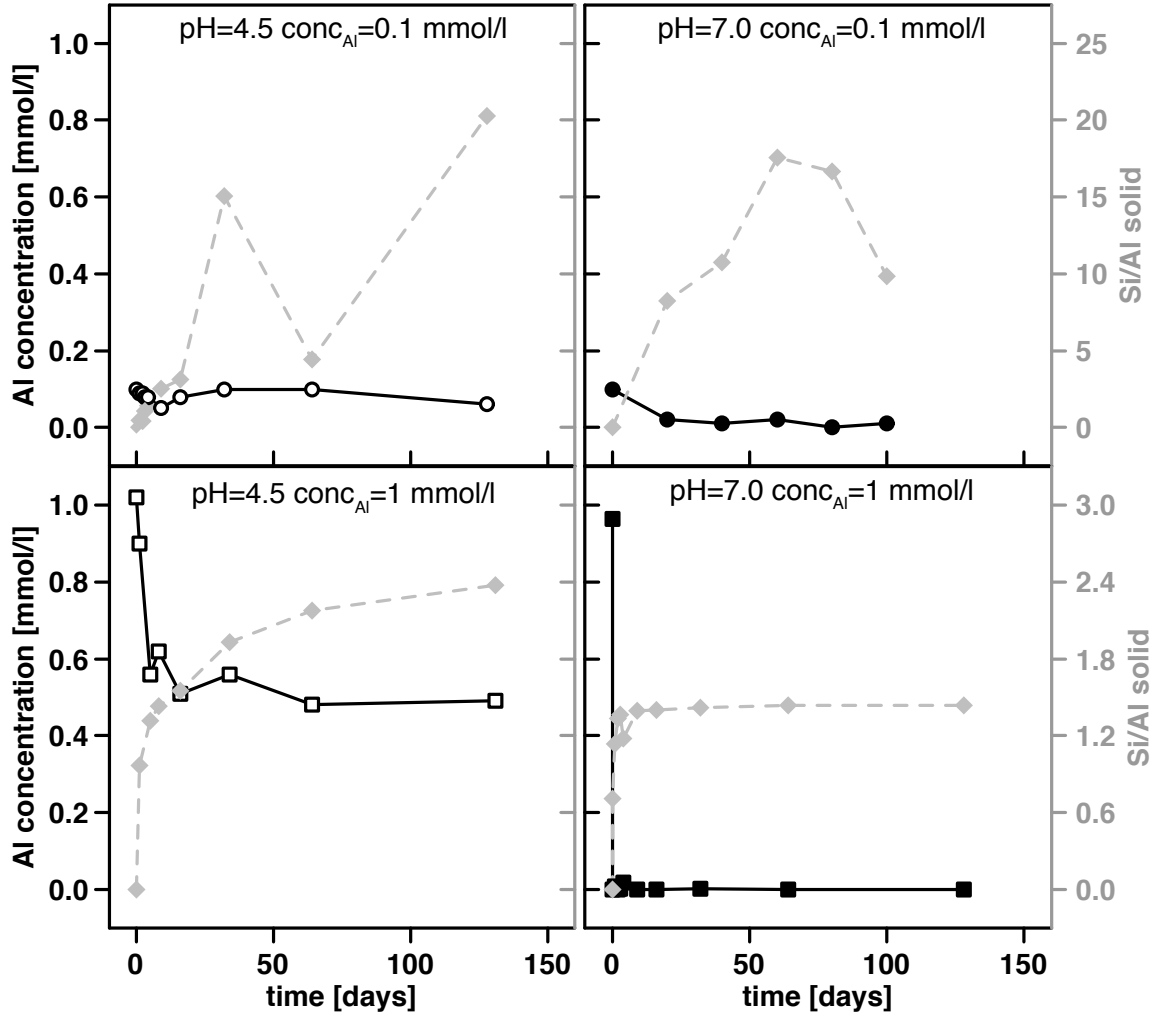
Figure 4.2: Evolution of Al concentration in solutions (left axis; open and solid black symbols) and evolution of Si/Al$_{solid}$ ratios (right axis; grey symbols) in solids. Open symbols depict experiments at pH 4.5 and solid those at pH 7. Circles represent experiments low-Al experiments (0.1 mmol/l Al) and squares high-Al experiments (1 mmol/l Al), respectively (an error of 5% was estimated for concentration measurements).

4.5.2 Silicon isotopes

We present Si isotope ratios measured in solution reported as $\Delta(^{30/28}Si)_{solution} = \delta(^{30/28}Si)_{solution(t)} - \delta(^{30/28}Si)_{solution(initial)}$ (see Figure 4.5 and Figure 4.6). Corresponding precipitates were also analyzed for the high-Al experiment (1 mmol/l Al; series (c)) at pH 4.5 (see Table 4.3). Mass balance shows that precipitates yield the complementary isotope reservoir to the dissolved phase.

For the zero- and low-Al experimental series (a) and (b), at both pH values the $\Delta(^{30/28}Si)_{solution}$ values are stable (within the error of analyses) and remain close to the initial value of the solution of $\Delta(^{30/28}Si)_{solution} \approx 0\permil$. This observation remains valid even after significant precipitation of silica has occurred, in particular at acidic conditions in series (a) and at neutral conditions in series (b) (see Figure 4.1).
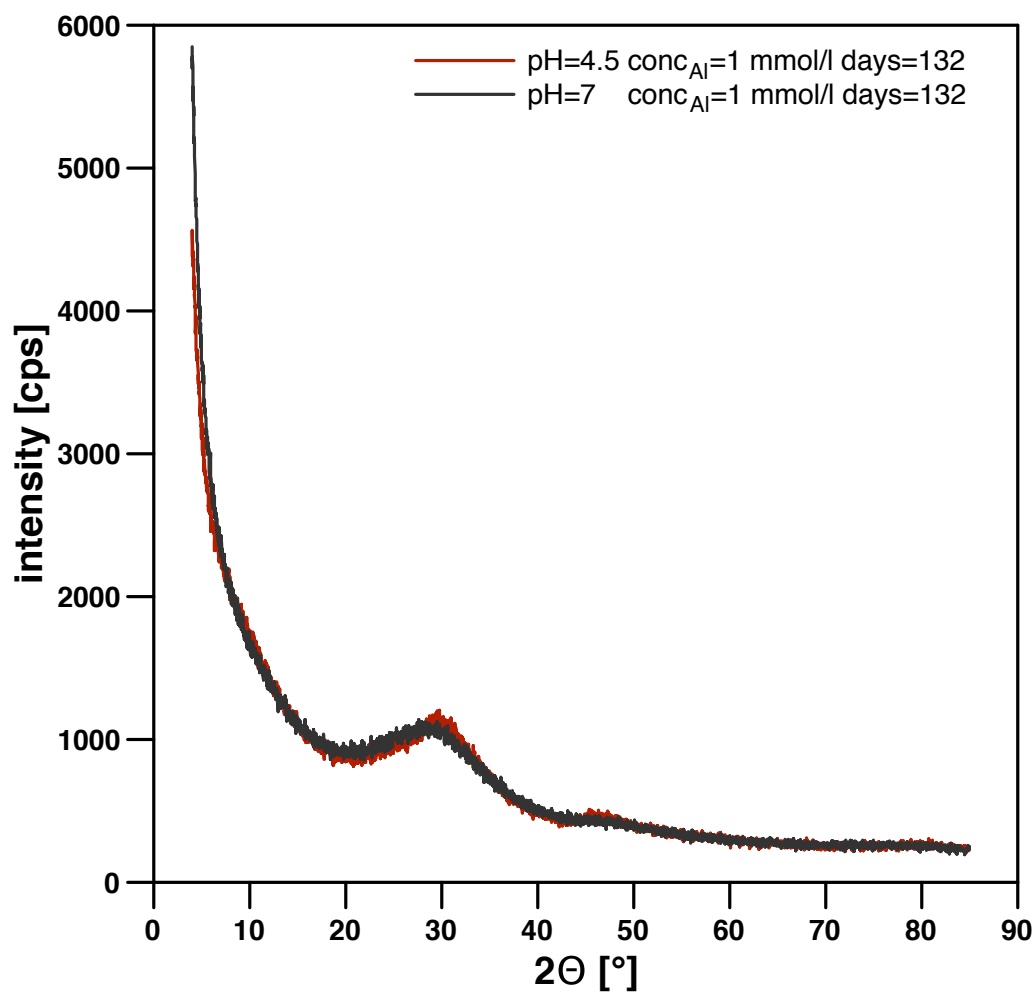
Figure 4.3: XRD patterns (Co-Kα) of the precipitated solid after 132 days in the high-Al experiment at pH=4.5 and pH=7. No sharp peaks can be identified and only a broad amorphous pattern is observed.
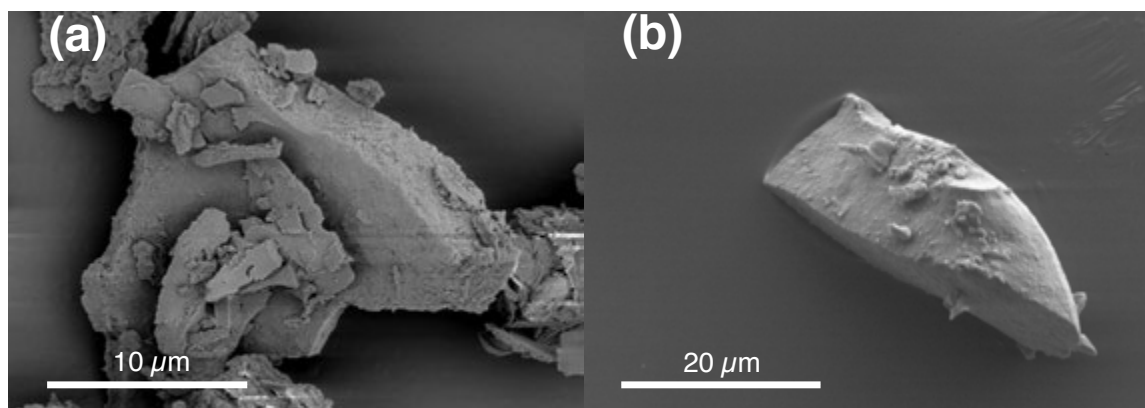
Figure 4.4: SEM images of precipitates (a) low-Al experiment (0.1 mmol/l Al) at pH 7, after 60 days/freeze-thaw cycles; (b) high-Al experiment (1 mmol/l Al) at pH 7, after 1 day/freeze-thaw cycles

For the high-Al experimental series (c) (1 mmol/l Al), a pronounced increase in $\Delta(^{30/28}Si)_{solution}$ is observed during the first 20 days, followed by a decline to almost initial compositions after reaching a peak value (see Figure 4.5). In the high-Al experiment at pH 7, the initial $\Delta(^{30/28}Si)_{solution}$ is 1.30‰, as Al is removed from solution before cyclic freezing even starts (see Figure 4.2 and discussion above), which leads to simultaneous removal of Si and to associated isotope fractionation. With repeated cyclic freeze-thaw, more Si is removed from the solution and the $\Delta(^{30/28}Si)_{solution}$ increases with runtime to a peak value of 2.72‰ after 3 days. After reaching this value the Si isotope signature in the solution declines to a value of $\Delta(^{30/28}Si)_{solution}$ of 0.78‰ after 16 days, increases to values around 1.50‰, and finally stabilizes at this level. The high-Al experiment (1 mmol/l Al) at pH 4.5 shows a similar behavior, except that at this pH no initial Al precipitation occurred (Figure 4.5), resulting in an initial $\Delta(^{30/28}Si)_{solution}$ of 0‰. After 5 days, a peak value of $\Delta(^{30/28}Si)_{solution}$ of 2.42‰ is reached. The $\Delta(^{30/28}Si)_{solution}$ remains then stable for 11 further days. After the 16th cycle or day, the $\Delta(^{30/28}Si)_{solution}$ declines continuously to a value of -0.47‰ at 131 days.

Figure 4.6 shows $\Delta(^{30/28}Si)_{solution}$ vs. the fraction Si remaining in solution $f_{solution}$. The high-Al experimental series (c) (1 mmol/l Al) cannot be explained with either a simple "open-system" or "closed-system" approach (Johnson et al., 2004). Therefore, the apparent Si isotope fractionation factor $\alpha^{30/28}Si_{solid/solution}$ varied during the experimental runtime. Experimental series (a) and (b) are showing no evolution in their $\Delta(^{30/28}Si)_{solution}$ values with time despite Si removal. This implies that the apparent Si isotope fractionation factor during precipitation under these conditions is $\alpha^{30/28}Si_{solid/solution} \approx 1$.
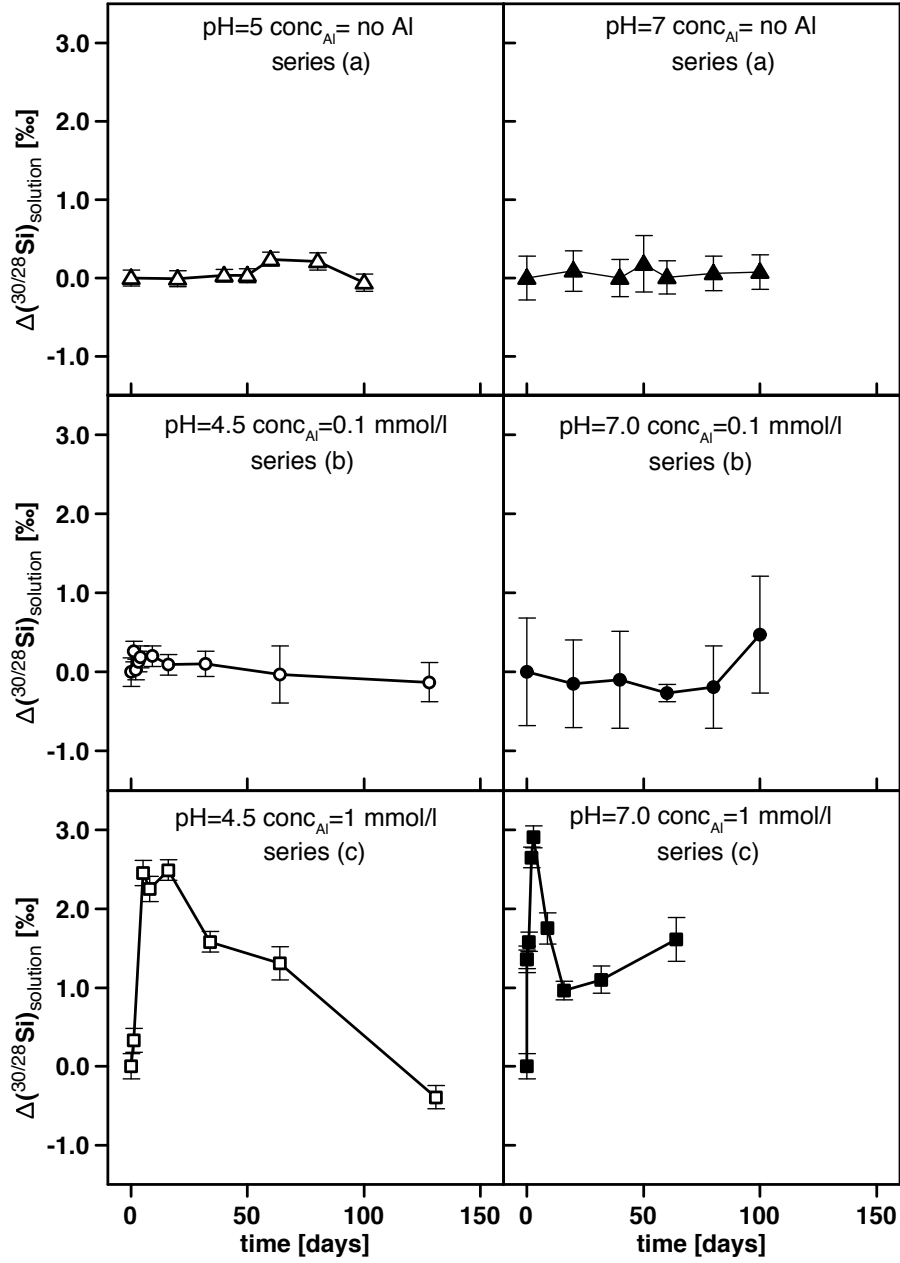
Figure 4.5: $\Delta(^{30/28}Si)_{solution} = \delta(^{30/28}Si)_{solution(t)} - \delta(^{30/28}Si)_{solution(initial)}$ during freeze-thaw experiments. Open symbols depict experiments at pH 4.5 or pH 5 and solid symbols those at pH 7. Triangles represent zero-Al experiments, circles represent low-Al experiments (0.1 mmol/l Al) and squares high-Al experiments (1 mmol/l Al), respectively.
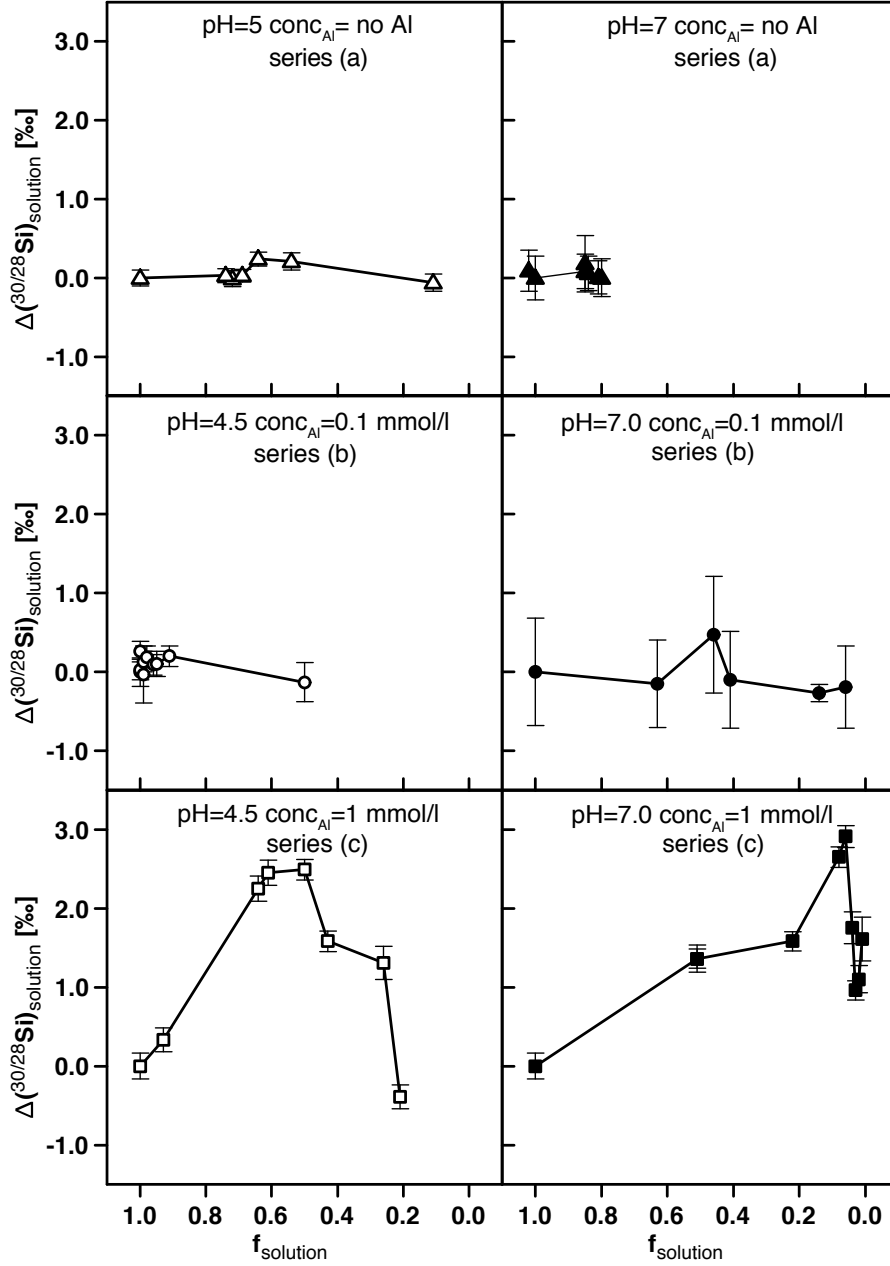
Figure 4.6: $\Delta(^{30/28}Si)_{solution} = \delta(^{30/28}Si)_{solution(t)} - \delta(^{30/28}Si)_{solution(initial)}$ vs. fraction Si remaining in solution ($f_{solution}$). Open symbols depict experiments at pH 4.5 or pH 5 and solid symbols those at pH 7. Triangles represent zero-Al experiments, circles represent low-Al experiments (0.1 mmol/l Al) and squares high-Al experiments (1 mmol/l Al), respectively.

4.6   Discussion

4.6.1   Potential removal processes

During freezing, four main processes govern the removal of Si from solution (Dietzel, 2005): (i) The solubility of Si decreases with decreasing temperature in pure Si-containing solutions (Rimstidt and Barnes, 1980). (ii) During ice formation, the total amount of liquid H_2O decreases and the remaining solution becomes supersaturated with respect to amorphous silica. (iii) Al-hydroxide can precipitate from solution as the solution gets supersaturated with respect to amorphous $Al(OH)_3$ or gibbsite. Dissolved Si can then sorb onto Al-hydroxide particles. As a result hydroxyaluminosilicates (HAS), gel- or allophane-like solids that incorporate both Si and Al can form.

The removal of Si by precipitation of amorphous silica, HAS, gel or allophane-like solids from a solution that contains monosilicic acid involves polymerization of monosilicic acid to polysilicic acid. During this so-called condensation process, the reaction of monosilicic acid molecules forms disilicic acid. Disilicic acid reacts further with monosilicic acid to form trisilicic acid and tetrasilicic acid (Iler, 1979). With ongoing oligomerization cyclic tetramers form and higher orders of polymerized silicic acid, silica colloids, gel and particles form (Greenberg and Sinclair, 1955; Iler, 1979; Tarutani, 1989). In the zero-Al experimental series (a) and the low-Al experimental series (b) the removal of Si from solution is only induced by polymerization of monosilicic acid, which leads to the formation of the solid. In contrast, the removal of Si in experimental series (c) is probably forced by the formation of Al-hydroxides with which monomeric Si can co-precipitate or onto which monosilicic acid will adsorb. As a result HAS phases might form. Precipitation of Al from solution provides $\equiv$Al-OH surface sites which are known to be highly attractive for $Si(OH)_4$ to form Al-O-Si bonds (see Dietzel (2002) and references therein). This process ultimately leads to the formation of crystalline silicate phases such as halloysite or kaolinite (Exley et al., 2002). Therefore the presence of Al (and other ions, see e.g. Marshall and Warakomski (1980); Marshall (1980b,a)) in the system can significantly decrease the solubility of silica (Dixit et al., 2001; Van Cappellen et al., 2002). Hence in precipitation experiments Si removal is usually accelerated by the presence of Al (Willey, 1975a,b; Wada and Kubo, 1975).

We compared the number of adsorption sites available for Si fixation in our high-Al experiments to the amount of Si removed. We therefore compare the amount of Al that is precipitated (0.05 mmol Al) to the precipitated amount of Si (1.2 mmol Si; both values for the high-Al experiment (1m mmol/l Al) pH 4.5, measured after 131 days). Assuming that only monosilicic acid is adsorbed (assumption: 1 mol Al binds 1 mol Si), the amount of Al precipitated is insufficient to fixate all Si removed from solution. We therefore suggest that the high degree of supersaturation attained already during the first freeze-thaw cycles leads to the formation of negatively charged polysilicic acid molecules (see subsection 4.8.2 Figure 4.9). These polysilicic acid molecules have a much higher affinity for Al precipitates surfaces, as shown experimentally (Dietzel and Böhme, 1997; Taylor et al., 1997). Furthermore polysilicic acid molecules form at the surface of Al-hydroxides, which provides an important mechanism to fixate Si onto Al-hydroxides (Jepson et al., 1976; Yokoyama et al., 1982; Dietzel, 2002). Therefore, the adsorption of polysilicic acid can account for the relatively large amount of Si adsorbed/precipitated in our high-Al experiments.

4.6.2   Isotope fractionation associated with Si removal

Our experimental design does not allow us to determine Si removal rates and the isotopic composition under constant conditions. Parameters like temperature, Si saturation index, Si solubility and ionic strength change during freeze-thaw cycles. However, the system does evolve into a state where Si concentration and therefore the net solid formation rate is constant. To illustrate these different stages we next explore the kinetics and their change during a freeze-thaw experiment.

The kinetics of monosilicic acid removal from solution, as observed in our zero- and low-Al series (a) and (b), has been investigated over decades. A range of possible kinetic models have been derived from measurements of the time-dependent decrease of monosilicic acid in solution (see summary in Tobler et al. (2009)). Icopini et al. (2005) suggested that during the formation of di- and trisilicic acid an equilibrium is immediately attained and that further oligomerization of silicic acid is a fast process (Conrad et al., 2007). The ongoing formation from nanocolloidal silica to a solid precipitate in contrast is a slow process (Conrad et al., 2007). Given these previous findings we suggest that for the experimental series (a) and (b) the mechanisms responsible for the potentially entailing isotope fractionation (Si isotope fractionation during the formation of di-, tri and tetrasilicic acid; as no Al is involved) occur rapidly. One possible explanation for the stable Si isotopic composition of the solution despite fast reaction rates in the zero-Al and low-Al experimental series (a) and (b) is that the a net isotope fractionation between the original Si in solution, the polymerized form of silicic acid and the solid that eventually forms is $\alpha^{30/28}Si_{solid/solution} = 1$. During reactions of tetrasilicic acids to higher polymerized silicic acid no further isotope fractionation is expected due to the high mass of these molecules (molecular mass > 120). We therefore suggest that in the absence of Al the rate at which pure Si precipitates are formed does not impact the resulting isotope fractionation.

In contrast to series (a) and (b) a strong initial Si isotope fractionation accompanies Si removal from solution in the high-Al series (c). We tested different kinetic rate laws (zeroth-order, first-order, second-order) for unidirectional precipitation only to explain the evolution of Si concentration with time. Only an irreversible second-order kinetic rate law, assuming a net rate constant, is able to fit the measured evolution of Si concentration with time assuming irreversible precipitation (see subsection 4.8.3). We use the Si isotope results to further evaluate this description whether the governing process of net solid formation is a unidirectional and irreversible precipitation reaction. In this case an open-system type isotope mass balance fractionation model should be applicable (Johnson et al., 2004). For the first freeze-thaw cycles such precipitation results in a reasonable fractionation factor ($\Delta(^{30/28}Si)_{solid-solution} \approx -4.3‰$, subsection 4.8.3). However this mass balance approach fails with ongoing experimental runtime, as unusually large Si isotope fractionation between solid and solution result for the later stages of the experiment ($\Delta(^{30/28}Si)_{solid-solution} \approx +8‰$, subsection 4.8.3). Such large enrichment of heavy ^{30}Si within a solid product has never been observed nor predicted by first principle equilibrium isotope fractionation calculations (Méheut et al., 2007, 2009; Méheut and Schauble, 2014; Opfergelt and Delmelle, 2012). Hence we conclude that solely unidirectional precipitation is not a process in operation in these experiments.

We propose instead that the evolution of dissolved Si is governed by the alternation between precipitation (freezing-stage) and dissolution of the precipitated solid (thawing-stage). We propose further that net precipitation and net dissolution both follow a first-order rate law, as shown for quartz dissolution-precipitation reactions (Dove and Rimstidt (1994); see subsection 4.8.3). An important prerequisite of this model is that the Si

fixated during freezing can dissolve rapidly during thawing. Dietzel (2005) showed that up to 95% of the fixated Si during freezing-thawing experiments is released into solution within 3 days. This release translates into rates of $\approx 1*10^{-10}$ mol*m^{-2}*sec^{-1} (assuming a surface area of hydrated amorphous silica of ≈ 1000 m^2*g^{-1}; Iler (1979)). This rate is much faster than dissolution rates for amorphous silica determined experimentally at constant temperature ($1*10^{-12}$ mol*m^{-2}*sec^{-1} at 20℃; e.g. Icenhower and Dove (2000)). The reason for such high dissolution rates observed in our experiments might be the metastability of the amorphous silica formed or its small particle size, where surface areas might be much higher than the assumed 1000 m^2*g^{-1}.

Using this framework of precipitation and dissolution reactions, results from the high-Al experimental series (c) (1 mmol/l Al) can be described as follows:

(1.) The increase of $\Delta(^{30/28}Si)_{solution}$ during the first 20 days can be attributed to kinetic isotope fractionation during unidirectional attachment of Si onto Al-hydroxides (precipitation dominates over dissolution). As a result, the precipitate is strongly enriched in ^{28}Si (Oelze et al., 2014).

(2.) In the second phase of the experiment, $\Delta(^{30/28}Si)_{solution}$ values return to the initial isotopic composition (close to 0‰ for the experiment at pH 4.5 and close to 1.30‰ for the experiment pH 7). Although the dissolved Si concentrations do not change, solids have to undergo dissolution-reprecipitation cycles for their isotope composition to change.

At the end of the experiments, concentrations are at steady-state. Therefore the $\Delta(^{30/28}Si)_{solution}$ value at the end of the experiment reflects what we call here dynamic steady-state isotope fractionation. It is difficult to attribute this steady-state isotope fractionation to either equilibrium or kinetic effects, as we lack independent estimates of the equilibrium fractionation factor. Theoretical calculations predict that the phase with the higher degree of polymerization should be enriched in ^{30}Si (Ding et al., 1996; Méheut et al., 2007). Further calculations of Méheut et al. (2009), Polyakov and Mineev (2000) and Schauble (2001) show that in a covalent bonding environment heavy isotopes are favored, because they lower the zero-point energy and therefore stronger bonds are formed. Considering these previous studies we expect that at equilibrium either no isotope fractionation or preferential incorporation of heavy Si isotopes into the formed solids occurs. Therefore it seems that our experimental results are consistent with theoretical predictions of isotopic equilibrium, although the system does not reach thermodynamic or isotopic equilibrium.

4.6.3 Rate dependence of Si isotope fractionation

We suggest that both precipitation and dissolution reactions are accompanied by Si isotope fractionation. The change of the net precipitation and net dissolution rates through time, combined with two associated isotope fractionation factors, leads to a change in the bulk fractionation factor due to simple mass balance effects. Figure 4.7 shows how the measured net solid formation rate changes along with the relative isotopic difference between solid and solution.

It is possible that a change in surface area of the solids influences the apparent fractionation factor, as it will affect the exchange flux. Unfortunately the determination of the actual surface area of the formed reactive solids is virtually impossible, as the area will be altered once the solids are removed from the ambient solution.

Regardless of this effect, we can infer that the isotopic difference between solid and solution $\Delta(^{30/28}Si)_{solid-solution}$ changes with time from a kinetically dominated regime at high net

solid formation rates, where light Si isotopes are rapidly withdrawn from the solution into the solid, to a dynamic steady-state regime, where the Si concentration is nearly constant between cycles. In this regime the isotopic difference between solid and solution, compared to the kinetic regime, is very small. We show a model of this evolution in Figure 4.7 for the high-Al experiment at pH 4.5 (1 mmol/l Al) (see Model 3 in subsection 4.8.3). We model continuous precipitation and dissolution assuming two opposing first-order reactions, which are associated with respective isotope fractionation factors $\alpha^{30/28} Si_{prec}$ and $\alpha^{30/28} Si_{diss}$. We find that for the high Al experiments the most likely case is one where the major part of the formed solid redissolves and exchanges with the solution at each cycle. The best fit values of the developed isotope mass balance model (see Figure 4.11 in the subsection 4.8.3) yields isotope fractionation factors for precipitation and dissolution of $\alpha^{30/28} Si_{prec}$ =0.9953 ($10^3 ln\alpha_{prec}$ = -4.7‰) and $\alpha^{30/28} Si_{diss}$ =0.9947 ($10^3 ln\alpha_{diss}$ = -5.3‰) for the experiment at pH 4.5 and $\alpha^{30/28} Si_{prec}$ =0.9989 to 0.9991 ($10^3 ln\alpha_{prec}$ = -1.1 to -0.9‰) and $\alpha^{30/28} Si_{diss}$ =0.9992 to 0.9994 ($10^3 ln\alpha_{diss}$ = -0.8 to -0.6‰) for the experiment at pH 7, respectively.

The initial kinetic isotope fractionation factor, where net-precipitation dominates, is likely governed by chemisorption processes. These values are similar to the fractionation factors found in the Oelze et al. (2014) adsorption experiments (-1.8‰ to -3‰, depending on Si concentration). This initial Si isotope fractionation factor, probably reaches the kinetic limit of Si isotope fractionation (Nielsen et al., 2012; Druhan et al., 2013). Therefore it might represent the absolute maximum kinetic Si isotope fractionation factor for Si during precipitation. Above this kinetic limit an increase of the precipitation rate is not accompanied by a further increase in the isotope fractionation factor (see Figure 8 in Nielsen et al. (2012)).

In the zero-Al and low-Al experimental series (a) and (b), the initial phase involving kinetic isotope fractionation is not encountered, and the system evolves with an apparent isotope fractionation factor of $\alpha^{30/28} Si_{solid/solution}$ =1 ($10^3 ln\alpha_{solid/solution}$ = 0‰). In all high-Al experiments, towards the end the Si isotope fractionation at steady-state is also close to $\alpha^{30/28} Si_{solid/solution}$ =1 ($10^3 ln\alpha_{solid/solution}$ = 0‰).
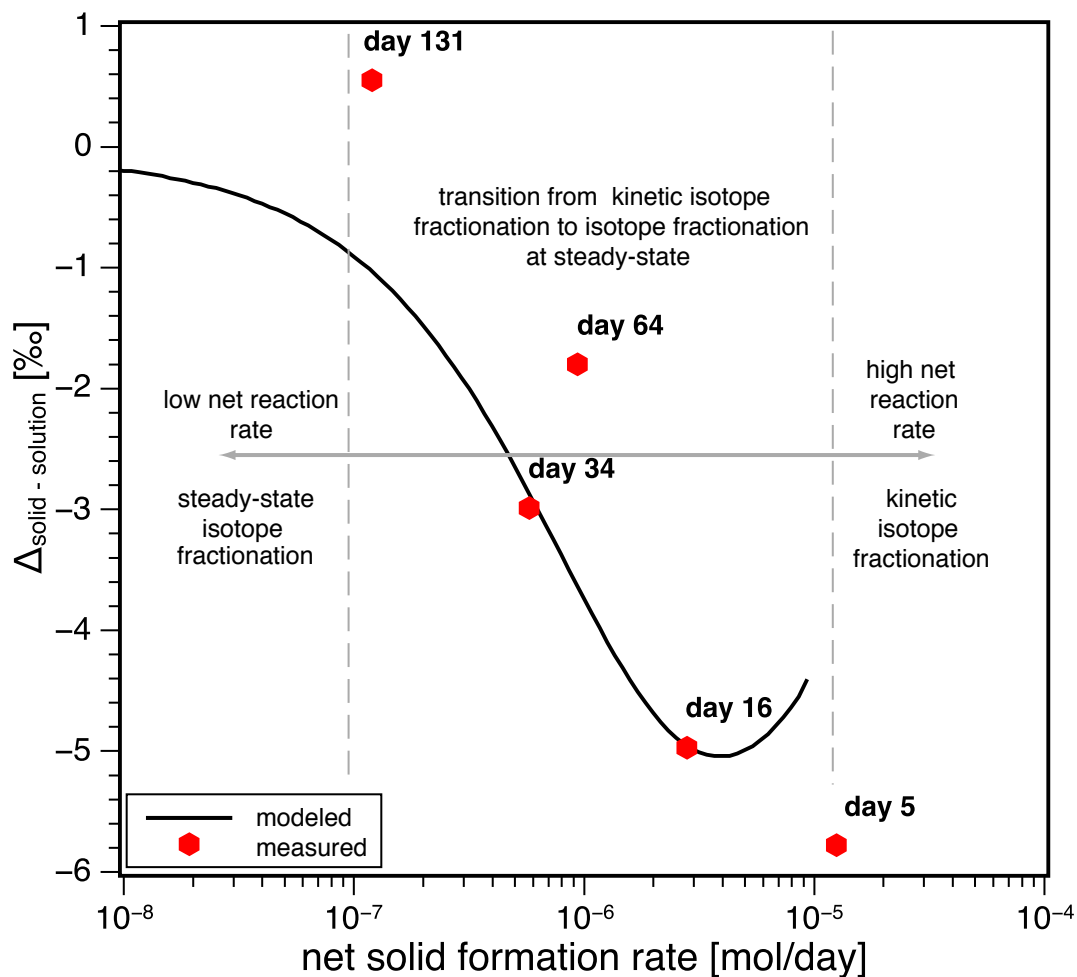
Figure 4.7: Isotopic difference between solid and solution $\Delta_{solid-solution}$ vs. net solid formation rate. The symbols show the measured $\Delta_{solid-solution}$ at the associated net solid formation rate, calculated from the amounts of Si in the solution and the solid, respectively. The black curve shows a mass balance model of the high-Al freeze-thaw experiment (1 mmol/l, series (c)) at pH 4.5, see Appendix Section 4.8.3; Model 3 calculated from Equation 4.7. The early stages of the experiment are dominated by kinetic isotope fractionation, whereas the second stage records isotope fractionation at steady-state with $\Delta_{solid-solution} \cong 0$.

4.7 Summary and implications

We have demonstrated that, during cyclic freeze-thaw of dissolved Si-containing solutions, Si is removed from the solution. In the absence of appreciable amounts of Al this removal is not accompanied by the fractionation of Si isotopes. The formation of di-, tri- and tetrasilicic acid apparently proceeds with a Si isotope fractionation factor $\alpha^{30/28}Si_{solid/solution}$ =1 ($10^3 ln\alpha_{solid/solution}$ = 0‰). With subsequent oligomerization and formation of almost pure Si solids no further Si isotope fractionation is expected due to the high molecular masses involved. To conclude, the precipitation of pure Si solids does not lead to any Si isotope fractionation.

In contrast if Al is present in these solutions at high concentrations (i.e. here 1 mmol/l), Si removal is faster and accompanied by strong Si isotope fractionation favoring the light isotopes in the solids. For these high Al experiments we calculate a fractionation factor of up to $\alpha^{30/28}Si_{solid/solution}$ =0.9950 ($10^3 ln\alpha_{solid/solution}$ = -5‰) for the first 20 days of the experiment . This strong initial isotope fractionation occurs during adsorption or binding of Si onto Al-hydroxide (Oelze et al., 2014). With ongoing runtime the early formed precipitates are reorganized wholesale, such that $\alpha^{30/28}Si_{solid/solution}$ =1 ($10^3 ln\alpha_{solid/solution}$ = 0‰). Hence after attaining steady-state conditions no Si isotope fractionation during solid reorganization occurs. It is likely that the zero fractionation factor observed in the final phase of the high-Al experimental series (c) and in the low- and zero-Al experiments represents the equilibrium isotope fractionation factor of silica precipitation.

Regarding silicate weathering this study implies that where secondary precipitates (such as metastable silica-containing solids) are formed, kinetic isotope effects will be dominating. Secondary minerals formed with high Al/Si ratios, will be enriched in [28]Si (see Savage et al. (2013); Cornelis et al. (2014)). This conclusion is supported by the observation that Si measured in river water is enriched in [30]Si over the host rock (e.g. Ziegler et al. (2005b); Georg et al. (2006a); Opfergelt et al. (2009); Bern et al. (2010); Steinhoefel et al. (2011), while secondary soil minerals are mostly depleted in [30]Si. Moreover, this study suggests that slowly re-organization or recrystallization of these solids is likely accompanied by negligible Si isotope fractionation.

During silicification of sediments a variety of isotope fractionation factors are likely to be in operation, depending on individual environmental conditions. If solutions are supersaturated with respect to opal-A or opal-CT and free of "impurities" (no Al or other carrier phases present) they will probably precipitate with an Si isotope fractionation factor of $\alpha^{30/28}Si_{solid/solution}$ =1 ($10^3 ln\alpha^{30/28}Si_{solid/solution}$ of 0‰). In contrast, the presence of Al in the system increases the precipitation rate (Wada and Kubo, 1975; Willey, 1975b) and therefore Si isotopes will fractionate according to the Al/Si ratio. The difference between the rapidly precipitating Al-containing phase compared to the slowly precipitating Al-free phase is then reflected in the Si isotope composition of these two phases, with the higher enrichment of [28]Si in the Al-containing phase.

The inferred absence of any $\alpha^{30/28}Si_{solid/solution}$ >1 ($10^3 ln\alpha^{30/28}Si_{solid/solution}$ > 0‰) between solid and solution implies that in the geologic record Si isotope ratios exceeding that of their source materials are likely to be a mass balance effect stemming from fast precipitation of solids enriched in light Si isotope.

To conclude, the enrichment of light Si isotopes in geologic low-temperature processes is related to fast precipitation of secondary solids as induced by co-precipitation of Al phases or another carrier phase (e.g. Fe(III)). In contrast no Si isotope fractionation can be expected between solid and solution during slow precipitation under equilibrium

conditions.

4.8 Appendix Chapter 4

4.8.1 Tables

Table 4.1: Freeze-thaw experiments series (a), Si concentration values and $\delta(^{29/28}Si)_{NBS28}$ and $\delta(^{30/28}Si)_{NBS28}$ values as well as 95% confidence interval (CI) for experiments with no Al.

name	pH	sampling time [day]	Al [mmol/l]	Si [ppm]	$\delta(^{29/28}Si)$ [‰]	CI [‰]	$\delta(^{30/28}Si)$ [‰]	CI [‰]
5_0_0_s	5.0	0	-	1.77	0.01	0.07	-0.04	0.07
5_20_0_s	5.0	20	-	1.28	-0.02	0.12	-0.05	0.07
5_40_0_s	5.0	40	-	1.22	0.01	0.04	-0.01	0.02
5_50_0_s	5.0	50	-	1.30	0.03	0.04	-0.01	0.05
5_60_0_s	5.0	60	-	1.13	0.08	0.01	0.20	0.06
5_80_0_s	5.0	80	-	0.95	0.08	0.07	0.17	0.08
5_100_0_s	5.0	100	-	0.20	-0.01	0.10	-0.10	0.08
7_0_0_s	7.0	0	-	1.75	0.00	0.06	-0.13	0.20
7_20_0_s	7.0	20	-	1.79	-0.01	0.03	-0.04	0.17
7_40_0_s	7.0	40	-	1.40	-0.08	0.05	-0.13	0.14
7_50_0_s	7.0	50	-	1.50	0.01	0.07	0.05	0.31
7_60_0_s	7.0	60	-	1.41	-0.07	0.06	-0.12	0.08
7_80_0_s	7.0	80	-	1.46	-0.05	0.07	-0.08	0.11
7_100_0_s	7.0	100	-	1.49	-0.06	0.12	-0.05	0.09

[*] sample names: (pH)_(day)_(Al-start-conc[mmol/l])_(solution[s]

Table 4.2: Freeze-thaw experiments series (b), Si concentration values and $\delta(^{29/28}Si)_{NBS28}$ and $\delta(^{30/28}Si)_{NBS28}$ values as well as 95% confidence interval (CI) for experiments with 0.1 mmol/l initial Al concentration.

name	pH	sampling time [day]	Al [mmol/l]	Si [ppm]	$\delta(^{29/28}Si)$ [‰]	CI [‰]	$\delta(^{30/28}Si)$ [‰]	CI [‰]
4.5_start_0.1_s	4.5	start	0.08	1.42	-0.05	0.02	-0.12	0.13
4.5_1_0.1_s	4.5	1	0.09	1.42	-0.01	0.07	0.14	0.02
4.5_2_0.1_s	4.5	2	0.09	1.42	0.00	0.24	-0.09	0.03
4.5_3_0.1_s	4.5	3	0.08	1.40	0.00	0.04	0.02	0.03
4.5_4_0.1_s	4.5	4	0.08	1.39	0.05	0.00	0.07	0.05
4.5_9_0.1_s	4.5	9	0.05	1.29	0.05	0.08	0.09	0.04
4.5_16_0.1_s	4.5	16	0.08	1.36	0.00	0.05	-0.03	0.05
4.5_32_0.1_s	4.5	32	0.10	1.35	0.01	0.04	-0.02	0.09
4.5_64_0.1_s	4.5	64	0.10	1.40	-0.05	0.13	-0.14	0.34
4.5_128_0.1_s	4.5	128	0.06	0.71	-0.12	0.13	-0.24	0.21
7_0_0.1_s	7.0	0	0.10	1.71	0.04	0.78	0.03	0.67
7_20_0.1_s	7.0	20	0.02	1.08	-0.19	0.26	-0.12	0.54
7_40_0.1_s	7.0	40	0.01	0.71	-0.27	1.14	-0.08	0.60
7_60_0.1_s	7.0	60	0.02	0.24	-0.05	1.22	-0.25	0.01
7_80_0.1_s	7.0	80	0.00	0.10	-0.18	0.88	-0.16	0.50
7_100_0.1_s	7.0	100	0.01	0.79	0.19	0.06	0.50	0.74

[*] sample names: (pH)_(day)_(Al-start-conc[mmol/l])_(solution[s])

Table 4.3: Freeze-thaw experiments series (c), Si concentration values and $\delta(^{29/28}Si)_{NBS28}$ and $\delta(^{30/28}Si)_{NBS28}$ values as well as 95% confidence interval (CI) for experiments with 1 mmol/l initial Al concentration.

name[*]	pH	sampling time [day]	Al [mmol/l]	Si [ppm]	$\delta(^{29/28}Si)$ [‰]	CI [‰]	$\delta(^{30/28}Si)$ [‰]	CI [‰]
4.5_start_1_s	4.5	start	1.02	1.59	-0.11	0.26	-0.08	0.11
4.5_1_1_s	4.5	1	0.90	1.47	0.14	0.13	0.25	0.10
4.5_5_1_s	4.5	5	0.56	0.98	1.16	0.11	2.37	0.11
4.5_8_1_s	4.5	8	0.62	1.02	1.14	0.15	2.17	0.11
4.5_16_1_s	4.5	16	0.51	0.79	1.22	0.12	2.41	0.07
4.5_34_1_s	4.5	34	0.56	0.69	0.80	0.16	1.50	0.07
4.5_64_1_s	4.5	64	0.48	0.41	0.71	0.29	1.23	0.18
4.5_131_1_s	4.5	131	0.49	0.33	-0.25	0.05	-0.47	0.09
4.5_start_1_p	4.5	start	-	-	-	-	-	-
4.5_1_1_p	4.5	1	-	-	-	-	-	-
4.5_5_1_p	4.5	5	-	-	-1.54	0.41	-3.41	0.24
4.5_8_1_p	4.5	8	-	-	-1.58	0.32	-3.06	0.17
4.5_16_1_p	4.5	16	-	-	-1.18	0.40	-2.56	0.17
4.5_34_1_p	4.5	34	-	-	-0.77	0.47	-1.48	0.21
4.5_64_1_p	4.5	64	-	-	-0.26	0.19	-0.57	0.22
4.5_131_1_p	4.5	131	-	-	0.04	0.19	0.08	0.09
7_0_1_s	7.0	0	0.00	0.72	0.65	0.04	1.28	0.04
7_1_1_s	7.0	1	0.01	0.31	0.76	0.03	1.50	0.05
7_2_1_s	7.0	2	0.00	0.11	1.33	0.02	2.57	0.06
7_3_1_s	7.0	3	0.00	0.09	1.47	0.03	2.83	0.08
7_4_1_s	7.0	4	0.02	0.29	0.21	0.02	0.41	0.04
7_9_1_s	7.0	9	0.00	0.05	0.88	0.06	1.67	0.16
7_16_1_s	7.0	16	0.00	0.05	0.51	0.05	0.88	0.04
7_32_1_s	7.0	32	0.00	0.03	0.60	0.08	1.02	0.13
7_64_1_s	7.0	64	0.00	0.02	0.86	0.43	1.53	0.25
7_128_1_s	7.0	128	-	0.01				

[*] sample names: (pH)_(day)_(Al-start-conc[mmol/l])_(solution[s]-or-precipitate[p]

4.8.2 Determination of mono-and polysilicic acid using the β-silicomolybdate method

We verified that the Si stock solution contains only monomeric silicic acid by using the β-silicomolybdate method (described in detail by Iler (1982) and Dietzel (2000)). This method is based on the reaction of molybdate with dissolved Si to a yellow colored β-silicomolybdate aquocomplex, detected at 390 nm by spectrometry for 10 min (UV-VIS Cary 100, Varian). The reaction rate constant, k, for the unidirectional reaction of molybdate with dissolved silica, obtained by fitting a second-order reaction, is 2.1 $\pm$0.2 min^{-1} for the prepared solution. This measured range of k values clearly indicates that only monomeric silicic acid, Si(OH)$_4$, is present in solution as polymeric silica induces k values of 0.9, 0.4 and up to 0.030 min^{-1} for dimeric and octameric silica and for silica colloids with about 40 silicon atoms in its structure, respectively (e.g. Iler (1979)).
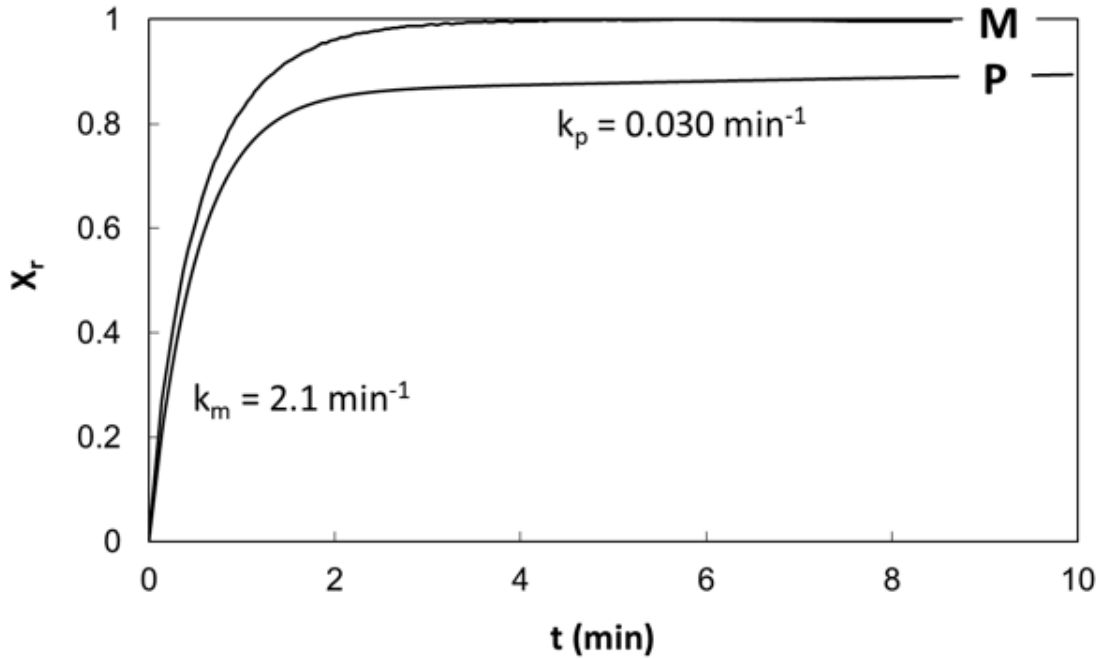
Figure 4.8: Evolution of the β-silicomolybdate complex formation in the reaction of molybdate with dissolved Si. t: reaction time of the measurement, X$_r$: molar fraction of total dissolved Si that has reacted to the silicomolybdate complex (see Dietzel, 2000 for details), M: monosilicic acid stock solution, P: solution containing both monosilicic (86%) and polysilicic acid (14%) (soil solution from Wonisch et al., 2008). Polysilicic acid was not detected in our experimental initial solutions (evolution according to curve M); k$_m$ and k$_p$ denote the reaction rate constant for the reaction of monosilicic and polysilicic acid to the β-complex, respectively.

We also determined the degree of polymerization of some experimental solutions after certain freeze-thaw cycles. The supersaturation during freezing leads to the formation of polysilicic acid even after 1 freeze-thaw cycle. The results are shown in Figure 4.9.
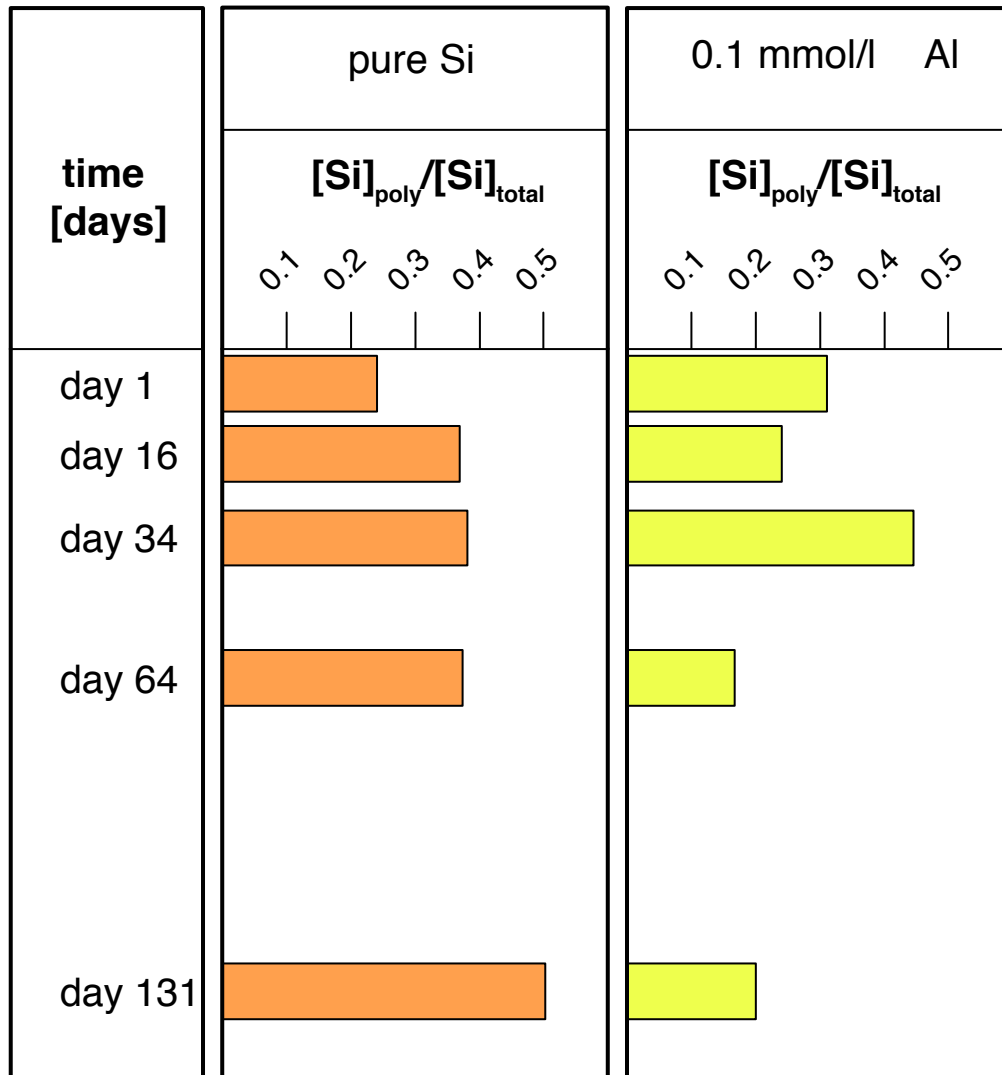
Figure 4.9: Degree of polymerization of dissolved silicic acid expressed as the ratio of Si concentration of polysilicic acid ($[Si]_{poly}$) to the total amount of dissolved Si ($[Si]_{total}$) with and without Al at acidic conditions. The high degree of supersaturation during freezing stages leads to the formation of polysilicic acid already after one freeze-thaw cycle.

4.8.3   Modeling a net precipitation-dissolution process associated with isotope fractionation

The aim of this modeling approach is not to determine exact rates or rate constants for attachment or detachment of Si. Determining rate constants would require that conditions (temperature, degree of under- and oversaturation, etc.) and solid properties (surface area) were constant during our experiments. This is not the case here. We rather intend to narrow the range of possible parameters that potentially explain the observed isotopic evolution of Si during our experiments. In order to test whether the experimental kinetics of the freezing-thawing approach can be described as two opposing first-order reactions for net precipitation and net dissolution, we tested several different kinetic rate models (zeroth-order, first-order, second-order, etc.) for the high-Al experiments. The net reaction rate constants used represent parameters that integrate over the changing conditions during the experiments.

First we modeled the evolution of Si concentration. A pure precipitation mechanism following a kinetic rate law of zeroth-order can be dismissed, as the evolution of Si concentration with time clearly shows no linear dependence (see Figure 4.10). A pure precipitation mechanism following a first-order kinetic rate law (Equation 4.4) can neither be reconciled with the measured Si concentration data for a best fit through the measured data (see Figure 4.10 Model A) nor when we force the model to fit the Si concentration at t=131 days (see Figure 4.10 Model B).

$$\frac{d}{dt}(M_d) = F_{prec} = -p \times M_d \tag{4.4}$$

Where M_d is the mass of dissolved Si in the experiment, F_{prec} is the net precipitation of Si and p is the rate constant.

Assuming a second-order kinetic rate law (Equation 4.5) results in a reasonable fit to the measured Si concentration data (see Model C in Figure 4.10).

$$\frac{d}{dt}(M_d) = F_{prec} = -p \times M_d^2 \tag{4.5}$$

We next explored whether this second-order precipitation model is compatible with the measured isotope ratios. Unidirectional precipitation without back reaction can be quantified with an open-system mass balance model (Johnson et al., 2004). For the high-Al experiment (1mmol/l Al) at pH 4.5, the open-system model was applied incrementally from sampling point to sampling point. The initial Si concentration and initial isotope composition $\delta(^{30/28}Si)_{initial}$ in solution were those of the previous step. This mass balance calculation shows that the isotope fractionation factors change with each time-step. These isotope fractionation factors $10^3 ln\alpha_{solid/solution}$ are: day0-1: -4.3‰, day1-5: -5.2‰, day8-16: -1.0‰, day16-34: 6.4‰, day34-64: 0.5‰, day64-131: 7.8‰). Isotope fractionation factors for Si as high as 7.8‰ calculated for the final steps have never been observed for Si isotope, and are regarded as highly unlikely. We therefore conclude that unidirectional precipitation is not a feasible mechanism to explain the observed Si isotopic evolution.

Therefore we assume that two opposing reactions are in operation, and model these with a first-order kinetic rate law for precipitation and a first-order kinetic rate law for dissolution. In the mass balance equation (Equation 4.6), M_d is the total mass of Si dissolved
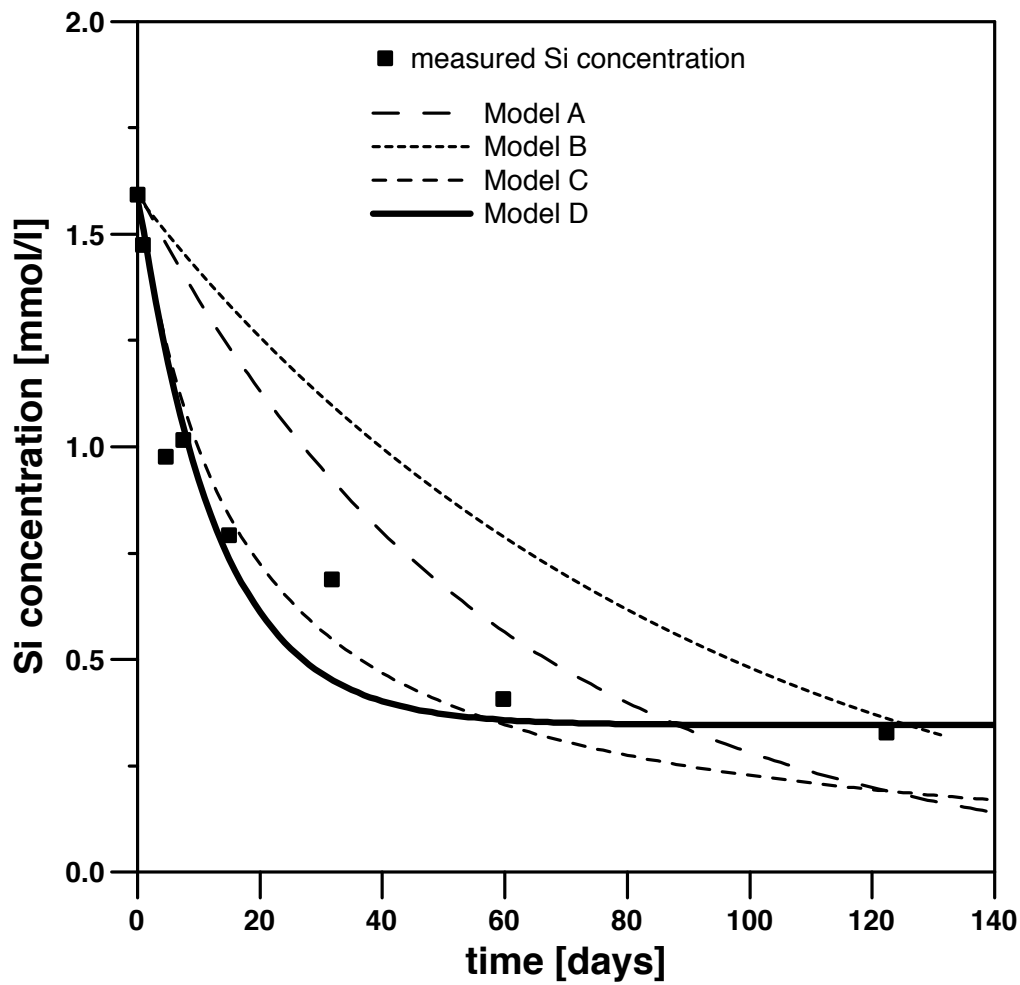
Figure 4.10: Model fits using different kinetic rate laws of Si solution concentrations in our high-Al experiments (1 mmol/l al) at pH 4.5. Model A: first-order kinetic rate law for precipitation only, best fit to all measured data; Model B: first-order kinetic rate law for precipitation only, model forced through the Si concentration at t=131 days; Model C: second-order kinetic rate law for precipitation only, best fit to all measured data; Model D: first-order kinetic rate law for precipitation and a first-order kinetic rate law for dissolution, best fit to all measured data.

in solution, M_s is the total mass of Si solid and p and d are net reaction rate constants, p for precipitation and d for dissolution, respectively.

$$\frac{d}{dt}(M_d) = F_{diss} - F_{prec} = d \times M_s - p \times M_d \tag{4.6}$$

Assuming that the dissolved Si concentration at the end of the experiments reflects the steady-state concentration, we can use the steady-state ratio $(M_d/M_s)_{steady-state})$ which equals the d/p ratio (Table 4.4), Which reduces the number of adjustable parameters to one.

$$d = p \times \left(\frac{M_d}{M_s}\right)_{steady-state} \tag{4.7}$$

The evolution of M_d (and hence of dissolved Si concentration) was then numerically modeled and fitted to the measured data according to Equation 4.8, using $M_s = M_{total} - M_d$ with M_{total} being the total mass of Si to determine a value for p (Table 4.4).

$$\frac{d}{dt}(M_d) = p \times \left(\frac{M_d}{M_s}\right)_{steady-state} \times (M_{total} - M_d) - p \times M_d \tag{4.8}$$

This assumption yields a reasonable fit to the measured Si concentration data (see Model D in Figure 4.10).

Next we develop an isotope mass balance model based on these simultaneous first-order kinetic rate laws for precipitation as well as for dissolution. The basic approach is the same for all scenarios explored. First, the evolution of dissolved Si concentration was modeled by using simple first-order irreversible kinetic descriptions of precipitation as well as for dissolution (Equation 4.6). The evolution of the Si isotopic signature was modeled as follows:

$$\frac{d}{dt}(M_d\delta_d) = F_{last} \times (\delta_l + \Delta_{diss}) + F_{cumulative} \times (\delta_c + \Delta_{diss})$$
$$- F_{prec} \times (\delta_d + \Delta_{prec}) \tag{4.9}$$

where Δ_{diss} ($\Delta_{diss} \approx 10^3 ln\alpha_{diss}$) is the kinetic isotope fractionation factor during dissolution and Δ_{prec} ($\Delta_{prec} \approx 10^3 ln\alpha_{prec}$) is the kinetic isotope fractionation factor during precipitation. Here, the solid dissolution flux F_{diss} (Equation 4.4) has been separated into two components: the mass supplied by the outermost layer that precipitated at the previous step F_{last} and the mass from the cumulative solid $F_{cumulative}$ (formed since the beginning of the experiment). Therefore we also make a distinction between the isotopic signature of the outermost ("last") layer δ_l and the isotopic signature of the cumulative solid δ_c. The use of Equation 4.9 allows us to treat the solid as zoned or unzoned. To simplify Equation 4.9 we assume that the end of the experiments represents steady-state. Equation 4.9 dictates that at steady-state $(\delta_s - \delta_d)_{steady-state} = \Delta_{prec} - \Delta_{diss}$, regardless of the value of F_{diss} vs. $F_{cumulative}$. Therefore we constrain the difference $\Delta_{prec} - \Delta_{diss}$ from the isotope data obtained at the end of our experiment (Table 4.4). We calculate the relative contribution of the cumulative solid $f_{cumulative}$ to the total dissolution as:

$$f_{cumulative} = F_{cumulative}/(F_{last} + F_{cumulative}) \qquad (4.10)$$

We then model the measured δ_d values numerically, by using p, d (as previously determined from Si concentrations), and measured $\delta_s - \delta_d$ values from Table 4.4 and put them into Equation 4.9. By using these values we fit the model (Equation 4.9) to the transient part of the experimental data by varying Δ_{prec} (hence Δ_{diss}). We repeat the above procedure by incrementally modeling the solid from being isotopically homogeneous ($f_{cumulative} = 1$) to being fully zoned ($f_{cumulative} = 0$). For each of these calculations, we obtain a pair of Δ_{prec} and Δ_{diss} values which is fitted to the measured isotopic evolution of dissolved Si. In particular we show here the results of the four following models:

Model I and II assume no Si isotope fractionation during dissolution, whereas Model III and IV assume Si isotope fractionation during dissolution. Model I assumes that the solid has a uniform isotopic composition ($f_{cumulative} = 1$), whereas Model II assumes that the isotopic composition of the last precipitated layer reflects the isotopic evolution of the solution with time ($f_{cumulative} = 0$). Hence in this model the solids are assumed to be isotopically zoned and dissolution only redissolves the last precipitated layer. Models III (solid has a uniform isotopic composition) and IV (solid is isotopically zoned) are identical to models I to II, but they further assume that Si isotope fractionation occurs also during solid dissolution. The results of these models are shown for the high-Al experiments in Figures 4.11 for the experiment at pH 4.5 and in Figure 4.12 for the experiment at pH 7.

Table 4.4: Summary of modeling parameters $(M_s/M_d)_{steady-state}$, p, d and $(\delta_s - \delta_d)_{steady-state}$ used in Equation 4.4 and Equation 4.7

	$(M_d/M_s)_{steady-state}$	p [day^{-1}]	d [day^{-1}]	$(\delta_s - \delta_d)_{steady-state}$ [‰]
pH4.5/27 ppm Al	0.28	0.06	0.02	0.55
pH7/27 ppm Al	0.02	0.57	0.01	-0.26

For the high-Al experiment (1 mmol/l) at pH 4.5 we find the best fit for an isotopically homogeneous solid ($f_{cumulative} = 1$) with Si isotope fractionation factors of $\alpha^{30/28}Si_{prec} = 0.9953$ ($10^3 ln\alpha_{prec}$ = -4.7‰) and $\alpha^{30/28}Si_{diss} = 0.9947$ ($10^3 ln\alpha_{diss}$ = -5.3‰) .

For the high-Al experiment (1 mmol/l Al) at pH 7 the best fit were obtained either by assuming an isotopically homogeneous solid ($f_{cumulative} = 1$) or a solid comprising a mixture between an isotopically homogeneous solid and the last precipitated layer ($f_{cumulative} = 0.9$ to $f_{cumulative} = 0.5$). All models yielded similar Si isotope fractionation factors of $\alpha^{30/28}Si_{prec} = 0.9989$ to 0.9991 ($10^3 ln\alpha_{prec}$ = -1.1 to -0.9‰) and $\alpha^{30/28}Si_{diss} = 0.9992$ to 0.9994 ($10^3 ln\alpha_{diss}$ = -0.8 to -0.6‰).

The results for both high-Al experiments at pH 4.5 and at pH 7 are:

a) Isotope fractionation during precipitation only (Δ_{prec}) is not the sole cause, as models I to II fail to explain the data, regardless of whether the solid is treated as homogeneous or zoned. In these cases the solution would evolve towards a steady state characterized by high $\Delta(^{30/28}Si)_{solution}$ values, which cannot be reconciled with the data.

b) For the experiment at pH 4.5, only model III assuming two independent fractionation factors, Δ_{prec} during forward reaction and Δ_{diss} during the backward reaction and further assuming an isotopically homogeneous solid ($f_{cumulative} = 1$), yield a reasonable fit to the data.

c) For the experiment at pH 7, models between $f_{cumulative} = 1$ and $f_{cumulative} = 0.5$ assuming two independent fractionation factors, Δ_{prec} during forward reaction and Δ_{diss} during the backward reaction yield reasonable fits to the data.

c) The models in which only the outermost layer of zoned solids is dissolved (Model II and Model IV) do not yield results that can be reconciled with the data, even when applying two different fractionation factors (Δ_{prec} & Δ_{diss}).

It follows that the major part, or even the entire solid is homogenized during the course of the experiment, presumably due to redissolution. In Tables 4.5 and 4.6, the best-fit values for the described models I to VI for the high Al experiments are presented.

To conclude, for the high Al experiments the major part of the formed solid is redissolved and exchanges with the solution. The best fit values of the isotope fractionation factors associated with precipitation are similar to those of dissolution and are $\alpha^{30/28}Si_{prec} = 0.9953$ ($10^3 ln\alpha_{prec} = -4.7‰$) and $\alpha^{30/28}Si_{diss} = 0.9947$ ($10^3 ln\alpha_{diss} = -5.3‰$) for the experiment at pH=4.5 and $\alpha^{30/28}Si_{prec} = 0.9989$ to 0.9991 ($10^3 ln\alpha_{prec} = -1.1$ to $-0.9‰$) and $\alpha^{30/28}Si_{diss} = 0.9992$ to 0.9994 ($10^3 ln\alpha_{diss} = -0.8$ to $-0.6‰$) for the experiment at pH=7.

Table 4.5: Best fit values of Equation 4.9 for the modeled curves in Figure 4.11 for the high-Al experiment (1 mmol/l Al) at pH 4.5.

	Δ_{prec} [‰]	Δ_{diss} [‰]	$f_{cumulative}$	f_{last}	RMSD[a]
Model I	-1.9	0.00	1.0	0.0	1.2
Model II	-1.1	0.00	0.0	1.0	1.4
Model III	-4.7	-5.3	1.0	0.0	0.7
Model IV	0.5	0.0	0.0	1.0	2.0

[a]root-mean-square deviation (RMSD) where y is the regression dependent variable, $\hat{y}$ is the predicted variable and n is the number of predictions; is calculated as follow:

$$RMSD = \sqrt{\frac{\sum_{t=1}^{n}(y_t - \hat{y}_t)^2}{n}}$$

Table 4.6: Best fit values of Equation 4.9 for the modeled curves in Figure 4.12 for the high-Al experiment (1 mmol/l Al) at pH 7.

	Δ_{prec} [‰]	Δ_{diss} [‰]	$f_{cumulative}$	f_{last}	RMSD[a]
Model I	-0.5	0.0	1.0	0.0	0.6
Model II	-0.2	0.0	0.0	1.0	0.75
Model III	-1.1	-0.8	1.0	0.0	0.3
Model IV	-0.3	0.0	0.0	1.0	0.7

[a]root-mean-square deviation (RMSD) where y is the regression dependent variable, $\hat{y}$ is the predicted variable and n is the number of predictions; is calculated as follow:

$$RMSD = \sqrt{\frac{\sum_{t=1}^{n}(y_t - \hat{y}_t)^2}{n}}$$
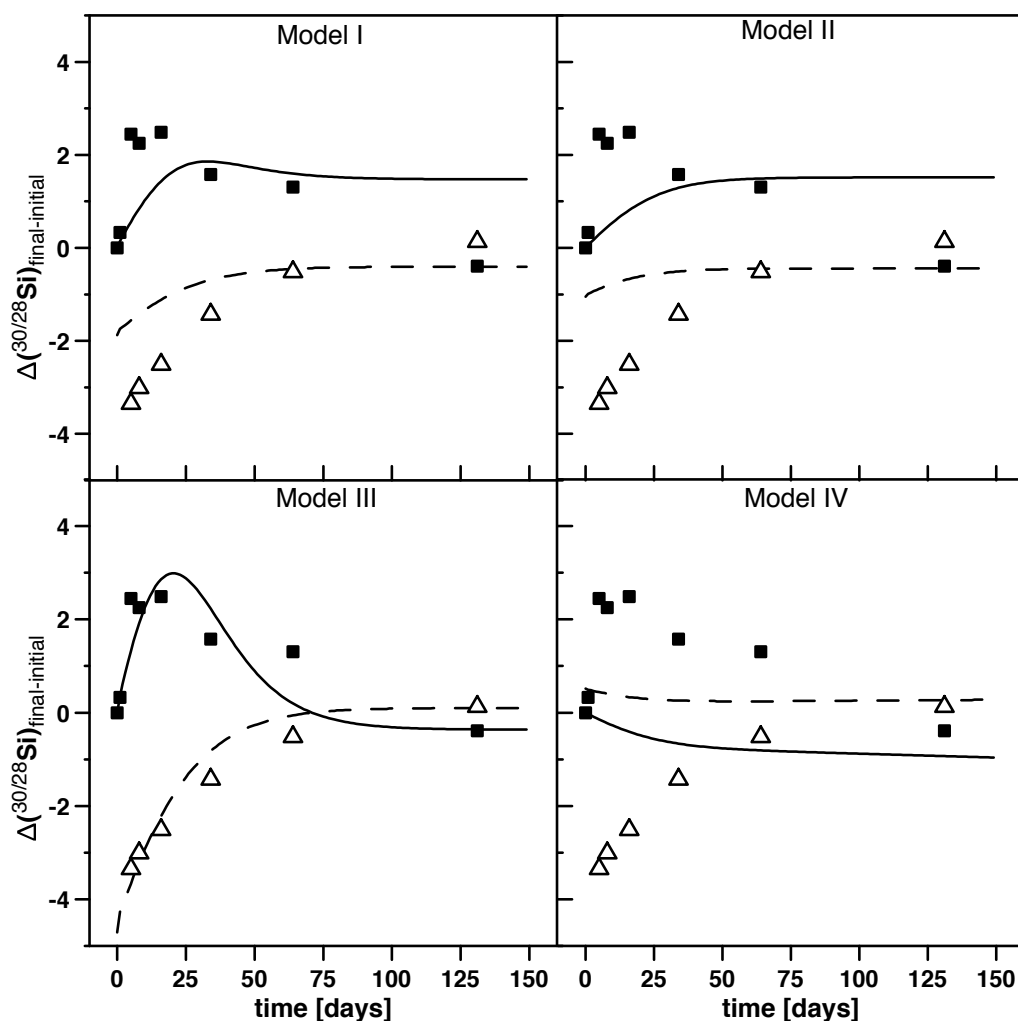
Figure 4.11: Modeled evolution of Si isotope composition in solutions and solids with time and comparison with data for the high-Al experiment (1 mmol/l Al) at pH 4.5. Modeled curves for the solution (black line) and solid (dashed line) are fitted to measured data. Squares depict measured solution and triangles depict the corresponding solid, respectively. Only Model III, assuming unzoned solids, yield reasonable fits to the data.
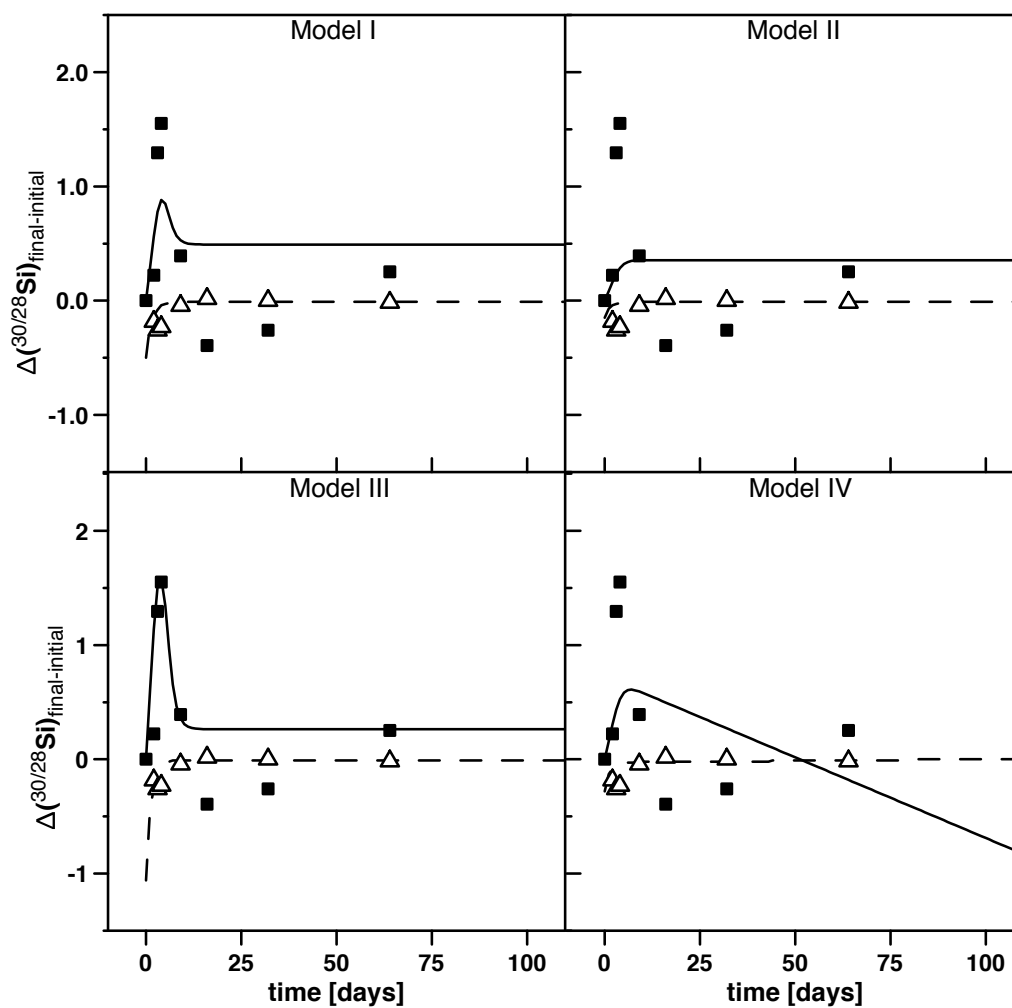
Figure 4.12: Modeled evolution of Si isotope composition in solutions and solids with time and comparison with data for the high-Al experiment (1 mmol/l Al) at pH 7. Modeled curves for the solution (black line) and solid (dashed line) are fitted to measured data. Squares depict measured solution and triangles depict the corresponding calculated solid, respectively. Only Model III, assuming unzoned solids, yield reasonable fits to the data.

Chapter 5

The Si isotope record of different weathering regimes

5.1 Abstract

Si stable isotopes measured in secondary precipitates of soils and saprolite reflect the change in the ratio of particulate export flux over the dissolved import Si flux and thus trace a change in weathering regime. Si isotope ratios measured on extracted amorphous and clay phases from soils and saprolites of three different weathering regimes (Sri Lanka, Sierra Nevada, Swiss Alps) show that the longer the regolith residence time (e.g. as in Sri Lanka), the lower are $\delta(^{30/28}Si)_{NBS28}$ values for the amorphous and clay phase. Thus, in general, a decrease in regolith residence time leads to an increase in the $\delta(^{30/28}Si)_{NBS28}$ values for the secondary silicates formed.

5.2 Introduction

The formation of soils and the sculpturing of landscapes is strongly related to the interplay between chemical weathering and physical erosion. Many studies showed that a close relationship between physical erosion and chemical weathering exists. Natural settings with very low total denudation rates, usually associated with low relief terrains and low denudation rates, show mineral supply rates into the weathering zone that are much lower than the rate at which minerals can be dissolved. In this case, the weathering regime is called "supply-limited" (or "transport-limited"), and all easily weatherable minerals are dissolved (Stallard, 1995; Riebe et al., 2004; West et al., 2005). In contrast, natural settings with very high denudation rates, where material is easily removed by physical processes, are usually associated with steep terrains and high tectonic activity. In these settings fresh unweathered rocks/ minerals are transported fast through the weathering zone, and mineral dissolution cannot follow pace. In this case, the weathering regime is called "kinetically - limited" (or "weathering - limited") (Stallard, 1995; Riebe et al., 2004; West et al., 2005). The objective of this Chapter is to use the Si isotopic composition of natural samples to gain insight into the dependence of Si isotope fractionation related to soil processes under different kinetic regimes. This can be studied by comparing different weathering regimes. Therefore the study of Si isotopes in different erosional regimes is favored over the "chronosequence" approach. Chronosequences are space for time substitutions and are often a necessary tool to study soil development, where all soil forming

factors remain constant except time (Walker et al., 2010).

During the weathering of silicates minerals, the Si flux of the dissolved minerals is partitioned in roughly equal proportions between the dissolved phase and a solid secondary mineral phase. From recent studies on natural samples the main findings are that the isotopically light Si is found in secondary siliceous solid phases and the heavy Si isotopes are relatively enriched in the ambient soil solution and river water (Ziegler et al., 2005a,b; Georg et al., 2006a, 2007b; Opfergelt et al., 2009; Bern et al., 2010; Opfergelt et al., 2011). Processes that fractionate Si isotopes within soils by taking up preferentially ^{28}Si, therefore leading to an enrichment of ^{30}Si in the soil solution are a) the formation of secondary silicates (including adsorption of Si onto soil particles) and b) Si uptake by plants. Experimental studies reveal that during Si adsorption experiments onto gibbsite (Chapter 3, also Oelze et al. (2014)) and Si-Al solid formation experiments (Chapter 4 also Oelze et al. (2015)), kinetically driven Si isotope fractionation is taking place. A strong enrichment of ^{28}Si in the solid phase during higher solid formation rates was found. Under these prerequisites it is tested whether the kinetic isotope effect explored in controlled laboratory experiments (Oelze et al. (2014) and Oelze et al. (2015)) is also visible from natural weathering reactions.

The goal here is to study the influence of parameters like soil residence time, denudation rate (erosion and weathering rate), elemental chemical depletion on Si isotope fractionation in settings that are steadily eroding. Isotope mass balance models of the weathering zone predict that the weathering regime, in particular the ratio of erosional export flux to dissolved import flux, controls the extent of isotope fractionation (Bouchez et al., 2013). A prerequisite for such a study is the ability to separate and isotopically characterize the various Si pools in the weathering zone. Sauer et al. (2006) have developed operationally defined separation techniques of these different Si pools (Figure 1 in Sauer et al. (2006)). These Si fractions are divided into the liquid phase (Si dissolved in soil solution), the adsorbed phase and the solid phase. The solid phase can be further subdivided into an amorphous pool, a poorly/ micro crystalline pool and the crystalline pool. The amorphous pool consist of a biogenic and a minerogenic pool and the crystalline pool is divided into primary and secondary silicates. The role of plants on Si isotopes has been investigated in detail by Ding et al. (2005, 2008a) and Opfergelt et al. (2006a,b, 2008). In this study, the focus is therefore on the inorganic Si pool, both for the adsorbed and solid phases and the potential formation path from amorphous Si precipitates to poorly crystalline solids to crystalline solids. Work by Georgiadis (2011) shows that the second largest fraction after the clay fraction is the minerogenic amorphous Si pool (excluding the organic rich top layer, where biogenic amorphous Si is present as phytoliths). Therefore, to reveal information about a potential Si isotope pathway, a sequential extraction procedure was employed to extract these Si pools. The most two important fractions are defined here as 1.) the amorphous Si fraction and 2.) the clay fraction.

Here I explore Si isotopes in different weathering regimes that range from highly weathered thick tropical soils in the tectonically inactive mountain range of the Highlands of Sri Lanka representing supply–limited conditions (von Blanckenburg et al., 2004), where the weathering erosion relationship is strongly controlled by chemical dissolution, to the rapidly uplifting Swiss Alps (Wittmann et al., 2007). There the sampling site is located in the upper Rhone valley, representing the kinetically limited counterpart where physical erosion dominates (Norton and von Blanckenburg, 2010; Norton et al., 2010). The intermediate weathering regime is located in the southern Sierra Nevada mountain range, California, where chemical weathering and physical erosion are roughly equal Dixon et al.

(2009b, 2012).

In this Chapter I make use of major and trace element concentrations on the weathering profiles used here. This data was obtained in an ongoing project at section "Earth Surface geochemistry" at the GFZ Potsdam (GFZ-ESG-DR). Some of this data is published in Hewawasam et al. (2013) and Norton et al. (2011). This dataset is called "Background data" from hereon.

5.2.1   Sri Lankan Highland study site

Here a short summary of the Sri Lankan sampling site is given. A more detailed description of the sampling site is presented in Hewawasam et al. (2013).

The study site is located in the central Highlands of Sri Lanka. The bedrock of the Sri Lankan central Highlands is mainly composed of metasediments, metabasites and charnockites. Approximately 50% of the central Highlands in Sri Lanka are underlain by charnockite or charnockitic rocks. Most of the landscape is mantled by a thick regolith cover. The sampled study site is a regolith profile located at 1753 m altitude that is exposed along the road from Nuwaraeliya to Welimada, close to the Hakgala Botanical garden (Figure 5.1). The mean annual temperature is 16 ℃ and the mean annual precipitation is 2013 mm. The regolith at the sampling site is located on a hillslope and developed from underlain charnockite ($SiO2$ >65%; plagioclase, K-feldspar and quartz as major mineral components and orthopyroxen and biotite as minor mineral components). The sampled profile has a depth of >10 m. In the uppermost 60 cm of the profile a red-yellow lateric soil layer has developed. The upper reddish and highly weathered saprolite horizon extends from the base of the soil layer down to 6 m (Figure 5.2). The lower part of the saprolite is banded with whitish and yellowish thin layers. In the lower saprolite, massive rounded charnockite blocks of a few to 50 cm in diameter were found. Below a depth of 8 m, charnockite corestones were found, indication first weathering reactions (Figure 5.2). The vegetation cover of the sampled profile consist of a typical tropical forest with a thick canopy up to a height of 20 m and hosts 97 tree species of which 62 are endemic. The average denudation rate derived from cosmogenic nuclides (^{10}Be) measured on soils in close vicinity to the sampled regolith profile is 14.5 mm/kyr (39.1 t/km^2/yr) (Hewawasam et al. (2003) and Table 5.19). Hewawasam et al. (2013) determined further a mean fraction of mass loss by chemical weathering (Chemical Depletion Fraction - CDF) of 0.5. Using the determined denudation rate and the mean chemical depletion fraction, chemical weathering rates of 7.2 mm/kyr (19.5 t/km^2/yr) and erosion rates of 7.2 mm/kyr (19.5 t/km^2/yr) were estimated.

Figure 5.1: Topographic map showing the location of the sampled regolith profile in the Sri Lankan Highlands near Hakgala (white star). Inset shows a map of Sri Lanka indicating the study area (http://www.geomapapp.org using the Global Multi-Resolution Topography (GMRT) by Ryan et al. (2009)).
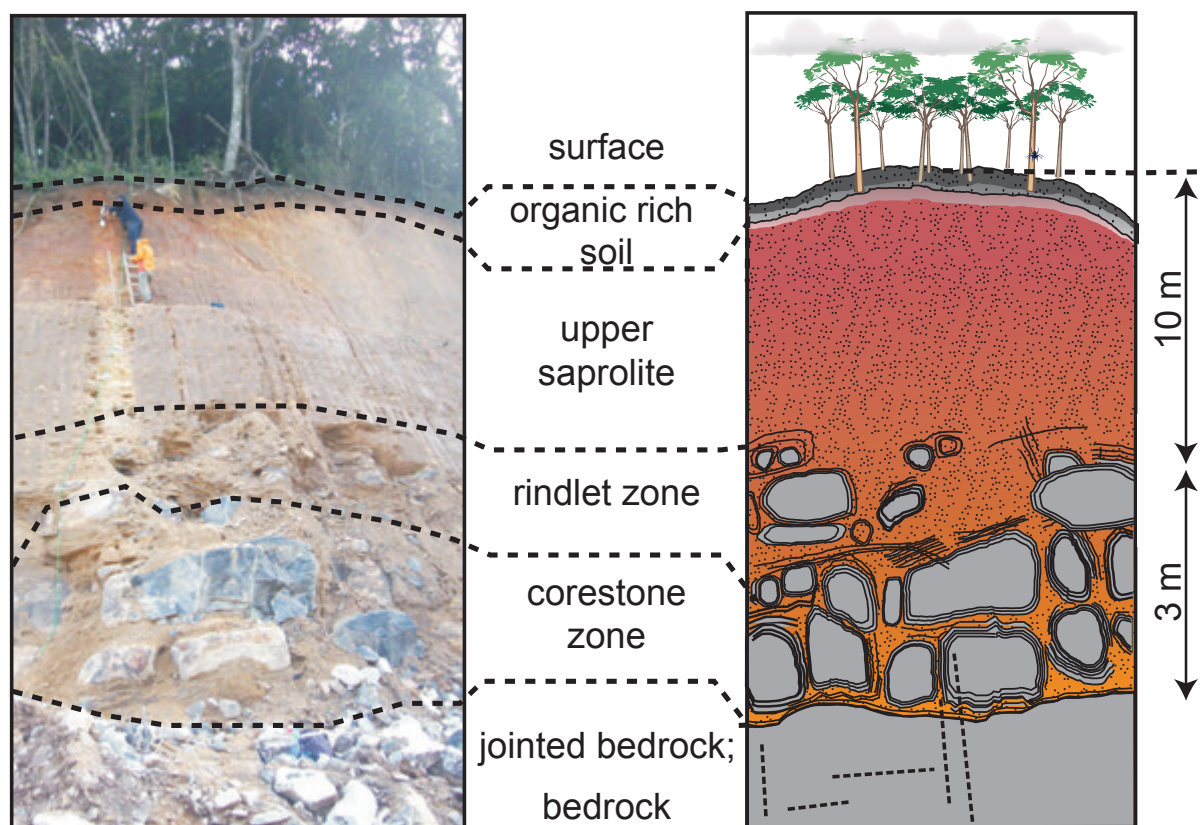
Figure 5.2: Sampled regolith profile in the Sri Lankan Highlands near Hakgala.

5.2.2   Swiss Alps study site

The sampling site is located on a soil–mantled ridge top of the Honegger Horn at 2565 m altitude on the northern site of the upper Rhone valley (Goms) and is underlain by rocks of the Aare Massif. Here the Aare Massif is mainly composed of foliated gneiss (major mineral components: 23% quartz, 53% plagioclase, 17% orthoclase, 4% biotite and 3% muscovite) and granite in the upper valley sections (major mineral components: 34% quartz, 35% plagioclase, 27% orthoclase, 4% biotite). At this sampling site young and minimally developed soils are present with soil thicknesses less than 50 cm at the ridge top site. According to Egli et al. (2008), soils in this part of the Alps are mostly Podzols in elevation regions between 1800 to 2600 m. The mean annual temperature and precipitation, recorded at Ulrichen in the Goms at 1345 m altitude are 3.1 °C and 1137 mm/yr, respectively. According to visual inspection, no saprolite is visible below the soil. The vegetation cover at the ridge top site is mainly grass. The average denudation rate derived from cosmogenic nuclides (^{10}Be) measured on soils of the sampling site are 29.7 mm/kyr (80.2 t/km^2/yr) (Hil-R in Norton et al. (2010) and Table 5.19). Norton and von Blanckenburg (2010) determined a mean fraction of mass loss by chemical weathering (CDF) of 0.30. Using the determined denudation rate and the mean chemical depletion fraction, chemical weathering rates of 8.9 mm/kyr (24 t/km^2/yr) and erosion rates of 20.8 mm/kyr (56.2 t/km^2/yr) were estimated. A more detailed description of the sampling site can be found in Norton and von Blanckenburg (2010) and Norton et al. (2010).
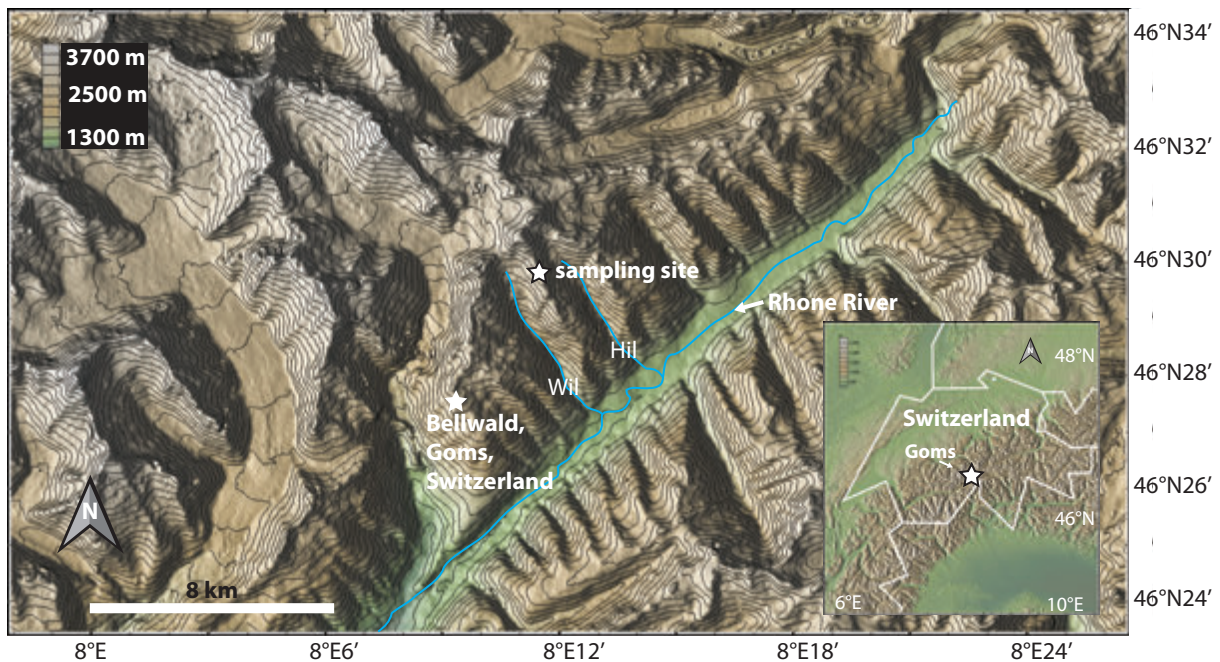
Figure 5.3: Location map showing the upper Rhone valley. Soil sample location is shown as white star. Further marked are the draining streams of the sampling location the Wilerbach (Wil) and Hilperschbach (Hil). (http://www.geomapapp.org using the Global Multi-Resolution Topography (GMRT) by Ryan et al. (2009))

mountain grassland

organic rich top layer
with roots

reddish/brown
immature B horizon;
stony matrix with
weathered clasts of
different sizes

(weathered)
parent rock

30 – 50 cm
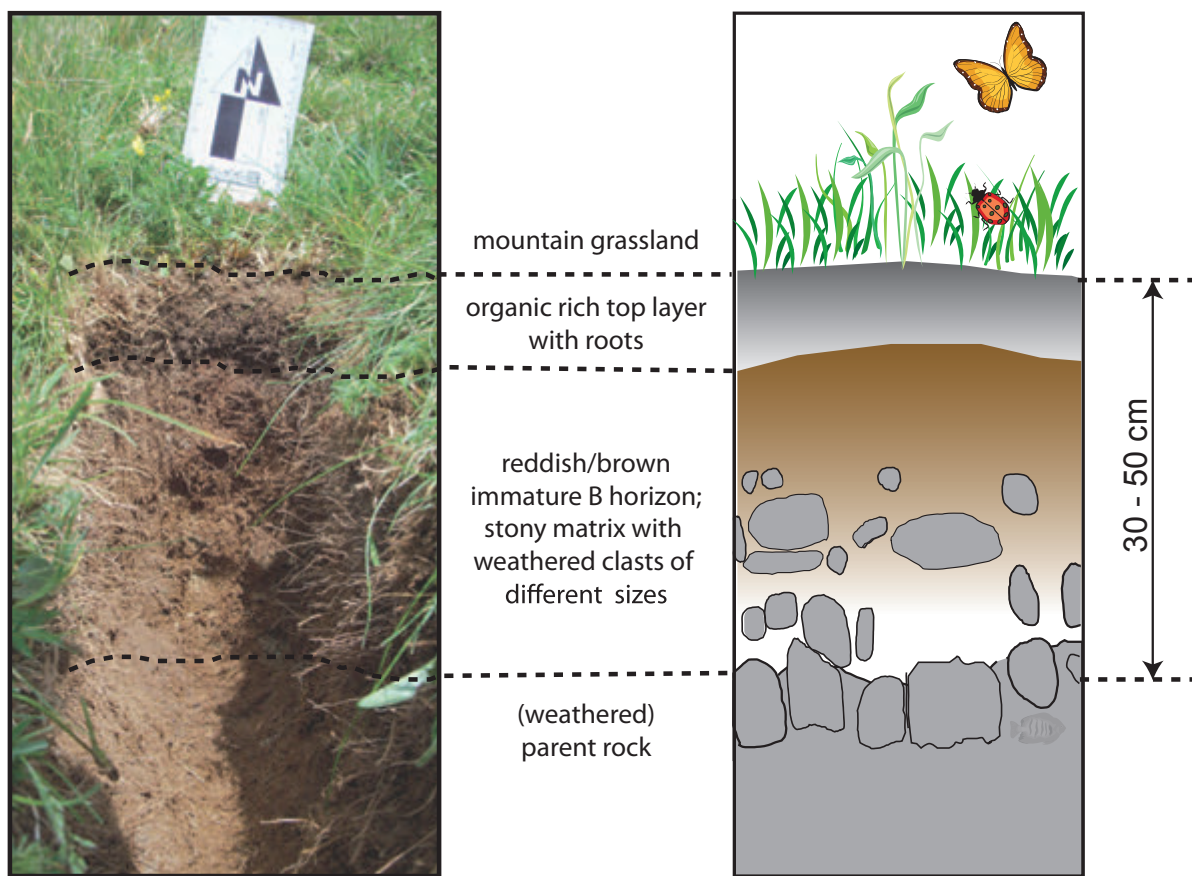
Figure 5.4: Example of a sampled soil profile at the ridge top (Honegger Horn) in the upper Rhone Valley.

5.2.3   Sierra Nevada study sites

The sampled soil profiles are located in the Kings River experimental watersheds ("KREW") in the southern Sierra Nevada (USA) mountain range (Figure 5.5 and Figure 5.6). Within this critical zone observatory (CZO) soil profiles were sampled within catchments located at the Providence Creek (PC) site. Associated PC catchments (P301, P303, P304) range in size between 0.49 to 1.32 km^2 at an elevation between 1479 to 2113 m, with an annual precipitation of 750 - 2000 mm (Hunsaker and Neary, 2012) and a mean annual air temperature of 7.8 °C (Liu et al., 2012). The soils in these catchments are well–drained and are mainly underlain by granitic rocks.

The sampled regolith profile is located NE of shaver lake exposed along the Tollhouse Road (168) (Figure 5.6). The bedrock at both locations is dominated by the "Dinky Creek Granodiorite" a medium, grained, equigranular, strongly foliated biotite-hornblende granodiorite/tonalite with sphene, plagioclas and opaque minerals (Bateman and Wones, 1972). It further contains abundant disc-shaped mafic inclusions (Bateman and Wones, 1972). Further a quartz rich diorite is present at the PC sites ("Quartz diorite of Blue Canyon"). This rock is equigranular and well–foliated and contains conspicuous euhedral hornblende prisms and biotite plates of uniform size (Bateman and Wones, 1972).

The well developed soils at the PC sites are dominated by the "Shaver soil series", a coarse-loamy, mixed soil. This soil series has a balanced supply of moisture, is free of carbonates and has an organic rich surface soil horizon (Soil Survey Staff, 1998). Further soil types are from the "Gerle-Cagwin soil series", with a coarse-loamy to fine sand or coarser texture, mixed, superactive to frigid soil with less than 35 % (by volume) rock fragments (Soil Survey Staff, 1998). Dahlgren et al. (1997) described these soil types to be dominated by hydroxyl-Al interlayered vermiculite and gibbsite. The intense weathering of feldspar and plagioclase under these environmental conditions promotes the formation of kaolinite.

The vegetation cover mainly consist of conifer forest with some chaparral, barren and meadow. More detailed description of the sampling sites can be found in Johnson et al. (2011), Bales et al. (2011), Liu et al. (2012) and Hunsaker and Neary (2012). The average denudation rate derived from cosmogenic nuclides ([10]Be) measured on soils of the sampling site is 81.5 mm/kyr (220 $t/km^2/yr$) (Dixon et al. (2009a) and and Table 5.19). Dixon et al. (2009a) determined a mean fraction of mass loss by chemical weathering (CDF) of 0.58. Using the determined denudation rate and the mean chemical depletion fraction, chemical weathering rates of 47.4 mm/kyr (128.1 $t/km^2/yr$) and erosion rates of 34 mm/kyr (91.9 $t/km^2/yr$) were estimated.
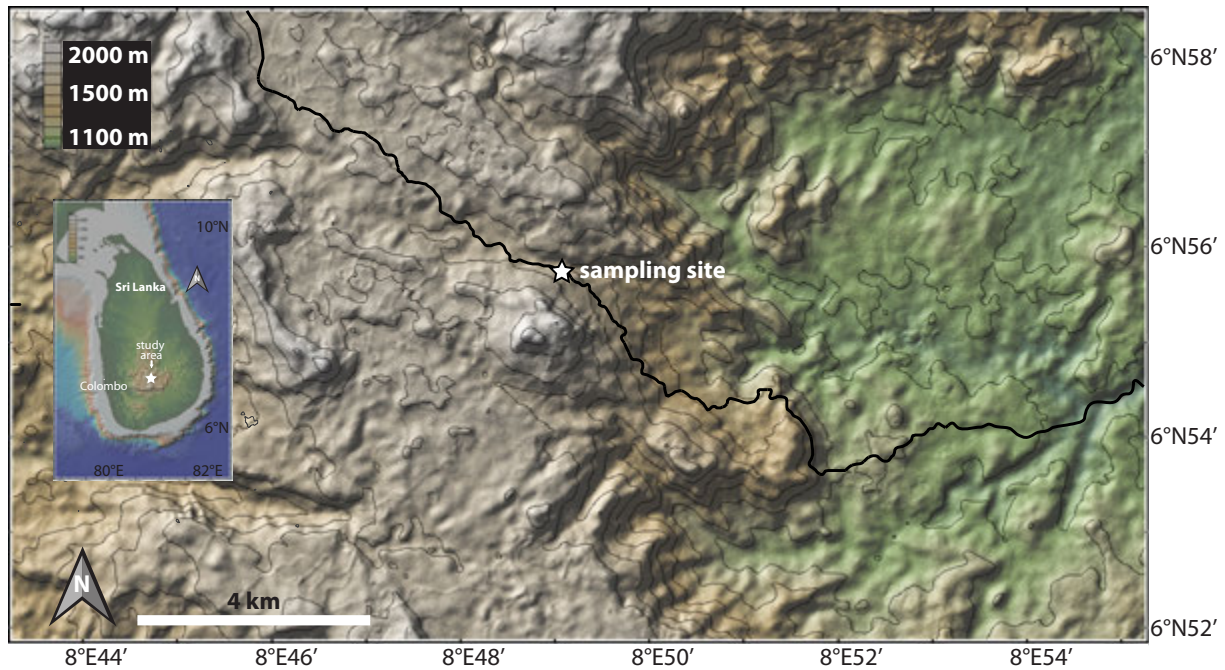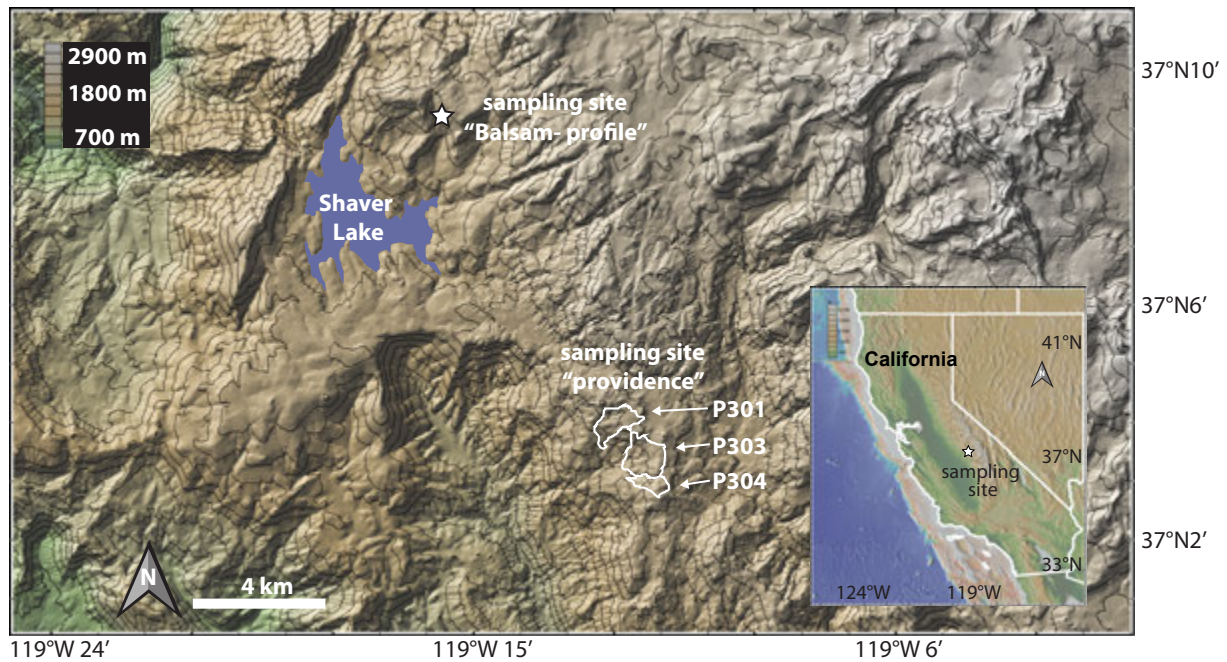
Figure 5.5:   Location map of the sampled regolith profile ("Balsam-profile") and the Providence Creek (PC) site, southern Sierra Nevada, California, USA (http://www.geomapapp.org using the Global Multi-Resolution Topography (GMRT) by Ryan et al. (2009)).
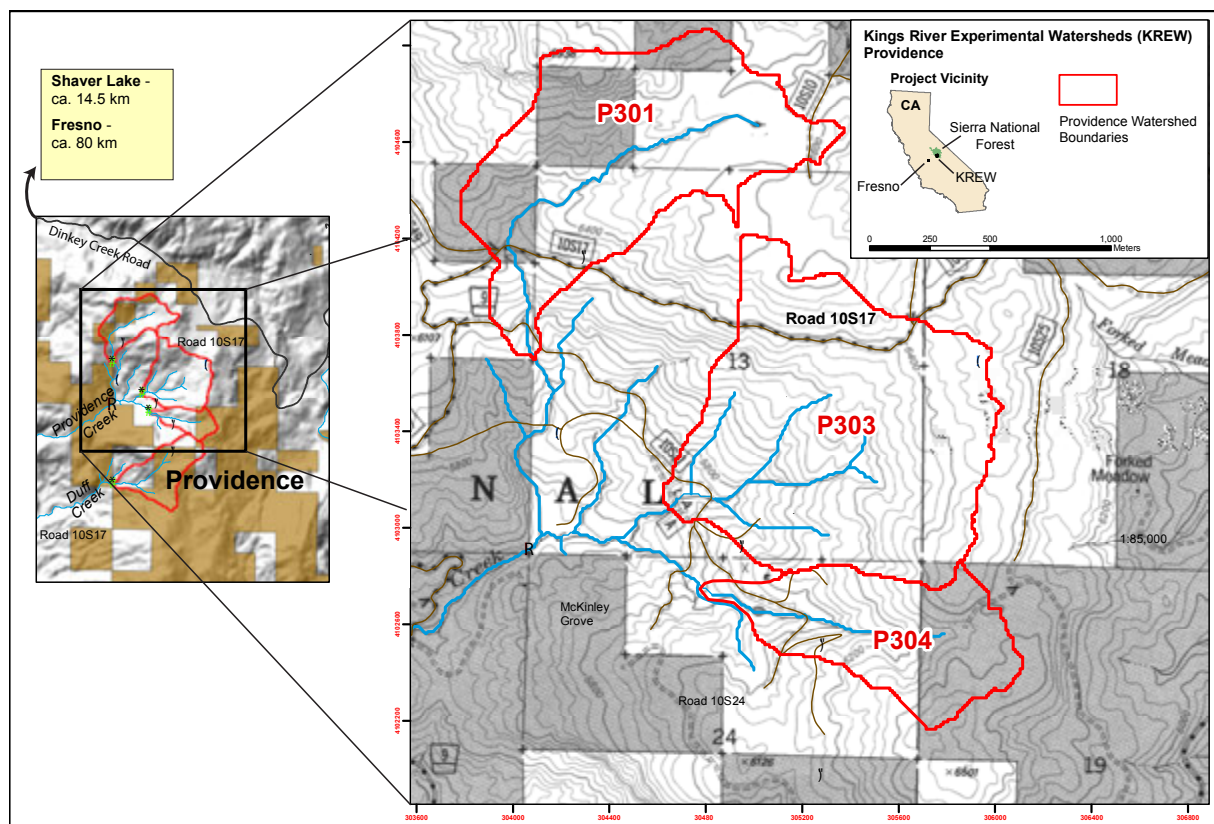
Figure 5.6: Location and topographic map of the Kings River experimental watershed (KREW) at the Providence Creek (PC) site, southern Sierra Nevada, California, USA (modified from http://www.fs.fed.us/psw/topics/water/kingsriver/).
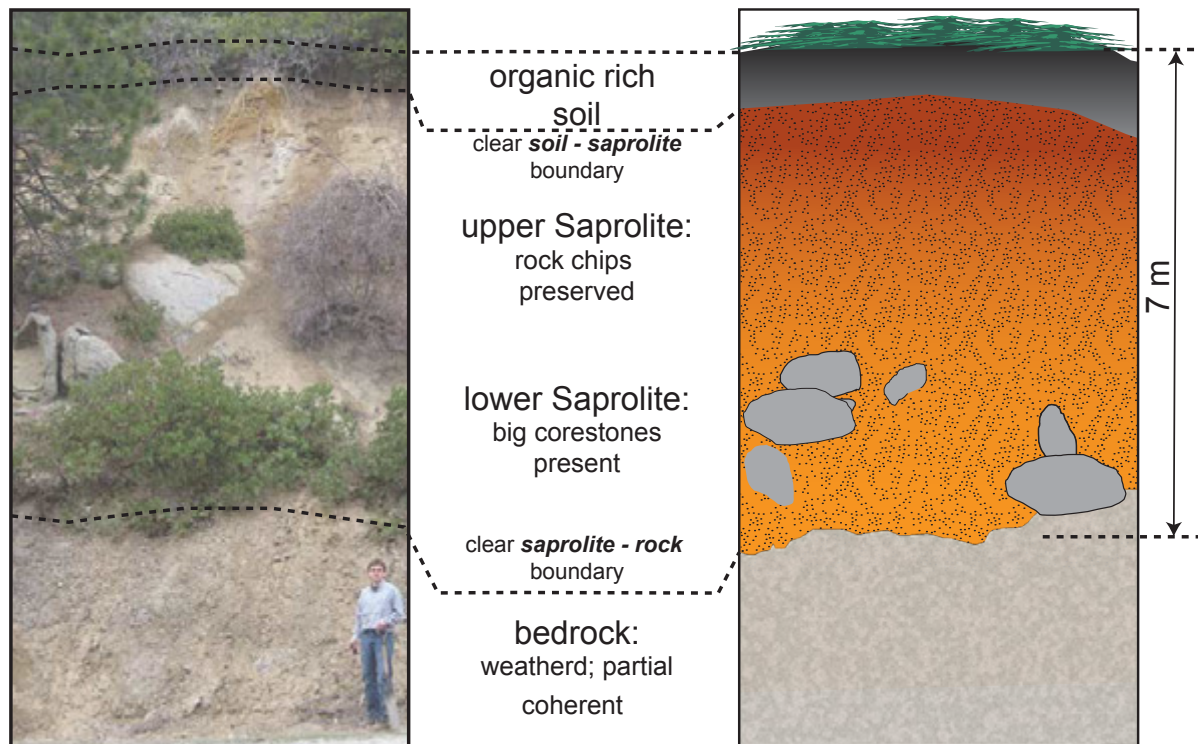
Figure 5.7: Sampled saprolite profile ("Balsam-Profile") in the southern Sierra Nevada, California, USA. Field picture with isotope geochemist for scale (left) and schematic profile (right).

5.3 Methods and Materials

5.3.1 Sampling

Sri Lankan Highlands

Samples were taken on a field campaign taking place in October 2010 and described in detail in Hewawasam et al. (2013). The soil and saprolith samples were collected from a vertical section of a regolith profile (samples SL6 to SL29), exposed as a fresh road cut during ongoing construction works. Five horizontal density cores (15 cm - long and 4.6 cm - diameter plastic core sleeves) were taken throughout the saprolite for density measurement. Approximately 10 m upslope from the regolith profile, nine additional soil samples were collected at three parallel sub-sections within the 60 cm thick soil zone using a soil corer, integrating over depth intervals from 0 to 20 cm, 20 to 40 cm, and 40 to 60 cm. The soil subsections were located about 1.5 m apart from each other in order to account for potential lateral variability. These soil samples were afterwards combined to produce an average soil sample for each depth interval (Hakgala combined soil SL88, SL89 and SL90, respectively). Further, nine unweathered bedrock samples (SL61 and SL63-SL71) were taken beneath the regolith profile to determine source rock element concentration and Si isotope composition (SL61, SL64, SL66, SL68 and SL70).

European Swiss Alps

The samples were taken during a field campaign in July 2010; 6 (B1 to B6) soil depth profiles were sampled on a soil-mantled ridge top using a soil corer. Soil samples were

taken from the soil surface down to ∼30 cm depending on soil thickness.

Southern Sierra Nevada

The samples were taken during a field campaign in May 2010. Several soils were sampled at the PC CZO and a deep saprolith profile ("Balsam-profile") located further away near the NE of Shaver Lake (Figure 5.5 and Figure 5.6). The soil samples were taken as depth profiles using a soil corer for shallow soil horizons and using an auger for deeper soil horizons. A soil depth profile was sampled in catchment P301 from surface down to a depth of ∼120 cm (samples SN1 to SN10). Further soil depth profiles were sampled in PC catchments P303 (samples SN21 to SN23) and P304 (samples SN24 to SN26) from the surface down to 30 cm depth using a soil corer. The individual soil core samples or augered soil samples were afterwards mixed and represent therefore an average of the sampled depth.
At the "Balsam" study site the first sample was taken at ∼180 cm below the soil surface. Several samples were taken down to a depth of ∼800 cm below the surface. The surface of the exposed saprolite was scraped of and samples were taken from the "fresh" saprolite surface with a soil corer where possible. The sampled profile starts at the soil/saprolite border, includes the whole saprolite and extends down to the source-rock/saprolite border (samples SN11 to SN20). The soil on top of the sampled saprolite profile was not sampled. Also, bedload sediments of the stream draining catchment P301 (SN27) and at the outlet of the stream integrating over the whole PC site (PIG; SN28) were sampled.

5.3.2 Sample preparation for Si isotope measurements

Rock samples were crushed < 68 μm and digested using alkaline fusion with NaOH following methods adapted from Georg et al. (2006b) and Zambardi and Poitrasson (2011). Samples of the soil/ saprolite compartment were sieved < 2 mm and treated according to the used Si extraction procedure (subsection 5.3.3).

5.3.3 Extraction procedures for different Si fractions

To determine the Si isotope composition of different reservoirs in the weathering zone a sequential extraction procedure developed in detail by Georgiadis (2011) was used. This extraction method targeted the following operationally defined Si pools: dissolved and easily soluble silicic acid, adsorbed silicic acid, organically bounded silicic acid, sesquioxide–bounded silicic acid, bioopal(phytolits) and amorphous silicic acid. Here the focus is on the major Si reservoirs in weathering environments. These are primary rocks, secondary amorphous Si precipitates and secondary clays. Therefore the extraction procedure developed for amorphous Si precipitates is applied to all processed samples (Georgiadis, 2011) followed by a clay separation procedure (USGS OFR01–041; http://pubs.usgs.gov/of/2001/of01-041/htmldocs/methods/centrifu.htm). The clay separation procedure employed here differs in an important way from the original method. As the aim here is to obtain the isotope composition of the clay fraction, rather than obtain its full mass. Therefore clay extractions was applied only once. Thus pure end-member isotope composition were obtained, but not complete mass of the clay fraction.
Soil and saprolite samples were weighed in (∼500 mg) into 15 ml centrifuge tubes and 10 ml Milli-Q water was added. To disperse clay minerals, an ultrasonic treatment procedure was applied (comprising a 12 h treatment in the ultrasonic bath; Schmidt et al. (2008)).

After clay dispersion, 0.42 ml 5 M NaOH was added to reach a final concentration of 0.2 M NaOH to separate the amorphous Si fraction. Samples were heated and stored at 80℃ in a water bath for 5 hours, and were regularly shaken. Before extracting the solutions, samples were centrifuged for 25 min at 4400 rpm. The extracted solutions were filtered using a 0.2 μm PES (Polyethersulfone) syringe filter and stored for further treatment in pre-acid-cleaned 15 ml PP tubes. To separate the clay fraction from the residuum after amorphous phase extraction, a centrifugation procedure was used (USGS OFR01–041; http://pubs.usgs.gov/of/2001/of01-041/htmldocs/methods/centrifu.htm). Residual samples were filled up with 5 ml Milli-Q water and centrifuged for 97 seconds at 500 rpm. It should be noted that all processed samples after extraction from the bulk sample were treated before digestion to destroy organic carbon except for primary rocks samples. The amorphous phase solution and the solution containing the extracted clay phase, were evaporated in Ag crucibles. The dried samples were combusted at 700 ℃ in a muffle furnace to remove the organic residue. To redissolve the organic-free residuals 3 ml of 1.6 M NaOH was added to the Ag crucibles, evaporated again, and alkaline fusion was conducted at 700 ℃. The fusion cake was dissolved in two steps following a method from Zambardi and Poitrasson (2011): in the first step 20 ml Milli-Q water was added to the Ag crucibles and the samples were stored for 24 hours. Afterwards, the supernate was pipetted off and acidified with HCl to a final molarity of 0.5 M HCl. In the second step 20 ml 0.5 M HCl were added to the Ag crucibles and samples were treated for 3 hours in an ultrasonic bath. Solutions from step 1 and step 2 were combined to obtain a final solution of a volume of $\sim$40 ml 0.5 M HCl.

Silicon was separated from the cationic sample matrix using the well - established method from Georg et al. (2006b). Si blanks of the fusion and column separation procedure were in general below 1 μg which is less than 1 % of the total amount of Si processed.
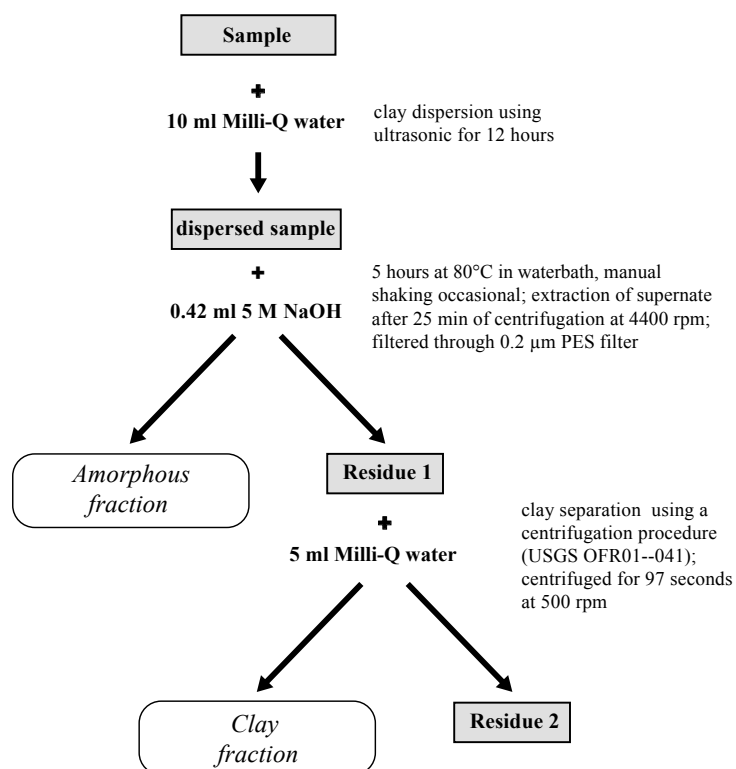
Figure 5.8: Sequential extraction procedure for separating the amorphous and clay Si fraction from the bulk soil.

Preparation for Si isotope measurements
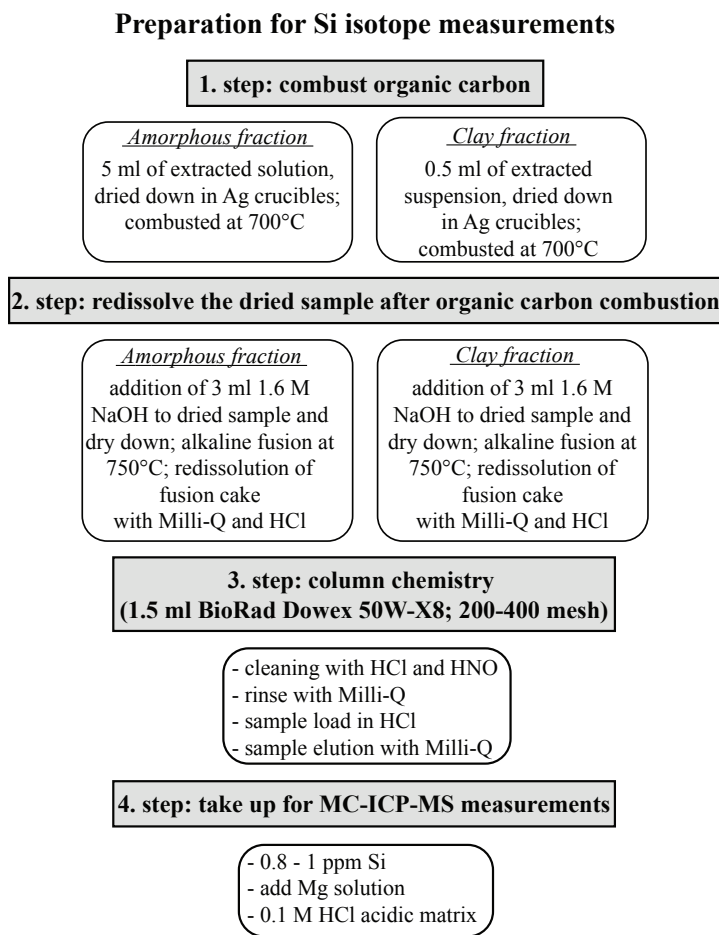
Figure 5.9: Preparation procedure to measure the Si isotope composition of the extracted amorphous and clay Si fractions.

5.3.4 Element concentration measurements

Major and minor element concentrations of the amorphous and clay fractions were determined after alkaline fusion (NaOH) using an optical emission spectrometry (ICP-OES, Varian 720 - ES at GFZ Potsdam). Samples and standards were measured in a weak HNO_3 matrix with an addition of 1000 ppm Cs^+ as matrix modifier element. To further account for the high Na load of the digested samples after alkaline fusion, a known amount of Na was added to the calibration standard solutions. Precision and accuracy were assessed by repeated measurements of an in-house artificial standard solution, showing a reproducibility of better than <5%. Analyses of reference materials over the course of this study indicated an accuracy of better than 8% for all elements analyzed in this study.

Isotope ratio measurements

The Silicon isotope composition was measured on a Thermo Neptune multi - collector inductively coupled plasma mass spectrometer (MC-ICP-MS) equipped with an H-skimmer cone and the Thermo Scientific® Jet - interface in high - resolution mode (m/Δm > 5000). The purified sample solutions were introduced into the plasma via a desolvation unit for dry plasma conditions (Apex, ESI®, no N_2 addition, no further membrane desolvation) equipped with a 120 μl/min nebulizer.

We used Mg doping combined with standard-sample-bracketing to correct for mass bias during measurements by using an exponential mass bias law (Cardinal et al. (2003) and see Chapter 2). A magnesium solution was added to samples and standards to yield a final concentration of 1 ppm Mg. Sample solutions were diluted to 1 ppm Si concentration in 0.1 M HCl, which typically resulted in an intensity of $\sim$15 V/ppm on ^{28}Si (using a $10^{11}\Omega$ resistor).

Measurements were conducted on the interference-free low-mass side of the three Si isotopes. The most critical interference, caused by ^{14}N^{16}O on the ^{30}Si signal, is usually below 5V which is resolvable from the ^{30}Si signal in the high-resolution mode used. Each sample and standard was measured at least 4 times during a sequence; each sample or standard was measured in dynamic mode for 30 cycles with an integration time for each cycle of 4 s for Si as well as for Mg with an idle time of 3 s after magnet switching. Pure 0.1 M HCl solutions were measured before and after each standard-sample-standard block and were used for on-peak zero correction. Typical intensities of ^{28}Si in blank solutions were below 10 mV. We report Si isotope data relative to the standard reference material NBS28 (quartz sand) in the delta notation according to Coplen (2011) as $\delta(^{29/28}\text{Si})_{\text{NBS28}}$ and $\delta(^{30/28}\text{Si})_{\text{NBS28}}$ expressed in per mill (‰) by multiplication of Equation 5.1 and 5.2 with a factor of 10^3:

$$\delta(^{29/28}\text{Si})_{\text{NBS28}} = \left(\frac{\left(\frac{^{29}\text{Si}}{^{28}\text{Si}}\right)_{\text{sample}}}{\left(\frac{^{29}\text{Si}}{^{28}\text{Si}}\right)_{\text{NBS28}}} - 1 \right) \tag{5.1}$$

$$\delta(^{30/28}\text{Si})_{\text{NBS28}} = \left(\frac{\left(\frac{^{30}\text{Si}}{^{28}\text{Si}}\right)_{\text{sample}}}{\left(\frac{^{30}\text{Si}}{^{28}\text{Si}}\right)_{\text{NBS28}}} - 1 \right) \tag{5.2}$$

All reported errors on delta values are the 95% confidence interval (CI) calculated according to Eq.5.3 where $\overline{\delta(^{30/28}\text{Si})_{\text{NBS28}}}$ is the mean of the measured delta values for the sample or standard (at least n=4), t_{n-1} is a critical value from tables of the *Student's t*-law and SE is the standard error of the mean.

$$\text{CI} = \overline{\delta(^{30/28}\text{Si})_{\text{NBS28}}} \pm t_{n-1} \times \text{SE} \tag{5.3}$$

The well-defined Si isotope reference material BHVO-2g, a basalt standard (measured over a 12 months period of analysis ; including several individual chemical separations as well as several digestions procedures; $\delta(^{30/28}\text{Si})_{\text{NBS28}} = -0.27 \pm 0.02$; n=73), was usually measured as control standard during measured sequences.

5.4 Isotope results

5.4.1 Isotope Results - Sri Lanka

The bulk isotope composition of the source rock is $\delta(^{30/28}Si)_{bedrock}$: average= -0.11 ‰ (see Figure 5.10 and Table 5.1) which is within the expected range of granitic rocks (Savage et al. (2012); $\delta(^{30/28}Si)_{granite}$ = -0.23 $\pm$ 0.15 ‰). The amorphous fraction in the saprolite yields in general heavier Si isotopic values than the clay fraction, whereas in the soil

section the extracted amorphous fractions shows lighter values then the clay fraction (see Figure 5.10 and Table 5.1).

Table 5.1: Average $\delta(^{29/28}Si)_{NBS28}$ and $\delta(^{30/28}Si)_{NBS28}$ values, confidence intervals and standard deviation for the extracted amorphous and clay fractions from soil/ saprolite profiles of the Sri Lankan sampling site.

	fraction	$\delta(^{29/28}Si)_{NBS28}$ [‰]	CI [‰]	SD [‰]	$\delta(^{30/28}Si)_{NBS28}$ [‰]	CI [‰]	SD [‰]
soil	amorphous	-0.955	0.094	0.075	-1.877	0.183	0.148
	clay	-0.853	0.077	0.062	-1.670	0.144	0.116
saprolite	amorphous	-0.900	0.061	0.137	-1.755	0.115	0.260
	clay	-1.086	0.064	0.145	-2.108	0.124	0.281
bedrock	bulk	-0.058	0.010	0.012	-0.109	0.025	0.029
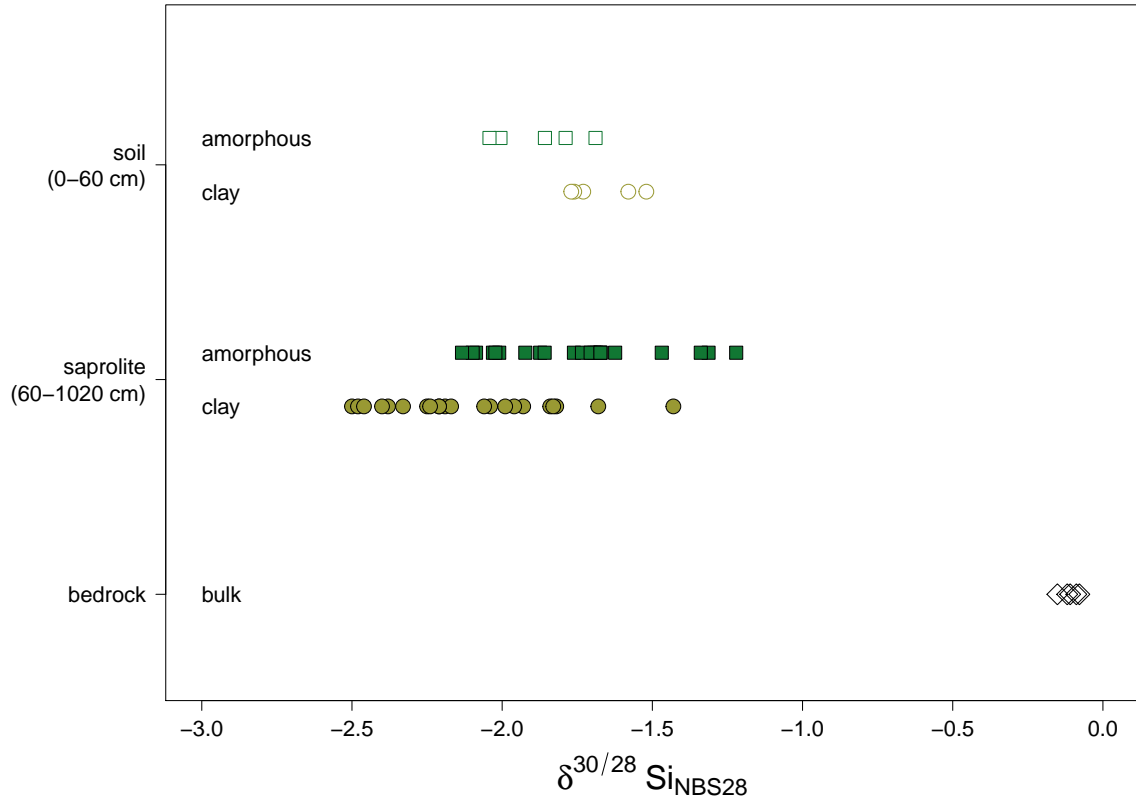
Figure 5.10: $\delta(^{30/28}Si)$ values of the extracted amorphous and clay fractions of the sampled regolith profile of the Sri Lankan sampling site. Squares denote the amorphous fraction, circles the clay fraction and open diamonds represent bedrock. Open and closed symbols represent soil and saprolite, respectively.

5.4.2 Isotope Results - Swiss Alps

The bulk isotope composition of the source rock is $\delta(^{30/28}Si)_{bedrock}$: average= -0.14‰ (see Figure 5.11 and Table 5.2) which is within the expected range of granitic rock (Savage et al. (2012); $\delta(^{30/28}Si)_{granite}$ = -0.23 ± 0.15 ‰).

Within the topsoil layer show the extracts of the amorphous fraction always lighter Si isotopic signatures than the clay fraction, whereas in the subsoil the extracts of the amorphous fraction show in general heavier Si isotopic values than the clay fraction (see Figure 5.11 and Table 5.2). The isotopic signature of the clay fraction are fairly constant and fall within a range between $\delta(^{30/28}Si_{NBS28})$= -0.54‰ to -0.21‰.

Table 5.2: Average $\delta(^{29/28}Si)_{NBS28}$ and $\delta(^{30/28}Si)_{NBS28}$ values, confidence intervals and standard deviation for the extracted amorphous and clay fractions from soil profiles of the Swiss Alps sampling site.

	fraction	$\delta(^{29/28}Si)_{NBS28}$ [‰]	CI [‰]	SD [‰]	$\delta(^{30/28}Si)_{NBS28}$ [‰]	CI [‰]	SD [‰]
topsoil	amorphous	-0.497	0.155	0.148	-0.984	0.308	0.294
	clay	-0.213	0.069	0.065	-0.404	0.125	0.119
subsoil	amorphous	-0.054	0.053	0.088	-0.100	0.103	0.170
	clay	-0.176	0.024	0.040	-0.340	0.050	0.083
bedrock	bulk	-0.077	0.014	0.018	-0.143	0.024	0.032
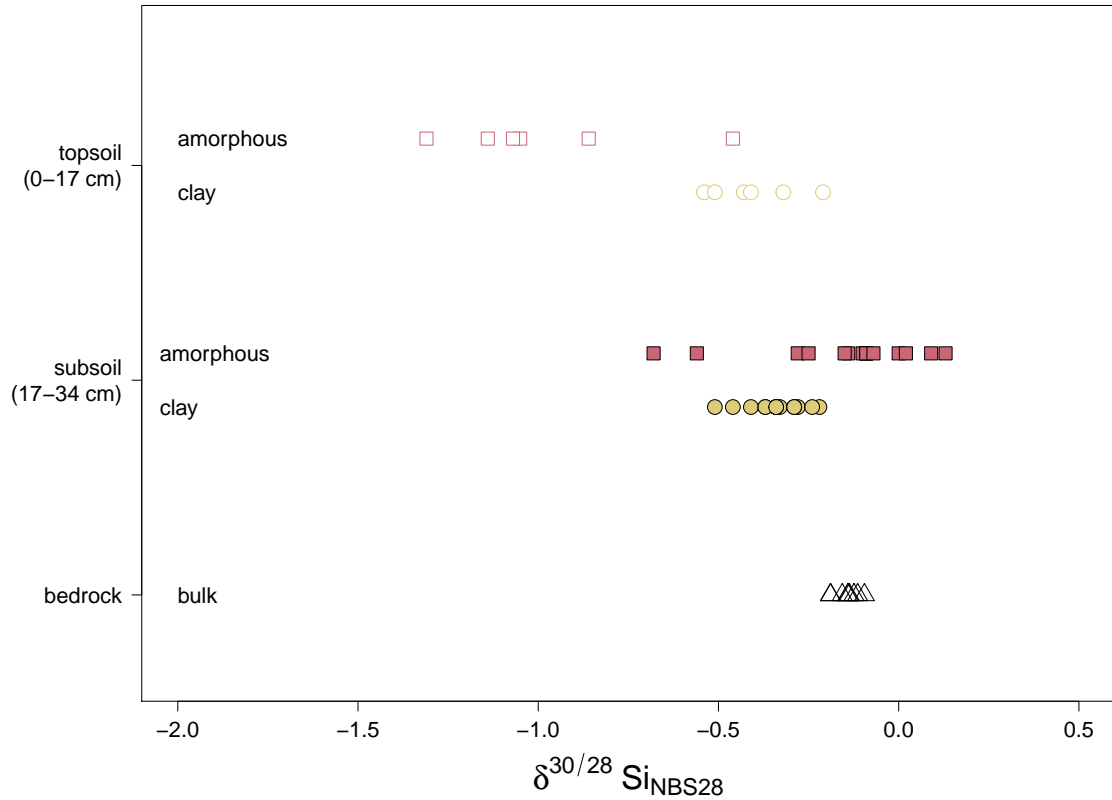
Figure 5.11: $\delta(^{30/28}Si)$ values of the extracted amorphous and clay fractions of the sampled soil profiles of the Swiss Alps sampling site. Squares denote the amorphous fraction, circles the clay fraction and open triangles represent bedrock. Open and closed symbols represent topsoil and subsoil, respectively.

5.4.3   Isotope Results - Sierra Nevada

The bulk isotope composition of the source rock is $\delta(^{30/28}Si)_{bedrock}$: average=-0.19‰ (see Figure 5.12 and Table 5.3) which is within the expected range of granitic rock (Savage

et al. (2012); $\delta(^{30/28}Si)_{granite} = -0.23 \pm 0.15$ ‰).

Within soil profiles the clay fraction yields systematically heavier $\delta^{30/28}Si_{NBS28}$ values than the amorphous fraction. This is in contrast to the sampled saprolite, where the amorphous fraction show systematically heavier $\delta(^{30/28}Si)_{NBS28}$ values than the clay fraction (see Figure 5.12 and Table 5.3).

Table 5.3: Average $\delta(^{29/28}Si)_{NBS28}$ and $\delta(^{30/28}Si)_{NBS28}$ values, confidence intervals and standard deviation for the extracted amorphous and clay fractions from soil/ saprolite profiles of the Sierra Nevada sampling site.

	fraction	$\delta(^{29/28}Si)_{NBS28}$ [‰]	CI [‰]	SD [‰]	$\delta(^{30/28}Si)_{NBS28}$ [‰]	CI [‰]	SD [‰]
soil	amorphous	-0.755	0.139	0.262	-1.487	0.273	0.513
	clay	-0.566	0.093	0.174	-1.097	0.176	0.329
saprolite	amorphous	-0.431	0.132	0.185	-0.830	0.261	0.365
	clay	-0.836	0.206	0.288	-1.609	0.402	0.562
bedrock	bulk	-0.101	0.024	0.023	-0.191	0.039	0.037
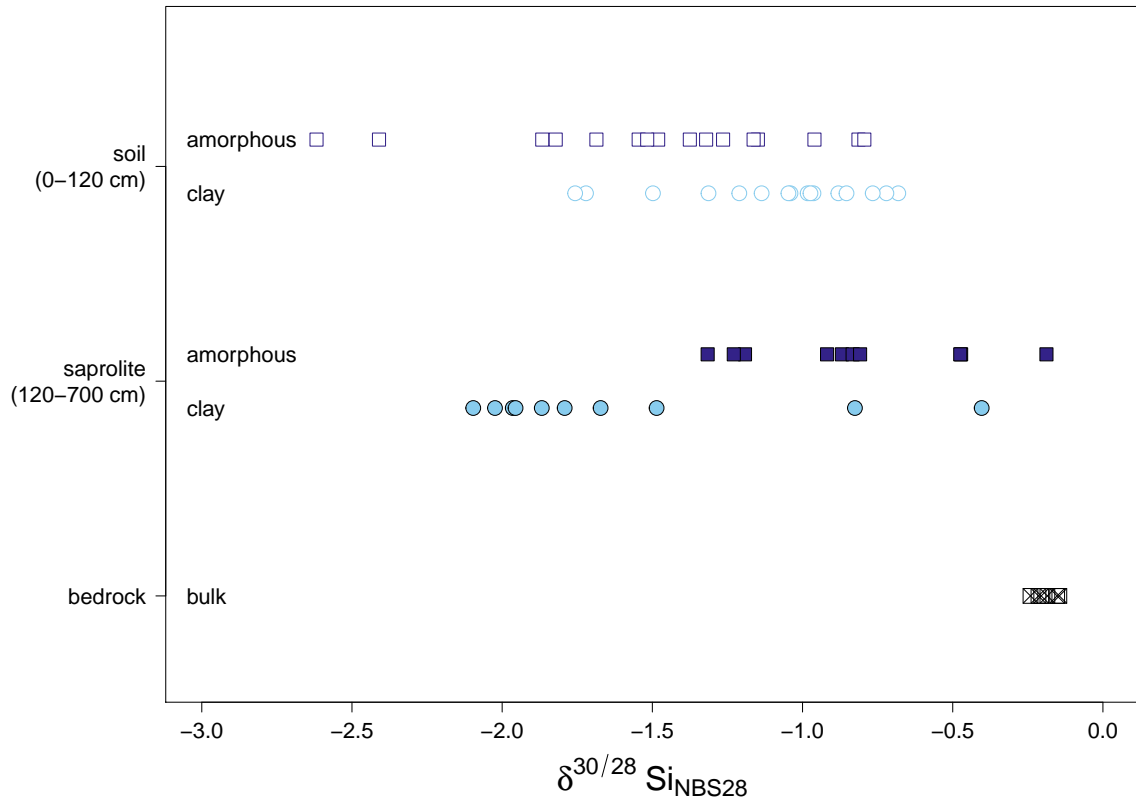
Figure 5.12: $\delta(^{30/28}Si)$ values of the extracted amorphous and clay fractions of the sampled soil and saprolite profiles of the Sierra Nevada sampling site. Squares denote the amorphous fraction, circles the clay fraction and crossed squares represent bedrock. Open and closed symbols represent soil and saprolite, respectively.

5.5 Discussion

5.5.1 Control of the export- to import flux ratio of Si in the weathering zone on the Si isotopic composition of secondary weathering products

At first, the relation between the Si isotopic composition of the amorphous and clay fractions with denudation, weathering and erosion rates derived from local soil samples is investigated (Table 5.19). No regular relationship between The Si isotope composition of secondary soil phases and either denudation rate, weathering rate or erosion rate is apparent (Figure 5.13).
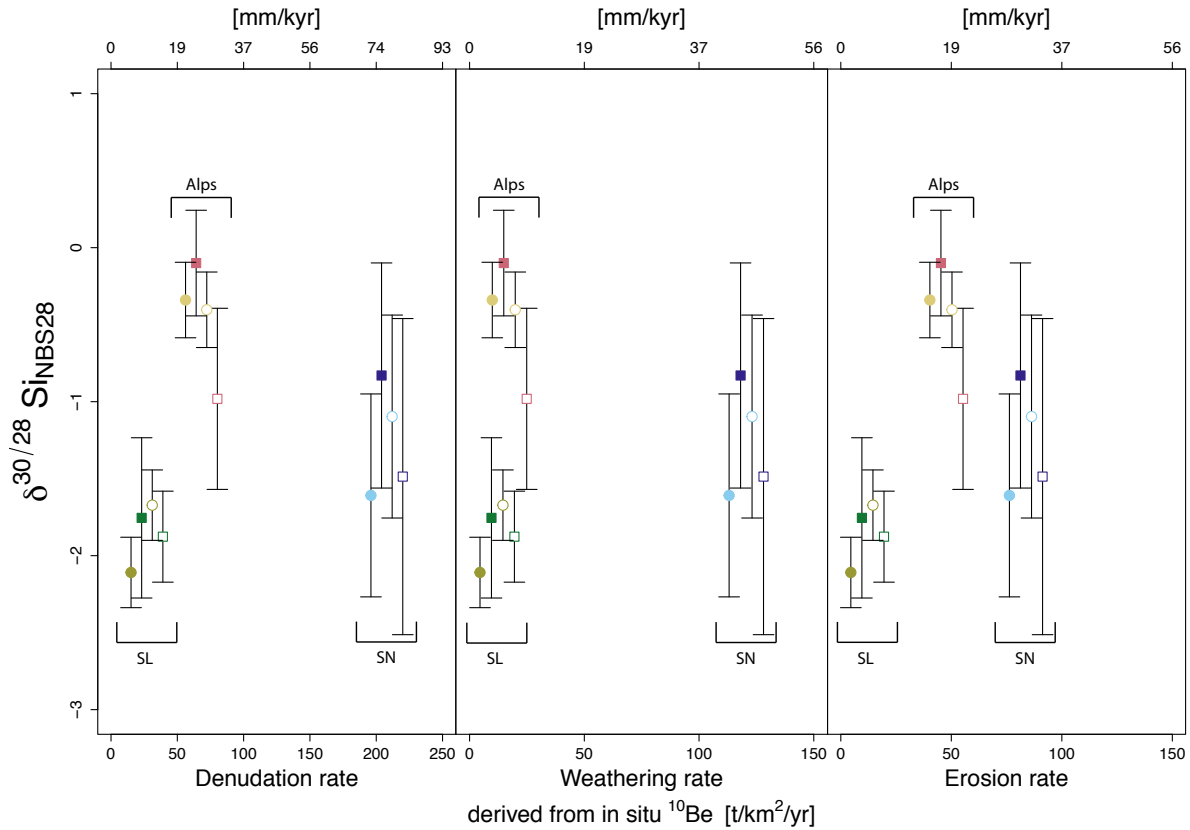
Figure 5.13: $\delta(^{30/28}Si)_{NBS28}$ of the amorphous (squares) and clay (circles) fraction extracted from soil and saprolite against total denudation rate, weathering rate and erosion rate. Open symbols denote extracted fractions from soils/topsoils and closed symbols denote extracted fractions from saprolite/subsoils. Abbreviations SL and SN denote Sri Lanka and Sierra Nevada, respectively. Note: Denudation, weathering and erosion rates are identical for an individual sampling site; they are shown with some spread for clarity (see Appendix Table 5.19).

Bouchez et al. (2013) developed an isotope mass balance framework for interpreting stable metal and metalloid isotopes quantitatively in a geomorphic context. The model is based on a simple steady–state mass balance assumption, that is, that the element flux into the weathering zone by regolith production equals elements flux out of the weathering zone by erosion and weathering. Within this isotope mass balance framework it is assumed that 1) formation of secondary minerals and 2) uptake of nutrients by plants are the processes that set the dominant isotope fractionation in the weathering zone.

107

I use this model to quantitatively explain the pattern found in Figure 5.13.

In the following the notation of Bouchez et al. (2013) is used for isotopic compositions, isotope fractionation factors and elemental fluxes of Si. The isotopic composition of secondary precipitates δ_{sec}^{Si} can be predicted using Equation 5.4:

$$\delta_{sec}^{Si} = \delta_{diss}^{Si} + \Delta_{prec}^{Si} \tag{5.4}$$

where δ_{diss}^{Si} denotes the Si isotopic composition of the dissolved fraction of Si and Δ_{prec}^{Si} denotes the Si isotope fractionation factor of secondary silicate formation. Combining Equation 5.4 with Equation 5e from Bouchez et al. (2013) results in:

$$\delta_{sec}^{Si} = \delta_{rock}^{Si} - \frac{E_{sec}^{Si} * \Delta_{prec}^{Si} + E_{org}^{Si} * \Delta_{upt}^{Si}}{S_{rock}^{Si} + S_{prim}^{Si}} + \Delta_{prec}^{Si} \tag{5.5}$$

where δ_{rock}^{Si} denotes the Si isotopic composition of the bedrock, E_{sec}^{Si} and E_{org}^{Si} are export fluxes of Si ($mol_{Si} * m^{-2} * yr^{-1}$) by particulate erosion of Si contained in secondary silicates and in biogenic products such as phytoliths, respectively. S_{rock}^{Si} and S_{prim}^{Si} are the import fluxes of dissolved Si ($mol_{Si} * m^{-2} * yr^{-1}$) into the weathering zone resulting from the dissolution of bedrock and from primary minerals, respectively. Δ_{upt}^{Si} denotes the Si isotope fractionation factor during Si uptake by plants. Following the approach of Bouchez et al. (2013) and normalizing a given element flux F^{Si} (E_{sec}^{Si}, E_{org}^{Si}, S_{rock}^{Si} and S_{prim}^{Si}; capital letters) to the flux of matter crossing the weathering front ($S_{rock}^{Si} + RP_{prim}^{Si}$), where RP_{prim}^{Si} denotes the Regolith production rate:

$$f^{Si} = \frac{F^{Si}}{S_{rock}^{Si} + RP_{prim}^{Si}} \tag{5.6}$$

results in non - dimensional fluxes f^{Si} (e_{sec}^{Si}, e_{org}^{Si}, s_{rock}^{Si} and s_{prim}^{Si}; lower case letters). A flux - weighted isotope fractionation factor $\overline{\Delta^{Si}}$ can be calculated comprising both Δ_{prec}^{Si} and Δ_{upt}^{Si}:

$$\overline{\Delta^{Si}} = \frac{E_{sec}^{Si} * \Delta_{prec}^{Si} + E_{org}^{Si} * \Delta_{upt}^{Si}}{E_{sec}^{Si} + E_{org}^{Si}} \tag{5.7}$$

Combining Equation 5.5, 5.6 and 5.7 results in:

$$\frac{\delta_{sec}^{Si} - \delta_{rock}^{Si} - \Delta_{prec}^{Si}}{\overline{\Delta^{Si}}} = -\frac{e_{sec}^{Si} + e_{org}^{Si}}{s_{rock}^{Si} + s_{prim}^{Si}} \tag{5.8}$$

where e_{sec}^{Si} and e_{org}^{Si} are the normalized, non - dimensional export fluxes of Si by particulate erosion of Si contained in secondary silicates and in organic matter, respectively. s_{rock}^{Si} and s_{prim}^{Si} are the normalized, non - dimensional dissolved Si import fluxes resulting from the dissolution of bedrock and from primary minerals, respectively. Experiments and field studies show that the direction and magnitude of Δ_{prec}^{Si} and Δ_{upt}^{Si} can be assumed to be similar (Opfergelt et al., 2006a; Ding et al., 2008b; Georg et al., 2009; Oelze et al., 2014, 2015) and therefore Equation 5.8 can be simplified to:

$$1 - \frac{\delta_{sec}^{Si} - \delta_{rock}^{Si}}{\overline{\Delta^{Si}}} = \frac{e_{sec}^{Si} + e_{org}^{Si}}{s_{rock}^{Si} + s_{prim}^{Si}} \tag{5.9}$$

As δ_{rock}^{Si} is rather uniform between these three sites, the difference $\delta_{sec}^{Si} - \delta_{rock}^{Si}$ is only controlled by δ_{sec}^{Si}. Hence Equation 5.9 results in a positive linear relationship between

the isotopic value of secondary silicates δ_{sec}^{Si} and the $(e_{sec}^{Si} + e_{org}^{Si})/(s_{rock}^{Si} + s_{prim}^{Si})$ ratio (Figure 5.14).
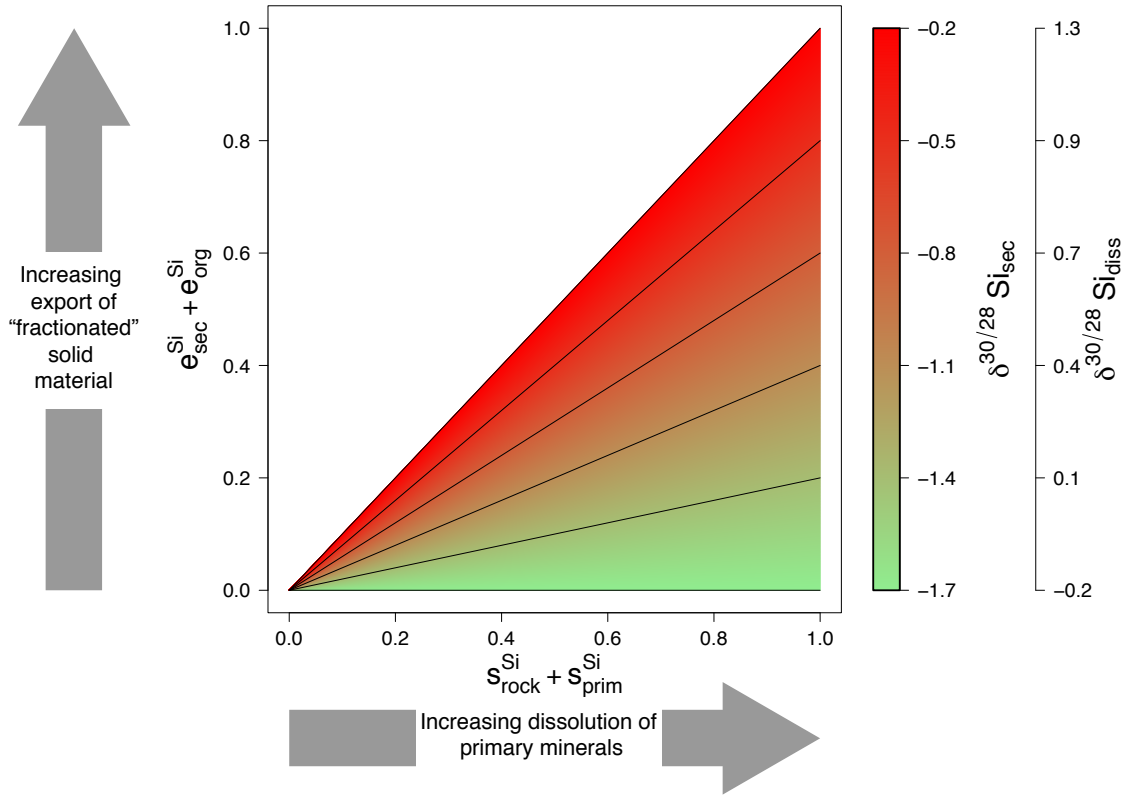
Figure 5.14: $\delta(^{30/28}Si)_{sec}$ as well as $\delta(^{30/28}Si)_{diss}$ as a function of $(e_{sec}^{Si} + e_{org}^{Si})$ and $(s_{rock}^{Si} + s_{prim}^{Si})$ after Bouchez et al. (2013). Further shown are isolines for constant $\delta(^{30/28}Si)_{sec}$ values. It is assumed that $\delta(^{30/28}Si)_{rock}$ and $\overline{\Delta^{Si}}$ are constant and have a value of -0.2 ‰ and -1.5 ‰, respectively.

At steady-state the normalized value of $(e_{sec}^{Si} + e_{org}^{Si})$ cannot exceed the value of $(s_{rock}^{Si} + s_{prim}^{Si})$ as Si needs to be dissolved from primary minerals before it enters solid secondary phases. Larger ratios of $(e_{sec}^{Si} + e_{org}^{Si})/(s_{rock}^{Si} + s_{prim}^{Si})$ (maximum at steady-state =1) result in relative higher $\delta(^{30/28}Si)_{sec}$ values of the formed secondary silicates. In settings where $(e_{sec}^{Si} + e_{org}^{Si})$ is low the $\delta(^{30/28}Si)_{diss}$ values of the soil water is close to the $\delta(^{30/28}Si)_{rock}$ value of the bedrock and therefore the precipitating secondary phases show light Si isotopic values, which are offset from the $\delta(^{30/28}Si)_{diss}$ value by the Si isotope fractionation factor Δ_{prec}^{Si}. Therefore, the lowest $\delta(^{30/28}Si)_{sec}$ values are obtained at low values of $(e_{sec}^{Si} + e_{org}^{Si})$ where a large fraction of Si is exported as primary minerals or in dissolved form.

A plot of $1 - (\delta_{sec}^{Si} - \delta_{rock}^{Si})/\overline{\Delta^{Si}}$ against denudation rate reveals changes in the $(e_{sec}^{Si} + e_{org}^{Si})/(s_{rock}^{Si} + s_{prim}^{Si})$ ratio (Equation 5.9 and Figure 5.15). The isotopic signatures of the amorphous and clay fraction do not reveal whether the erosional export fluxes $(e_{sec}^{Si} + e_{org}^{Si})$ increase or the dissolved import fluxes $(s_{rock}^{Si} + s_{prim}^{Si})$ decrease; they only reveal that the proportion of particulate Si erosion changes relative to the supply of dissolved Si into the weathering zone. Nevertheless, it is apparent from Figure 5.15 that in Sri Lanka, virtually all Si released leaves the weathering zone in the dissolved form, whereas in the Alps all Si leaves in the secondary minerals that are eroded, and in the Sierra Nevada both export forms are similar.
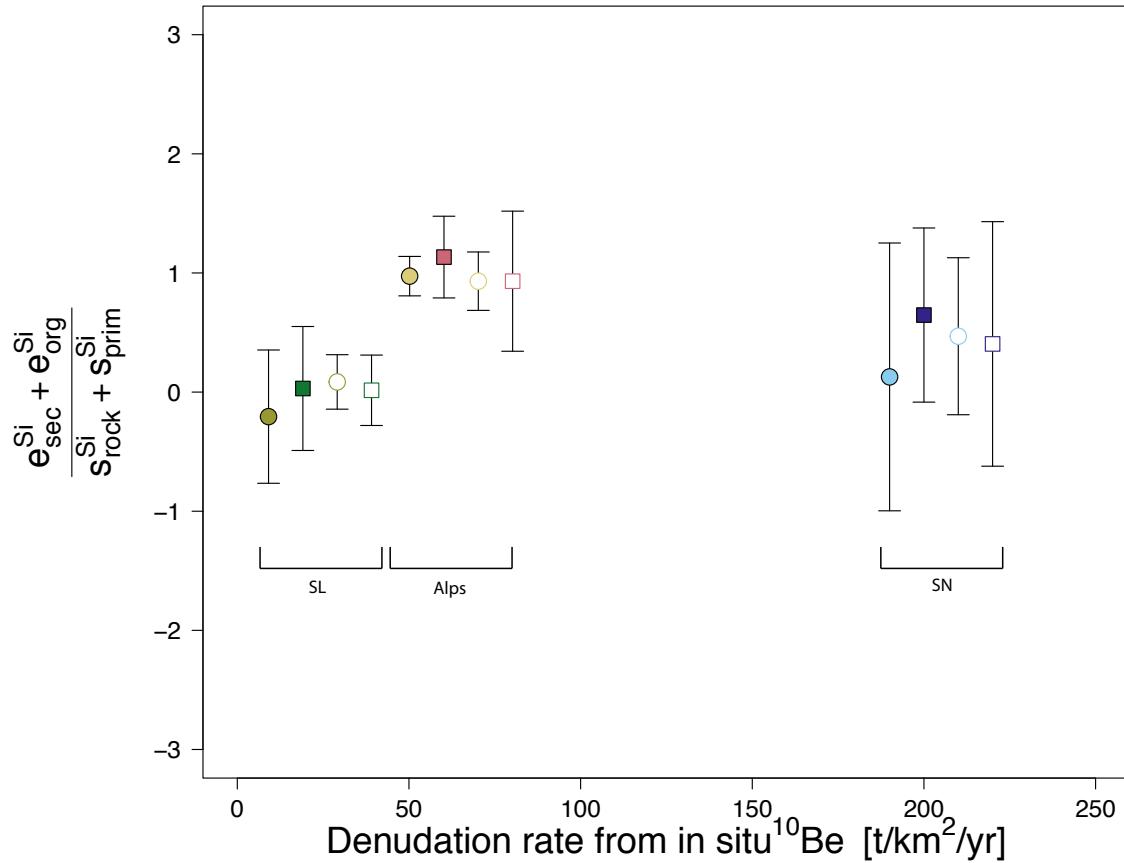
Figure 5.15: Ratio of Si erosion to Si release (Equation 5.9) from Si isotope ratios in the amorphous (squares) and clay (circles) fraction against total denudation rate. Open symbols denote extracted fractions from soils/topsoils and closed symbols denote extracted fractions from saprolite/subsoils. Abbreviations SL, SN and SA denote Sri Lanka, Sierra Nevada and Swiss Alps, respectively. Error bars are the 2SD of all measured amorphous and clay samples. Note: Denudation, weathering and erosion rates are identical for an individual sampling site; they are shown with some spread for clarity (see Appendix Table 5.19).

In order to evaluate the function of time on dissolution of primary minerals and subsequent formation of secondary phases a first-order estimate on the time Si spends in the weathering zone is made. The residence time can be estimated from the method of cosmogenic nuclide-based denudation rates itself. Such rates integrate over the time it takes to erode one cosmogenic adsorption depth scale, which is 60 cm in bedrock and about 100 cm in soils, once cosmogenic steady state is reached. In slowly eroding settings, this so–called "apparent age" is long (in the order of tens to hundred of kyr), as erosion rate is low. In tectonically active settings, where erosion rate is high this time is short (in the order of a few kyr)(see von Blanckenburg (2005) for a comprehensive summary). An extension of the above-presented cosmogenic nuclide based concept of residence time made by inferring a regolith residence time, for the entire soil or regolith thickness, by assuming that no large changes in the weathering and erosion rates over the formation time of the regolith occurred. Thus, the regolith total apparent age is calculated by dividing the total regolith thickness by the cosmogenic nuclide–derived denudation rate. Using the soil derived denudation rates (see Appendix Table 5.19) for the three sampling sites and regolith thicknesses of 13 m for Sri Lanka, 8 m for the Sierra Nevada and 0.6 m for the Swiss Alps, regolith residence times of 900, 90 and 20 kyr for the Sri Lankan, Sierra Nevada and the Swiss Alps sampling sites are calculated, respectively. These rough estimates of regolith residence times appear to exert a first-order control over the relative proportions of the erosional export flux (see Figure 5.16). In contrast, the control of the denudation rate itself on the exported proportions seems to be minor (Figure 5.15). As shown in Figure 5.16, the $(e^{Si}_{sec} + e^{Si}_{org})/(s^{Si}_{rock} + s^{Si}_{prim})$ decreases from a high ratio (close to 1) at short regolith residence time in the Swiss Alps sampling site, to intermediate values for the Sierra Nevada sampling site to the lowest values for very long regolith residence time of the Sri Lankan sampling site, respectively.

In detail, the Swiss Alps sampling site is characterized by an intermediate denudation rate and shallow soil depth. The combination of both denudation rate and shallow regolith depth results in a short regolith residence time. This short residence time results in a $(e^{Si}_{sec} + e^{Si}_{org})/(s^{Si}_{rock} + s^{Si}_{prim})$ ratio of close to 1. What this means is that the Si released from bedrock and primary minerals is incorporated into secondary precipitates and that these secondary precipitates are mainly eroded in the particulate form.

Due to the short regolith residence time, redissolution of the formed secondary precipitates is limited. The Sierra Nevada sampling site is characterized by regolith residence times that are much longer compared to the Swiss Alps sampling site even at the higher denudation rate due to the large regolith thickness. The supply of dissolved Si into the weathering zone is high (as inferred from the high denudation rates) and the regolith residence is sufficiently short such that the formed secondary precipitates are transported through the regolith reactor without complete redissolution. The $\delta(^{30/28}Si)_{sec}$ values are lower than in the Swiss Alps as about 50% of the Si released is exported in the dissolved form (Figure 5.15 and Figure 5.16). This dissolved compartment contains the complimentary heavy Si. The isotopic signature of the clay and amorphous fraction in settings with very low denudation rates show the lowest $\delta(^{30/28}Si)_{NBS28}$ values of all sampled settings. At the low denudation rates (supply limited regimes) of the Sri Lankan highlands, where the regolith residence time is very long, the secondary Si precipitates although formed are almost fully redissolved at a later stage, the export of Si in particular form is reduced and the proportion of Si export in dissolved form is higher compared to the two other sampled settings.

Another way to envisage this process is that previously formed secondary precipitates
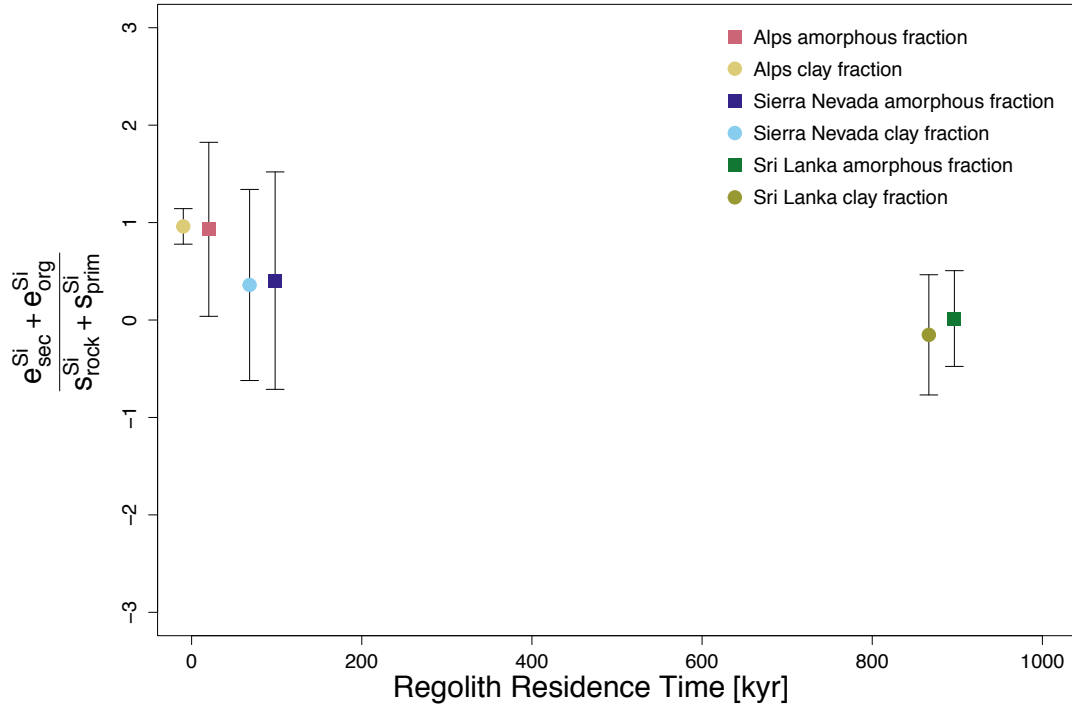
Figure 5.16: $1 - (\delta^{Si}_{sec} - \delta^{Si}_{rock})/\overline{\Delta^{Si}}$ of the amorphous and clay fraction against regolith residence time. For simplicity mean values for the amorphous and clay fraction of the individual sampling sites are shown. Error bars are the 2SD of all measured amorphous and clay samples. Note: Denudation rates are the same for all extracted fractions of an individual sampling site.

become redissolved and new "secondary" silicates (better named as tertiary, quaternary or even higher silicates) are formed out of an already light solution and are in consequence even lighter than the initial secondary precipitate (Cornelis et al., 2014).

It must be noted that the $(e^{Si}_{sec} + e^{Si}_{org})/(s^{Si}_{rock} + s^{Si}_{prim})$ ratio from Equation 5.9 is highly sensitive to the choice of the used $\overline{\Delta^{Si}}$ value. The dependence on the $\overline{\Delta^{Si}}$ value is large when the isotopic difference between $\delta(^{30/28}Si)_{sec}$ and $\delta(^{30/28}Si)_{rock}$ is large (Sri Lanka) and minor when the isotopic difference between $\delta(^{30/28}Si)_{sec}$ and $\delta(^{30/28}Si)_{rock}$ is small (Swiss Alps). It follows from Chapter 3 and Chapter 4 that the formation rate of secondary precipitates influences the isotope fractionation factor. The formation rates of secondary precipitates is also strongly related to the Al/Si ratio. A high Al/Si ratio indicates more available surface area, which might result in higher formation rates which correspond to larger Si isotope fractionation. Indeed a relation between the Al/Si ratio and the $\delta(^{30/28}Si)_{NBS28}$ value is observed for the amorphous as well as for the clay extracts in the three sampled sites. Higher Al/Si ratios result in lower $\delta(^{30/28}Si)_{NBS28}$ values of the amorphous and clay fraction (see Appendix Figure 5.55 and Figure 5.57). To account for this uncertainty, the $(e^{Si}_{sec} + e^{Si}_{org})/(s^{Si}_{rock} + s^{Si}_{prim})$ ratio is shown for $\overline{\Delta^{Si}}$ ranging from -1.5‰ to -5‰ (Figure 5.17).

While the choice of the $\overline{\Delta^{Si}}$ value alters the absolute value of the $(e^{Si}_{sec} + e^{Si}_{org})/(s^{Si}_{rock} + s^{Si}_{prim})$ ratio the pattern between the three individual sampling sites remains the same (Figure 5.17).
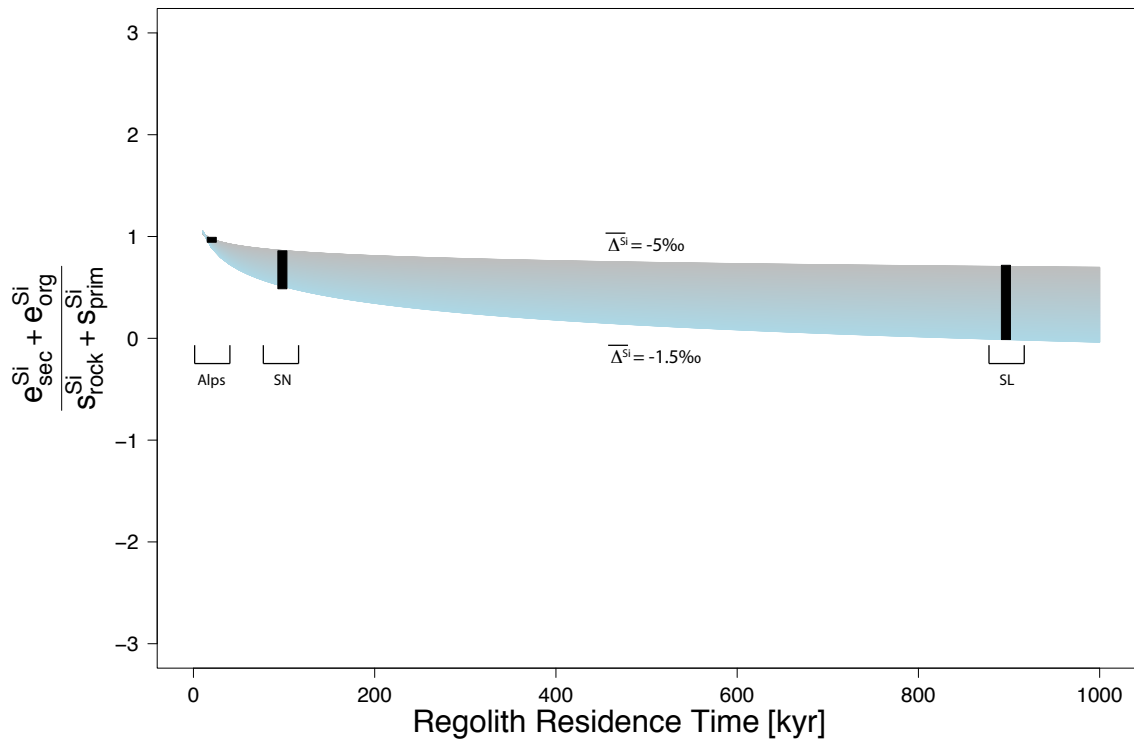
Figure 5.17: Relationship between the $(e^{Si}_{sec} + e^{Si}_{org})/(s^{Si}_{rock} + s^{Si}_{prim})$ ratio and regolith residence time. The colored area represent different $\overline{\Delta^{Si}}$ values from -1.5 ‰ (blue) to -5 ‰ (grey). Black rectangles represent corresponding $(e^{Si}_{sec} + e^{Si}_{org})/(s^{Si}_{rock} + s^{Si}_{prim})$ ratio for the different sampling site assuming different $\overline{\Delta^{Si}}$ values. Abbreviations SL, SN and SA denote Sri Lanka, Sierra Nevada and Swiss Alps, respectively.

5.6 Summary

This chapter summarizes $\delta(^{30/28}Si)_{NBS28}$ values derived from three different weathering regimes of extracted amorphous and clay phases from soils and saprolites. A method was derived to sequentially extract the amorphous and clay phase and subsequently measure them for their $\delta(^{30/28}Si)_{NBS28}$ values.

It is shown here for the first time that a strong relationship between Si isotopic composition of amorphous and clay phases extracted from soils and saprolites and the regolith residence time of the three different weathering regimes exists. An increase in regolith residence time leads to lower $\delta(^{30/28}Si)_{NBS28}$ values for secondary silicates formed. In Sri Lanka, the setting with the longest regolith residence time, the lowest $\delta(^{30/28}Si)_{NBS28}$ values for the amorphous and clay phase are measured. Extracted phases of the Sierra Nevada sampling site, where regolith residence time are shorter, show relative higher $\delta(^{30/28}Si)_{NBS28}$ values for the amorphous and clay phase. Amorphous and clay fractions of the Swiss Alps sampling site (lowest regolith residence time of all settings) show the highest $\delta(^{30/28}Si)_{NBS28}$ values of three sampled weathering regimes. An isotope mass balance model (Bouchez et al., 2013) reveal that the proportion of particulate export flux increases over the dissolved import Si flux according to the decrease in regolith residence time. This proportion is reflected in the $\delta(^{30/28}Si)_{NBS28}$ values of secondary precipitates.

5.7 Appendix Chapter 5

5.7.1 Background data

In this section all available data for the three described sites is provided to get a full overview of all settings. Most of the background data results from an ongoing "Section 3.4 - Earth Surface Geochemistry" project with the focus to better understand the processes of soil and saprolite formation in these three sites. The background data presented here are stored in the GFZ-EarthSurfaceGeochemistry-DataRepository (GFZ-ESG-DR).

Total element concentrations (see subsection 5.7.1 and subsection 5.7.4) were analyzed on bulk samples using X-ray fluorescence spectrometry (XRF, Panalytical Axios Advanced at German Research Center for Geosciences (GFZ)). All samples (bedrock, saprolite and soil) were oven dried at 60 ℃, and representative aliquots of the samples were pulverized in an agate mill to <60 μm grain size. Sample powders were weighed before and after treating them for 5 h at 600 ℃ to determine the loss on ignition (LOI). The remaining powder was then used for alkali fusion using Li-metaborate to produce glass beads that were analyzed for bulk chemical composition. Relative analytical uncertainties on the reported XRF data are about 5% for major elements and about 10% on trace elements.

Calculation of element concentrations and elemental chemical depletion

In the weathering literature a series of measurable parameters, such as the chemical depletion fraction (CDF) or the elemental mass transfer coefficient (τ), are used to describe the weathering regime of the sampled setting. The fraction of mass that is lost in their dissolved form due to chemical weathering has been termed by Riebe et al. (2001) as the chemical depletion fraction (CDF; Equation 5.10).

$$CDF = 1 - \frac{[Zr]_{rock}}{[Zr]_{weathered}} \tag{5.10}$$

where $[Zr]_{rock}$ and $[Zr]_{weathered}$ represent Zr concentrations in the parent bedrock and in the weathered material, respectively. When CDF $= 0$, no loss of soluble elements has occurred from saprolite or soil as compared to the parent material. A value of CDF > 0 quantifies the fraction of total mass lost during chemical weathering. In many lithologies the CDF value will not be >0.5. One reason for this is the large fraction of the primary SiO$_2$ that is locked in insoluble quartz. Another reason is the formation of secondary minerals and therefore the retention of Si, Fe, and Al released from primary minerals (Dixon and von Blanckenburg, 2012). Critical for the correct calculation of CDF values are a homogeneous and known concentrations of Zr in the parent material. Reported relative uncertainties of calculated CDF values are about 14% and result from error propagation of element concentration measured by XRF (relative uncertainty: major elements 5% and trace elements 10%).

The mass change of an element (X) in the soil/saprolite relative to the parent bedrock is defined as the dimensionless element-mass-transfer coefficient τ_X:

$$\tau_X = \frac{[X]_{weathered}}{[X]_{rock}} - \frac{[Zr]_{rock}}{[Zr]_{weathered}} - 1 \tag{5.11}$$

where $[X]_{weathered}$ and $[X]_{rock}$ represent concentrations of an element X in the weathered and parent bedrock material, respectively. When $\tau_X = 0$, X has not been lost as compared to the parent material; when $\tau_X < 0$ or $\tau_X > 0$, there is elemental loss or gain of element

115

X during weathering, respectively; τ_X = -1 means 100% loss of the element from parent bedrock to weathered material. It seems justified to use Zr as immobile element to calculate CDF and τ_X values in all sampled settings, see details in Hewawasam et al. (2013), Dixon et al. (2009a) and Norton and von Blanckenburg (2010).

Reported major element composition and Zr concentration of bulk samples in Table 5.8, Table 5.13 and Table 5.18 are derived from XRF analyses and are corrected for LOI. Using this LOI corrected element composition, CDF values as well as element-mass-transfer coefficient τ_X are calculated.

Background data - Sri Lanka

The presented background data for the Sri Lankan sampling site is discussed and described in detail in Hewawasam et al. (2013). Here only the main findings are summarized:

Element concentrations of the bulk soil samples of the sampled regolith profile show the expected picture of a soil developed over a Charnockite bedrock where Si, Al, Fe, K, Na, Fe and Ca are the dominant major elements (Figure 5.18). The dominating elements in the extracted amorphous fraction are Al and Si (see Figure 5.19 and Table 5.17). The element pattern of the clay fraction shows a clear enrichment of Al, Si and Fe compared the bulk soil (see Figure 5.20 and Table 5.17).

A significant variability in CDF is observed (using Zr as immobile element) within the regolith profile. The chemical depletion fractions (CDF; Equation 5.10) vary significantly within the sampled regolith profile. The upward gradual increase of CDF values from 0.1 to 0.6 from the saprolite bedrock interface at 10 m to the soil - saprolite boundary at a depth of 0.6 m indicates increasing chemical mass loss during bedrock to saprolite conversion (Figure 5.21). Chemical depletion fraction values of 0.6 within the saprolite indicate that up to 60% of the original rock mass is lost through chemical weathering.

Using again Zr as immobile element, element depletion profiles (τ-plots; Equation 5.11) were calculated for the entire profile (Figure 5.22). Depletion of Ca and Na throughout the whole regolith section can be observed (Figure 5.22). Mg, K, P, and Si show a depletion trend towards the surface of the regolith. Within the saprolite only Al shows no strong elemental depletion, but exhibits τ-values of -0.5 in the soil, indication Al loss in this upper zone. The element depletion profile for Mn shows a broad pattern from -0.5 at the saprolite-corestone zone boundary to values > 0.5 in 250 cm depth, to again depletion values of 0.5 at the saprolite - soil boundary. Only Fe and Ti show an enrichment within the saprolite and the soil relative to bedrock.

Large differences are observed for the evolution of the Al/Si ratio with depth of the different extracted fractions (Figure 5.23). The amorphous fraction always shows larger Al/Si ratios than the clay fraction. At the saprolite - soil boundary, at the saprolite - corestone zone boundary and within the corestone zone, large difference between the Al/Si ratios of the amorphous and clay fraction are observed. In contrast, differences in the Al/Si ratios of the amorphous and clay fractions between the two boundaries are minor. The Al/Si ratios of the clay fraction stay nearly constant over the whole regolith profile.
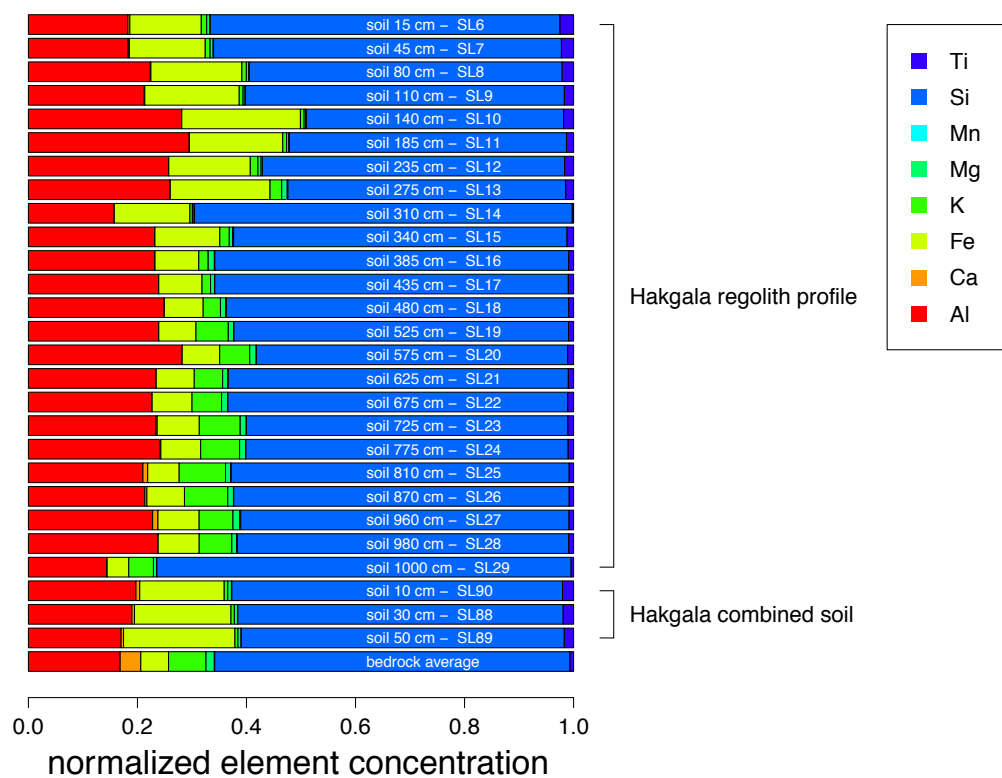
Figure 5.18: Element concentrations determined with XRF of bulk soil and saprolite samples of the Sri Lankan sampling site normalized to 100%.

Figure 5.19: Element concentrations determined with ICP-OES of the amorphous fraction calculated relative to total soil and normalized to 100%, extracted from soil and saprolite samples of the Sri Lankan sampling site.

117

Figure 5.20: Element concentration determined with ICP-OES of the clay fraction calculated relative to total soil, extracted from soil and saprolite samples of the Sri Lankan sampling site.
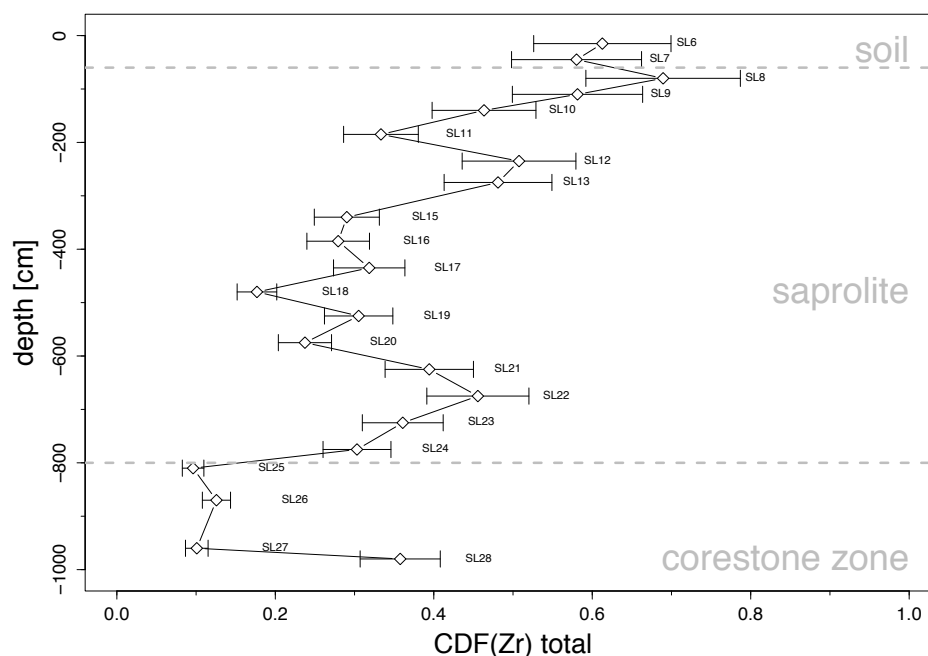
Figure 5.21: Depth profile of the chemical depletion fractions (CDF) based on Zr. The stippled lines at 60 cm and 800 cm denote the soil and the partially weathered corestones zone (Figure 5.2). The sampled regolith profile shows an increase in the degree of weathering from bottom to the top. Samples SL14 and SL29 showed unusual Zr concentrations (SL14: 4 times greater than the average Zr concentration in saprolite; SL29: half the Zr concentration of the bedrock) and were thus considered as outliers. Relative analytical uncertainty in CDF values is about 14%.
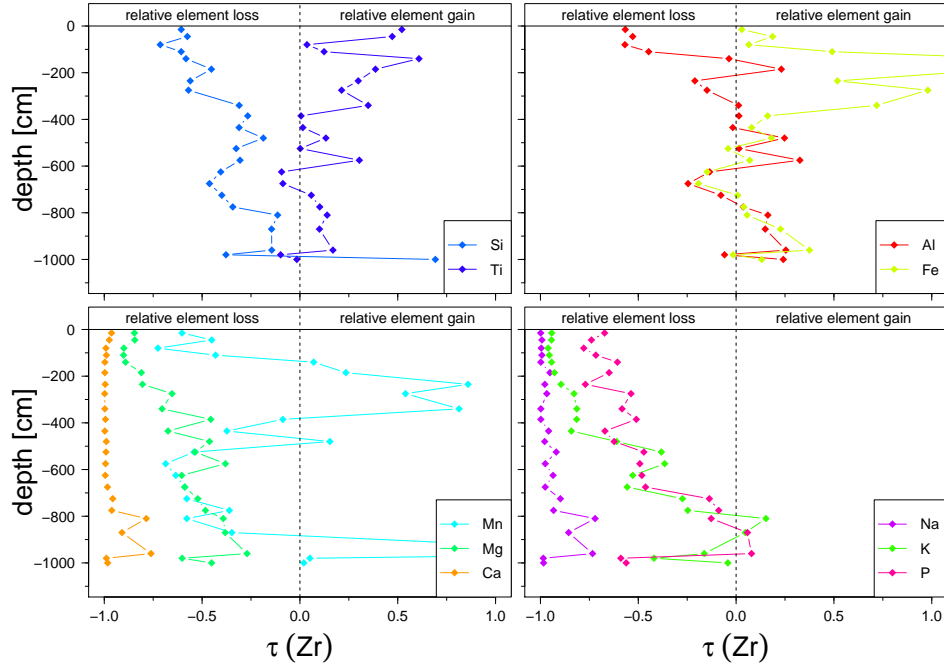
Figure 5.22: Depth profile of the element-mass-transfer coefficient $\tau(Zr)$ for the regolith profile of the Sri Lankan sampling site. The stippled lines at 60 cm and 800 cm denote the soil and partially weathered corestones zone (Figure 5.2). The "corestone-zone" shows highly variable $\tau(Zr)$ values. Based on analytical uncertainties of XRF measurements, the relative uncertainties in $\tau(Zr)$ values are estimated to be about 16% for major elements and about 20% for minor elements.
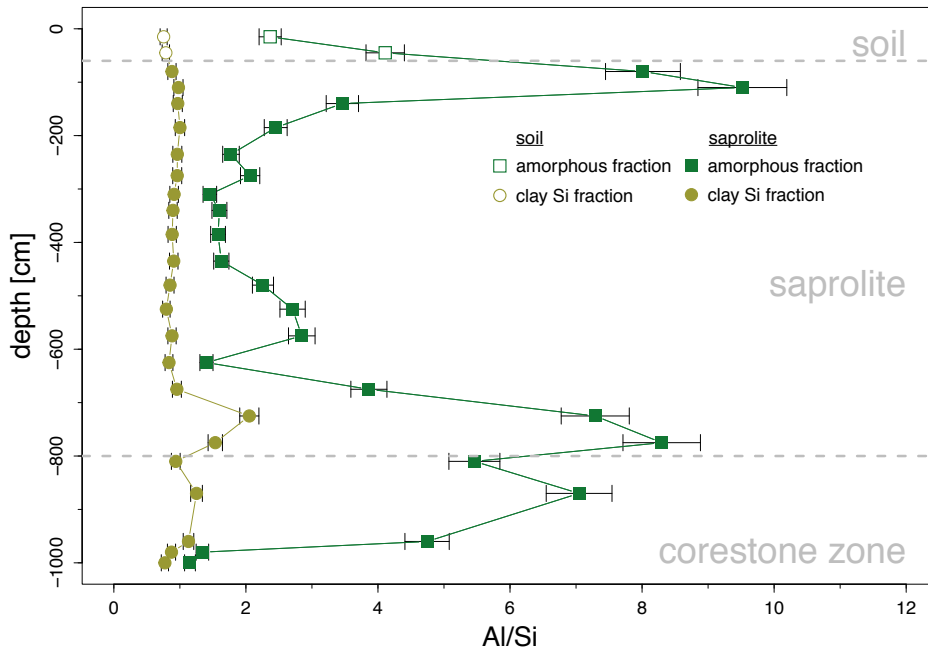
Figure 5.23: Depth profile of the Al/Si ratio of the amorphous and clay fractions for the regolith profile of the Sri Lankan sampling site. The Al/Si ratio of the amorphous fraction is always larger than the Al/Si ratio of the clay fraction. Large difference between the Al/Si ratios of the amorphous and clay fraction are observed at the saprolite-soil boundary, at the saprolite-corestone zone boundary and within the corestone zone. In contrast, the Al/Si ratios of the amorphous and clay fraction between the two boundaries do not show large differences.

119

Background data - Swiss Alps

In the following bulk soil element composition, CDF values, τ-profiles and the proportion of the amorphous and clay fraction for the soil profile B2 are shown. Representative element rock compositions, which are needed to calculate CDF and τ values have not been analyzed at the sampling site. Therefore the published average element concentrations of the gneissic bedrock in Table 2 in Norton and von Blanckenburg (2010) is used.

Element concentrations of the bulk soil samples of soil profile B2 show the expected picture of a soil developed over a gneissic bedrock where Si, Al, Fe, Ca, K, Mg and Na are the dominate major elements (Figure 5.24). The dominating elements in the extracted amorphous fraction are Si and Al and further Fe and K (see Figure 5.25 and Table 5.17). The clay fraction shows a pattern closer to the bulk soil, with the major elements being Si, Al, Fe, K and Mg (see Figure 5.26 and Table 5.17). Element ratios are different comparing bulk soil and the clay fraction (see Figure 5.24 and Figure 5.26).

The evolution of CDF values with depth of soil profile B2 shows that on average 30 to 40% of the original rock mass is lost through chemical weathering. For the B2 soil profile I observe that with decreasing depth the soil is more strongly weathered (CDF > 0.4) compared to the bottom of the soil profile (CDF < 0.4; Figure 5.27).

The constructed element-mass-transfer profiles (τ plots) for the sampled soil B2 shows a general depletion of Na, Si, Al and Ca and an enrichment for Fe, Ti, Mg and K at depth compared to the published bedrock values. The τ-profiles for Si, Al, Ca, Ti and K are fairly constant throughout the whole depth profile. Na and Mg show a trend towards higher element depletion with decreasing depth, whereas Fe first shows an enrichment and then a decrease with decreasing depth.

The evolution of calculated Al/Si ratios show large differences with depth for different extracted fractions. In general the amorphous fraction shows larger Al/Si ratios than the clay fraction, but no systematic pattern for the amorphous fraction with depth is observed when comparing the sampled soil profiles (Figure 5.29). Notably, a "bulge" structure exists within some soil profiles (e.g. B1,B2 and B5 in Figure 5.29). The Al/Si ratios of the clay fraction stay nearly constant within these soil profiles.
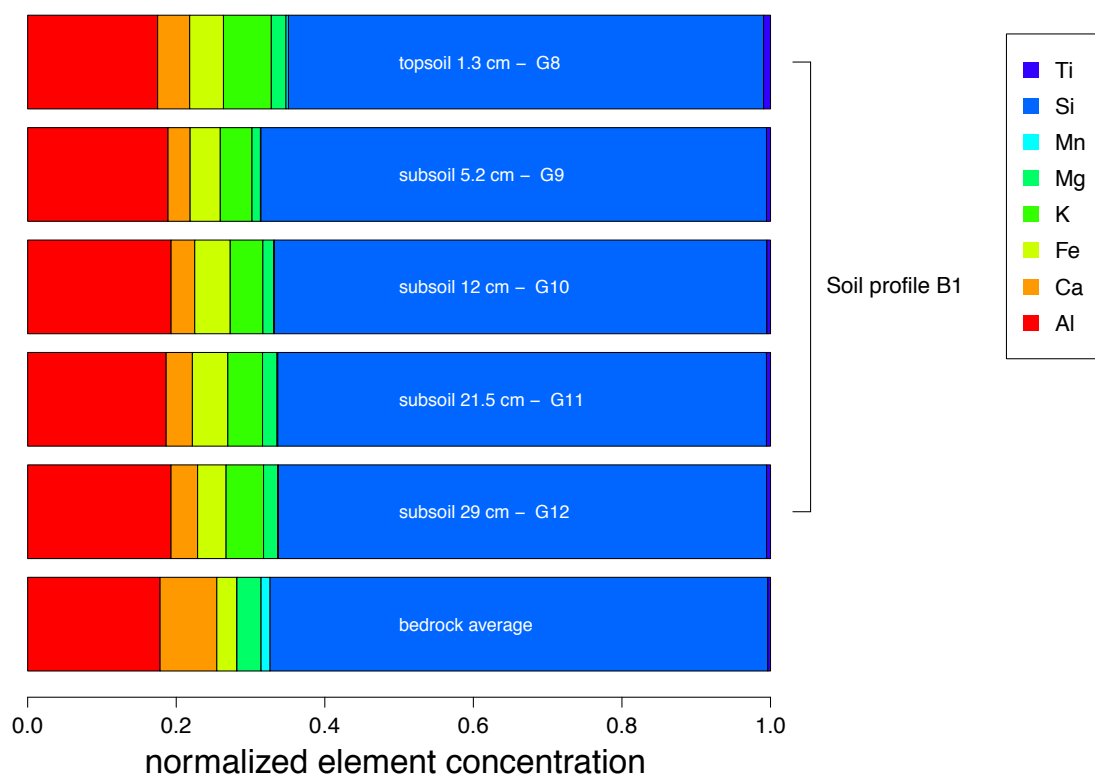
Figure 5.24: Element concentrations determined with XRF of bulk soil samples and normalized to 100% of the Swiss Alps sampling site in the upper Rhone valley.
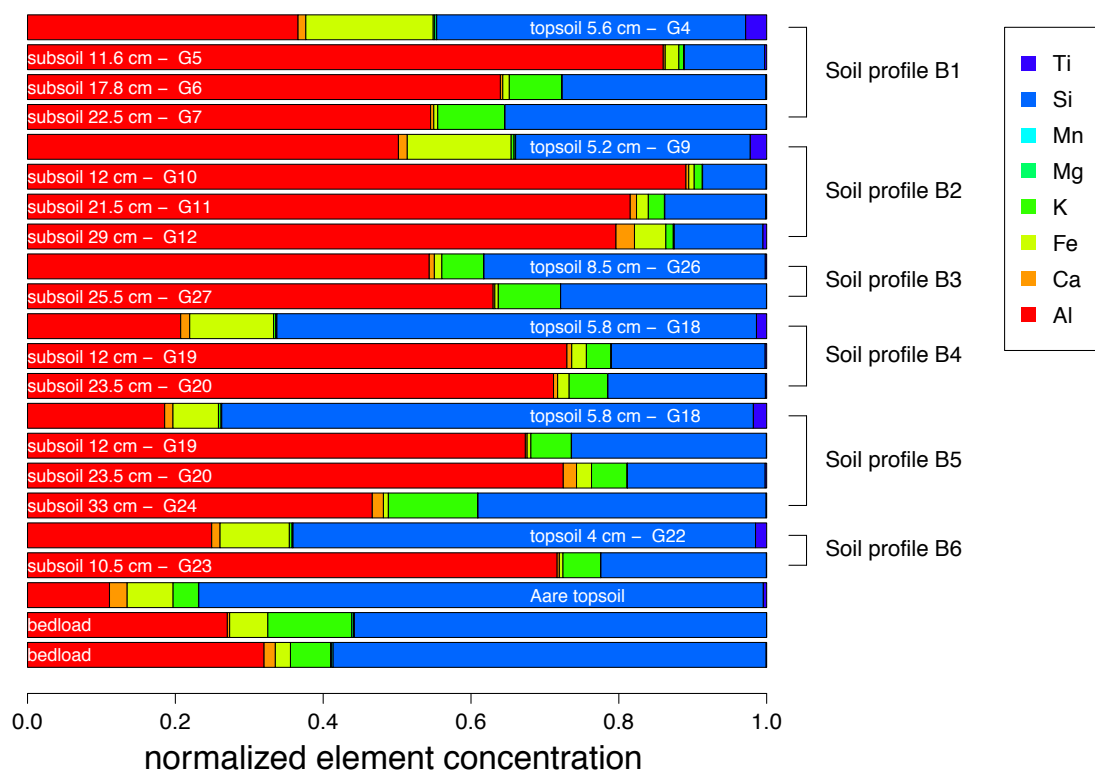
Figure 5.25: Element concentration determined with ICP-OES of the amorphous fraction calculated to total soil and normalized to 100%, extracted from soil of the Swiss Alps sampling site in the upper Rhone valley.
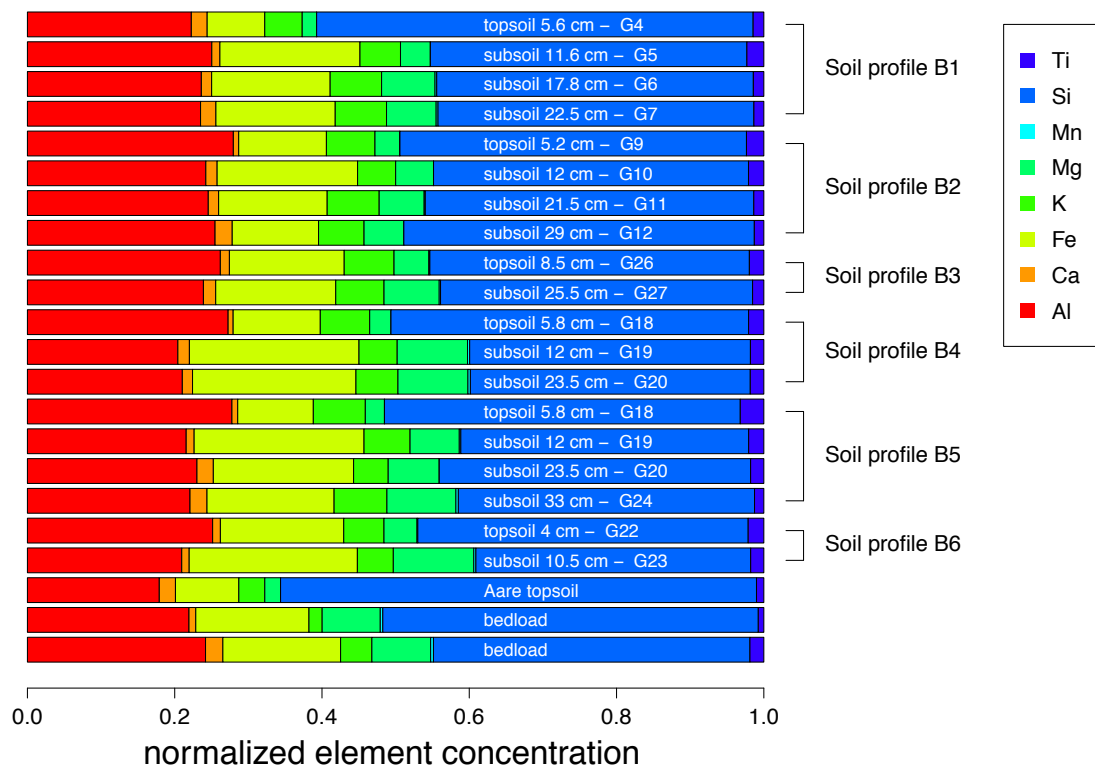
Figure 5.26: Element concentrations determined with ICP-OES of the clay fraction calculated to total soil and normalized to 100%, extracted from soil of the Swiss Alps sampling site in the upper Rhone valley.
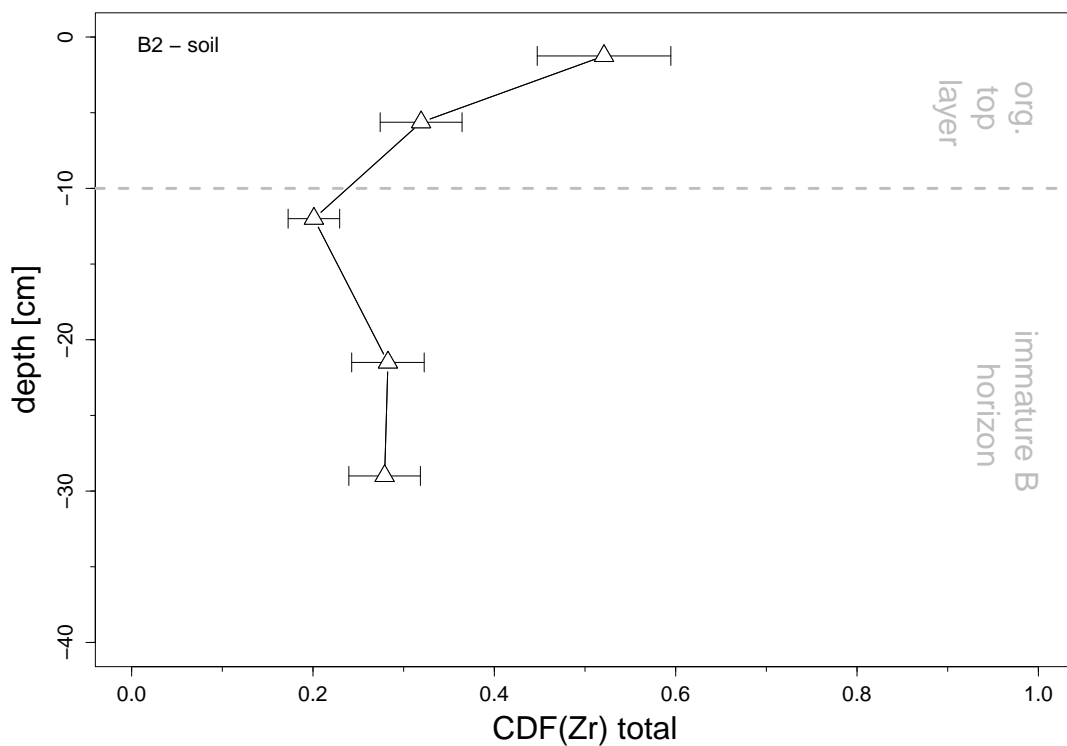
Figure 5.27: Depth profile of the chemical depletion fraction (CDF) of the B2 soil profile of the Swiss Alps sampling site in the upper Rhone valley.
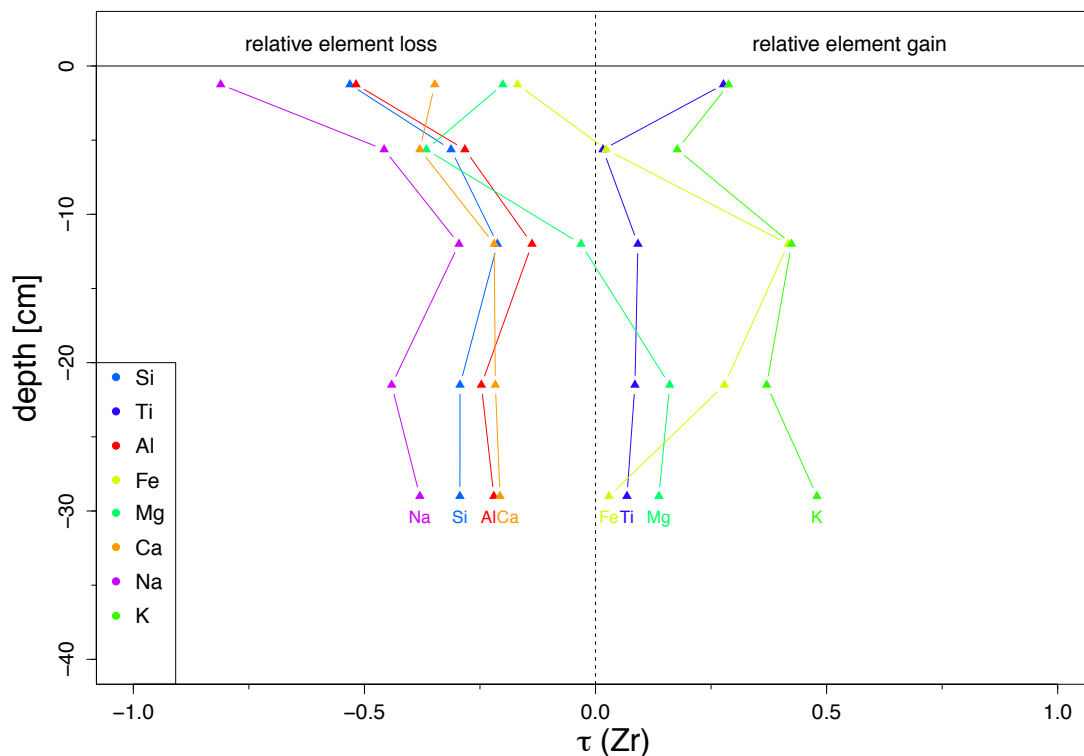
Figure 5.28: Depth profile of the element mass transfer coefficient $\tau(Zr)$ for the B2 soil profile of the Swiss Alps sampling site in the upper Rhone valley.
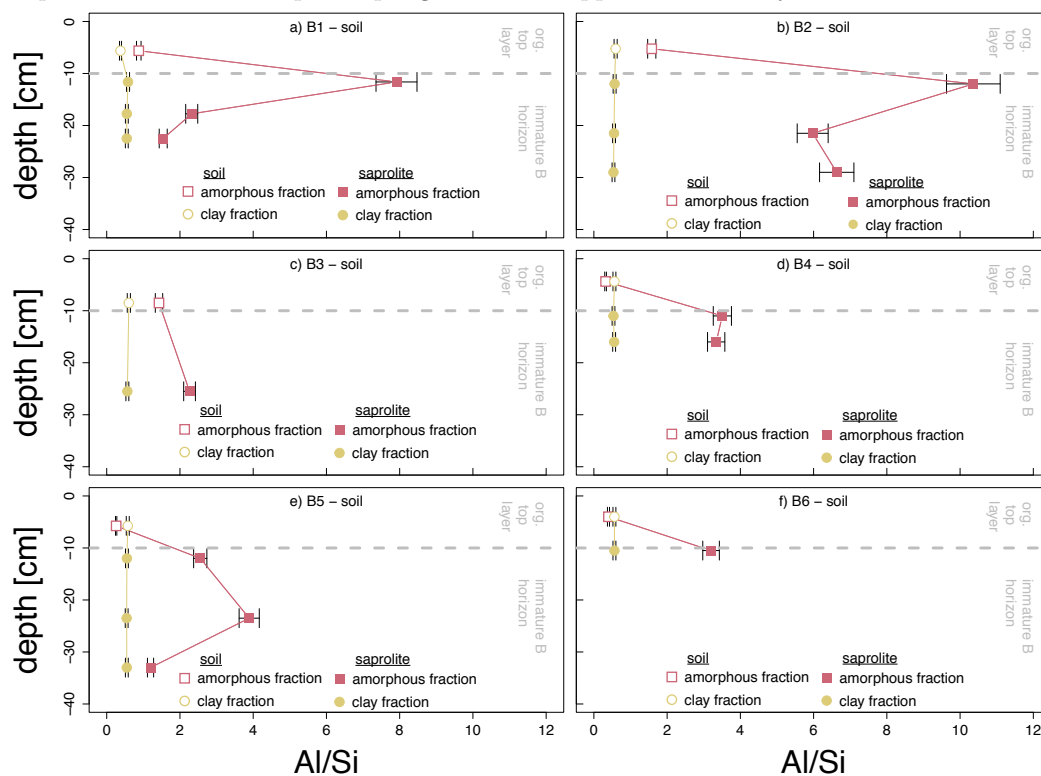
Figure 5.29: Depth profile of the Al/Si ratio of the amorphous and clay fraction for the soil profiles of the Swiss Alps sampling site in the upper Rhone valley. The Al/Si ratio of the amorphous fraction is always larger than the Al/Si ratio of the clay fraction. Large difference are observed between Al/Si ratios of the amorphous and clay fraction within the individual soil profiles.

Background data - Sierra Nevada

Element concentrations of bulk soil and saprolith samples show the expected picture of a soil/saprolith developed over a granitic bedrock where Si, Al, Fe, Ca, K, Mg and Na are the dominate major elements (Figure 5.30). The dominating elements in the extracted amorphous fraction are Si and Al (Figure 5.31 and Table 5.17). The clay fraction shows an elemental pattern closer to the bulk soil/saprolith, with the major elements being Si, Al, Fe, Ca, K and Mg (Figure 5.32 and Table 5.17). It seems that the element ratios are different when comparing bulk soil and clay fraction (compare Figure 5.30 and Figure 5.32).

To calculate correct CDF values and element-mass-transfer coefficients, it is important to use the parent material the weathered products are sourced from as reference material. To circumvent difficulties arising from inhomogeneous bedrock, we used the average of many sampled and analyzed source rocks and data from Hahm et al. (2014) for the major rock type ("Dinky Creek Granodiorite"). Therefore the elemental average of the available source rock data (GFZ and Hahm et al. (2014)) were used to calculate CDF values and element-mass-transfer coefficient.

The CDF values for the sampled Sierra Nevada soil and saprolite profiles show, that on average 30 to 40% of the original rock mass is lost through chemical weathering. For the deep soil profile of PC watershed P301, it can be observed that with decreasing depth the soil is less weathered compared to the bottom of the soil profile (Figure 5.33). A similar picture arises also for the shallow soil profiles of the watershed catchments P303 and P304 (Figure 5.34). The saprolite at the "Balsam" sampling site shows no trend with depth in terms of chemical depletion and shows CDF values of ~ 0.3. In contrast, the soil at the "Balsam" sampling site shows a strong chemical depletion of ~ 0.5.

Element-mass-transfer profiles (τ plots) for the sampled soil and saprolite profiles were calculated. The deep soil profile of the PC watershed P301 shows a general depletion of Ca, K, Mg, Mn, Na, Si, P, Al and Fe compared to the bedrock. Most of the τ-profiles are fairly constant throughout the whole depth profile, with the exception of Ca and K that show an enrichment in the topsoil compared to the subsoil. The two elements Mn and P show a strong enrichment in the topsoil.

The sampled shallow soil profiles in PC watersheds P303 and P304 show no evolution with depth for Ca, Mg, Na, Si, Al and Fe and a general element depletion in the soil. In both soil profiles Mn and P show a strong enrichment with decreasing depth in the topsoil. Only K shows an opposing trend for these two profils A general depletion of K in P303 and a general enrichment of K in P304.

The τ-profiles of the sampled saprolite at the "Balsam" sampling site shows a similar trend as the soil profiles. All measured elements are depleted compared to the averaged source rock, except the deepest sample that shows an enrichment of Si and K. The elements Mg, Mn, Si, K, Ti, Al and Fe are depleted in the saprolite profile and are relative constant from the bottom to the top of the profile. P, Na and Ca show a strong depletion trend with decreasing depth from τ-values < -0.25 to τ values < -0.75. The soil at the "Balsam" sampling site shows an enrichment of P and Mn relative to the saprolite.

Large differences are observed for the evolution of the Al/Si ratio with depth for the different extracted fractions. The amorphous fraction always shows larger Al/Si ratios than the clay fraction and a strong depth dependency with the soil. Within the deep soil profile of the PC watershed P301 Al/Si ratios are largest at depth and decrease with decreasing depth. The Al/Si ratios of the clay fraction stay nearly constant within this soil profile. Within the saprolite profile, Al/Si ratios of the clay and amorphous fraction

are similar and show no depth dependency.
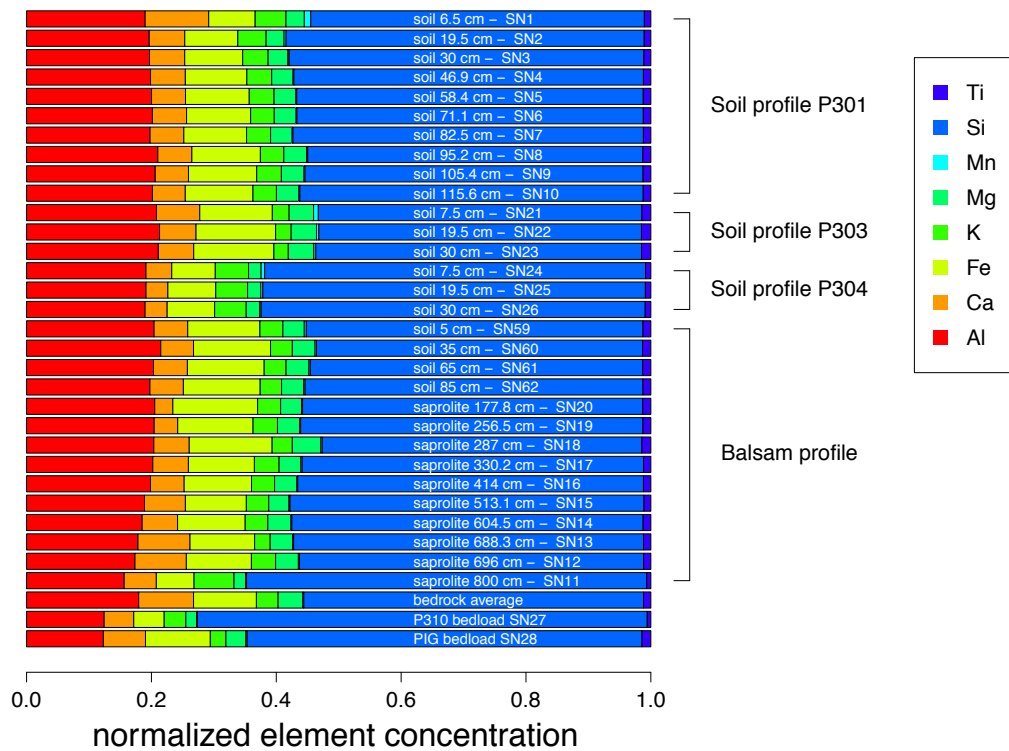
Figure 5.30: Element concentrations determined with XRF of bulk soil and saprolite samples of the Sierra Nevada sampling sites and normalized to 100%.
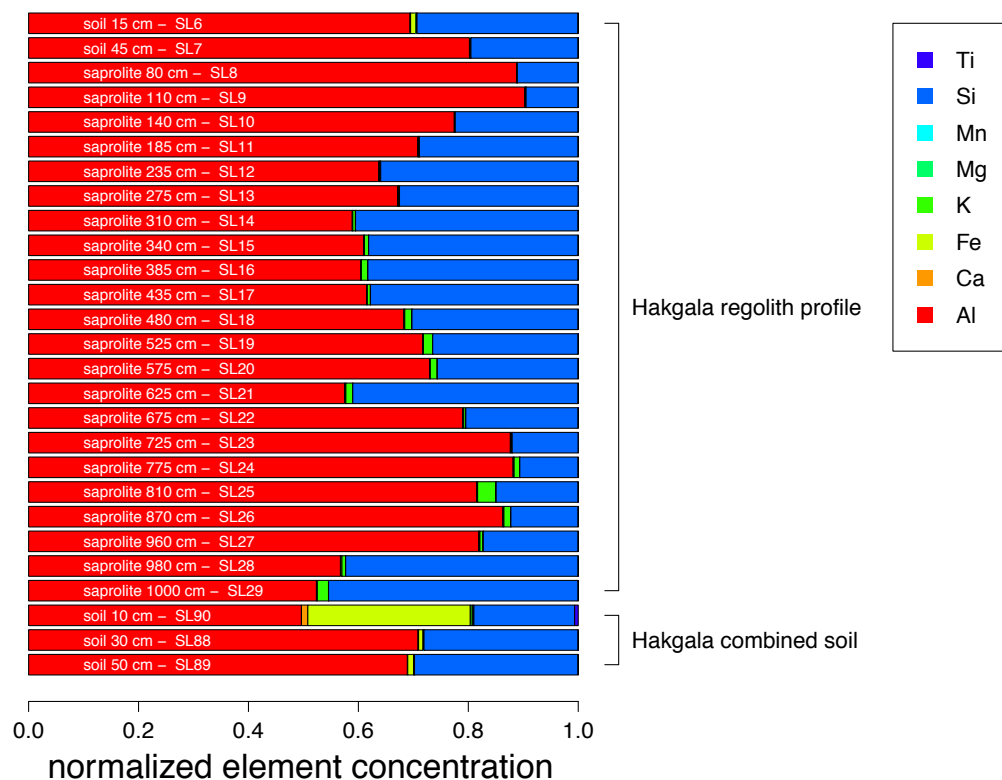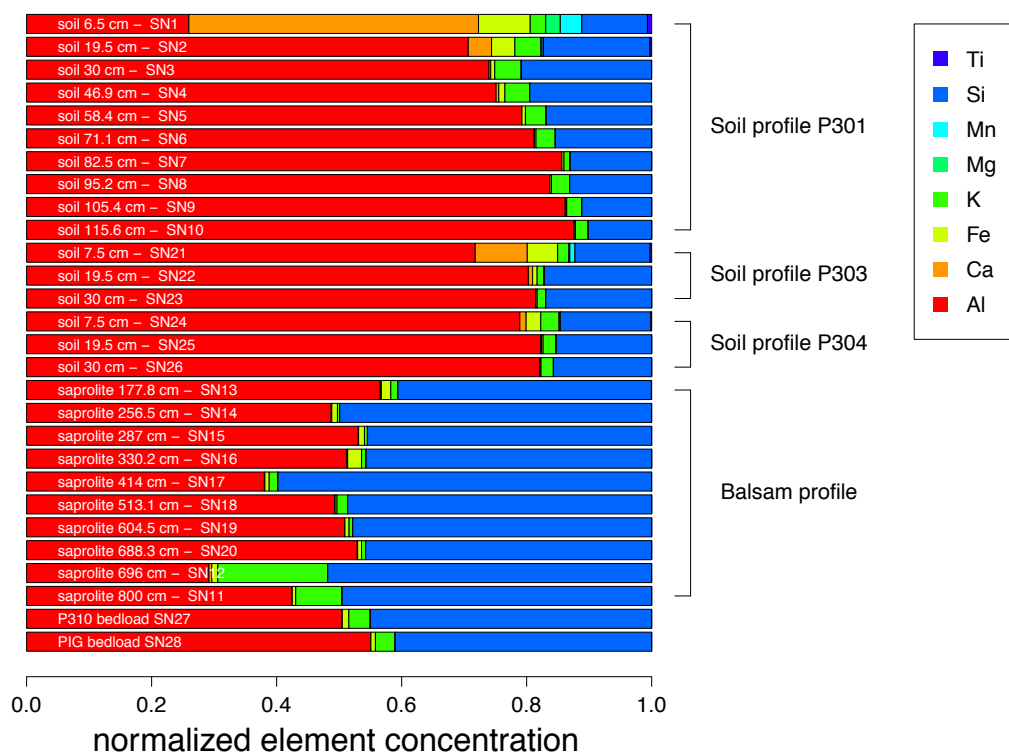
Figure 5.31: Element concentrations determined with ICP-OES of the amorphous fraction calculated relative to total soil and normalized to 100%, extracted from soil and saprolite samples of the Sierra Nevada sampling sites.
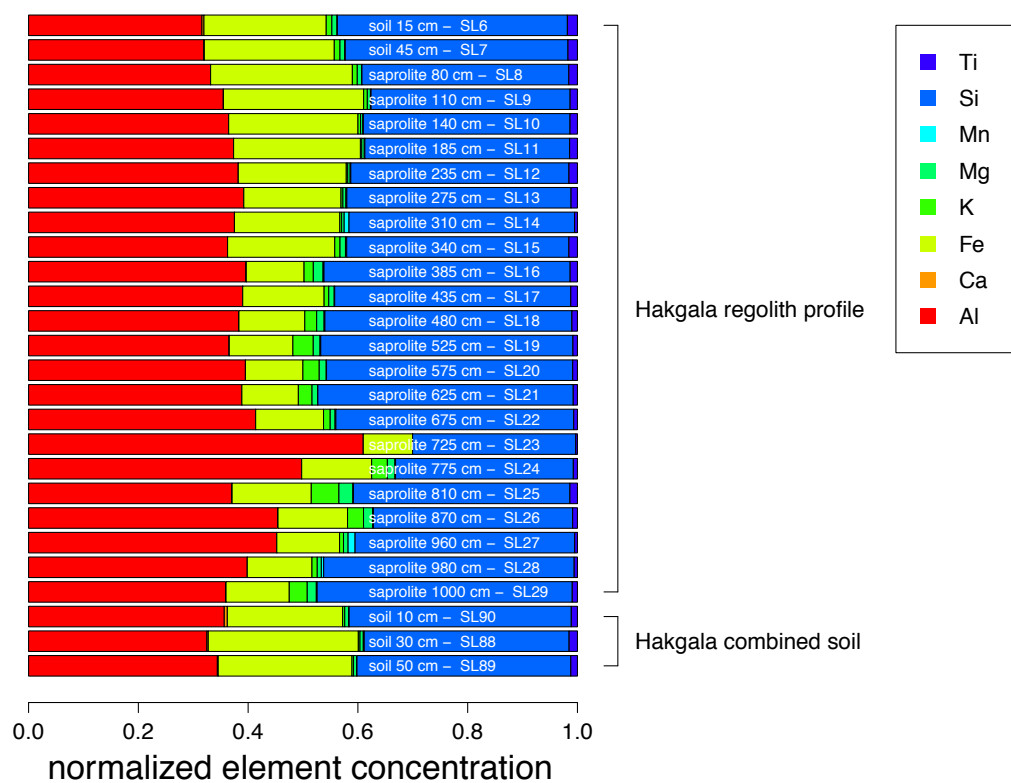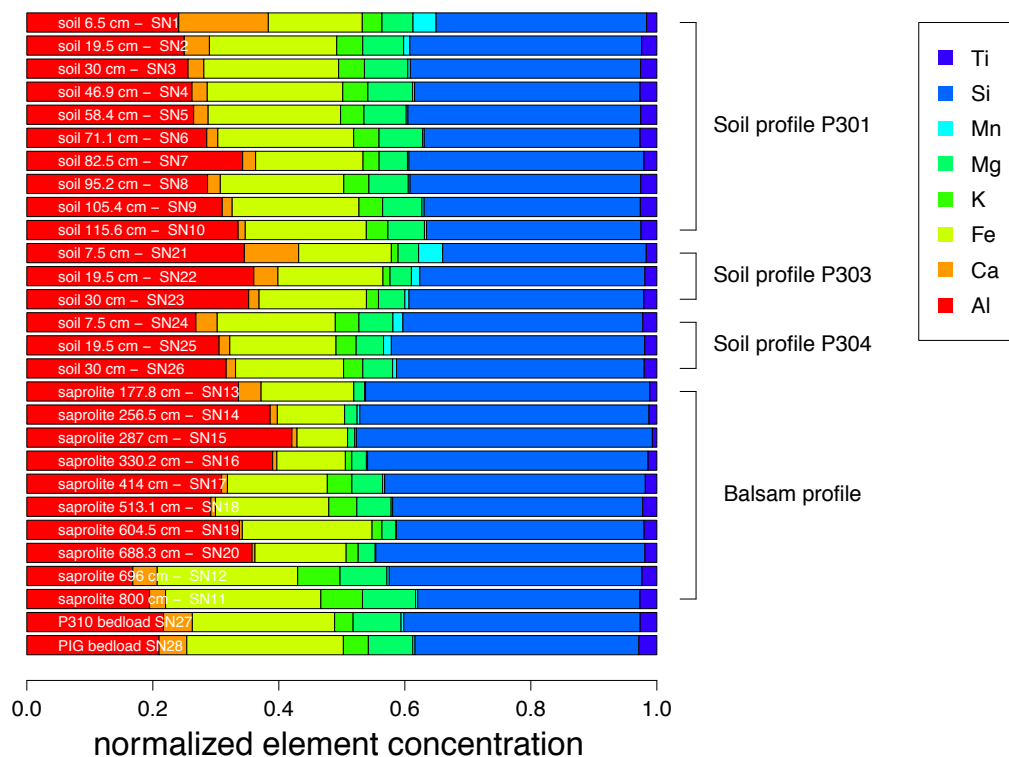

Figure 5.32: Element concentrations determined with ICP-OES of the clay fraction calculated relative to total soil and normalized to 100%, extracted from soil and saprolite samples of the Sierra Nevada sampling sites.
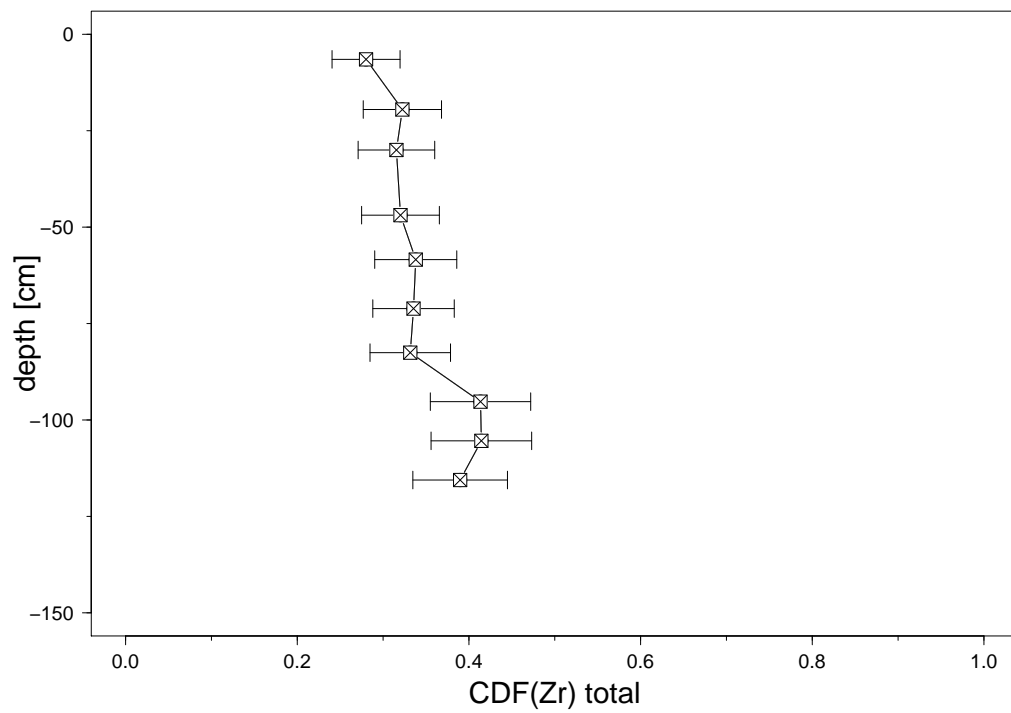
Figure 5.33: Depth profile of the chemical depletion fraction (CDF) of the deep soil profile of the PC watershed catchment P301.
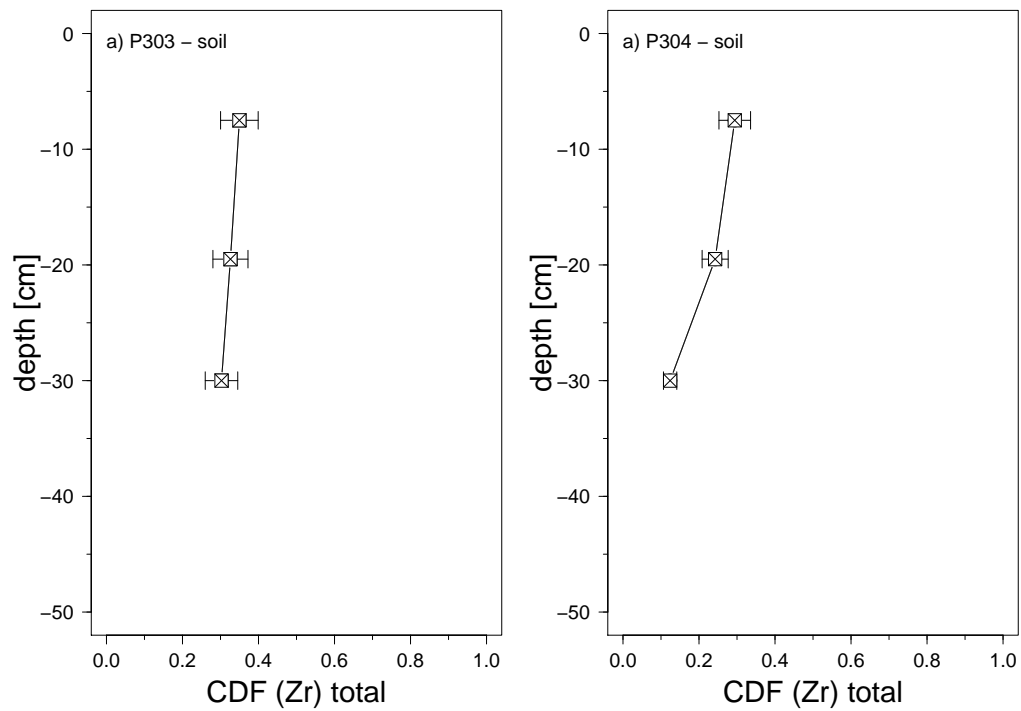
Figure 5.34: Depth profile of the chemical depletion fraction (CDF) of the shallow soil profiles of the PC watershed catchment P303 and P304.
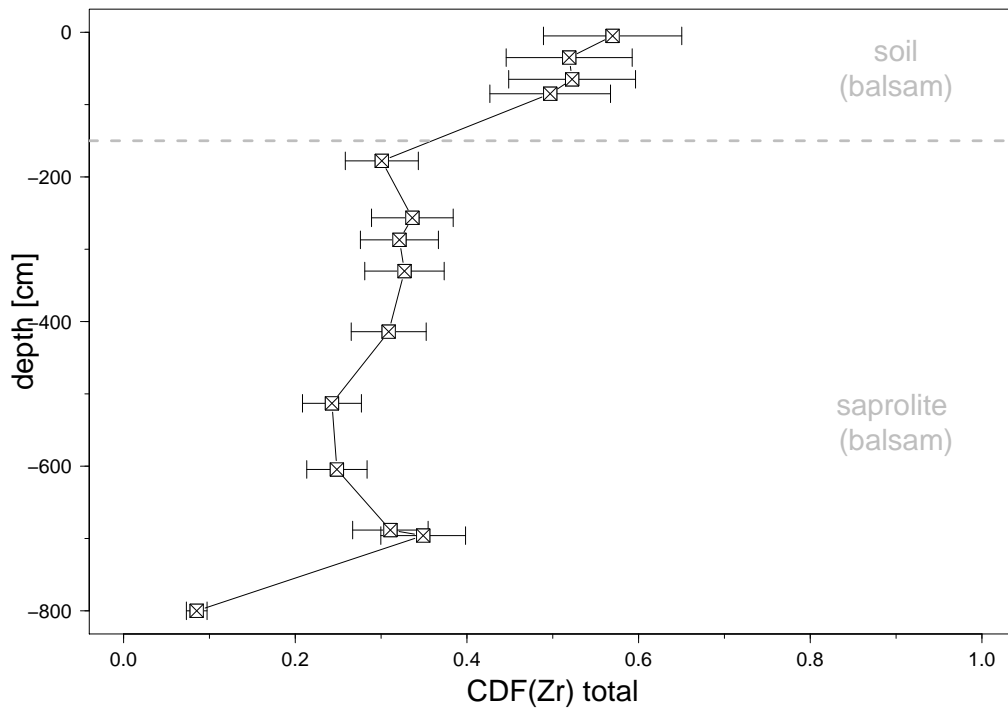
Figure 5.35: Depth profile of the chemical depletion fraction (CDF) for the "Balsam" regolith profile
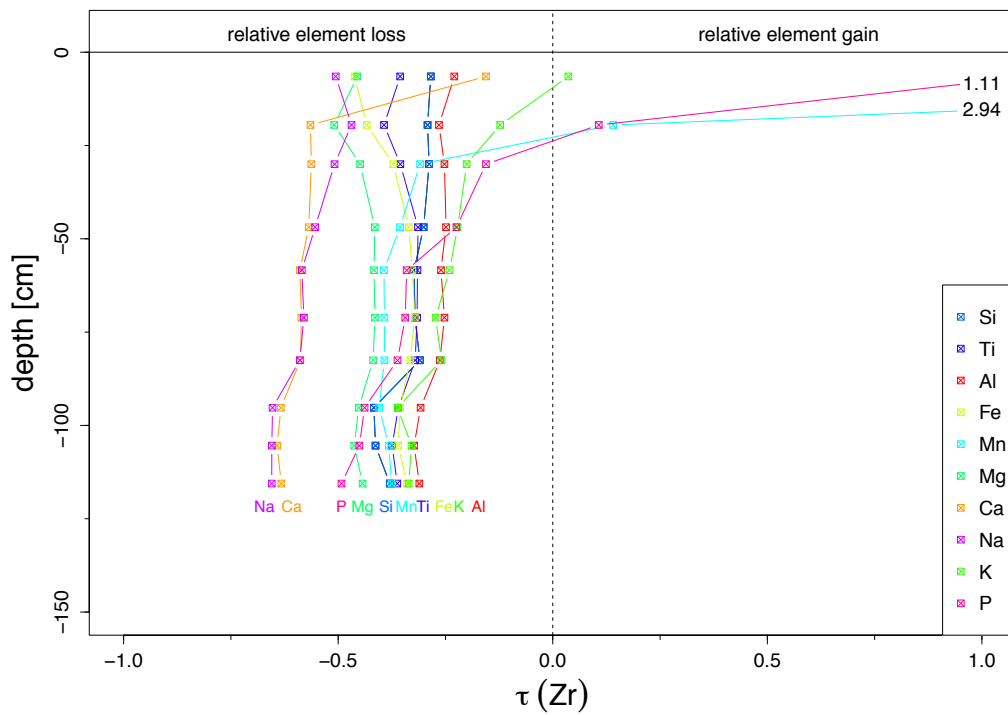
Figure 5.36: Depth profile of the element mass transfer coefficient $\tau(Zr)$ for the deep soil profile of the PC watershed P301.

128
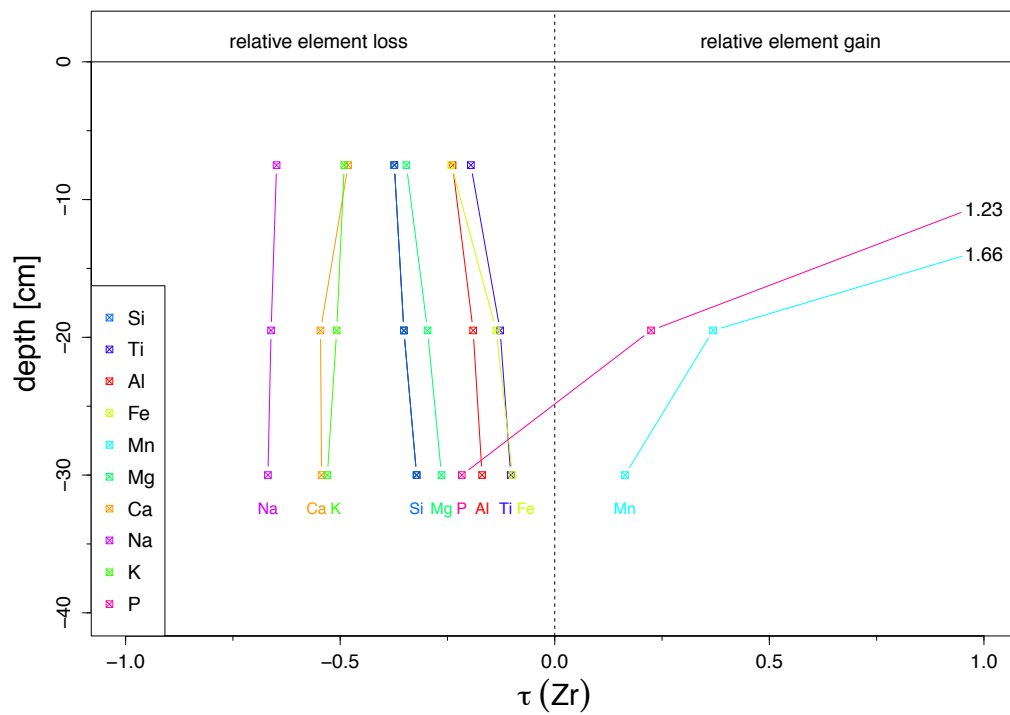
Figure 5.37: Depth profile of the element mass transfer coefficient $\tau(Zr)$ for the soil profile of the PC watershed P303.
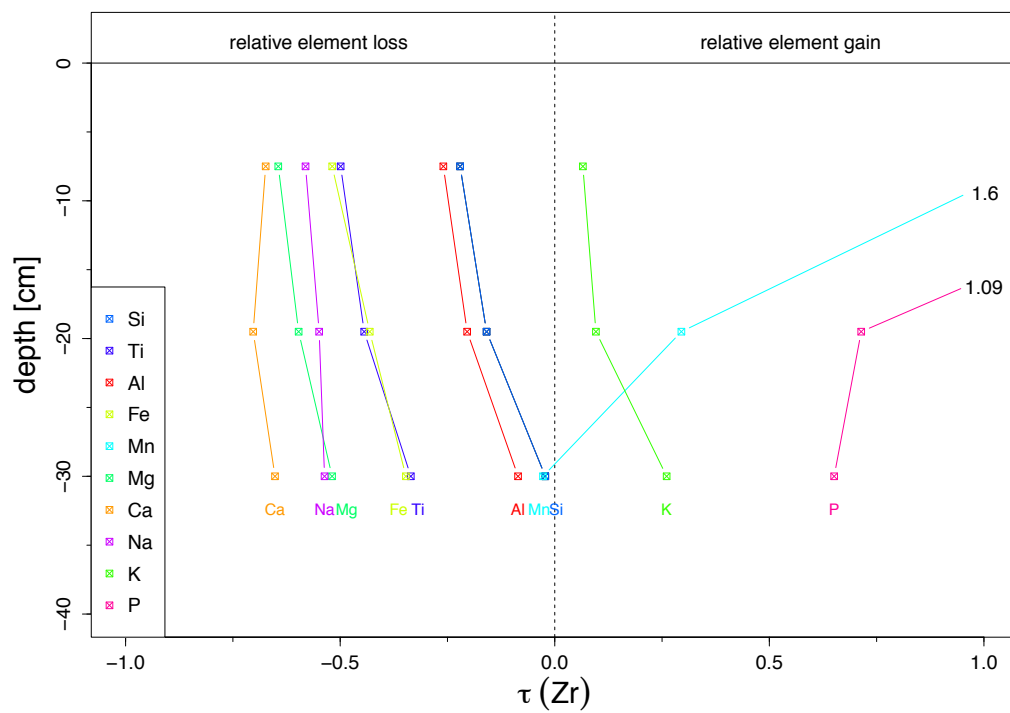
Figure 5.38: Depth profile of the element mass transfer coefficient $\tau(Zr)$ for the soil profile of the PC watershed P304.
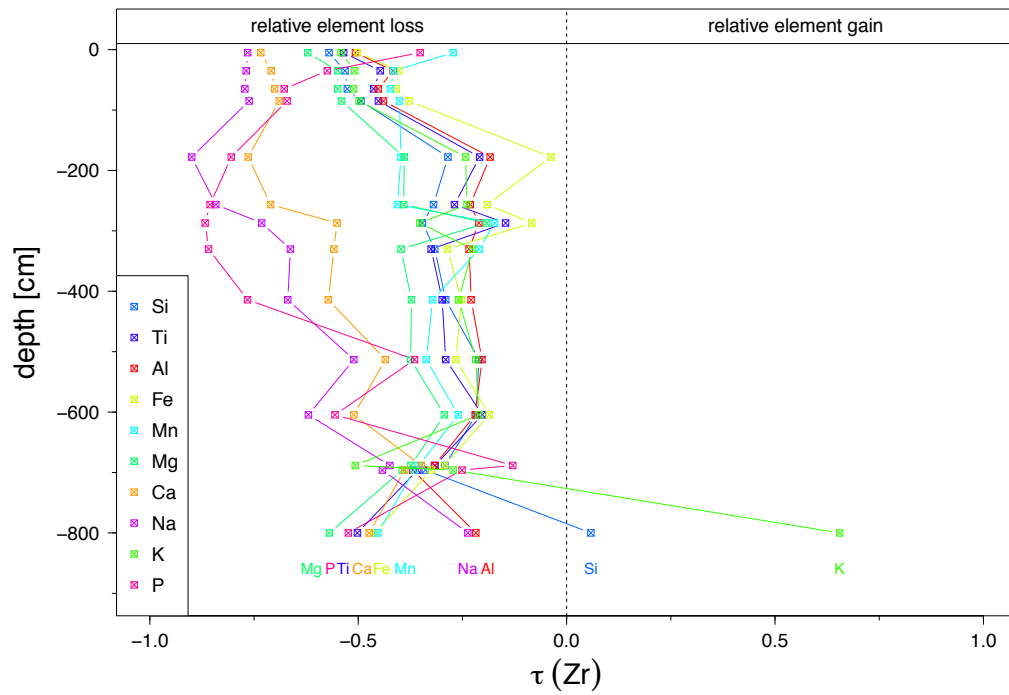
Figure 5.39: Depth profile of the element mass transfer coefficient $\tau(Zr)$ for the "Balsam" saprolite profile
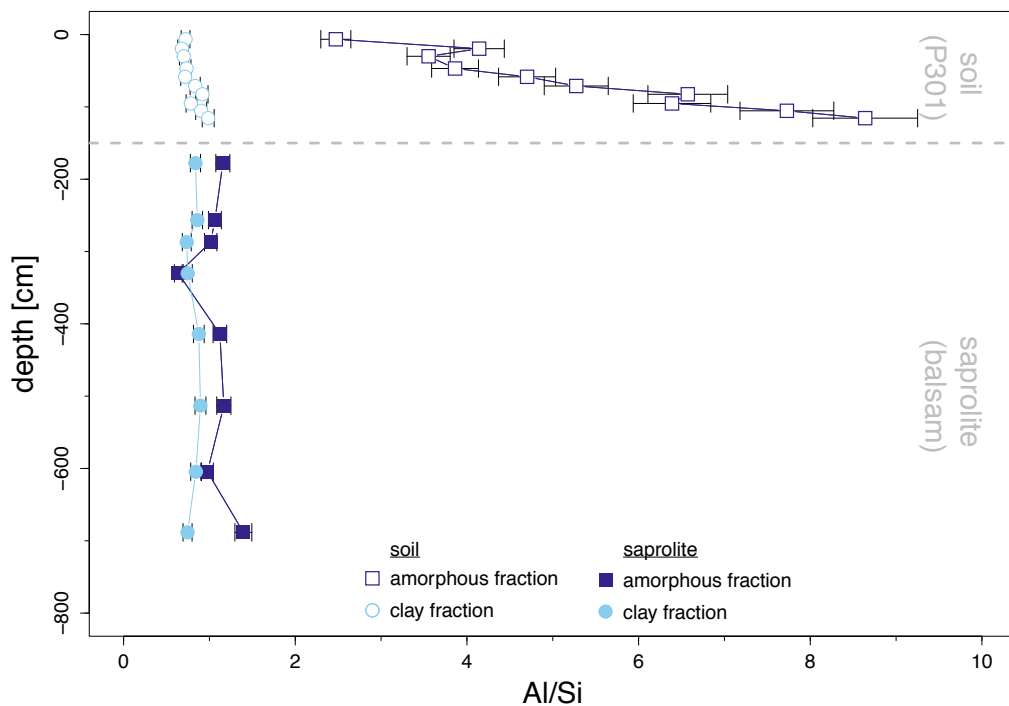
Figure 5.40: Depth profile of the Al/Si ratio of the amorphous and clay fraction for the deep soil profile of the PC watershed P301 and the "Balsam" saprolite profile. The Al/Si ratio of the amorphous fraction is always larger than the Al/Si ratio of the clay fraction. Large difference are observed between Al/Si ratios of the amorphous and clay fraction within the soil, whereas the Al/Si ratios of the amorphous and clay fraction within the saprolite show no large difference.
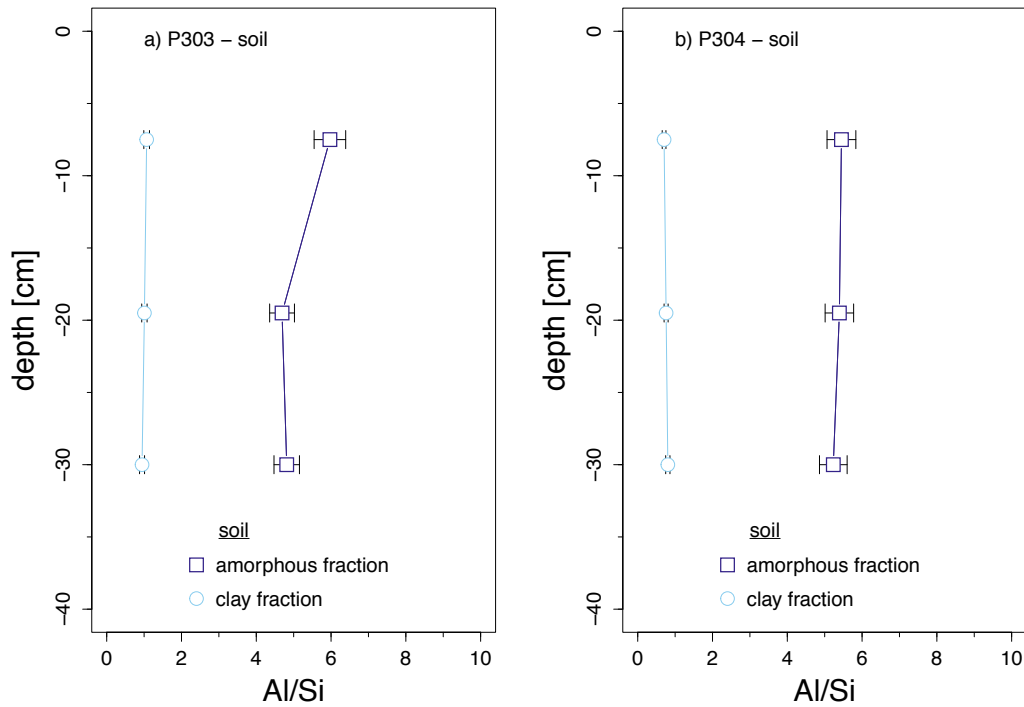
Figure 5.41: Depth profile of the Al/Si ratio of the amorphous and clay fraction for the shallow soil profiles of the PC watershed P303 and P304. The Al/Si ratio of the amorphous fraction is always much larger than the Al/Si ratio of the clay fraction.

5.7.2   Si isotope depth profiles

Sri Lanka

Within the sampled regolith and combined soil profile of the Sri Lankan sampling site the following isotopic patterns of the extracted amorphous and clay fractions were observed. The amorphous fraction in the regolith profile shows in general heavier isotopic values than the clay fraction without any gradual evolution with depth. Within the regolith profile two areas exist that do no follow this pattern. Extracted amorphous and clay fractions within the soil zone and extractions at the saprolite - corestone zone boundary of the regolith profile show lighter isotopic values for the amorphous fraction compared to the clay fraction (Figure 5.42). Within the soil zone of the regolith profile, both extracted fractions show a trend to heavier $\delta(^{30/28}Si)_{NBS28}$ values with decreasing depth.
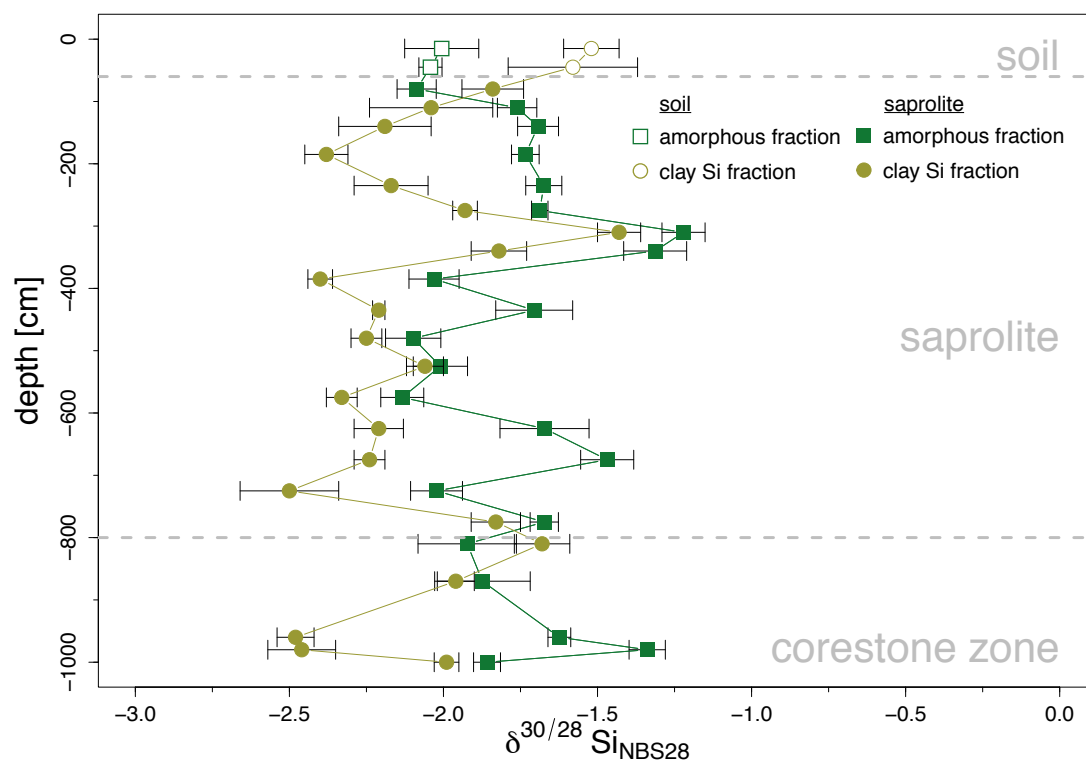
Figure 5.42: Si isotope depth profiles of the sampled regolith profile of the Sri Lankan sampling site. The isotopic signature of the amorphous fraction in general shows a larger $\delta(^{30/28}Si)$ value compared to the isotopic composition of the clay fraction, except for the soil and the saprolite - corestone zone boundary. Both fractions do not show a gradual evolution with depth in their Si isotopic signature within the saprolite, which is in contrast to the soil profile where with decreasing depth both fractions become heavier in their $\delta(^{30/28}Si)_{NBS28}$ values.
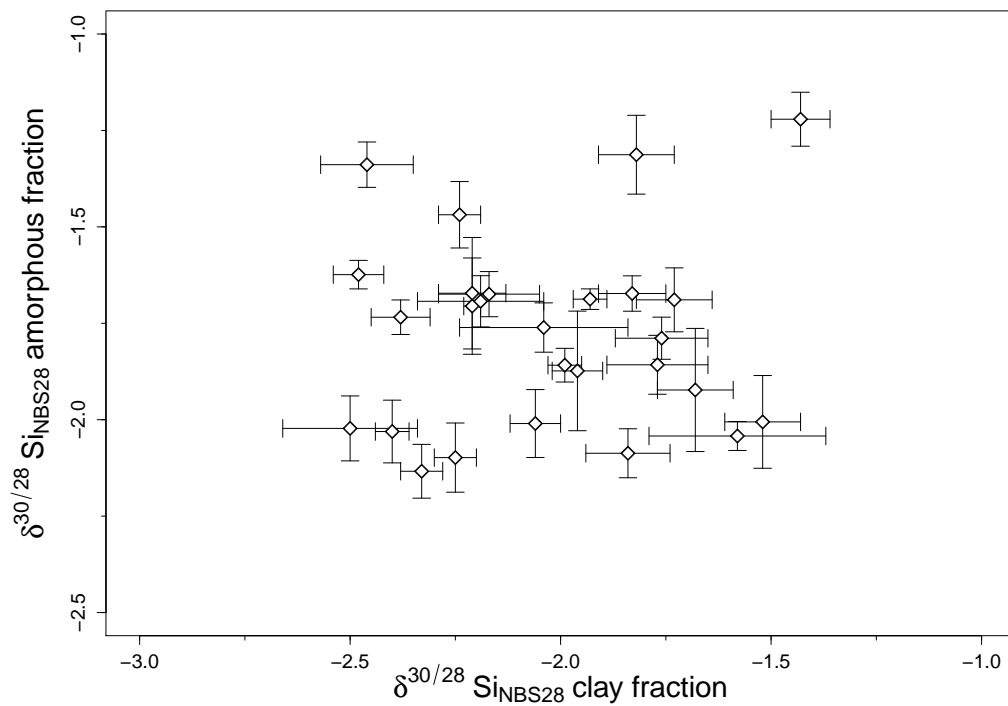
Figure 5.43: The $\delta^{30/28}Si_{NBS28}$ of the amorphous fraction plotted against the $\delta^{30/28}Si_{NBS28}$ of the clay fraction. No correlation between the two fractions is observed.
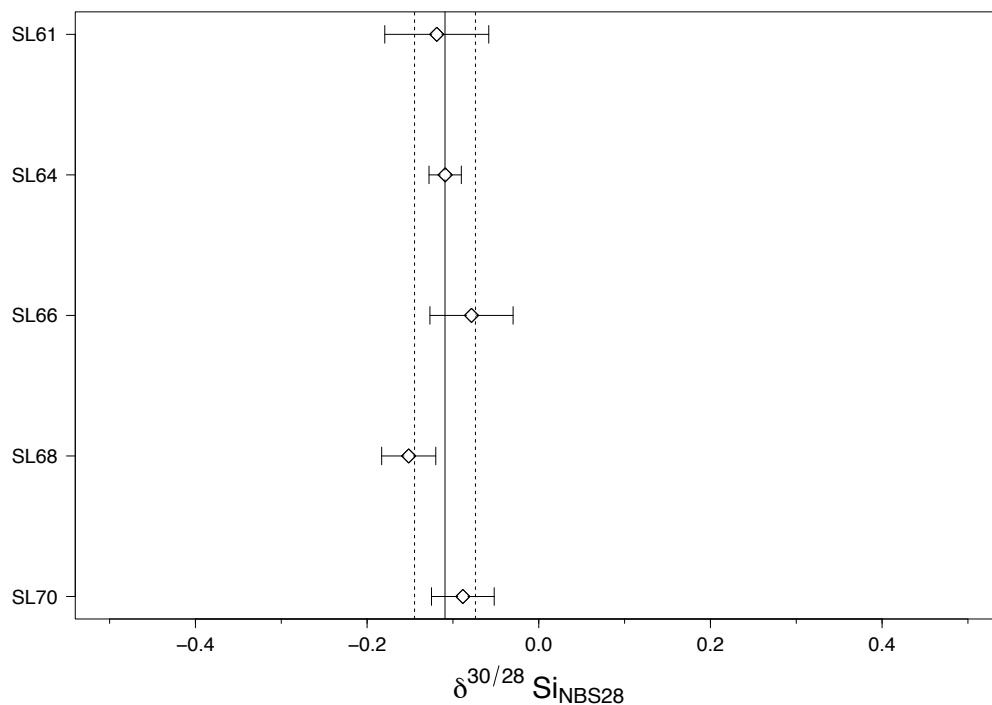
Figure 5.44: Si isotope composition of bulk bedrock samples of the Sri Lankan sampling site resulting in an average bulk bedrock signature of $\delta(^{30/28}Si)_{bedrock}=$ -0.11 ‰. The black line represent the mean value of the 6 measured bedrock samples and the dotted line represent the 95% confidence interval.

Swiss Alps

Within the sampled soil profiles in the Swiss Alps the following isotopic trends of the extracted amorphous and clay fractions are observed. The amorphous fraction shows in general heavier isotopic values than the clay fraction in the subsoil. One exception of this pattern is the deepest sample in soil profile B2 which shows lighter isotopic values in the amorphous fraction compared to the clay fraction. Where the soil profiles were deep enough for taking several depth samples, I note that the isotopic signature of the amorphous fraction is fairly constant with depth in the subsoil. Without exception, all extracts of the amorphous fraction in the topsoil layer show always lighter isotopic signatures than the clay fraction.

The isotopic signature of the clay fraction are fairly constant with depth and fall within a range between $\delta(^{30/28}Si_{NBS28})$= -0.54‰ to -0.21‰, which is the expected range of $\delta(^{30/28}Si)_{NBS28}$ values for primary minerals in the clay phase (Ding et al., 1996; Georg et al., 2009).
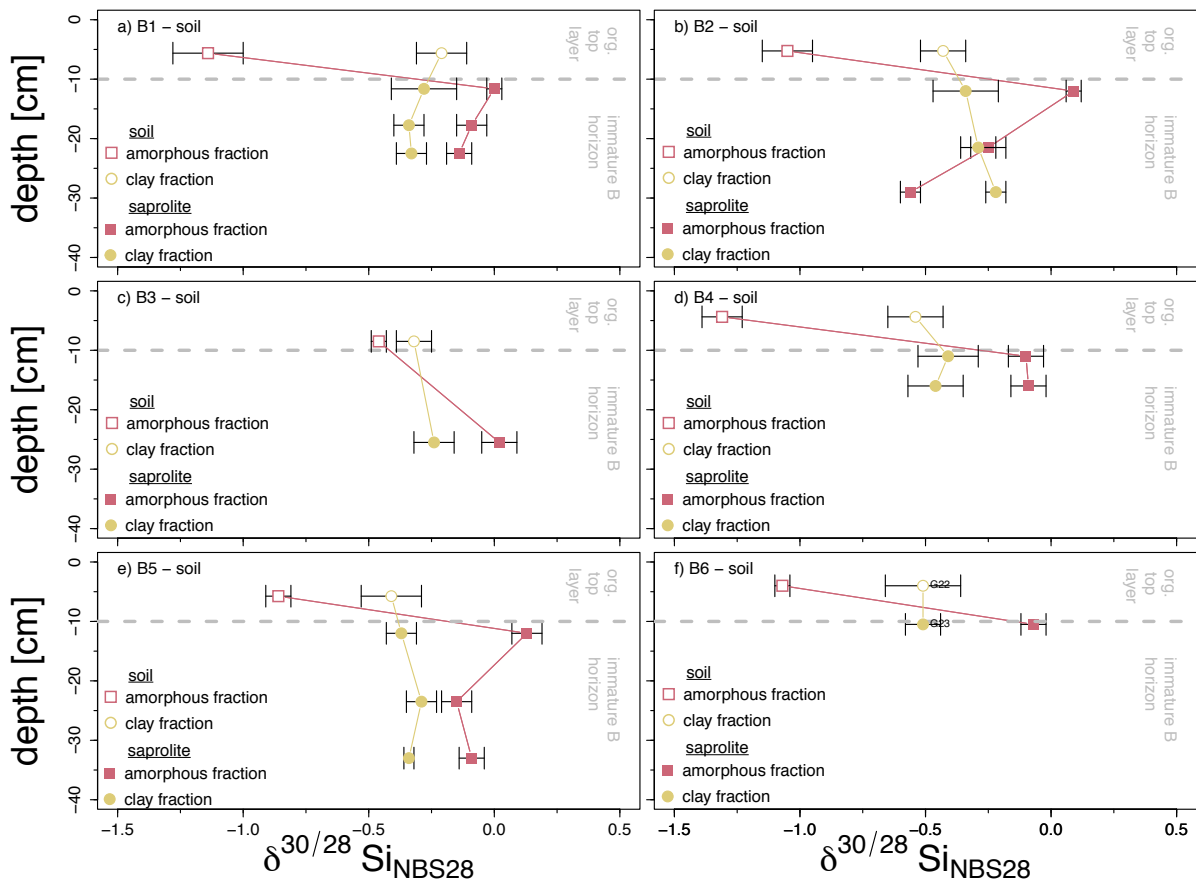
Figure 5.45: Si isotope depth profiles of the sampled soil profiles of the Swiss Alps sampling site in the upper Rhone valley. The isotopic signature of the amorphous fraction shows that in the subsoil, with one exception in soil profile B2, always a heavier signature in $\delta(^{30/28}Si)$ values exists compared to the isotopic composition of the clay fraction. In contrast to the subsoil extracts, the topsoil shows in all sampled profiles always lighter $\delta(^{30/28}Si)_{NBS28}$ values for the amorphous fraction compared to the clay fraction. The isotopic signature of the clay fraction is fairly constant and nearly similar within all sampled soil profiles.
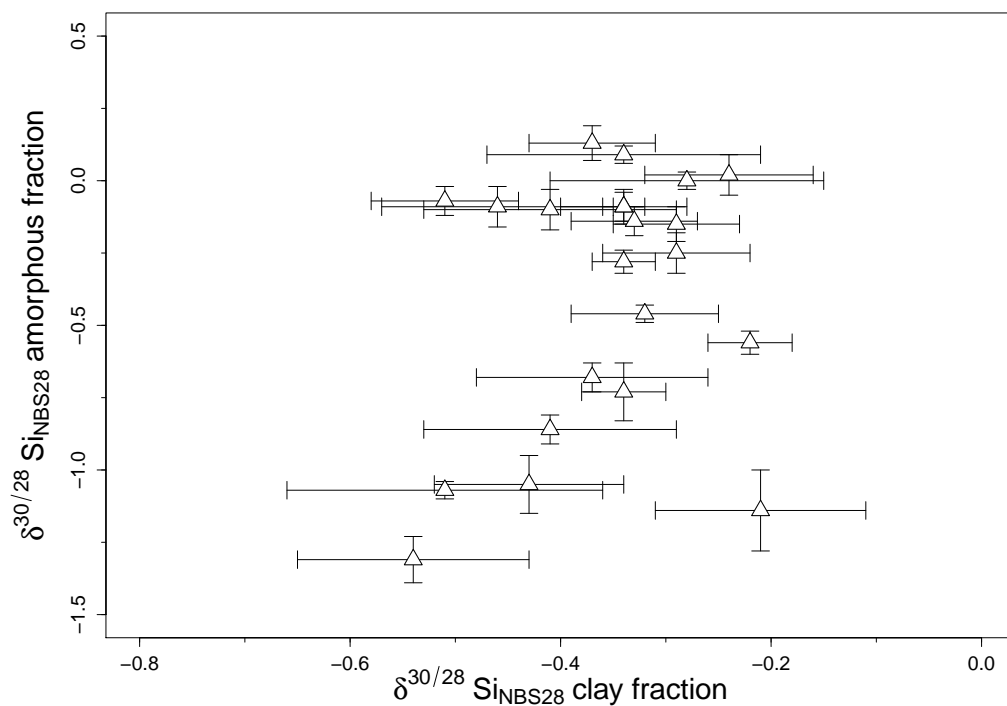
Figure 5.46: The $\delta^{30/28}Si_{NBS28}$ of the amorphous fraction plotted against the $\delta^{30/28}Si_{NBS28}$ of the clay fraction. Only a weak correlation between the isotopic composition of the amorphous fraction and the clay fraction for extracted fractions of the Swiss Alps sampling site is noted.
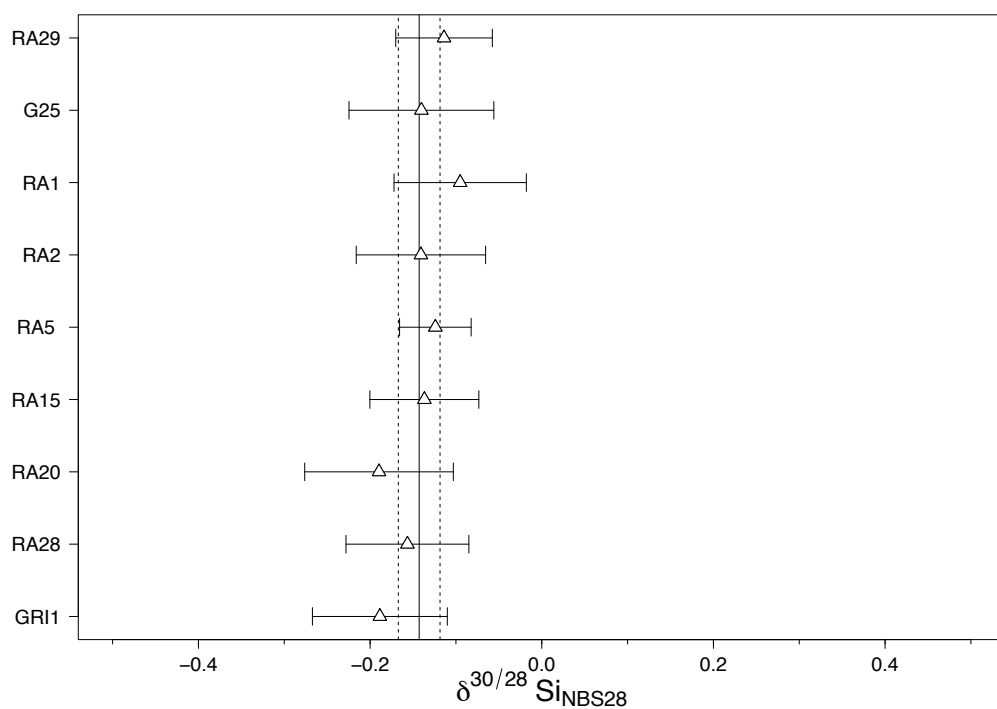
Figure 5.47: Si isotope composition of bulk bedrock samples of the Swiss Alps sampling site resulting in an average bulk bedrock signature of $\delta(^{30/28}Si)_{bedrock}$= -0.14 ‰. The black line represent the mean value of the 9 measured bedrock samples and the dotted line represent the 95% confidence interval.

Sierra Nevada

The isotopic composition of the amorphous and clay fractions of the deep (0-120 cm) soil profile P301 show a strong dependency with depth (Figure 5.48): The amorphous fraction shows Si isotope signatures $\delta(^{30/28}Si)_{amorphous}$ from -0.8‰ at the surface, to -1.9‰ in 120 cm depth (Figure 5.48). The clay fraction of this soil profile shows Si isotope signatures $\delta(^{30/28}Si)_{clay}$ from -0.7‰ at the surface, to -1.3‰ in 120 cm depth (Figure 5.48). The shallow soil profiles of the PC watersheds P303 and P304 show in general also an enrichment of ^{28}Si in the amorphous fraction, with one exception: For the upper most sample in the soil profile in watershed P303, the $\delta^{30/28}Si_{NBS28}$ value for the amorphous fraction is indistinguishable from the clay fraction within uncertainty. Both soil profiles in these catchment show a depth dependency, where both profiles show much lighter $\delta^{30/28}Si_{NBS28}$ values at depth compared to the top soil for the amorphous fraction, and slightly lighter $\delta^{30/28}Si_{NBS28}$ values at depth compared to the top soil for the clay fraction. I further observe a strong linear correlation between $\delta(^{30/28}Si)_{amorphous}$ and $\delta(^{30/28}Si)_{clay}$ for all soil profiles (Figure 5.51). Within the deep "Balsam" saprolite profile a different picture emerges. Here I observe an enrichment of ^{28}Si in the clay fraction compared to the amorphous fraction. The amorphous fractionation does not show an evolution with depth, but a large spread in their isotopic composition ($\delta(^{30/28}Si)_{amorphous}$: average=-0.9‰, sd=0.3‰, ul=-1.3‰, ll=-0.5‰). The clay fraction also does not show an evolution with depth and a slightly smaller variation in their isotopic composition compared to the amorphous fraction ($\delta(^{30/28}Si)_{clay}$: average=-1.9‰, sd=0.2‰, ul=-2.1‰, ll=-1.5‰).
No correlation between the isotopic composition of the amorphous fraction $\delta(^{30/28}Si)_{amorphous}$ and the clay fraction $\delta(^{30/28}Si)_{clay}$ is observed in the "Balsam" saprolite profile (Figure 5.51).

136
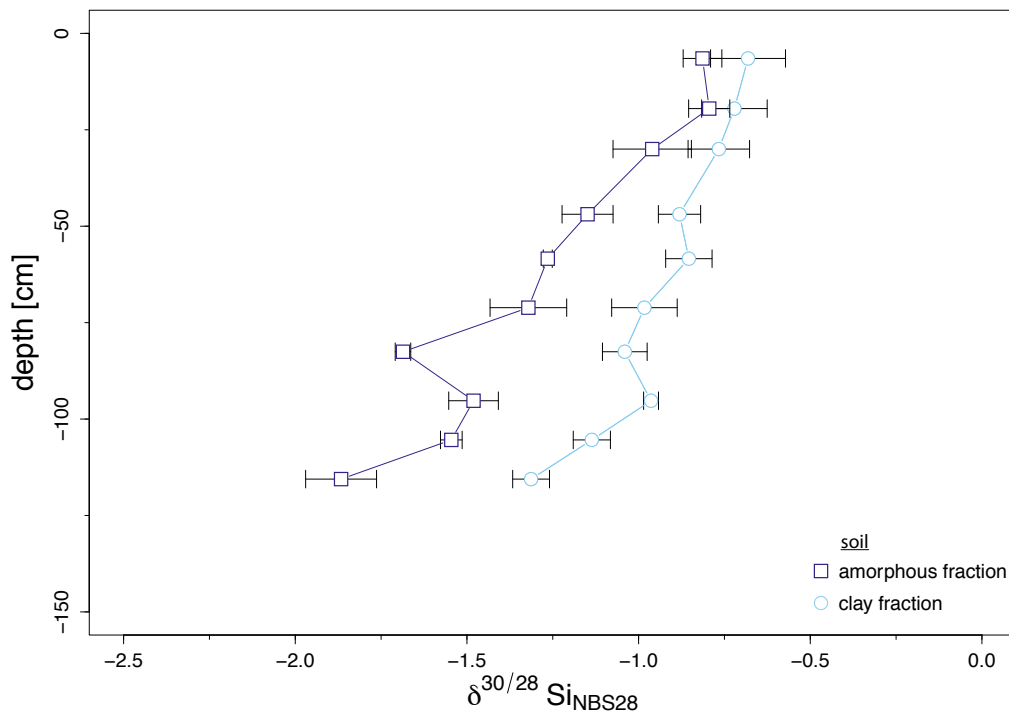
Figure 5.48: Si isotope depth profiles of the sampled soil profile at PC watershed P301. The isotopic signature of the amorphous fraction always shows a lower $\delta(^{30/28}Si)$ value compared to the isotopic composition of the clay fraction. Both fractions show a decrease in their Si isotopic signature from the top of the soil profile to the bottom.
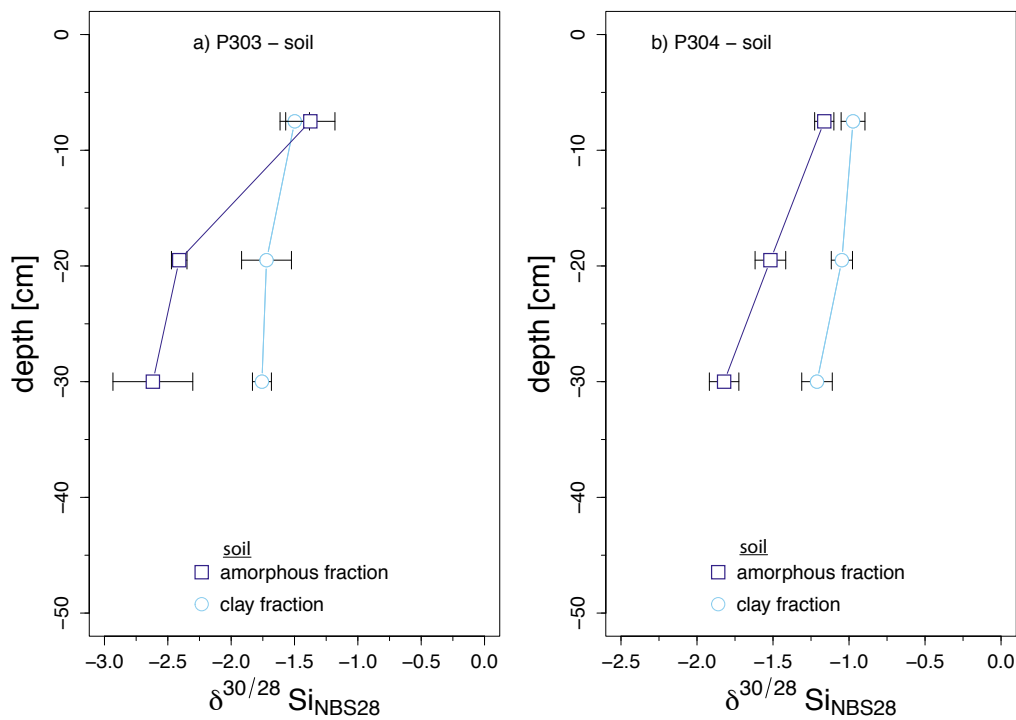
Figure 5.49: Si isotope depth profiles of the sampled soil profile at PC watershed P303 and P304. The isotopic signature of the amorphous fraction always shows a lower $\delta(^{30/28}Si)$ value compared to the isotopic composition of the clay fraction.

137
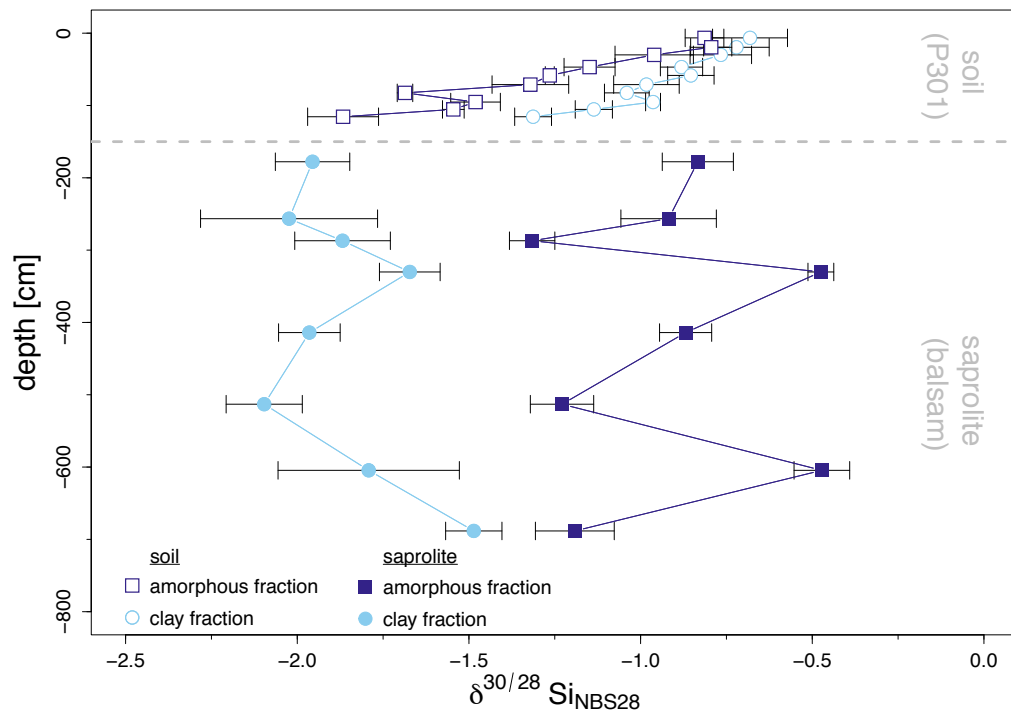
Figure 5.50: Depth profile of the isotopic composition of the amorphous and clay fraction of the saprolite. On top of the "Balsam" saprolite profile, the isotopic composition of the deep soil profile P301 is plotted for comparison (Figure 5.48). There exist a clear distinction between the soil and saprolite regarding their isotopic compostion of the amorphous and clay fraction. Whereas the amorphous fraction in the soil is isotopically lighter than the clay fraction we see the reverse effect in the saprolite with an isotopically lighter clay fraction compared to the amorphous fraction.
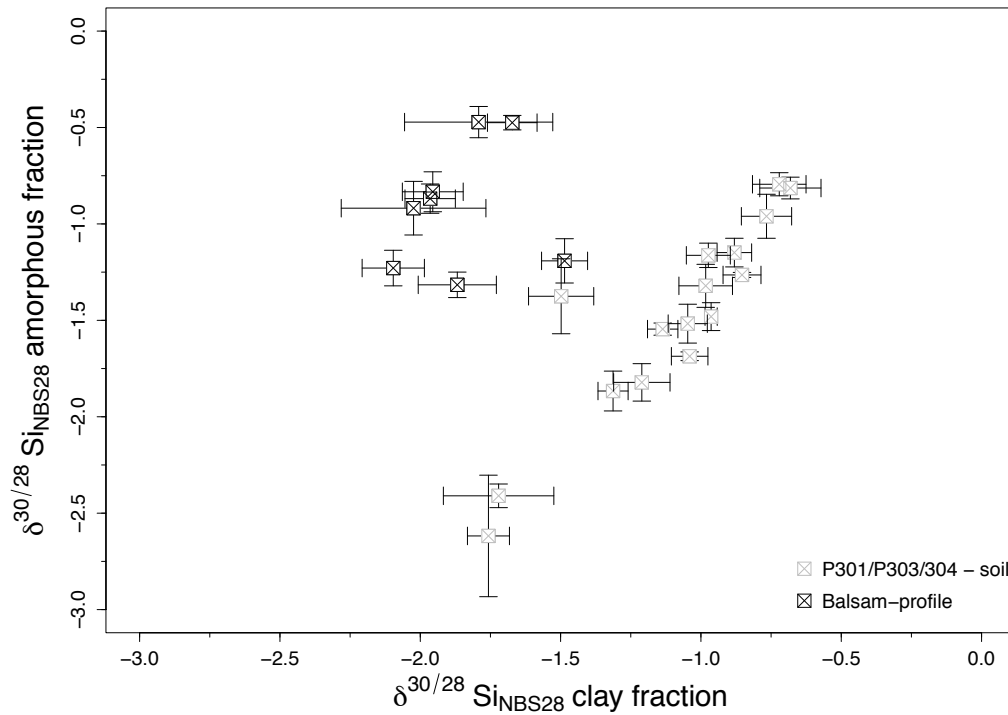
Figure 5.51: The $\delta^{30/28}Si_{amorphous}$ of the amorphous fraction plotted against the $\delta^{30/28}Si_{clay}$ of the clay fraction. A linear dependence of the isotopic composition of the amorphous fraction and the clay fraction is observed in the soil profiles (grey triangles). In contrast to the saprolite profile where no correlation is observed (black triangles).
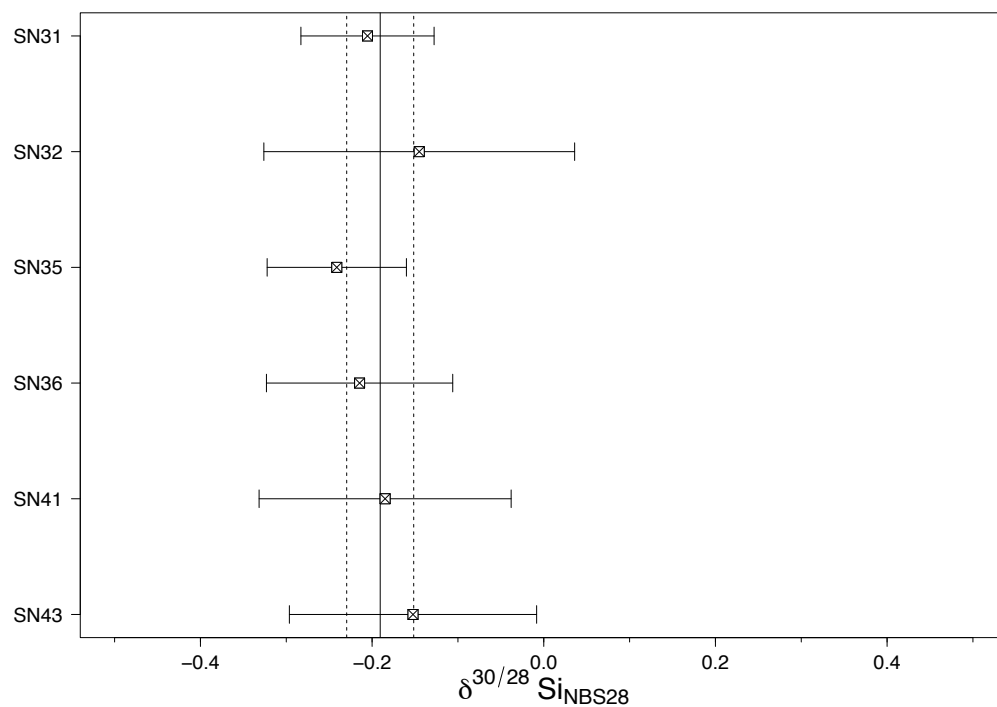
Figure 5.52: Si isotope composition of bulk bedrock samples of the Sierra Nevada sampling site resulting in an average bulk bedrock signature of $\delta(^{30/28}Si)_{bedrock}$= -0.19 ‰. The black line represent the mean value of the 6 measured bedrock samples and the dotted line represent the 95% confidence interval.

5.7.3   Combining the findings of the individual sampling sites

In this section the results of the former separately treated weathering regimes are combined to better understand the behavior of Si isotopes in different weathering regimes. Figure 5.53 shows the distribution of the chemical depletion fraction for the different sampling sites. More intense weathering takes place in the tropical regolith profile in Sri Lanka where up to 60% of the initial rock mass is lost through chemical weathering. A less intense chemical depletion in the Sierra Nevada sampling site is noted by CDF values in the range of 0.3 to 0.4. The kinetically limited weathering regime in the Swiss Alps shows the lowest chemical depletion fractions.

In Chapter 3 and Chapter 4 a strong dependency of Si isotope fractionation with solid formation rate is noted. The observation is made that the rate of solid formation is dependent on the Al/Si ratio. Therefore it is straightforward to plot the isotopic composition of the extracted amorphous and clay fractions against the measured Al/Si ratio.

All three settings show the same range of Al/Si ratios from 0.5 to up to 10. Three areas are distinguishable in Figure 5.54 for the three sampled settings in the Swiss Alps, Sierra Nevada and Sri Lanka, respectively. However, no general relationship between the isotopic composition and the Al/Si ratio of the amorphous fractions extracted from soil and saprolite seem to exists (Figure 5.54). If only the isotopic composition of the amorphous fraction extracted from soils is plotted against their corresponding Al/Si, ratio a significant general relationship exist (Figure 5.55), whereas the isotopic composition of the amorphous fraction extracted from saprolite does not show any relation with their corresponding Al/Si ratio (Figure 5.56). The amorphous fraction extracted from soils evidently becomes lower in their $\delta(^{30/28}Si)_{NBS28}$ ratios with increasing Al/Si ratio.

In contrast to the observation made for the amorphous fraction, the clay fraction shows a general trend between the isotopic composition and the corresponding Al/Si ratio (Figure 5.57). An increase in the Al/Si ratio is accompanied by lower $\delta(^{30/28}Si)_{NBS28}$ ratios in the clay fraction.

This trend, that lower $\delta(^{30/28}Si)_{NBS28}$ ratios are accompanied with an increase in the Al/Si ratio, is also observed for bulk rocks of the upper continental crust (Savage et al., 2013). However, this relationship becomes less apparent if we focus on the individual sites. For the Sierra Nevada and the Sri Lankan sampling sites this relationship still holds, but for the Swiss Alps no relationship exists. Further a much narrower range of Al/Si ratios (< 2.5) for the clay fraction compared to the amorphous fraction (< 12) is observed in the three sampled settings (Sri Lanka, Sierra Nevada, Swiss Alps).
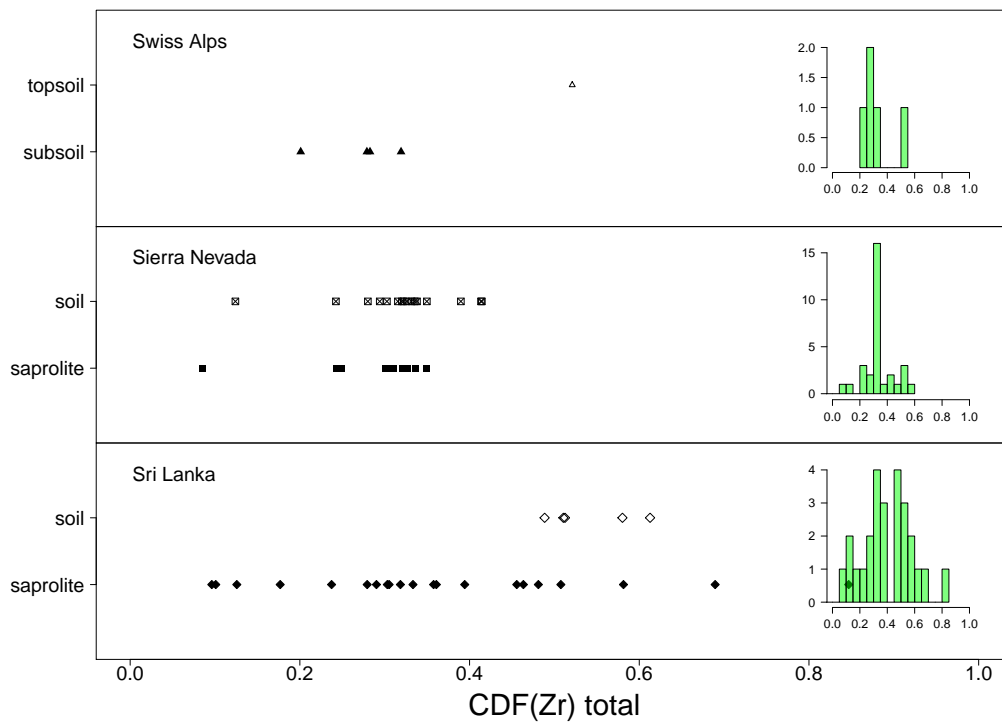
Figure 5.53: The chemical depletion fraction calculated for bulk samples for the three different study sites and the frequency distribution of the CDF values of the individual sampling sites.
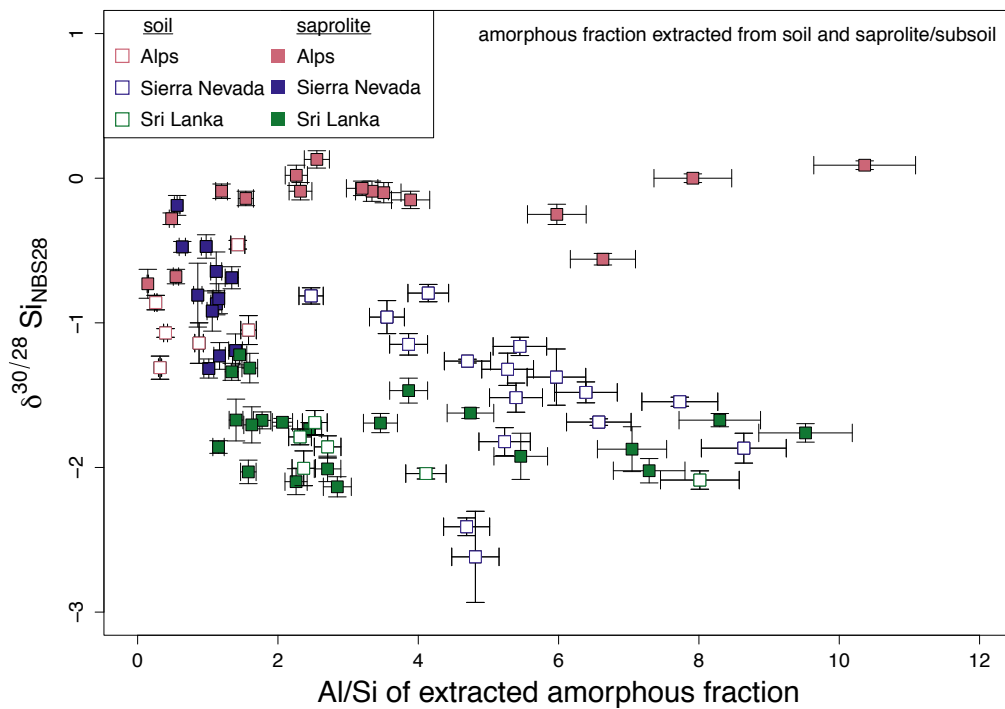
Figure 5.54: The isotopic signature of the amorphous fraction plotted against the corresponding Al/Si ratio of the amorphous fraction extracted from soil and saprolite of the three sampling sites.

141
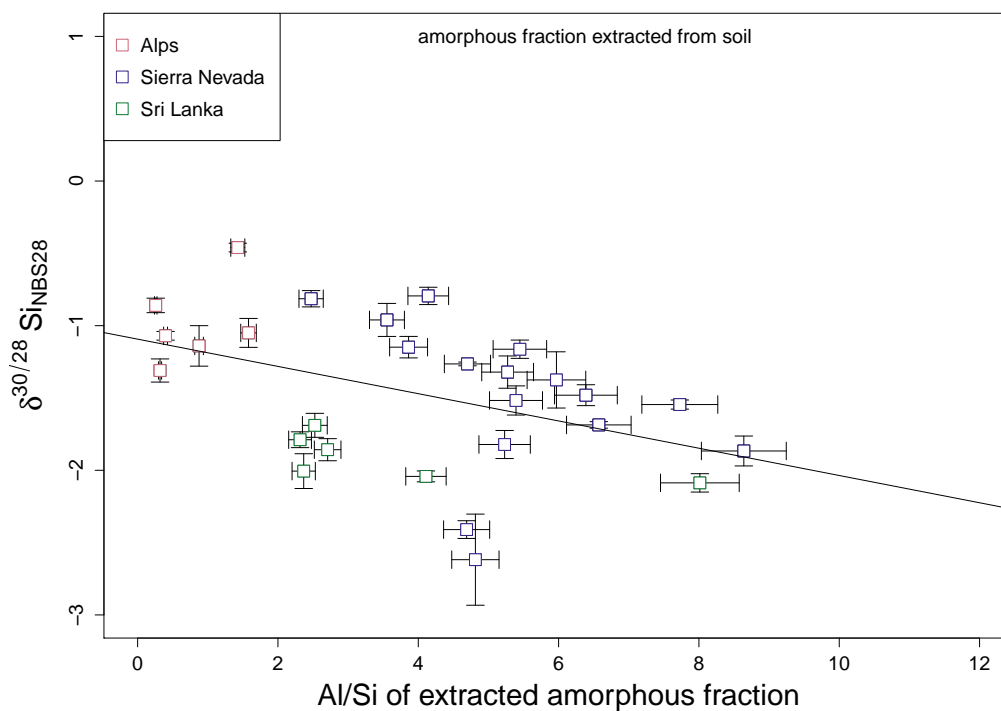
Figure 5.55: The isotopic signature of the amorphous fraction plotted against the corresponding Al/Si ratio of the amorphous fraction extracted from the soil of the three sampling sites (Sierra Nevada, Sri Lanka, Swiss Alps). The amorphous fraction of the three sampling sites show a significant (significance level $\alpha < 0.05$) negative linear correlation between the $\delta(^{30/28}Si)_{NBS28}$ ratios and the Al/Si ratio.
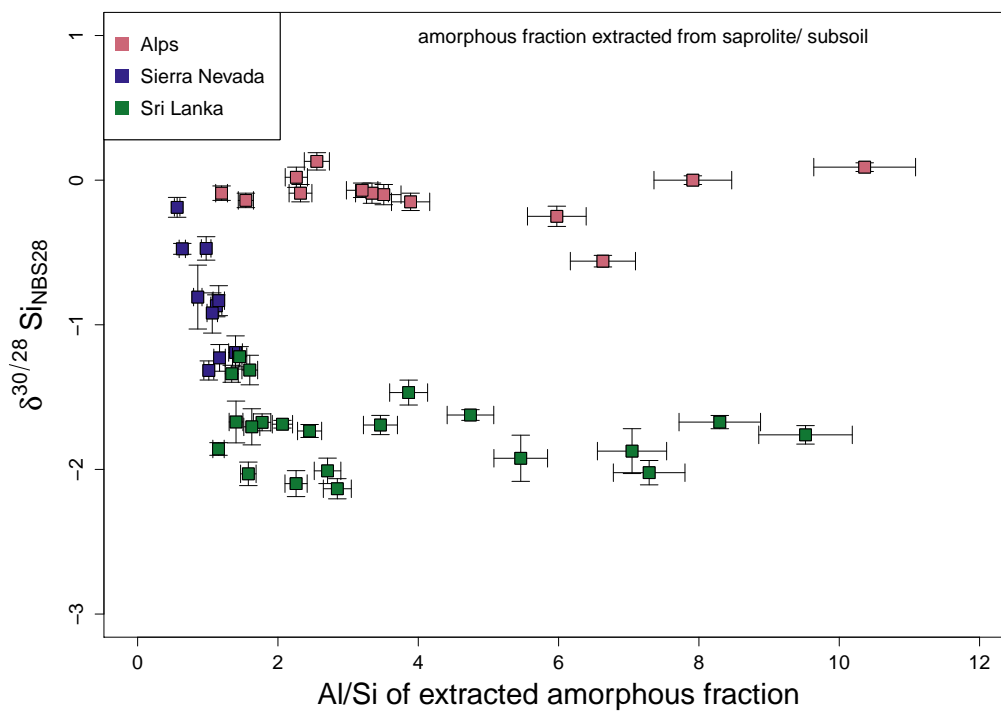
Figure 5.56: The isotopic signature of the amorphous fraction plotted against the corresponding Al/Si ratio of the amorphous fraction extracted from the saprolite/subsoil of the three sampling sites (Sierra Nevada, Sri Lanka, Swiss Alps).
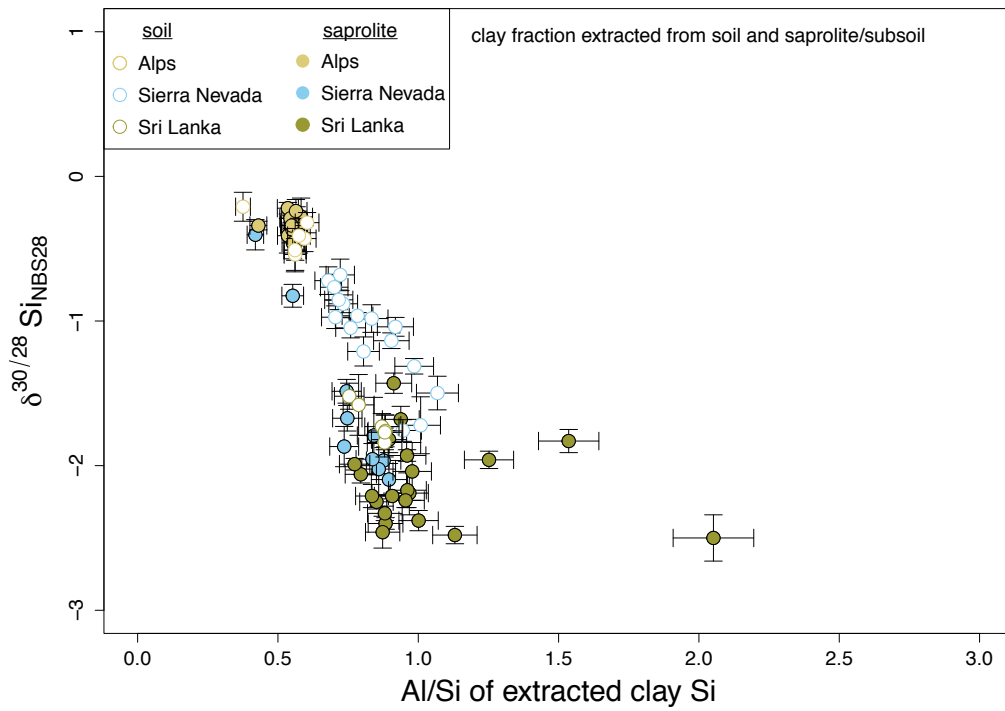
Figure 5.57: The isotopic signature of the clay fraction plotted against the corresponding Al/Si ratio of the clay fraction. A trend is noted showing an increase in the Al/Si clay ratio that is accompanied by lower $\delta(^{30/28}Si)_{NBS28}$ ratios of the clay fraction.
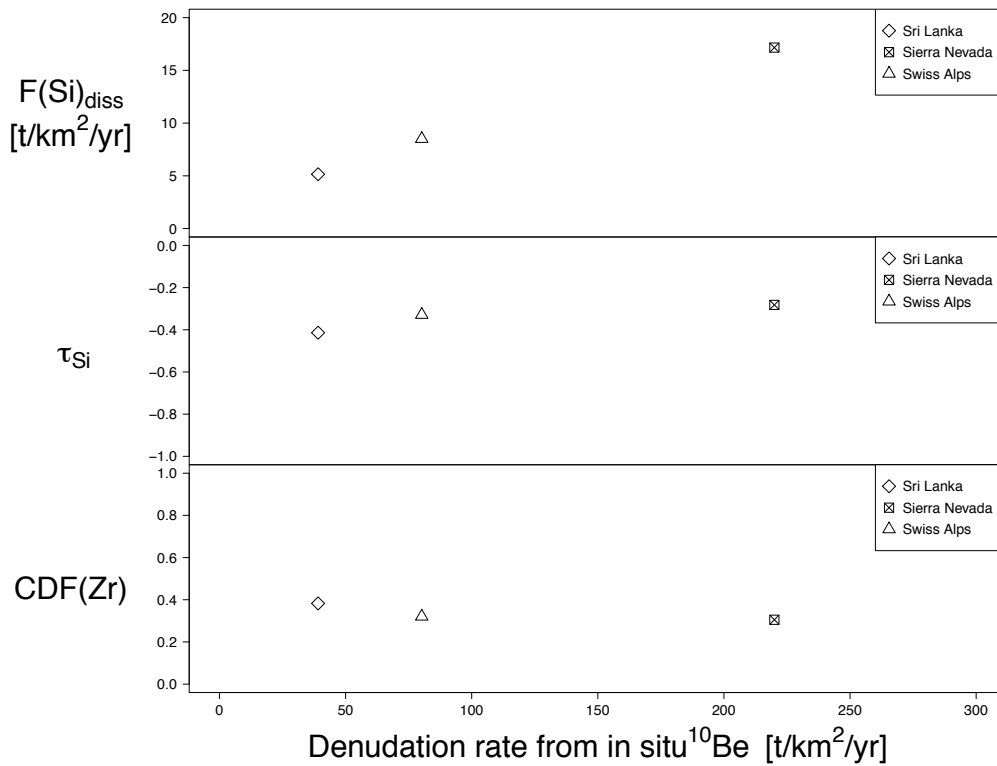
Figure 5.58: Comparison between the mean Si dissolved flux $F(Si)_{diss} = D * [Si]_{bedrock} * (-\tau_{Si})$, the mean element-mass transfer coefficient τ_{Si} and the mean CDF value with denudation rate determined from cosmogenic nuclides of the three sampled sites.

5.7.4   Tables

Tables Sri Lanka

This page is intentionally left blank.

Table 5.4: $\delta(^{29/28}Si)_{NBS28}$ and $\delta(^{30/28}Si)_{NBS28}$ values as well as 95% confidence interval (CI) of the amorphous and clay fraction of the Sri Lankan sampling site. Sampling depth is given after sample name in [cm] below surface.

sample name	sample description	amorphous fraction				clay fraction			
		$\delta(^{29/28}Si)$ [‰]	CI [‰]	$\delta(^{30/28}Si)$ [‰]	CI [‰]	$\delta(^{29/28}Si)$ [‰]	CI [‰]	$\delta(^{30/28}Si)$ [‰]	CI [‰]
SL6	soil 0-30 cm	-1.027	0.076	-2.006	0.120	-0.779	0.043	-1.516	0.094
SL7	soil 30-60 cm	-1.032	0.012	-2.042	0.038	-0.793	0.120	-1.577	0.213
SL8	saprolite 60-100 cm	-1.068	0.045	-2.087	0.064	-0.944	0.069	-1.836	0.100
SL9	saprolite 100-125 cm	-0.908	0.036	-1.761	0.064	-1.056	0.128	-2.037	0.204
SL10	saprolite 150-125 cm	-0.868	0.025	-1.693	0.066	-1.141	0.089	-2.187	0.148
SL11	saprolite 150-220 cm	-0.894	0.024	-1.734	0.045	-1.223	0.034	-2.381	0.072
SL12	saprolite 220-250 cm	-0.876	0.035	-1.674	0.059	-1.112	0.061	-2.173	0.116
SL13	saprolite 250-300 cm	-0.858	0.055	-1.687	0.027	-0.994	0.029	-1.927	0.038
SL14	saprolite 300-320 cm	-0.633	0.034	-1.221	0.070	-0.732	0.034	-1.429	0.074
SL15	saprolite 320-360 cm	-0.648	0.053	-1.313	0.102	-0.936	0.081	-1.819	0.091
SL16	saprolite 360-410 cm	-1.053	0.047	-2.031	0.081	-1.222	0.060	-2.399	0.041
SL17	saprolite 410-460 cm	-0.882	0.055	-1.705	0.125	-1.134	0.029	-2.205	0.022
SL18	saprolite 460-500 cm	-1.072	0.038	-2.098	0.090	-1.166	0.019	-2.252	0.047
SL19	saprolite 500-550 cm	-1.065	0.065	-2.010	0.088	-1.058	0.027	-2.058	0.061
SL20	saprolite 550-600 cm	-1.107	0.008	-2.134	0.070	-1.202	0.032	-2.329	0.050
SL21	saprolite 600-650 cm	-0.874	0.056	-1.672	0.145	-1.130	0.042	-2.213	0.082
SL22	saprolite 650-700 cm	-0.749	0.052	-1.469	0.086	-1.132	0.017	-2.241	0.051
SL23	saprolite 700-750 cm	-1.030	0.084	-2.023	0.084	-1.298	0.070	-2.496	0.156
SL24	saprolite 750-800 cm	-0.848	0.025	-1.673	0.046	-0.947	0.078	-1.829	0.083
SL25	saprolite 800-820 cm	-0.966	0.089	-1.923	0.160	-0.856	0.049	-1.678	0.088
SL26	saprolite 850-885 cm	-0.953	0.068	-1.873	0.155	-1.012	0.039	-1.956	0.058
SL27	saprolite 955-970 cm	-0.829	0.065	-1.624	0.037	-1.293	0.048	-2.483	0.061
SL28	saprolite 970-995 cm	-0.686	0.053	-1.339	0.059	-1.262	0.107	-2.463	0.111
SL29	saprolite 985-1020 cm	-0.939	0.025	-1.859	0.044	-1.032	0.023	-1.994	0.040
SL90	combined soil (0-20 cm)	-0.948	0.040	-1.858	0.076	-0.893	0.049	-1.770	0.118
SL88	combined soil (20-40 cm)	-0.858	0.053	-1.689	0.083	-0.906	0.057	-1.729	0.086
SL89	combined soil (40-60 cm)	-0.907	0.038	-1.789	0.055	-0.896	0.029	-1.759	0.110

Table 5.5: Element concentrations of the leached amorphous fraction extracted from soil and saprolite of the Sri Lankan sampling site calculated relative to initial solid sample mass.

		amorphous fraction							
sample name	sample description	Al	Ca	Fe	K	Mg	Mn	Si	Ti
		$[\mu g/g]$	$[\mu g/g]$	$[\mu g/g]$	$[\mu g/g]$	$[\mu g/g]$	$[\mu g/g]$	$[\mu g/g]$	$[\mu g/g]$
SL6	soil 0-30 cm	3716	6	51	10	1	0	1570	1
SL7	soil 30-60 cm	5360	3	7	7	0	0	1304	0
SL8	saprolite 60-100 cm	7526	1	3	4	0	0	939	0
SL9	saprolite 100-125 cm	8118	2	6	9	0	0	853	0
SL10	saprolite 150-125 cm	4654	2	3	5	0	0	1345	0
SL11	saprolite 150-220 cm	3419	2	3	6	0	0	1395	0
SL12	saprolite 220-250 cm	2247	1	3	6	0	0	1266	0
SL13	saprolite 250-300 cm	2285	2	3	7	0	0	1107	0
SL14	saprolite 300-320 cm	2420	0	3	20	0	0	1665	0
SL15	saprolite 320-360 cm	2992	4	3	37	0	0	1871	0
SL16	saprolite 360-410 cm	3191	3	5	62	0	0	2022	0
SL17	saprolite 410-460 cm	2697	2	3	25	0	0	1657	0
SL18	saprolite 460-500 cm	3879	1	6	74	0	0	1718	0
SL19	saprolite 500-550 cm	4277	4	6	100	0	0	1580	0
SL20	saprolite 550-600 cm	4390	2	7	77	0	0	1543	0
SL21	saprolite 600-650 cm	2304	2	6	50	0	0	1643	0
SL22	saprolite 650-700 cm	3695	1	7	17	0	0	957	0
SL23	saprolite 700-750 cm	7624	1	15	12	0	0	1046	0
SL24	saprolite 750-800 cm	7503	1	12	88	0	0	904	0
SL25	saprolite 800-820 cm	6857	1	11	283	0	0	1256	0
SL26	saprolite 850-885 cm	7424	2	12	108	0	1	1054	0
SL27	saprolite 955-970 cm	4414	0	8	32	0	0	931	0
SL28	saprolite 970-995 cm	1606	1	7	19	0	0	1198	0
SL29	saprolite 985-1020 cm	2270	1	6	88	0	0	1969	0
SL88	combined soil (0-20 cm)	3863	6	44	9	0	0	1529	1
SL89	combined soil (20-40 cm)	3372	3	53	6	1	0	1457	1
SL90	combined soil (40-60 cm)	3517	82	2095	25	15	6	1299	46

Table 5.6: Element concentrations of the separated clay fraction extracted from soil and saprolite of the Sri Lankan sampling site calculated relative to initial solid sample mass.

		clay fraction							
sample name	sample description	Al	Ca	Fe	K	Mg	Mn	Si	Ti
		[$\mu g/g$]	[$\mu g/g$]	[$\mu g/g$]	[$\mu g/g$]	[$\mu g/g$]	[$\mu g/g$]	[$\mu g/g$]	[$\mu g/g$]
SL6	soil 0-30 cm	22024	251	15527	717	661	41	29211	1276
SL7	soil 30-60 cm	31633	66	23446	1028	884	68	40173	1709
SL8	saprolite 60-100 cm	36862	0	28711	997	870	77	41890	1749
SL9	saprolite 100-125 cm	41278	29	29718	778	656	135	42191	1555
SL10	saprolite 150-125 cm	36090	0	23326	468	423	76	37279	1339
SL11	saprolite 150-220 cm	18703	0	11573	123	229	52	18682	715
SL12	saprolite 220-250 cm	16680	0	8591	117	193	49	17351	678
SL13	saprolite 250-300 cm	17395	0	7856	153	245	73	18121	517
SL14	saprolite 300-320 cm	27779	0	14212	251	342	648	30440	384
SL15	saprolite 320-360 cm	24745	0	13326	654	680	153	27625	1066
SL16	saprolite 360-410 cm	33999	38	9035	1447	1521	146	38485	1143
SL17	saprolite 410-460 cm	23781	0	9040	514	605	53	26219	740
SL18	saprolite 460-500 cm	32667	24	10234	1843	1158	122	38388	858
SL19	saprolite 500-550 cm	31677	22	10048	3217	1067	111	39833	713
SL20	saprolite 550-600 cm	27314	0	7239	2055	880	37	31006	599
SL21	saprolite 600-650 cm	19373	0	5132	1242	499	29	23198	380
SL22	saprolite 650-700 cm	11309	0	3380	334	241	40	11846	185
SL23	saprolite 700-750 cm	5402	0	795	0	0	0	2633	28
SL24	saprolite 750-800 cm	25441	0	6518	1465	703	57	16564	383
SL25	saprolite 800-820 cm	28643	76	11173	3900	1975	73	30546	1063
SL26	saprolite 850-885 cm	21990	6	6130	1410	798	80	17563	423
SL27	saprolite 955-970 cm	15597	0	3943	248	288	439	13798	175
SL28	saprolite 970-995 cm	12338	0	3649	299	231	131	14133	184
SL29	saprolite 985-1020 cm	27285	33	8746	2488	1259	112	35292	719
SL88	combined soil (0-20 cm)	22733	175	19133	212	420	118	26119	1065
SL89	combined soil (20-40 cm)	19701	89	13958	161	334	27	22311	693
SL90	combined soil (40-60 cm)	29608	461	17440	323	615	49	33617	929

Table 5.7: Average elemental composition of the amorphous and clay fractions extracted from soil and saprolite of the Sri Lankan sampling site normalized to 1 mol Si.

	fraction	Al [mol]	Ca [mol]	Fe [mol]	K [mol]	Mg [mol]	Mn [mol]	Si [mol]	Ti [mol]
soil	amorphous	2.92	0.01	0.17	0.01	2.94E-03	5.97E-04	1.00	4.43E-03
	clay	0.87	0.00	0.30	0.01	2.17E-02	1.05E-03	1.00	2.18E-02
saprolite	amorphous	3.88	0.00	0.00	0.03	1.87E-04	1.16E-04	1.00	5.50E-05
	clay	1.05	0.00	0.20	0.03	2.81E-02	2.69E-03	1.00	1.49E-02
bedrock	bulk	0.27	0.04	0.04	0.08	2.72E-02	5.37E-04	1.00	5.93E-03

Table 5.8: LOI corrected major element and Zr concentrations measured with XRF as well as the CDF value for the soil and saprolite samples of the Sri Lankan sampling site.

sample name	sample description	SiO_2 [wt%]	TiO_2 [wt%]	Al_2O_3 [wt%]	Fe_2O_3 [wt%]	MnO [wt%]	MgO [wt%]	CaO [wt%]	Na_2O [wt%]	K_2O [wt%]	P_2O_5 [wt%]	Zr [ppm]	CDF	LOI [%]
SL6	soil 0-30 cm	69.2	2.107	17.4	9.45	0.0443	0.50	0.25	0.01	0.60	0.152	584	0.61	23.19
SL7	soil 30-60 cm	68.9	1.881	17.5	10.05	0.0564	0.46	0.16	0.07	0.54	0.112	539	0.58	11.39
SL8	saprolite 60-100 cm	62.8	1.790	21.6	12.19	0.0381	0.40	0.07	0.05	0.51	0.128	728	0.69	0.27
SL9	saprolite 100-125 cm	64.0	1.440	20.5	12.66	0.0586	0.29	0.07	0.07	0.44	0.122	540	0.58	11.27
SL10	saprolite 150-125 cm	53.0	1.608	27.9	16.35	0.0860	0.25	0.01	0.01	0.43	0.132	421	0.46	32.53
SL11	saprolite 150-220 cm	55.9	1.116	28.7	12.61	0.0799	0.35	0.01	0.27	0.43	0.095	339	0.33	12.37
SL12	saprolite 220-250 cm	60.8	1.414	24.9	10.96	0.1629	0.49	0.02	0.17	0.86	0.084	459	0.51	59.39
SL13	saprolite 250-300 cm	56.5	1.254	25.5	13.56	0.1280	0.83	0.01	0.24	1.34	0.161	436	0.48	10.89
SL14	saprolite 300-320 cm	74.0	0.197	14.8	9.91	0.1532	0.13	0.02	0.01	0.27	0.182	1476	0.85	7.31
SL15	saprolite 320-360 cm	66.2	1.020	22.2	8.61	0.1102	0.52	0.01	0.01	1.06	0.106	319	0.29	9.25
SL16	saprolite 360-410 cm	69.3	0.749	21.9	5.73	0.0547	0.94	0.02	0.01	1.04	0.122	314	0.28	8.5
SL17	saprolite 410-460 cm	68.9	0.799	22.4	5.63	0.0397	0.60	0.01	0.23	0.94	0.087	332	0.32	9.23
SL18	saprolite 460-500 cm	67.3	0.738	23.5	5.10	0.0604	0.81	0.03	0.10	1.91	0.082	275	0.18	8.94
SL19	saprolite 500-550 cm	66.1	0.773	22.7	4.91	0.0285	0.83	0.03	0.44	3.59	0.137	325	0.31	8.68
SL20	saprolite 550-600 cm	62.0	0.917	27.0	4.99	0.0178	1.01	0.02	0.12	3.36	0.120	296	0.24	9.89
SL21	saprolite 600-650 cm	66.9	0.803	22.2	5.00	0.0260	0.81	0.02	0.40	3.15	0.154	373	0.39	7.8
SL22	saprolite 650-700 cm	67.3	0.900	21.5	5.28	0.0327	0.94	0.08	0.17	3.29	0.178	415	0.46	23.36
SL23	saprolite 700-750 cm	64.0	0.888	22.4	5.61	0.0285	0.93	0.18	0.60	4.59	0.243	354	0.36	8.64
SL24	saprolite 750-800 cm	64.2	0.848	23.1	5.30	0.0396	0.92	0.14	0.36	4.37	0.235	324	0.30	9.02
SL25	saprolite 800-820 cm	66.8	0.676	20.0	4.16	0.0201	0.84	0.61	1.17	5.15	0.174	250	0.10	5.63
SL26	saprolite 850-885 cm	66.6	0.675	20.4	4.99	0.0322	0.88	0.27	0.62	4.84	0.218	259	0.13	6.77
SL27	saprolite 955-970 cm	64.8	0.697	21.7	5.44	0.1418	1.01	0.69	1.12	3.76	0.216	251	0.10	6.91
SL28	saprolite 970-995 cm	65.9	0.753	22.8	5.45	0.0706	0.77	0.04	0.09	3.65	0.115	352	0.36	7.91
SL29	saprolite 985-1020 cm	80.0	0.366	13.4	2.79	0.0305	0.47	0.03	0.04	2.68	0.055	157	-0.44	5.01
SL90	combined soil (0-20 cm)	64.4	1.606	18.1	12.77	0.0478	0.48	0.33	1.13	0.38	0.169	442	0.49	18.22
SL88	combined soil (20-40 cm)	64.7	1.449	16.4	14.92	0.0434	0.48	0.32	0.70	0.34	0.169	464	0.51	14.76
SL89	combined soil (40-60 cm)	65.8	1.720	18.9	11.23	0.0490	0.56	0.49	0.36	0.40	0.196	462	0.51	32.56

Tables Swiss Alps

This page is intentionally left blank.

Table 5.9: $\delta(^{29/28}Si)_{NBS28}$ and $\delta(^{30/28}Si)_{NBS28}$ values as well as 95% confidence interval (CI) of the amorphous and clay fraction of the Swiss Alps sampling site. Sampling depth is given after sample name in [cm] below surface.

sample name	sample description	amorphous fraction				clay fraction			
		$\delta(^{29/28}Si)$ [‰]	CI [‰]	$\delta(^{30/28}Si)$ [‰]	CI [‰]	$\delta(^{29/28}Si)$ [‰]	CI [‰]	$\delta(^{30/28}Si)$ [‰]	CI [‰]
G4	soil-B1 2-9 cm	-0.566	0.066	-1.144	0.136	-0.102	0.055	-0.215	0.097
G5	soil-B1 9-15 cm	0.008	0.027	-0.003	0.034	-0.146	0.072	-0.282	0.131
G6	soil-B1 15-21 cm	-0.057	0.044	-0.088	0.058	-0.183	0.022	-0.343	0.057
G7	soil-B1 21-24 cm	-0.074	0.039	-0.142	0.046	-0.174	0.035	-0.332	0.060
G9	soil-B2 2-9 cm	-0.535	0.062	-1.054	0.096	-0.227	0.054	-0.432	0.092
G10	soil-B2 9-15 cm	0.047	0.024	0.094	0.031	-0.165	0.025	-0.340	0.131
G11	soil-B2 15-28 cm	-0.126	0.016	-0.247	0.068	-0.141	0.027	-0.286	0.066
G12	soil-B2 28-30 cm	-0.294	0.008	-0.556	0.038	-0.120	0.028	-0.219	0.042
G26	soil-B3 0-17 cm	-0.228	0.051	-0.460	0.032	-0.181	0.040	-0.325	0.070
G27	soil-B3 17-34 cm	0.007	0.041	0.017	0.074	-0.138	0.040	-0.242	0.081
G14	soil-B4 2-7 cm	-0.654	0.037	-1.305	0.077	-0.272	0.069	-0.537	0.113
G15	soil-B4 7-15 cm	-0.047	0.066	-0.100	0.074	-0.207	0.072	-0.406	0.119
G16	soil-B4 15-17 cm	-0.047	0.052	-0.090	0.071	-0.222	0.046	-0.460	0.114
G18	soil-B5 2.5-9 cm	-0.445	0.029	-0.863	0.047	-0.216	0.086	-0.411	0.125
G19	soil-B5 9-15 cm	0.056	0.038	0.130	0.059	-0.196	0.020	-0.369	0.056
G20	soil-B5 15-32 cm	-0.074	0.016	-0.153	0.064	-0.160	0.034	-0.295	0.056
G24	soil-B5 32-34 cm	-0.063	0.032	-0.094	0.051	-0.170	0.016	-0.339	0.022
G22	soil-B6 2-6 cm	-0.552	0.052	-1.075	0.035	-0.280	0.060	-0.505	0.148
G23	soil-B6 6-15 cm	-0.036	0.019	-0.068	0.046	-0.267	0.050	-0.514	0.075
A9	A-2010-B1 0-6cm	-0.372	0.066	-0.733	0.099	-0.182	0.035	-0.345	0.043
G1	bedload	-0.137	0.062	-0.280	0.044	-0.162	0.042	-0.338	0.031
G2	bedload	-0.345	0.015	-0.684	0.051	-0.197	0.028	-0.365	0.111

Table 5.10: Element concentrations of the leached amorphous fraction extracted from top- and subsoil of the Swiss Alps sampling site calculated relative to initial solid sample mass.

sample name	sample description	amorphous fraction							
		Al	Ca	Fe	K	Mg	Mn	Si	Ti
		$[\mu g/g]$	$[\mu g/g]$	$[\mu g/g]$	$[\mu g/g]$	$[\mu g/g]$	$[\mu g/g]$	$[\mu g/g]$	$[\mu g/g]$
G4	soil-B1 2-9 cm	1008	29	474	5	7	1	1151	78
G5	soil-B1 9-15 cm	3829	12	82	30	3	0	484	12
G6	soil-B1 15-21 cm	2102	11	29	233	1	0	905	3
G7	soil-B1 21-24 cm	2088	17	20	347	1	0	1353	2
G9	soil-B2 2-9 cm	1493	36	418	11	6	1	944	66
G10	soil-B2 9-15 cm	2408	10	20	29	1	0	232	2
G11	soil-B2 15-28 cm	2260	24	44	60	1	0	378	4
G12	soil-B2 28-30 cm	1920	60	102	24	2	1	290	12
G26	soil-B3 0-17 cm	1841	23	34	192	0	0	1289	6
G27	soil-B3 17-34 cm	2043	7	15	273	0	0	903	1
G14	soil-B4 2-7 cm	652	39	357	9	5	1	2042	43
G15	soil-B4 7-15 cm	2033	18	55	93	1	0	579	6
G16	soil-B4 15-17 cm	2350	18	51	171	1	1	704	6
G18	soil-B5 2.5-9 cm	524	32	174	10	2	1	2033	51
G19	soil-B5 9-15 cm	1679	6	13	137	0	0	657	1
G20	soil-B5 15-32 cm	1868	46	52	124	1	0	480	5
G24	soil-B5 32-34 cm	1630	53	23	422	1	0	1362	2
G22	soil-B6 2-6 cm	951	43	358	14	4	1	2388	57
G23	soil-B6 6-15 cm	2505	10	17	178	1	0	783	1
A9	A-2010-B1 0-6cm	613	132	343	190	1	1	4220	25
G1	bedload	54	1	10	23	0	0	111	0
G2	bedload	221	11	14	38	1	1	405	0

Table 5.11: Element concentrations of the separated clay fraction extracted from top- and subsoil of the Swiss Alps sampling site calculated relative to initial solid sample mass.

sample name	sample description	clay fraction							
		Al	Ca	Fe	K	Mg	Mn	Si	Ti
		$[\mu g/g]$	$[\mu g/g]$	$[\mu g/g]$	$[\mu g/g]$	$[\mu g/g]$	$[\mu g/g]$	$[\mu g/g]$	$[\mu g/g]$
G4	soil-B1 2-9 cm	10463	1011	3676	2391	920	0	27865	683
G5	soil-B1 9-15 cm	4417	194	3355	970	715	0	7582	406
G6	soil-B1 15-21 cm	7946	470	5415	2349	2443	76	14466	479
G7	soil-B1 21-24 cm	11436	1015	7880	3388	3280	121	20865	656
G9	soil-B2 2-9 cm	5635	147	2400	1329	673	10	9484	475
G10	soil-B2 9-15 cm	2257	143	1777	482	479	0	3985	194
G11	soil-B2 15-28 cm	2870	164	1723	825	714	18	5213	159
G12	soil-B2 28-30 cm	2103	193	967	510	446	0	3929	106
G26	soil-B3 0-17 cm	4092	193	2435	1057	739	21	6778	306
G27	soil-B3 17-34 cm	3069	214	2093	842	963	22	5442	196
G14	soil-B4 2-7 cm	7542	189	3274	1856	800	0	13438	573
G15	soil-B4 7-15 cm	6358	487	7167	1614	2973	90	11865	566
G16	soil-B4 15-17 cm	9622	633	10152	2608	4349	147	17387	841
G18	soil-B5 2.5-9 cm	5259	149	1945	1337	492	0	9150	606
G19	soil-B5 9-15 cm	3672	184	3929	1064	1139	35	6657	351
G20	soil-B5 15-32 cm	1404	136	1161	287	423	0	2578	109
G24	soil-B5 32-34 cm	4204	440	3286	1366	1785	61	7659	241
G22	soil-B6 2-6 cm	4481	188	2984	974	799	19	7993	379
G23	soil-B6 6-15 cm	3933	190	4287	916	2052	53	7004	335
A9	A-2010-B1 0-6cm	3107	381	1492	612	371	0	11213	172
G1	bedload	194	8	136	16	70	3	450	7
G2	bedload	915	89	605	161	302	14	1626	71

Table 5.12: Average elemental composition of the amorphous and clay fractions extracted from top- and subsoil of the Swiss Alps sampling site normalized to 1 mol Si.

	fraction	Al [mol]	Ca [mol]	Fe [mol]	K [mol]	Mg [mol]	Mn [mol]	Si [mol]	Ti [mol]
topsoil	amorphous	0.84	0.02	0.11	0.02	3.31E-03	2.68E-04	1.00	2.08E-02
	clay	0.57	0.02	0.13	0.09	8.21E-02	5.58E-04	1.00	2.70E-02
subsoil	amorphous	4.38	0.03	0.04	0.15	2.62E-03	4.47E-04	1.00	5.56E-03
	clay	0.58	0.03	0.23	0.10	2.07E-01	2.18E-03	1.00	2.40E-02
bedrock	bulk	0.28	0.03	0.02	0.03	2.09E-02	-	1.00	3.16E-03

Table 5.13: LOI corrected major element and Zr concentrations measured with XRF as well as the CDF value for the soil and subsoil samples of the Swiss Alps sampling site.

sample name	sample description	SiO_2 [wt%]	TiO_2 [wt%]	Al_2O_3 [wt%]	Fe_2O_3 [wt%]	MnO [wt%]	MgO [wt%]	CaO [wt%]	Na_2O [wt%]	K_2O [wt%]	P_2O_5 [wt%]	Zr [ppm]	CDF	LOI [%]
G8	soil-B2 0-2 cm	67.6	0.773	16.3	3.21	0.2037	1.62	2.98	1.96	3.83	1.116	233	0.52	25.77
G9	soil-B2 2-9 cm	69.7	0.433	17.1	2.78	0.0387	0.90	1.99	3.95	2.46	0.219	164	0.32	14.70
G10	soil-B2 9-15 cm	68.1	0.396	17.5	3.28	0.0459	1.18	2.14	4.37	2.54	0.126	140	0.20	14.91
G11	soil-B2 15-28 cm	68.1	0.439	17.0	3.30	0.0608	1.57	2.39	3.86	2.72	0.171	156	0.28	6.30
G12	soil-B2 28-30 cm	67.7	0.430	17.6	2.64	0.0534	1.53	2.41	4.26	2.92	0.172	155	0.28	4.54
G1	bedload	78.3	0.107	12.0	1.00	0.0265	0.25	0.44	3.73	3.88	0.029	165	0.32	1.90
G2	bedload	71.4	0.249	15.8	1.81	0.0453	1.02	1.35	5.05	2.86	0.130	116	0.04	2.86

Tables Sierra Nevada

This page is intentionally left blank.

Table 5.14: $\delta(^{29/28}Si)_{NBS28}$ and $\delta(^{30/28}Si)_{NBS28}$ values as well as 95% confidence interval (CI) of the amorphous and clay fraction of the Sierra Nevada sampling site. Providence Creek sites are denoted with a P in front of the samples name (P301, P303, P304) and the Balsam profile is denoted with BP in front of the sample name. Sampling depth is given after sample name in [cm] below surface.

sample name	sample description	amorphous fraction				clay fraction			
		$\delta(^{29/28}Si)$ [‰]	CI [‰]	$\delta(^{30/28}Si)$ [‰]	CI [‰]	$\delta(^{29/28}Si)$ [‰]	CI [‰]	$\delta(^{30/28}Si)$ [‰]	CI [‰]
SN1	P301 soil core 0-13 cm	-0.415	0.029	-0.814	0.056	-0.333	0.048	-0.681	0.109
SN2	P301 soil core 13-26 cm	-0.388	0.025	-0.794	0.060	-0.368	0.043	-0.721	0.095
SN3	P301 soil core 26-34 cm	-0.491	0.065	-0.960	0.114	-0.396	0.046	-0.766	0.090
SN4	P301 augered soil 34-51 cm	-0.567	0.029	-1.149	0.074	-0.445	0.039	-0.881	0.062
SN5	P301 augered soil 51-66 cm	-0.657	0.046	-1.265	0.013	-0.435	0.061	-0.854	0.068
SN6	P301 augered soil 66-76 cm	-0.658	0.055	-1.321	0.112	-0.524	0.052	-0.983	0.095
SN7	P301 augered soil 76-89 cm	-0.852	0.032	-1.686	0.023	-0.542	0.025	-1.040	0.065
SN8	P301 augered soil 89-101 cm	-0.742	0.029	-1.481	0.072	-0.499	0.028	-0.964	0.022
SN9	P301 augered soil 101-109 cm	-0.785	0.030	-1.545	0.032	-0.573	0.029	-1.136	0.054
SN10	P301 augered soil 109-122 cm	-0.954	0.036	-1.867	0.103	-0.693	0.039	-1.313	0.054
SN21	P303 soil core 0-13cm	-0.716	0.120	-1.375	0.194	-0.782	0.075	-1.498	0.116
SN22	P303 soil core 13-26cm	-1.245	0.071	-2.410	0.061	-0.883	0.109	-1.721	0.197
SN23	P303 soil core 26-34cm	-1.303	0.080	-2.618	0.315	-0.922	0.026	-1.757	0.075
SN24	P304 soil core 0-13cm	-0.595	0.027	-1.163	0.063	-0.511	0.044	-0.974	0.078
SN25	P304 soil core 13-26cm	-0.777	0.018	-1.517	0.101	-0.538	0.038	-1.047	0.070
SN26	P304 soil core 26-34cm	-0.938	0.059	-1.822	0.097	-0.606	0.049	-1.211	0.100
SN20	BP 204 saprolite - 178 cm	-0.427	0.076	-0.833	0.104	-0.989	0.063	-1.955	0.108
SN19	BP 173 saprolite - 256 cm	-0.466	0.095	-0.918	0.139	-1.052	0.136	-2.024	0.258
SN18	BP 161 saprolite - 287 cm	-0.678	0.047	-1.316	0.066	-0.974	0.096	-1.868	0.139
SN17	BP 144 saprolite - 330 cm	-0.249	0.044	-0.475	0.038	-0.869	0.105	-1.672	0.088
SN16	BP 111 saprolite - 414 cm	-0.447	0.063	-0.869	0.076	-1.020	0.031	-1.965	0.090
SN15	BP 72 saprolite - 513 cm	-0.622	0.030	-1.229	0.092	-1.096	0.073	-2.096	0.111
SN14	BP 36 saprolite - 605 cm	-0.241	0.052	-0.472	0.081	-0.924	0.107	-1.792	0.264
SN13	BP 3 saprolite - 688 cm	-0.621	0.022	-1.192	0.115	-0.776	0.071	-1.486	0.082
SN12	BP 0 saprolite - 696 cm	-0.446	0.133	-0.808	0.221	-0.439	0.051	-0.826	0.079
SN11	BP Rock	-0.109	0.071	-0.188	0.069	-0.216	0.048	-0.404	0.105
SN27	P301 Bedload	-0.322	0.074	-0.644	0.134	-0.391	0.063	-0.761	0.110
SN28	PIG bedload	-0.378	0.048	-0.688	0.076	-0.459	0.022	-0.900	0.042

Table 5.15: Element concentrations of the leached amorphous fraction extracted from soil and saprolite of the Sierra Nevada sampling site calculated relative to initial solid sample mass.

sample name	sample description	amorphous fraction							
		Al [$\mu g/g$]	Ca [$\mu g/g$]	Fe [$\mu g/g$]	K [$\mu g/g$]	Mg [$\mu g/g$]	Mn [$\mu g/g$]	Si [$\mu g/g$]	Ti [$\mu g/g$]
SN1	P301 soil core 0-13 cm	5687	10148	1812	543	512	754	2300	148
SN2	P301 soil core 13-26 cm	8038	425	424	470	25	25	1941	30
SN3	P301 soil core 26-34 cm	9921	37	87	568	1	2	2792	3
SN4	P301 augered soil 34-51 cm	9471	54	123	502	1	1	2452	5
SN5	P301 augered soil 51-66 cm	11355	3	79	476	0	2	2415	1
SN6	P301 augered soil 66-76 cm	11631	6	37	443	0	1	2206	1
SN7	P301 augered soil 76-89 cm	11509	8	43	134	0	1	1751	0
SN8	P301 augered soil 89-101 cm	12101	3	34	422	0	1	1894	1
SN9	P301 augered soil 101-109 cm	13803	4	33	389	0	1	1786	1
SN10	P301 augered soil 109-122 cm	15598	2	33	365	0	1	1805	0
SN21	P303 soil core 0-13cm	5606	651	380	139	12	64	939	20
SN22	P303 soil core 13-26cm	7164	61	65	94	1	10	1528	2
SN23	P303 soil core 26-34cm	8524	3	22	143	1	2	1771	0
SN24	P304 soil core 0-13cm	10375	132	308	386	5	21	1904	16
SN25	P304 soil core 13-26cm	10211	16	30	257	1	3	1893	1
SN26	P304 soil core 26-34cm	11786	4	23	284	1	2	2253	1
SN20	BP 204 saprolite - 178 cm	2319	3	27	28	0	0	2005	0
SN19	BP 173 saprolite - 256 cm	2810	3	36	31	0	0	2642	0
SN18	BP 161 saprolite - 287 cm	3769	2	23	131	0	0	3714	0
SN17	BP 144 saprolite - 330 cm	1735	4	31	63	1	1	2725	1
SN16	BP 111 saprolite - 414 cm	2364	6	103	31	0	2	2108	0
SN15	BP 72 saprolite - 513 cm	1968	2	35	17	0	1	1685	0
SN14	BP 36 saprolite - 605 cm	1721	4	32	12	0	0	1762	1
SN13	BP 3 saprolite - 688 cm	1667	5	45	32	1	0	1194	1
SN12	BP 0 saprolite - 696 cm	2219	2	29	388	0	0	2587	0
SN11	BP Rock	1161	18	38	699	1	0	2061	0
SN27	P301 Bedload	1640	3	34	111	0	0	1464	0
SN28	PIG bedload	2051	2	27	118	0	0	1528	0

Table 5.16: Element concentrations of the separated clay fraction extracted from soil and saprolite of the Sierra Nevada sampling site calculated relative to initial solid sample mass.

sample name	sample description	clay fraction							
		Al [$\mu g/g$]	Ca [$\mu g/g$]	Fe [$\mu g/g$]	K [$\mu g/g$]	Mg [$\mu g/g$]	Mn [$\mu g/g$]	Si [$\mu g/g$]	Ti [$\mu g/g$]
SN1	P301 soil core 0-13 cm	7609	4486	4705	986	1553	1156	10539	515
SN2	P301 soil core 13-26 cm	22100	3534	17871	3646	5743	874	32541	2129
SN3	P301 soil core 26-34 cm	28243	2774	23602	4526	7602	439	40318	2856
SN4	P301 augered soil 34-51 cm	22766	2103	18672	3458	6162	269	31081	2310
SN5	P301 augered soil 51-66 cm	29044	2523	23053	4072	7357	295	40525	2805
SN6	P301 augered soil 66-76 cm	28856	1772	21780	4067	6973	271	34613	2689
SN7	P301 augered soil 76-89 cm	21320	1281	10612	1591	2797	144	23211	1277
SN8	P301 augered soil 89-101 cm	31270	2205	21362	4344	6812	307	39914	2777
SN9	P301 augered soil 101-109 cm	25730	1307	16690	3117	5184	280	28461	2171
SN10	P301 augered soil 109-122 cm	28154	951	16126	2875	4871	272	28569	2115
SN21	P303 soil core 0-13cm	7870	1963	3354	242	742	869	7366	382
SN22	P303 soil core 13-26cm	9925	1055	4592	309	936	369	9842	520
SN23	P303 soil core 26-34cm	19302	903	9339	1047	2296	360	20424	1135
SN24	P304 soil core 0-13cm	17822	2249	12443	2487	3586	1045	25291	1478
SN25	P304 soil core 13-26cm	15299	850	8451	1601	2178	623	20158	964
SN26	P304 soil core 26-34cm	21107	992	11439	2032	3155	417	26221	1337
SN20	BP 204 saprolite - 178 cm	10041	129	4063	537	757	26	11999	528
SN19	BP 173 saprolite - 256 cm	9796	131	5976	456	644	27	11404	588
SN18	BP 161 saprolite - 287 cm	44104	1095	27157	6720	8219	357	59920	3383
SN17	BP 144 saprolite - 330 cm	38662	1164	19826	4871	6098	409	51745	2283
SN16	BP 111 saprolite - 414 cm	7479	128	2084	194	445	35	8533	266
SN15	BP 72 saprolite - 513 cm	2992	58	570	0	80	19	3341	51
SN14	BP 36 saprolite - 605 cm	1683	50	465	0	87	19	1999	54
SN13	BP 3 saprolite - 688 cm	1186	127	519	0	61	5	1592	39
SN12	BP 0 saprolite - 696 cm	11114	1447	14055	3768	4809	195	20110	1529
SN11	BP Rock	6516	1500	8630	2602	2885	143	15531	914
SN27	P301 Bedload	4707	993	4898	637	1651	94	8138	574
SN28	PIG bedload	7328	1538	8676	1385	2463	121	12403	998

Table 5.17: Average elemental composition of the amorphous and clay fractions extracted from soil and saprolite of the Sierra Nevada sampling site normalized to 1 mol Si.

	fraction	Al [mol]	Ca [mol]	Fe [mol]	K [mol]	Mg [mol]	Mn [mol]	Si [mol]	Ti [mol]
soil	amorphous	5.72	0.05	0.04	0.12	2.53E-03	3.63E-03	1.00	2.04E-03
	clay	0.87	0.05	0.26	0.06	1.75E-01	1.21E-02	1.00	3.72E-02
saprolite	amorphous	1.04	0.00	0.01	0.05	3.00E-04	1.41E-04	1.00	1.65E-04
	clay	0.78	0.03	0.20	0.05	1.11E-01	3.06E-03	1.00	2.52E-02
bedrock	bulk	0.34	0.11	0.09	0.05	8.35E-02	1.77E-03	1.00	1.27E-02

Table 5.18: LOI corrected major element and Zr concentrations measured with XRF as well as the CDF value for the soil and saprolite samples of the Sierra Nevada sampling site.

sample name	sample description	SiO$_2$ [wt%]	TiO$_2$ [wt%]	Al$_2$O$_3$ [wt%]	Fe$_2$O$_3$ [wt%]	MnO [wt%]	MgO [wt%]	CaO [wt%]	Na$_2$O [wt%]	K$_2$O [wt%]	P$_2$O$_5$ [wt%]	Zr [ppm]	CDF	LOI [%]
SN1	P301 soil core 0-13 cm	58.8	0.890	18.5	5.47	0.6771	2.50	7.33	2.13	3.06	0.594	176	0.28	89.15
SN2	P301 soil core 13-26 cm	61.8	0.891	18.7	6.12	0.2081	2.40	4.01	2.44	2.75	0.330	187	0.32	18.23
SN3	P301 soil core 26-34 cm	61.5	0.937	18.8	6.72	0.1247	2.67	3.99	2.23	2.48	0.249	185	0.32	12.57
SN4	P301 augered soil 34-51 cm	60.8	1.004	19.1	7.15	0.1171	2.85	3.96	2.04	2.43	0.231	187	0.32	13.70
SN5	P301 augered soil 51-66 cm	60.5	1.029	19.3	7.44	0.1132	2.92	3.88	1.95	2.44	0.201	192	0.34	8.14
SN6	P301 augered soil 66-76 cm	60.4	1.024	19.4	7.47	0.1130	2.92	3.89	1.96	2.33	0.200	191	0.34	8.83
SN7	P301 augered soil 76-89 cm	61.1	1.011	19.0	7.31	0.1124	2.88	3.85	1.91	2.36	0.193	190	0.33	8.31
SN8	P301 augered soil 89-101 cm	58.8	1.086	20.3	8.04	0.1255	3.09	3.90	1.84	2.31	0.194	216	0.41	7.52
SN9	P301 augered soil 101-109 cm	59.3	1.063	19.9	8.00	0.1304	3.04	3.82	1.83	2.44	0.190	217	0.41	7.21
SN10	P301 augered soil 109-122 cm	60.1	1.040	19.5	7.92	0.1265	3.02	3.76	1.76	2.31	0.168	208	0.39	6.67
SN21	P303 soil core 0-13cm	56.9	1.231	20.2	8.54	0.5057	3.33	4.98	1.68	1.67	0.695	195	0.35	33.29
SN22	P303 soil core 13-26cm	56.9	1.288	20.7	9.38	0.2510	3.46	4.21	1.56	1.55	0.367	188	0.33	12.33
SN23	P303 soil core 26-34cm	57.5	1.280	20.5	9.46	0.2062	3.50	4.09	1.48	1.43	0.227	182	0.30	9.28
SN24	P304 soil core 0-13cm	65.3	0.706	18.1	4.99	0.3659	1.67	2.89	1.85	3.21	0.746	180	0.29	37.61
SN25	P304 soil core 13-26cm	65.7	0.730	18.1	5.49	0.2113	1.76	2.45	1.85	3.08	0.458	167	0.24	8.63
SN26	P304 soil core 26-34cm	66.0	0.755	18.0	5.46	0.1372	1.82	2.48	1.64	3.06	0.381	145	0.12	8.15
SN59	BP soil - 5 cm	59.1	1.075	19.8	8.47	0.2090	2.92	3.86	1.69	2.27	0.305	295	0.57	9.08
SN60	BP soil - 35 cm	57.6	1.143	20.9	9.09	0.1505	3.10	3.78	1.49	2.17	0.179	264	0.52	5.60
SN61	BP soil - 65 cm	58.7	1.118	19.8	9.06	0.1494	3.13	3.92	1.48	2.18	0.137	266	0.52	6.27
SN62	BP soil - 85 cm	59.6	1.085	19.2	9.05	0.1471	3.03	3.86	1.47	2.12	0.132	252	0.50	4.83
SN20	BP 204 saprolite - 178 cm	60.5	1.126	20.1	10.07	0.1065	2.89	2.11	0.45	2.30	0.057	181	0.30	7.95
SN19	BP 173 saprolite - 256 cm	60.7	1.096	20.0	8.93	0.1106	3.04	2.73	0.74	2.44	0.044	191	0.34	6.88
SN18	BP 161 saprolite - 287 cm	57.0	1.251	20.0	9.88	0.1506	3.94	4.13	1.23	2.03	0.040	187	0.32	6.37
SN17	BP 144 saprolite - 330 cm	60.1	0.998	19.6	7.77	0.1451	2.97	4.10	1.56	2.45	0.042	189	0.33	5.59
SN16	BP 111 saprolite - 414 cm	60.7	1.010	19.2	7.91	0.1213	3.01	3.87	1.49	2.28	0.069	184	0.31	5.19
SN15	BP 72 saprolite - 513 cm	61.7	0.932	18.1	7.10	0.1082	2.74	4.66	2.01	2.20	0.170	168	0.24	3.89
SN14	BP 36 saprolite - 605 cm	61.6	1.056	17.9	7.93	0.1216	3.11	4.07	1.57	2.23	0.120	169	0.25	4.62
SN13	BP 3 saprolite - 688 cm	60.7	0.988	17.1	7.50	0.1158	3.01	5.91	2.60	1.52	0.255	184	0.31	3.30
SN12	BP 0 saprolite - 696 cm	60.1	0.982	16.7	7.59	0.1204	3.08	5.87	2.66	2.38	0.233	195	0.35	1.99
SN11	BP Rock	68.4	0.542	14.7	4.31	0.0739	1.56	3.59	2.59	3.85	0.105	139	0.09	1.21
SN27	P301 Bedload	75.7	0.470	11.5	3.42	0.0644	1.41	3.26	1.83	2.05	0.090	94	-0.35	2.11
SN28	PIG bedload	68.3	1.200	11.7	7.50	0.1293	2.68	4.77	1.73	1.52	0.140	276	0.54	3.34

Denudation, weathering and erosion rates

This page is intentionally left blank.

Table 5.19: Denudation rates (D) determined for the different sampling sites on soil samples. Weathering rate (W) for the Swiss Alps sampling site is calculated with $W = D * CDF$ and erosion rate (E) with $E = D - W$. Weathering and erosion rates for the Sri Lankan and Sierra Nevada sampling site are literature values. Rates in t/km^2/yr were calculated assuming a rock density of 2700 kg/m^3.

sampling site	mean CDF	denudation rate [mm/kyr] ([t/km^2/yr])	weathering rate [mm/kyr] ([t/km^2/yr])	erosion rate [mm/kyr] ([t/km^2/yr])	source
Sri Lanka	0.5	14.5 (39.1)	7.2 (19.5)	7.2 (19.5)	Hewawasam et al. (2013)
Swiss Alps	0.30	29.7 (80.2)	8.9 (24.0)	20.8 (56.2)	Norton et al. (2010)
Sierra Nevada	0.58	81.5 (220)	47.4 (128.1)	34 (91.9)	Dixon et al. (2009a)

Bibliography

Abraham, K., Cardinal, D., Hofmann, A., Foley, S. F., Harris, C., Barth, M. G., and Andre, L. (2011). Coupled silicon–oxygen isotope fractionation traces Archaean silicification. *Earth and Planetary Science Letters*, 301(1-2):222–230.

Abraham, K., Opfergelt, S., and Fripiat, F. (2008). δ^{30}Si and δ^{29}Si Determinations on USGS BHVO-1 and BHVO-2 Reference Materials with a New Configuration on a Nu Plasma Multi-Collector ICP-MS. *Geostandards and Geoanalytical Research*.

Adu-Wusu, K. and Wilcox, W. R. (1991). Kinetics of silicate reaction with gibbsite. *Journal of Colloid and Interface Science*, 143(1):127–138.

Anderson, D. M. (1981). Some thermodynamic relationships governing the behavior of permafrost and patterned ground. Technical Report NASA TM-84211.

Anderson, D. M. and Tice, A. R. (1973). The Unfrozen Interfacial Phase in Frozen Soil Water Systems. In *Physical Aspects of Soil Water and Salts in Ecosystems*, pages 107–124. Springer Berlin Heidelberg, Berlin, Heidelberg.

Andre, L., Cardinal, D., Alleman, L. Y., and Moorbath, S. (2006). Silicon isotopes in 3.8 Ga West Greenland rocks as clues to the Eoarchaean supracrustal Si cycle. *Earth and Planetary Science Letters*, 245(1-2):162–173.

Armytage, R. M. G., Georg, R. B., Savage, P. S., Williams, H. M., and Halliday, A. N. (2011a). Silicon isotopes in meteorites and planetary core formation. *Geochimica et Cosmochimica Acta*, 75(13):3662–3676.

Armytage, R. M. G., Georg, R. B., Williams, H. M., and Halliday, A. N. (2011b). Silicon isotopes in lunar rocks: Implications for the Moon's formation and the early history of the Earth. *Geochimica et Cosmochimica Acta*, 77:504–514.

Baes, C. F. and Mesmer, R. E. . j. a. (1976). *The Hydrolysis of Cations*. New York : Wiley.

Bales, R. C., Hopmans, J. W., O'Geen, A. T., Meadows, M., Hartsough, P. C., Kirchner, P., Hunsaker, C. T., and Beaudette, D. (2011). Soil Moisture Response to Snowmelt and Rainfall in a Sierra Nevada Mixed-Conifer Forest. *Vadose Zone Journal*, 10(3):786–799.

Barling, J. and Weis, D. (2008). Influence of non-spectral matrix effects on the accuracy of Pb isotope ratio measurement by MC-ICP-MS: implications for the external normalization method of instrumental mass bias correction. *Journal of Analytical Atomic Spectrometry*, 23(7):1017–1025.

Basile-Doelsch, I. (2006). Si stable isotopes in the Earth's surface: A review. *Journal of Geochemical Exploration*, 88(1-3):252–256.

Basile-Doelsch, I., Meunier, J. D., and Parron, C. (2005). Another continental pool in the terrestrial silicon cycle. *Nature*, 433(7024):399–402.

Bateman, P. C. and Wones, D. R. (1972). Geologic map of the Huntington Lake quadrangle, central Sierra Nevada, California. *USGS Numbered Series*, page 1 map.

Bern, C. R., Brzezinski, M. A., Beucher, C., Ziegler, K., and Chadwick, O. A. (2010). Weathering, dust, and biocycling effects on soil silicon isotope ratios. *Geochimica et Cosmochimica Acta*, 74(3):876–889.

Bigeleisen, J. (1965). Chemistry of Isotopes: Isotope chemistry has opened new areas of chemical physics, geochemistry, and molecular biology. *Science*, 147(3657):463–471.

Bouchez, J., von Blanckenburg, F., and Schuessler, J. A. (2013). Modeling novel stable isotope ratios in the weathering zone. *American Journal Of Science*, 313(4):267–308.

Brzezinski, M. A., Jones, J. L., Beucher, C. P., Demarest, M. S., and Berg, H. L. (2006). Automated determination of silicon isotope natural abundance by the acid decomposition of cesium hexafluosilicate. *Analytical Chemistry*, 78(17):6109–6114.

Cardinal, D., Alleman, L., de Jong, J., Ziegler, K., and Andre, L. (2003). Isotopic composition of silicon measured by multicollector plasma source mass spectrometry in dry plasma mode. *Journal of Analytical Atomic Spectrometry*, 18(3):213–218.

Cardinal, D., Gaillardet, J., Hughes, H. J., Opfergelt, S., and Andre, L. (2010). Contrasting silicon isotope signatures in rivers from the Congo Basin and the specific behaviour of organic-rich waters. *Geophysical Research Letters*, 37(12):L12403.

Carroll, S., Mroczek, E., Alai, M., and Ebert, M. (1998). Amorphous silica precipitation (60 to 120°C): Comparison of laboratory and field rates. *Geochimica et Cosmochimica Acta*, 62(8):1379–1396.

Chakrabarti, R. and Jacobsen, S. B. (2010). Silicon isotopes in the inner Solar System: Implications for core formation, solar nebular processes and partial melting. *Geochimica et Cosmochimica Acta*, 74(23):6921–6933.

Chakrabarti, R., Knoll, A. H., Jacobsen, S. B., and Fischer, W. W. (2012). Si isotope variability in Proterozoic cherts. *Geochimica et Cosmochimica Acta*, 91:187–201.

Chen, Y., Jiang, S., Ling, H., Yang, J., and Wan, D. (2007). Isotopic compositions of small shelly fossil Anabarites from Lower Cambrian in Yangtze Platform of South China: Implications for palaeocean temperature. *Progress in Natural Science*, 17(10):1185–1191.

Chmeleff, J., Horn, I., Steinhoefel, G., and von Blanckenburg, F. (2008). In situ determination of precise stable Si isotope ratios by UV-femtosecond laser ablation high-resolution multi-collector ICP-MS. *Chemical Geology*, 249(1-2):155–166.

Cole, D. R., Ohmoto, H., and Lasaga, A. C. (1983). Isotopic exchange in mineral-fluid systems. I. Theoretical evaluation of oxygen isotopic exchange accompanying surface reactions and diffusion. *Geochimica et Cosmochimica Acta*, 47(10):1681–1693.

Conrad, C. F., Icopini, G. A., Yasuhara, H., Bandstra, J. Z., Brantley, S. L., and Heaney, P. J. (2007). Modeling the kinetics of silica nanocolloid formation and precipitation in geologically relevant aqueous solutions. *Geochimica et Cosmochimica Acta*, 71(3):531–542.

Coplen, T., Böhlke, J., de Bièvre, P., Ding, T., Holden, N., Hopple, J., Krouse, H., Lamberty, A., Peiser, H., and Revesz, K. (2002a). Isotope-abundance variations of selected elements:(IUPAC technical report). *Pure and applied chemistry*, 74(10):1987–2017.

Coplen, T., Hopple, J., Boehike, J., Peiser, H., and Rieder, S. (2002b). Compilation of minimum and maximum isotope ratios of selected elements in naturally occurring terrestrial materials and reagents. *Water-Resources Investigations Report 01-4222*.

Coplen, T. B. (2011). Guidelines and recommended terms for expression of stable-isotope-ratio and gas-ratio measurement results. *Rapid Communications in Mass Spectrometry*, 25(17):2538–2560.

Cornelis, J.-T., Weis, D., Lavkulich, L., Vermeire, M.-L., Delvaux, B., and Barling, J. (2014). Silicon isotopes record dissolution and re-precipitation of pedogenic clay minerals in a podzolic soil chronosequence. *Geoderma*, 235-236(C):19–29.

Criss, R. (1999). *Principles of stable isotope distribution* . Oxford University Press.

Criss, R. E., Gregory, R. T., and Taylor Jr, H. P. (1987). Kinetic theory of oxygen isotopic exchange between minerals and water. *Geochimica et Cosmochimica Acta*, 51(5):1099–1108.

Dahlgren, R. A., Boettinger, J. L., Huntington, G. L., and Amundson, R. G. (1997). Soil development along an elevational transect in the western Sierra Nevada, California. *Geoderma*, 78(3-4):207–236.

de La Rocha, C. L., Brzezinski, M. A., and DeNiro, M. J. (2000). A first look at the distribution of the stable isotopes of silicon in natural waters. *Geochimica et Cosmochimica Acta*, 64(14):2467–2477.

Delstanche, S., Opfergelt, S., Cardinal, D., Elsass, F., Elsass, F., André, L., and Delvaux, B. (2009). Silicon isotopic fractionation during adsorption of aqueous monosilicic acid onto iron oxide. *Geochimica et Cosmochimica Acta*, 73(4):923–934.

DePaolo, D. J. (2011). Surface kinetic model for isotopic and trace element fractionation during precipitation of calcite from aqueous solutions. *Geochimica et Cosmochimica Acta*, 75(4):1039–1056.

Dickinson, W. W. and Grapes, R. H. (1997). Authigenic chabazite and implications for weathering in Sirius Group diamictite, Table Mountain, dry valleys, Antarctica. *Journal of Sedimentary Research*, 67(5):815–820.

Dietzel, M. (1993). *Depolymerisation von hochpolymerer Kieselsäure in wässriger Lösung.* PhD thesis, University Göttingen, Göttingen.

Dietzel, M. (2000). Dissolution of silicates and the stability of polysilicic acid. *Geochimica et Cosmochimica Acta*, 64(19):3275–3281.

Dietzel, M. (2002). Interaction of polysilicic and monosilicic acid with mineral surfaces. In Stober, I. and Bucher, K., editors, *Water Science and Technology Library*, pages 207–235. Springer Netherlands.

Dietzel, M. (2005). Impact of cyclic freezing on precipitation of silica in Me-SiO2-H2O systems and geochemical implications for cryosoils and -sediments. *Chemical Geology*, 216(11):79–88.

Dietzel, M. and Böhme, G. (1997). Adsorption and Stability of Polymeric Silica — Adsorption und Stabilität von polymerer Kieselsäure. *Chemie der Erde - Geochemistry*, 57(2-3):189–203.

Ding, T., Jiang, S., Wan, D., Li, Y., Li, J., Song, H., Liu, Z., and Yao, X. (1996). *Silicon Isotope Geochemistry*. Geological Publishing House, Beijing, China.

Ding, T., Ma, G., Shui, M., Wan, D., and Li, R. (2005). Silicon isotope study on rice plants from the Zhejiang province, China. *Chemical Geology*, 218(1-2):41–50.

Ding, T., Tian, S. H., Sun, L., Wu, L. H., Zhou, J. X., and Chen, Z. Y. (2008a). Silicon isotope fractionation between rice plants and nutrient solution and its significance to the study of the silicon cycle. *Geochimica et Cosmochimica Acta*, 72(23):5600–5615.

Ding, T. P., Zhou, J. X., Wan, D. F., Chen, Z. Y., Wang, C. Y., and Zhang, F. (2008b). Silicon isotope fractionation in bamboo and its significance to the biogeochemical cycle of silicon. *Geochimica et Cosmochimica Acta*, 72(5):1381–1395.

Dixit, S., Van Cappellen, P., and van Bennekom, A. J. (2001). Processes controlling solubility of biogenic silica and pore water build-up of silicic acid in marine sediments. *Marine Chemistry*, 73(3-4):333–352.

Dixon, J. L., Hartshorn, A. S., Heimsath, A. M., DiBiase, R. A., and Whipple, K. X. (2012). Chemical weathering response to tectonic forcing: A soils perspective from the San Gabriel Mountains, California. *Earth and Planetary Science Letters*, 323:40–49.

Dixon, J. L., Heimsath, A. M., and Amundson, R. (2009a). The critical role of climate and saprolite weathering in landscape evolution. *Earth Surface Processes And Landforms*, 34(11):1507–1521.

Dixon, J. L., Heimsath, A. M., Kaste, J., and Amundson, R. (2009b). Climate-driven processes of hillslope weathering. *Geology*, 37(11):975–978.

Dixon, J. L. and von Blanckenburg, F. (2012). Soils as pacemakers and limiters of global silicate weathering. *Comptes rendus - Geoscience*, 344(11-12):597–609.

Doucet, F., Rotov, M., and Exley, C. (2001). Direct and indirect identification of the formation of hydroxyaluminosilicates in acidic solutions. *Journal of Inorganic Biochemistry*, 87:71–79.

Douthitt, C. B. (1982). The geochemistry of the stable isotopes of silicon. *Geochimica et Cosmochimica Acta*, 46(8):1449–1458.

Dove, P. M., Han, N., Wallace, A. F., and De Yoreo, J. J. (2008). Kinetics of amorphous silica dissolution and the paradox of the silica polymorphs. *Proceedings of the National Academy of Sciences*, 105(29):9903–9908.

Dove, P. M. and Rimstidt, J. D. (1994). Silica-water interactions. *Reviews in Mineralogy and Geochemistry*, 29(1):259–308.

Druhan, J. L., Steefel, C. I., Williams, K. H., and DePaolo, D. J. (2013). Calcium isotope fractionation in groundwater: Molecular scale processes influencing field scale behavior. *Geochimica et Cosmochimica Acta*, 119:93–116.

Egli, M., Mirabella, A., and Sartori, G. (2008). The role of climate and vegetation in weathering and clay mineral formation in late Quaternary soils of the Swiss and Italian Alps. *Geomorphology*, 102(3-4):307–324.

Engström, E., Rodushkin, I., Baxter, D. C., and Öhlander, B. (2006). Chromatographic Purification for the Determination of Dissolved Silicon Isotopic Compositions in Natural Waters by High-Resolution Multicollector Inductively Coupled Plasma Mass Spectrometry. *Analytical Chemistry*, 78(1):250–257.

Exley, C., Schneider, C., and Doucet, F. (2002). The reaction of aluminium with silicic acid in acidic solution: an important mechanism in controlling the biological availability of aluminium? *Coordination Chemistry Reviews*, 228(2):127–135.

Ferrier, K. and Kirchner, J. (2008). Effects of physical erosion on chemical denudation rates: A numerical modeling study of soil-mantled hillslopes. *Earth and Planetary Science Letters*, 272(3-4):591–599.

Fitoussi, C., Bourdon, B., Kleine, T., Oberli, F., and Reynolds, B. C. (2009). Si isotope systematics of meteorites and terrestrial peridotites: implications for Mg/Si fractionation in the solar nebula and for Si in the Earth's core. *Earth and Planetary Science Letters*, 287(1-2):77–85.

Fournier, R. O. and Potter II, R. W. (1982). An equation correlating the solubility of quartz in water from 25° to 900°C at pressures up to 10,000 bars. *Geochimica et Cosmochimica Acta*, 46(10):1969–1973.

Fournier, R. O. and Rowe, J. J. (1977). Solubility of amorphous silica in water at high temperatures and high pressure. *Am. Mineral.; (United States)*, 62:9-10.

Geilert, S., Vroon, P. Z., Roerdink, D. L., van CAPPELLEN, P., and van Bergen, M. J. (2014). Silicon isotope fractionation during abiotic silica precipitation at low temperatures: Inferences from flow-through experiments. *Geochimica et Cosmochimica Acta*, 142(1):95–114.

Georg, R. B., Halliday, A. N., Schauble, E. A., and Reynolds, B. C. (2007a). Silicon in the Earth's core. *Nature*, 447(7148):1102–1106.

Georg, R. B., Reynolds, B. C., Frank, M., and Halliday, A. N. (2006a). Mechanisms controlling the silicon isotopic compositions of river waters. *Earth and Planetary Science Letters*, 249:290–306.

Georg, R. B., Reynolds, B. C., Frank, M., and Halliday, A. N. (2006b). New sample preparation techniques for the determination of Si isotopic compositions using MC-ICPMS. *Chemical Geology*, 235(1-2):95–104.

Georg, R. B., Reynolds, B. C., West, A. J., Burton, K. W., and Halliday, A. N. (2007b). Silicon isotope variations accompanying basalt weathering in Iceland. *Earth and Planetary Science Letters*, 261:476–490.

Georg, R. B., Zhu, C., Reynolds, B. C., and Halliday, A. N. (2009). Stable silicon isotopes of groundwater, feldspars, and clay coatings in the Navajo Sandstone aquifer, Black Mesa, Arizona, USA. *Geochimica et Cosmochimica Acta*, 73(8):2229–2241.

Georgiadis, A. (2011). *Entwicklung einer Methode zur fraktionierten Si-Bestimmung in Böden des feucht-gemäßigten Klimas*. PhD thesis, Universität Hohenheim.

Gislason, S. R. and Oelkers, E. (2003). Mechanism, rates, and consequences of basaltic glass dissolution: II. An experimental study of the dissolution rates of basaltic glass as a function of pH and temperature. *Geochimica et Cosmochimica Acta*, 67(20):3817–3832.

Gray, A. L. (1986). Mass spectrometry with an inductively coupled plasma as an ion source: the influence on ultratrace analysis of background and matrix response. *Spectrochimica Acta Part B-Atomic Spectroscopy*, 41(1-2):151–167.

Greenberg, S. A. and Sinclair, D. (1955). The polymerization of silicic acid. *Journal of Physical Chemistry*, 59(5):435–440.

Guillaumont, R., Fanghänel, T., Neck, V., Fuger, J., Palmer, D. A., Grenthe, I., and Rand, M. H. (2003). *Update on the Chemical Thermodynamics of Uranium, Neptunium, Plutonium, Americium and Technetium*. Elsevier Science Limited.

Gunnarsson, I. and Arnorsson, S. (2000). Amorphous silica solubility and the thermodynamic properties of $H_4SiO°_4$ the range of 0° to 350°C at P_{sat}. *Geochimica et Cosmochimica Acta*, 64(13):2295–2307.

Hahm, W. J., Riebe, C. S., Lukens, C. E., and Araki, S. (2014). Bedrock composition regulates mountain ecosystems and landscape evolution. *Proceedings of the National Academy of Sciences*, 111(9):3338–3343.

Hewawasam, T., von Blanckenburg, F., Bouchez, J., Dixon, J. L., Schuessler, J. A., and Maekeler, R. (2013). Slow advance of the weathering front during deep, supply-limited saprolite formation in the tropical Highlands of Sri Lanka. *Geochimica et Cosmochimica Acta*, 118:202–230.

Hewawasam, T., von Blanckenburg, F., Schaller, M., and Kubik, P. (2003). Increase of human over natural erosion rates in tropical highlands constrained by cosmogenic nuclides. *Geology*, 31(7):597–600.

Hingston, F. and Raupach, M. (1967). The reaction between monosilicic acid and aluminium hydroxide. I. Kinetics of adsorption of silicic acid by aluminium hydroxide. *Australian Journal of Soil Research*, 5(2):295–309.

Hofmann, A. E., Bourg, I. C., and DePaolo, D. J. (2012). Ion desolvation as a mechanism for kinetic isotope fractionation in aqueous systems. *Proceedings of the National Academy of Sciences*, 109(46):18689–18694.

Holleman, A. F. and Wiberg, N. (1995). *Lehrbuch der anorganischen Chemie*. Berlin.

Hughes, H. J., Delvigne, C., Korntheuer, M., de Jong, J., André, L., and Cardinal, D. (2011). Controlling the mass bias introduced by anionic and organic matrices in silicon isotopic measurements by MC-ICP-MS. *Journal of Analytical Atomic Spectrometry*, 26(9):1892–1896.

Hughes, H. J., Sondag, F., Santos, R. V., André, L., and Cardinal, D. (2013). The riverine silicon isotope composition of the Amazon Basin. *Geochimica et Cosmochimica Acta*, 121:637–651.

Hunsaker, C. T. and Neary, D. G. (2012). Sediment loads and erosion in forest headwater streams of the Sierra Nevada, California. *Notes*.

Icenhower, J. and Dove, P. M. (2000). The dissolution kinetics of amorphous silica into sodium chloride solutions: Effects of temperature and ionic strength. *Geochimica et Cosmochimica Acta*, 64(24):4193–4203.

Icopini, G., Brantley, S. L., and Heaney, P. (2005). Kinetics of silica oligomerization and nanocolloid formation as a function of pH and ionic strength at 25°C. *Geochimica et Cosmochimica Acta*, 69(2):293–303.

Iler, R. K. (1979). *The chemistry of silica: solubility, polymerization, colloid and surface properties, and biochemistry*. John Wiley & Sons, Inc., New York.

Iler, R. K. (1982). Colloidal Components in Solutions of Sodium Silicate. In Falcone, J. S., editor, *Soluble Silicates*, pages 95–114. American Chemical Society.

Jepson, W., Jeffs, D., and Ferris, A. (1976). The adsorption of silica on gibbsite and its relevance to the kaolinite surface. *Journal of Colloid and Interface Science*, 55(2):454–461.

Johnson, C. M., Beard, B. L., and Albarede, F. (2004). Overview and general concepts. *Reviews in Mineralogy and Geochemistry*, 55:1–24.

Johnson, C. M., Skulan, J., Beard, B., Sun, H., Nealson, K., and Braterman, P. (2002). Isotopic fractionation between Fe(III) and Fe(II) in aqueous solutions. *Earth and Planetary Science Letters*, 195:141–153.

Johnson, D. W., Hunsaker, C. T., Glass, D. W., Rau, B. M., and Roath, B. A. (2011). Carbon and nutrient contents in soils from the Kings River Experimental Watersheds, Sierra Nevada Mountains, California. *Geoderma*, 160(3-4):490–502.

Joussein, E., Petit, S., Churchman, J., Theng, B., Righi, D., and Delvaux, B. (2005). Halloysite clay minerals—a review. *Clay Minerals*, 40(4):383–426.

Juillot, F., Maréchal, C., Ponthieu, M., Cacaly, S., Morin, G., Benedetti, M., Hazemann, J. L., Proux, O., and Guyot, F. (2008). Zn isotopic fractionation caused by sorption on goethite and 2-Lines ferrihydrite. *Geochimica et Cosmochimica Acta*, 72(19):4886–4900.

Karamalidis, A. K. and Dzombak, D. A. (2011). *Surface Complexation Modeling: Gibbsite*. John Wiley & Sons, Inc., Hoboken, New Jersey.

Lam, J. W. and McLaren, J. W. (1990). Use of aerosol processing and nitrogen-argon plasmas for reduction of oxide interference in inductively coupled plasma mass spectrometry. *Journal of Analytical Atomic Spectrometry*, 5(6):419–424.

Lemarchand, E., Schott, J., and Gaillardet, J. (2007). How surface complexes impact boron isotope fractionation: Evidence from Fe and Mn oxides sorption experiments. *Earth and Planetary Science Letters*, 260(1-2):277–296.

Li, W., Beard, B. L., and Johnson, C. M. (2011). Exchange and fractionation of Mg isotopes between epsomite and saturated $MgSO_4$ solution. *Geochimica et Cosmochimica Acta*, 75(7):1814–1828.

Li, Y., Ding, T., and Wan, D. (1995). Experimental study of silicon isotope dynamic fractionation and its application in geology. *Chinese Journal of Geochemistry*, 14(3):212–219.

Liu, F., Hunsaker, C., and Bales, R. C. (2012). Controls of streamflow generation in small catchments across the snow-rain transition in the Southern Sierra Nevada, California. *Hydrological Processes*, pages n/a–n/a.

Maher, K. (2011). The role of fluid residence time and topographic scales in determining chemical fluxes from landscapes. *Earth and Planetary Science Letters*, 312(1-2):48–58.

Marshall, W. L. (1980a). Amorphous silica solubilities—I. Behavior in aqueous sodium nitrate solutions; 25–300°C, 0–6 molal. *Geochimica et Cosmochimica Acta*, 44(7):907–913.

Marshall, W. L. (1980b). Amorphous silica solubilities—III. Activity coefficient relations and predictions of solubility behavior in salt solutions, 0–350°C. *Geochimica et Cosmochimica Acta*, 44(7):925–931.

Marshall, W. L. and Warakomski, J. M. (1980). Amorphous silica solubilities—II. Effect of aqueous salt solutions at 25°C. *Geochimica et Cosmochimica Acta*, 44(7):915–924.

Méheut, M., Lazzeri, M., Balan, E., and Mauri, F. (2007). Equilibrium isotopic fractionation in the kaolinite, quartz, water system: Prediction from first-principles density-functional theory. *Geochimica et Cosmochimica Acta*, 71(13):3170–3181.

Méheut, M., Lazzeri, M., Balan, E., and Mauri, F. (2009). Structural control over equilibrium silicon and oxygen isotopic fractionation: A first-principles density-functional theory study. *Chemical Geology*, 258(1-2):28–37.

Méheut, M. and Schauble, E. A. (2014). Silicon isotope fractionation in silicate minerals: Insights from first-principles models of phyllosilicates, albite and pyrope. *Geochimica et Cosmochimica Acta*, 134:137–154.

Mikutta, C., Wiederhold, J. G., Hofstetter, T. B., Cirpka, O. A., Bourdon, B., and von Gunten, U. (2008). Iron isotope fractionation during Fe(II) sorption to mineral surfaces. *Geochimica et Cosmochimica Acta*, 72(12):A627–A627.

Mills, G. A. and Urey, H. C. (1940). The Kinetics of Isotopic Exchange between Carbon Dioxide, Bicarbonate Ion, Carbonate Ion and Water1. *Journal of the American Chemical Society*, 62(5):1019–1026.

Nielsen, L. C., DePaolo, D. J., and de Yoreo, J. J. (2012). Self-consistent ion-by-ion growth model for kinetic isotopic fractionation during calcite precipitation. *Geochimica et Cosmochimica Acta*, 86:166–181.

Norton, K. P. and von Blanckenburg, F. (2010). Silicate weathering of soil-mantled slopes in an active Alpine landscape. *Geochimica et Cosmochimica Acta*.

Norton, K. P., von Blanckenburg, F., DiBiase, R., Schlunegger, F., and Kubik, P. W. (2011). Cosmogenic Be-10-derived denudation rates of the Eastern and Southern European Alps. *International Journal of Earth Sciences*, 100(5):1163–1179.

Norton, K. P., von Blanckenburg, F., and Kubik, P. W. (2010). Cosmogenic nuclide-derived rates of diffusive and episodic erosion in the glacially sculpted upper Rhone Valley, Swiss Alps. *Earth Surface Processes And Landforms*, 35(6):651–662.

Oelze, M., von Blanckenburg, F., Bouchez, J., Hoellen, D., and Dietzel, M. (2015). The effect of Al on Si isotope fractionation investigated by silica precipitation experiments. *Chemical Geology*, 397:94–105.

Oelze, M., von Blanckenburg, F., Hoellen, D., Dietzel, M., and Bouchez, J. (2014). Si stable isotope fractionation during adsorption and the competition between kinetic and equilibrium isotope fractionation: Implications for weathering systems. *Chemical Geology*, 380:161–171.

Opfergelt, S., Cardinal, D., Delvaux, B., and Andre, L. (2008). Plant silicon isotopic signature might reflect soil weathering degree. *Biogeochemistry*, 91(2-3):163–175.

Opfergelt, S., Cardinal, D., Henriet, C., Andre, L., and Delvaux, B. (2006a). Silicon isotope fractionation between plant parts in banana: In situ vs. in vitro. *Journal of Geochemical Exploration*, 88(1-3):224–227.

Opfergelt, S., Cardinal, D., Henriet, C., Draye, X., Andre, L., and Delvaux, B. (2006b). Silicon Isotopic Fractionation by Banana (Musa spp.) Grown in a Continuous Nutrient Flow Device. *Plant And Soil*, 285(1-2):333–345.

Opfergelt, S., de Bournonville, G., Cardinal, D., André, L., Delstanche, S., and Delvaux, B. (2009). Impact of soil weathering degree on silicon isotopic fractionation during adsorption onto iron oxides in basaltic ash soils, Cameroon. *Geochimica et Cosmochimica Acta*, 73(24):7226–7240.

Opfergelt, S. and Delmelle, P. (2012). Silicon isotopes and continental weathering processes: Assessing controls on Si transfer to the ocean. *Comptes rendus - Geoscience*, 344(11-12):723–738.

Opfergelt, S., Georg, R. B., Burton, K. W., Guicharnaud, R., Siebert, C., Gislason, S. R., and Halliday, A. N. (2011). Silicon isotopes in allophane as a proxy for mineral formation in volcanic soils. *Applied Geochemistry*, 26:S115–S118.

Papoulis, D., Tsolis-Katagas, P., and Katagas, C. (2004). Progressive stages in the formation of kaolin minerals of different morphologies in the weathering of plagioclase. *Clays and clay minerals*, 52(3):275–286.

Pinheiro, J., Bates, D., DebRoy, S., Sarkar, D., and R Core Team (2014). *nlme: Linear and Nonlinear Mixed Effects Models*.

Polyakov, V. B. and Mineev, S. D. (2000). The use of Mössbauer spectroscopy in stable isotope geochemistry. *Geochimica et Cosmochimica Acta*, 64(5):849–865.

Pringle, E. A., Savage, P. S., Badro, J., Barrat, J.-A., and Moynier, F. (2013). Redox state during core formation on asteroid 4-Vesta. *Earth and Planetary Science Letters*, 373:75–82.

R Core Team (2014). *R: A Language and Environment for Statistical Computing*. R Foundation for Statistical Computing, Vienna, Austria.

Railsback, L. B. (2003). An earth scientist's periodic table of the elements and their ions. *Geology*, 31(9):737.

Renders, P. J. N., Gammons, C. H., and Barnes, H. L. (1995). Precipitation and dissolution rate constants for cristobalite from 150 to 300°C. *Geochimica et Cosmochimica Acta*, 59(1):77–85.

Reynolds, B. C., Aggarwal, J., André, L., Baxter, D., Beucher, C., Brzezinski, M. A., Engström, E., Georg, R. B., Land, M., Leng, M. J., Opfergelt, S., Rodushkin, I., Sloane, H. J., van den Boorn, S. H. J. M., Vroon, P. Z., and Cardinal, D. (2007). An inter-laboratory comparison of Si isotope reference materials. *Journal of Analytical Atomic Spectrometry*, 22(5):561–568.

Reynolds, J. and Verhoogen, J. (1953). Natural variations in the isotopic constitution of silicon. *Geochimica et Cosmochimica Acta*, 3(5):224–234.

Richter, F. M., Mendybaev, R., Christensen, J., Hutcheon, I., Williams, R., Sturchio, N., and Beloso, A. (2006). Kinetic isotopic fractionation during diffusion of ionic species in water. *Geochimica et Cosmochimica Acta*, 70(2):277–289.

Riebe, C. S., Kirchner, J., and Finkel, R. (2004). Erosional and climatic effects on long-term chemical weathering rates in granitic landscapes spanning diverse climate regimes. *Earth and Planetary Science Letters*, 224(3-4):547–562.

Riebe, C. S., Kirchner, J. W., Granger, D. E., and Finkel, R. C. (2001). Strong tectonic and weak climatic control of long-term chemical weathering rates. *Geology*, 29(6):511–514.

Rimstidt, J. D. and Barnes, H. L. (1980). The kinetics of silica-water reactions. *Geochimica et Cosmochimica Acta*, 44(11):1683–1699.

Robert, F. and Chaussidon, M. (2006). A palaeotemperature curve for the Precambrian oceans based on silicon isotopes in cherts. *Nature*, 443(7114):969–972.

Ryan, W. B. F., Carbotte, S. M., Coplan, J. O., O'Hara, S., Melkonian, A., Arko, R., Weissel, R. A., Ferrini, V., Goodwillie, A., Nitsche, F., Bonczkowski, J., and Zemsky, R. (2009). Global Multi-Resolution Topography synthesis. *Geochemistry Geophysics Geosystems*, 10(3):n/a–n/a.

Sauer, D., Saccone, L., Conley, D. J., Herrmann, L., and Sommer, M. (2006). Review of methodologies for extracting plant-available and amorphous Si from soils and aquatic sediments. *Biogeochemistry*, 80(1):89–108.

Savage, P. S., Georg, R. B., Armytage, R. M. G., Williams, H. M., and Halliday, A. N. (2010). Silicon isotope homogeneity in the mantle. *Earth and Planetary Science Letters*, 295(1-2):139–146.

Savage, P. S., Georg, R. B., Williams, H. M., Burton, K. W., and Halliday, A. N. (2011). Silicon Isotope Fractionation During Magmatic Differentiation. *Geochimica et Cosmochimica Acta.*

Savage, P. S., Georg, R. B., Williams, H. M., and Halliday, A. N. (2013). The silicon isotope composition of the upper continental crust. *Geochimica et Cosmochimica Acta*, 109:384–399.

Savage, P. S., Georg, R. B., Williams, H. M., Turner, S., Halliday, A. N., and Chappell, B. W. (2012). The Silicon Isotope Composition of Granites. *Geochimica et Cosmochimica Acta.*

Schauble, E. (2001). Theoretical estimates of equilibrium Fe-isotope fractionations from vibrational spectroscopy. *Geochimica et Cosmochimica Acta*, 65(15):2487–2497.

Schauble, E. A. (2004). Applying Stable Isotope Fractionation Theory to New Systems. *Reviews in Mineralogy and Geochemistry*, 55(1):65–111.

Schmidt, M., Rumpel, C., and Kögel Knabner, I. (2008). Evaluation of an ultrasonic dispersion procedure to isolate primary organomineral complexes from soils. *Journal of Soil Science*, 50(1):87–94.

Schuessler, J. A., Schoenberg, R., Behrens, H., and von Blanckenburg, F. (2007). The experimental calibration of the iron isotope fractionation factor between pyrrhotite and peralkaline rhyolitic melt. *Geochimica et Cosmochimica Acta*, 71(2):417–433.

Schwertmann, U. and Fischer, W. R. (1982). PH-Verteilung und Pufferung von Böden. *Zeitschrift für Pflanzenernährung und Bodenkunde*, 145(2):221–223.

Soil Survey Staff (1998). Soil Survey Staff, Natural Resources Conservation Service, United States Department of Agriculture.

Sposito, G. (1996). *The Environmental Chemistry of Aluminum.* CRC Press.

Stallard, R. F. (1995). Tectonic, environmental, and human aspects of weathering and erosion: a global review from a steady-state perspective. *Annual Review of Earth and Planetary Sciences.*

Steefel, C. I. and Van Cappellen, P. (1990). A new kinetic approach to modeling water-rock interaction: The role of nucleation, precursors, and Ostwald ripening. *Geochimica et Cosmochimica Acta*, 54(10):2657–2677.

Steinhoefel, G., Breuer, J., von Blanckenburg, F., Horn, I., Kaczorek, D., and Sommer, M. (2011). Micrometer silicon isotope diagnostics of soils by UV femtosecond laser ablation. *Chemical Geology*, 286(3-4):280–289.

Steinhoefel, G., Horn, I., and von Blanckenburg, F. (2009). Micro-scale tracing of Fe and Si isotope signatures in banded iron formation using femtosecond laser ablation. *Geochimica et Cosmochimica Acta*, 73(18):5343–5360.

Steinhoefel, G., von Blanckenburg, F., Horn, I., Konhauser, K. O., Beukes, N. J., and Gutzmer, J. (2010). Deciphering formation processes of banded iron formations from the Transvaal and the Hamersley successions by combined Si and Fe isotope analysis

using UV femtosecond laser ablation. *Geochimica et Cosmochimica Acta*, 74(9):2677–2696.

Strekopytov, S., Jarry, E., and Exley, C. (2006). Further insight into the mechanism of formation of hydroxyaluminosilicates. *Polyhedron*, 25(17):3399–3404.

Tang, J., Dietzel, M., Böhm, F., Köhler, S. J., and Eisenhauer, A. (2008). Sr^{2+}/Ca^{2+} and $^{44}Ca/^{40}Ca$ fractionation during inorganic calcite formation: II. Ca isotopes. *Geochimica et Cosmochimica Acta*, 72(15):3733–3745.

Tarutani, T. (1989). Polymerization of Silicic Acid A Review. *Analytical Sciences*, 5(3):245–253.

Taylor, P. D., Jugdaohsingh, R., and Powell, J. J. (1997). Soluble Silica with High Affinity for Aluminum under Physiological and Natural Conditions. *Journal of the American Chemical Society*, 119(38):8852–8856.

Tedrow, J. C. F. (1966). Polar Desert Soils. *Soil Science Society of America Journal*, 30(3):381.

Tobler, D. J., Shaw, S., and Benning, L. G. (2009). Quantification of initial steps of nucleation and growth of silica nanoparticles: An in-situ SAXS and DLS study. *Geochimica et Cosmochimica Acta*, 73(18):5377–5393.

Tsukahara, R. and Kubota, M. (1990). Studies with desolvation in inductively coupled plasma-mass spectrometry. *Spectrochimica Acta Part B-Atomic Spectroscopy*, 45(6):581–589.

Urey, H. C. (1947). The thermodynamic properties of isotopic substances. . *Journal of the Chemical Society*, pages 562–581.

Van Cappellen, P., Dixit, S., and van Beusekom, J. (2002). Biogenic silica dissolution in the oceans: Reconciling experimental and field-based dissolution rates. *Global Biogeochemical Cycles*, 16(4):23–1–23–10.

van den Boorn, S. H. J. M., van Bergen, M. J., Vroon, P. Z., de Vries, S. T., and Nijman, W. (2010). Silicon isotope and trace element constraints on the origin of similar to 3.5 Ga cherts: Implications for Early Archaean marine environments. *Geochimica et Cosmochimica Acta*, 74(3):1077–1103.

van den Boorn, S. H. J. M., Vroon, P. Z., van Belle, C. C., van der Wagt, B., Schwieters, J., and van Bergen, M. J. (2006). Determination of silicon isotope ratios in silicate materials by high-resolution MC-ICP-MS using a sodium hydroxide sample digestion method. *Journal of Analytical Atomic Spectrometry*, 21(8):734–742.

van den Boorn, S. H. J. M., Vroon, P. Z., and van Bergen, M. J. (2009). Sulfur-induced offsets in MC-ICP-MS silicon-isotope measurements. *Journal of Analytical Atomic Spectrometry*, 24(8):1111–1114.

Volosov, A. G., Khodakovskiy, I. L., and N, R. B. (1972). Equilibria in the system SiO2-H2O at elevated temperatures along the lower three-phase curve. *Geochem. Internat.*, pages 362–377.

von Blanckenburg, F. (2005). The control mechanisms of erosion and weathering at basin scale from cosmogenic nuclides in river sediment. *Earth and Planetary Science Letters*, 237(3-4):462–479.

von Blanckenburg, F., Hewawasam, T., and Kubik, P. (2004). Cosmogenic nuclide evidence for low weathering and denudation in the wet, tropical highlands of Sri Lanka. *Journal of Geophysical Research-Earth Surface*, 109(F3).

Wada, K. and Kubo, H. (1975). Precipitation of amorphous aluminosilicates from solutions containing monomeric silica and aluminium ions. *Journal of Soil Science*, 26(2):100–111.

Walker, L. R., Wardle, D. A., Bardgett, R. D., and Clarkson, B. D. (2010). The use of chronosequences in studies of ecological succession and soil development. *Journal of Ecology*, 98(4):725–736.

Wasylenki, L. E., Rolfe, B. A., Weeks, C. L., Spiro, T. G., and Anbar, A. D. (2008). Experimental investigation of the effects of temperatureand ionic strength on Mo isotope fractionation during adsorption to manganese oxides. *Geochimica et Cosmochimica Acta*, 72(24):5997–6005.

Wasylenki, L. E., Weeks, C. L., Bargar, J. R., Spiro, T. G., Hein, J. R., and Anbar, A. D. (2011). The molecular mechanism of Mo isotope fractionation during adsorption to birnessite. *Geochimica et Cosmochimica Acta*, 75(17):5019–5031.

Welch, S., Beard, B., Johnson, C. M., and Braterman, P. (2003). Kinetic and equilibrium Fe isotope fractionation between aqueous Fe(II) and Fe(III). *Geochimica et Cosmochimica Acta*, 67(22):4231–4250.

West, A. J., Galy, A., and Bickle, M. (2005). Tectonic and climatic controls on silicate weathering. *Earth and Planetary Science Letters*, 235(1-2):211–228.

Willey, J. (1975a). Silica-alumina interactions in seawater. *Marine Chemistry*, 3(3):241–251.

Willey, J. D. (1975b). Reactions which remove dissolved alumina from seawater. *Marine Chemistry*, 3(3):227–240.

Wittmann, H., von Blanckenburg, F., Kruesmann, T., Norton, K. P., and Kubik, P. W. (2007). Relation between rock uplift and denudation from cosmogenic nuclides in river sediment in the Central Alps of Switzerland. *Journal of Geophysical Research-Earth Surface*, 112:–.

Wonisch, H., Gerard, F., Dietzel, M., Jaffrain, J., Nestroy, O., and Boudot, J. P. (2008). Occurrence of polymerized silicic acid and aluminum species in two forest soil solutions with different acidity. *Geoderma*, 144(3-4):435–445.

Yokoyama, T., Nakamura, O., and Tarutani, T. (1982). Polymerization of silicic acid adsorbed on aluminium hydroxide. *Bulletin of the Chemical Society of Japan*, 55(4):975–978.

Young, E. D., Galy, A., and Nagahara, H. (2002). Kinetic and equilibrium mass-dependent isotope fractionation laws in nature and their geochemical and cosmochemical significance. *Geochimica et Cosmochimica Acta*, 66(6):1095–1104.

Zambardi, T. and Poitrasson, F. (2011). Precise Determination of Silicon Isotopes in Silicate Rock Reference Materials by MC-ICP-MS. *Geostandards and Geoanalytical Research*, 35(1):89–99.

Ziegler, K., Chadwick, O. A., Brzezinski, M. A., and Kelly, E. (2005a). Natural variations of delta Si-30 ratios during progressive basalt weathering, Hawaiian Islands. *Geochimica et Cosmochimica Acta*, 69(19):4597–4610.

Ziegler, K., Chadwick, O. A., White, A. F., and Brzezinski, M. A. (2005b). (DSi)-Si-30 systematics in a granitic saprolite, Puerto Rico. *Geology*, 33(10):817–820.

Ziegler, K., Hsieh, J. C., Chadwick, O. A., Kelly, E. F., Hendricks, D. M., and Savin, S. M. (2003). Halloysite as a kinetically controlled end product of arid-zone basalt weathering. *Chemical Geology*, 202(3–4):461–478.